INVESTIGATION OF BASE-ISOLATED STRUCTURES DURING RECENT EARTHQUAKES AND COMPUTER SIMULATIONS UTILIZING NEAR-SOURCE LONG-PERIOD GROUND MOTIONS

Thesis by

Marvin Wilford Halling

In Partial Fulfillment of the Requirements
for the Degree of
Doctor of Philosophy

California Institute of Technology
Pasadena, California

1995

(Submitted January 3, 1995)

ACKNOWLEDGMENTS

I would like to thank my advisor, John Hall, for his continual support, understanding, and direction. He has been a worthy example for me to follow. I also appreciate the support of other faculty members in the Civil Engineering, the Applied Mechanics, and the Geological Sciences departments. Their courses were extremely challenging, but enjoyable (for the most part).

It has been a pleasure to work with Dave Wald and Tom Heaton. Their contributions to this thesis are very much appreciated. Dave was always helpful and willing to help in a moments' notice.

I would like to acknowledge W. Taylor, R. Bachman, J. Asher, and S. Hussain who provided me with the information required for the analyses.

The rigors of life as a graduate student would have been unbearable were it not for the friendship of fellow students. Thanks to the sub-basement crowd of first year, to the SOPS softball team, and to the Thursday lunch group. These good times will not soon be forgotten.

I appreciate the many people who turned Caltech from a cold academic institution, into a community of which I have felt a part. Thanks to Cecilia Lin for her many hours spent drawing figures and her cheerful outlook on life. Sharon Beckenbach, Denise Okamoto, Jackie Beard, Dana Young, and Connie Yehle have taken good care of me during my stay in Thomas Lab. Each has gone to extra lengths to help me whenever possible. Donna Covarrubias and Raul Relles have provided me with many hours of enjoyable conversation which I will miss.

Thanks to A.R.C.S. for the generous fellowship, and Caltech for the financial support during my graduate studies.

Thanks to my parents, W. Merrill and Bertha Halling, who gave me life and the direction I have needed through the years. Their constant love and encouragement have carried me through the difficult times.

Thanks to my four beautiful daughters, Meredith, Chelsea, Alexis, and Andrea. They have brought me more joy and happiness than I could have ever imagined. No father could be more blessed or proud.

Finally, thanks to my wife, Shelly, who is my greatest love and closest friend. None of this would have been possible without her unconditional love and years of sacrifice on my behalf. I will always be grateful.

ABSTRACT

Base isolation is a recently applied technology for building structures in the United States. To date, the three base-isolated buildings considered in this study have been subjected to earthquakes of varying magnitudes and epicentral distances. The records obtained from these instrumented buildings demonstrate low levels of excitation and small structural responses. In all cases, the maximum relative displacement of the roof to the foundation is less than 3 cm. However, an increasing quantity of near-source strong-motion records produces large spectral displacements of up to approximately 50-55 cm in the 2 to 2.5 sec period range for 15% damping. This suggests that long-period structures such as base-isolated structures would be vulnerable to these near-source ground motions.

The current study contains two major parts. Part One consists of the identification and analysis of three existing base-isolated buildings in Southern California. The identification and analysis utilize the recorded motions of these structures from past earthquakes. System identification is useful for understanding the extent to which the structures enter the nonlinear realm and how much their properties change.

Models are constructed assuming completely elastic three-dimensional superstructures, with idealized bi-linear hysteretic elements for the isolating bearings. The properties used in the bearing models were taken from tests of the actual bearings before installation. The models were then verified by comparing their responses computed using the various recorded foundation ground motions, with the recorded responses of the actual structures. The models were adjusted to minimize the error of several response quantities.

Part Two contains computer simulations for the three structural models developed in Part One subjected to large-amplitude near-source ground motions. These structural models were subjected to two classes of ground motions. The first is a sampling of near-source recorded motion from past moderate-to-large earthquakes. The second is a group of synthetic near-source motions generated for a hypothetical M 7.0 earthquake. In some cases, the lateral response of the models exceeds the isolation gap, indicating that the displacement barrier would be impacted.

In order to further study base-isolated buildings when the isolation bearings undergo large displacements, a typical base-isolated building (TBIB) model is used and the computer program 2D-BUMP is developed. This program includes the effects of a fully nonlinear superstructure, nonlinear springs acting as displacement barriers which engage at specified distances, and a tri-linear model for the elastomeric bearings. Using this model, several conclusions are drawn regarding the probable areal extent of damaging near-source ground motions from the M 7.0 event, as well as the behavior of base-isolated structures due to these near-source long-period ground motions.

TABLE OF CONTENTS

LIST OF TABLES

LIST OF FIGURES

1. Introduction

Under many conditions, seismic isolation is an effective method of earthquake-resistant construction. This method relies upon the reduction of accelerations and induced dynamic forces by lengthening the fundamental period of vibration. However, for a given structural mass and damping, an increase in period generally results in an increase in displacements. Contrary to conventional construction, a base-isolated structure accommodates the larger part of this displacement at a single location, namely, at the plane of isolation.

There are circumstances where the displacement at the plane of isolation may be significantly larger than conventional analysis would predict. One such circumstance is when the structure is located close to an earthquake source. Conventional analysis is based on accepted spectral shapes developed from recorded past earthquake motions. Unfortunately, this data is extremely sparse for sites located very close to the earthquake source, i.e., 0-15 km, especially for large events.

The purpose of this study is to investigate the behavior of base-isolated structures when subjected to near-source ground motions from a moderate-to-large seismic event. This includes results regarding the performance of a typical base-isolated structure model when contact with the displacement barrier occurs. Also included are simulations showing the area of vulnerability (i.e., the ground-surface area within which the typical base-isolated building model would contact its barrier) from a hypothetical M 7.0 blind thrust event.

In order to achieve these objectives, this thesis is divided into two major parts.

Part One consists of chapters 3, 4, and 5. Part One is dedicated to investigating the behavior of the three base-isolated structures during past earthquakes. Its goal is to determine the extent to which base-isolated structures have been driven into the nonlinear range and, in the process, acquire as much information as possible using system identification and analysis to calibrate the mathematical models used in the simulations of Part Two where strong near-source ground motions are used. Chapter 3 contains descriptions of the three existing buildings which are considered in this study, a description of the program MODE-ID [Beck, 1978], which was later extended to handle multiple inputs and outputs by Werner, Beck, and Levine [1989], and presents the system identification results. Chapter 4 contains the descriptions and development of the numerical models which were analyzed using the nonlinear base-isolation program 3D-BASIS [Nagarajaiah *et al.*, 1991] in conjunction with the program ETABS [Habibullah, 1992]. Also included in this chapter are the verification studies, which compare several response quantities of the modeled structures with the same response quantities recorded from the actual structures. Chapter 5 contains the conclusions for Part One of the thesis.

Part Two consists of chapters 6, 7, and 8. This part is dedicated to the study of the type of motion to be expected from a near-source event, and of the response of structural models to this type of ground motion. Chapter 6 contains a discussion of the available near-source recorded motions from recent moderate-to-large events. Because of pronounced directivity effects in the area close to a fault, the ground motions contain coherent velocity and displacement pulses which tend to be very severe for long-period structures. The nature of this motion will be further discussed in chapter 6. Also presented in this chapter is a set of synthetic ground motions, developed by D. Wald and T. Heaton which are very similar to those used by Heaton *et al.* [1994], for a hypothetical M 7.0 earthquake on a blind-thrust fault. The three numerical models from chapter 4 are again analyzed utilizing 3D-BASIS in conjunction with ETABS using a sampling of recorded near-source acceleration records as well as three synthetic acceleration histories from the above-mentioned set of synthetic motions.

In several cases, the analysis indicates that the resulting isolation bearing displacements of the numerical models exceed the isolation gap width, D_{TM}, for each particular structure. Since the program ETABS considers only linear elastic models, and the program 3D-BASIS has no provisions for a "gap" type element, any resulting bearing displacement which exceeds the specified D_{TM} indicates that the base would impact the displacement barrier (i.e., concrete wall, concrete pedestals, or steel chain restraints). Beyond that point, the behavior of the model would not reflect the behavior of an actual structure. Therefore, in order to further investigate the structural response if impact occurs, a typical base-isolated building (TBIB) model is developed in chapter 7. TBIB is designed following the provisions of the 1991 Uniform Building Code [ICBO, 1991]. Analysis using 3D-BASIS indicates that the TBIB also exceeds its D_{TM} distance, in some cases, when analyzed using the same sampling of near-source ground motions. Therefore, the nonlinear program 2D-BUMP was conceptualized and developed by J. F. Hall and M. W. Halling and written by J. F. Hall to analyze TBIB. This program includes modeling for a nonlinear yielding superstructure, a nonlinear isolation system, and a "gap" element for modeling the contact at each side of the 2-D model with a nonlinear spring. The TBIB was analyzed utilizing 2D-BUMP using the same recorded near-source acceleration records as well as the complete set of synthetic acceleration histories described in chapter 6. Also included in chapter 7 are the results and a discussion.

Chapter 8 contains the conclusions for Part Two of the thesis and general overall conclusions.

2. Background

The concept of seismic isolation is very old. Many researchers over the years have proposed systems intended to separate a structure from the destructive forces of an earthquake. Kelly [1986] writes,

> "The idea behind base isolation is a very simple one and it has been proposed again and again for at least a century. It is recognized that it is usually the horizontal ground movement in an earthquake that causes damage to the building, so that if it is possible at one and the same time to hold up the building and let the ground move underneath, then the damage will be greatly reduced. The idea is so appealing that inventors have found it irresistible and scores of ways to do this have been patented or proposed. Structural engineers have until now found all of these proposals highly resistible and have remained faithful to the conviction that a building should be firmly attached to its foundation."

Kelly goes on to outline developments from 1908 up to the construction in 1985 of the Foothills Communities Law and Justice Center which was the first base-isolated building in the United States.

The systems proposed consist of a designated location in the structure to release the structure from the proposed ground motions. Early ideas included the use of a layer of talc or sand to provide a low-friction surface. Others propose other types of sliding surfaces, or rolling systems. More recently, flexible systems have been proposed, such as rubber bearings or spring systems. Flexibility can also be achieved by allowing rocking of a structure, or by founding a structure on a soft foundation material [Kelly, 1986].

Tarics *et al.* [1984a] describe three items which are considered necessary to a modern base isolation system, 1) a method of decoupling the building and the foundation, 2) a method whereby utility lines could be made to withstand large relative displacement, and 3) a wind restraint system. Mayes [in Naeim, ed. 1989] has indicated that developments in five areas were responsible for elevating seismic isolation to practical reality. These are:

1) The design and manufacture of high-quality laminated elastomeric bearings.
2) The design and manufacture of mechanical energy-dissipating devices.
3) The development and acceptance of analysis software.
4) The ability to perform shaking-table tests.
5) The development and acceptance of procedures for estimating site-specific earthquake ground motions.

Although number one listed above was important for the development of base isolation, and the majority of applications to date have used laminated elastomeric bearings, there are many other systems which have been successfully applied in practice. Significant developments in each of these areas have occurred, and many base-isolated structures exist worldwide including a growing number in the United States. On closer examination of the numbered items above, there is still considerable uncertainty regarding the generation of site-specific response spectra. Whereas numbers 1, 2, 3, and 4 have developed at the rate of controlling technological advances, the development of reliable site-specific response spectra is hampered by the extremely sparse data set worldwide, especially from records located close to large earthquakes. This issue will be discussed in more depth in chapter 6.

The benefits of isolation are substantial and can be thought of as approaching the earthquake-induced structural vibration problem from a prevention point of view, rather than a cure. Stanton and Roeder [1991] itemize the benefits of isolation as:

1) Reduced floor accelerations and interstory drift.
2) Reduced (or no) damage to structural elements.

3) Better protection of building contents.

4) Concentration of nonlinear, large deformation behavior into one group of elements (the isolation bearings and dampers). These can be designed, tested, and built with great care to fulfill their purpose. Since the remainder of the structure will remain elastic (or nearly so) prediction of its response is more reliable and economical.

In order to appreciate the benefits of base isolation, it is important to understand the development and intent of current seismic building codes. Conventional buildings designed and constructed to meet the 1991 Uniform Building Code [ICBO, 1991] requirements, "...are intended to safeguard against major failures and loss of life, not to limit damage, maintain functions, or provide for easy repair" [SEAOC, 1990]. As building owners of certain types of structures become more sophisticated, many are seeking performance levels which are well above code-provided minimums, i.e., limited damage, maintenance of function, and provisions for easy repair. In conventional buildings, the goals of reduced floor accelerations and better protection of contents generally compete with the goals of reduced structural damage and reduced interstory drift. These competing goals necessarily lead to a compromise in design. However, through the use of seismic isolation technology, all of the above mentioned goals are more closely realizable. Figure 2.1 illustrates, in an idealized form, the benefits of seismic isolation.

Indeed, the potential benefits of seismic isolation are substantial. The demand is driven by owners who require higher performance than a "code building." This need for higher performance justifies examining these structures' response when subjected to ground motions which are possible, but may have a relatively long return period.

PART ONE

3. System Identification

System identification is used in this thesis as a systematic approach to determine the structures' modal periods, mode shapes, and estimated damping, as well as the level of response which each building experienced during each of the recorded earthquakes.

System identification techniques have been used for many years to determine best fit, or most probable linear system parameters [Söderström and Stoica, 1989; Natke and Yao, ed., 1988; Beck, 1978]. Researchers are also exploring techniques to identify nonlinear multi-degree-of-freedom systems from the input and output data [Peng, 1988; Udwadia and Kuo, 1981; Masri *et al.*, 1981; Distefano and Todeschini, 1976; Caughey, 1975]

In this study, the program MODE-ID [Beck, 1978], as extended by Werner, Beck, and Levine [1987], is used. This program estimates the modal parameters for the desired number of modes of a linear system. More details are given in section 3.2.

3.1 General Building Descriptions

The three buildings considered in this study are the Foothill Communities Law and Justice Center (FCLJC) located in Rancho Cucamonga, San Bernardino County, California; the Los Angeles County Fire Command and Control Facility (FCCF) located in East Los Angeles, Los Angeles County, California; and the University of Southern California University Hospital (USCUH) located in East Los Angeles, Los Angeles County, California. Each building was designed and constructed as a base-isolated structure using laminated steel and rubber bearing systems. Figure 3.1 is a map showing the location of each of these structures as well as the epicenters of the earthquakes considered in this study.

3.1.1 The FCLJC

The Foothill Communities Law and Justice Center (FCLJC) was built in 1985 and consists of a basement level, a ground or first floor, second floor, third floor, fourth floor, and roof level. The FCLJC is owned by the County of San Bernardino, and is utilized as a courthouse, legal center, and houses other government offices. The isolation level is below the basement, with substantial retaining walls all around, with an isolation gap between the wall and the structure. Figure 3.2 is a photograph of the FCLJC taken in 1994.

The structure is a steel braced frame building from the first floor to the roof, with concrete shear walls from the basement to the first floor. The floors are concrete over metal deck, and the structure is mounted on 98 high-damping rubber isolators. The isolators are 76 cm (30 in.) in diameter, 46 cm (18 in.) in height, with approximately 30.5 cm (12 in.) of effective rubber height.

The overall building is rectangular shaped in plan and measures 126 m (414 ft.) by 33.5 m (110 ft.) with approximately 21,180 m^2 (228,000 sq. ft.) of floor area. The roof height above adjacent grade is 18.3 m (60 ft.), and 22.6 m (74 ft.) above the top of the isolators. The estimated dead weight is 129,440 kN (29,100,000 lbs). Figure 3.5 is a schematic diagram of this building. For additional details refer to Kelly and Celebi [1984], Papageorgiou and Lin [1989], Kelly *et al.* [1991], or Maison and Ventura [1992].

The original design of this structure is based on stringent design criteria, namely, that the structure would sustain only minor structural damage in a maximum probable event and would not suffer permanent damage to the main structural members in a maximum credible event. The maximum probable event is defined as the maximum event that could be expected within a 100-year period. The maximum credible event is defined as the worst seismic event postulated within the geotechnical framework of the site [Tarics *et al.*, 1984a]. This maximum credible event (MCE) was postulated to be a M 8.3 event on the San Andreas fault located a distance of 21.7 km (13.5 miles) from the site. The site response spectrum developed for this MCE event was a 5% damped spectrum with a peak ground acceleration of 0.6 g and constant spectral velocity of 127 cm/sec (50 in/sec) in the period range from 0.8 seconds to 4 seconds. This level of spectral velocity corresponds to spectral displacements of 40 cm at a period of 2 seconds and 81 cm at a period of 4 seconds. Three existing time histories were scaled to conform to this response spectrum and used in analysis. The maximum displacement across the isolators (bearing displacement) calculated by the designers for this MCE event was 38.1 cm. (15 in.). The total seismic gap provided at the perimeter of the building is 40.6 cm (16 in.) [Kelly *et al.*, 1991].

3.1.2 The FCCF

The Los Angeles County Fire Command and Control Facility (FCCF) was built in 1989 and consists of a first floor or base level at adjacent grade, a second floor, and a roof level. The FCCF is owned by the County of Los Angeles, and is utilized as the emergency 911 dispatch center for the county, administered by the fire department. The isolation level is just below the first floor. Figure 3.3 is a photograph of the structure taken in 1994.

The structure is a steel braced frame with concrete fill over metal deck for the floors. The roof consists of insulating concrete over metal deck. Each of the 32 wide-flange steel columns is mounted on high-damping rubber isolators. The perimeter isolators contain a slack chain in the center of the unit, which engages at a horizontal offset of approximately 32 cm (12.5 in). These chains in the 20 perimeter isolation bearings act as the displacement restraint for this building should the bearing displacements exceed 32 cm. The chain in each isolator is designed to resist 125% of the design lateral bearing shear force of the isolator [Anderson, 1990]. The structure has no additional engineered lateral displacement barriers.

The overall building is rectangular shaped in plan, and measures 57.3 m (188 ft.) by 25.6 m (84 ft.) with a total floor area of approximately 2970 m^2 (32,000 sq. ft.). The roof height above adjacent grade and the top of the isolators is 10.1 m (33 ft.). The estimated building dead weight is 18,816 kN (4,230,000 lbs). Figure 3.13 is a schematic diagram of this building. For additional details, refer to Anderson [1990], Bachman *et al.* [1990], or Anderson *et al.* [1992].

The design of this structure is based on two postulated levels of shaking. The maximum probable event is defined as an event having a return period of 500 years. The maximum credible event is defined as an event having a return period of 1000 years. Site-specific design elastic response spectra were developed by Woodward Clyde, Inc. [Woodward-Clyde Consultants, 1988]. The 500-year spectra and 1000-year spectra have zero-period accelerations of 0.42 g and 0.50 g, respectively. The maximum credible event is characterized by the two horizontal components from the 1949 Western Washington earthquake, each scaled to conform to the developed response spectrum for the 1000 year event. The components were then factored by 1.0 and 0.3 and applied simultaneously in each direction [Anderson, 1990]. Analysis resulted in a maximum bearing displacement at the corner of the building of 21.8 cm (8.6 in).

3.1.3 The USCUH

The University of Southern California University Hospital (USCUH) was also built in 1989 and consists of a basement level, a ground or first floor, second through seventh floors, a roof, and a penthouse roof level. The USCUH is owned by National Medical Enterprises. The isolation level is below the basement with retaining walls surrounding the structure outside of the isolation gap. Figure 3.4 is a photograph of this building taken in 1994.

The structure is a steel braced frame building with a thick concrete slab at the basement level and concrete over metal deck on the other floors. The structure is mounted on a total of 149 isolating bearings, 68 lead / rubber isolators at the perimeter of the building and 81 elastomeric isolators at remaining columns. The bearings vary in size, from 55.9 cm (22 in) square, to 66.0 cm (26 in) square. They have an overall height of 34.6 cm (13.625 in).

The building has an "S" shape in plan, with a narrow throat in the middle and two lobes, one at each end. It has overall measurements of 92.4 m (303 ft.) in the north-south (longitudinal) direction, and 77.1 m (253 ft.) in the east-west (transverse) direction with a total floor area of 32,520 m^2 (350,000 sq. ft.). The penthouse roof is at a height of approximately 35.4 m (116 ft.) above adjacent grade and 39.9 m (131 ft.) above the isolators. The total dead weight for this structure is estimated to be 233,500 kN (52,500,000 lbs). Figure 3.21 is a schematic diagram of this building. For additional details regarding this structure, refer to Asher *et al.* [1990].

The design of this structure is based on two criteria. The first is the site-specific response spectra for maximum probable and maximum credible events as defined in Sec. 2312(d), 1A of Part 2, Title 24, C.A.C. [California, 1981] and the second is the ATC 3-06 spectrum for zone 4, soil type 1 (rock and stiff soils) [ATC, 1978] scaled by a factor of 1.2. Three existing time histories were scaled in the frequency domain to conform to these response spectra and used for design and analysis [KPFF, 1988]. The maximum bearing displacement at the corner of the building from these analyses was 17.0 cm (6.7 in.) which was multiplied by 1.5 and rounded up to 26.0 cm (10.25 in.), which is the distance to the concrete pedestals provided adjacent to the isolator bearings. A distance of 33.7 cm (13.25 in.) was provided to the surrounding retaining wall and for utility connection details.

3.2 System Identification Using MODE-ID

In this study, the computer program MODE-ID, developed by Beck [1978], and later extended to handle multiple inputs and outputs by Werner, Beck, and Levine [1987], has been utilized to determine the best-fit equivalent linear properties for each of the buildings. For each direction, a single input and multiple outputs were used. The identified properties include the modal periods of vibration, modal damping, modal participation factors, and the mode shapes.

Structural identification using MODE-ID is a relatively straight forward process for estimating the modal properties of a linear system. No structural model is required and classical normal modes are assumed. A linear model is excited by the input at multiple degrees-of-freedom. The parameters of the model are estimated by nonlinear least-squares matching of the model response and the measured response at each degree of freedom, that is, the mean-square output error is minimized using the output channels of data corresponding to the response signals. The optimal parameter estimates so obtained can be viewed as the most probable values given the data [McVerry and Beck, 1983; Beck, 1989]. Although a linear structure is assumed, the identification can be repeatedly applied from one time segment to another to determine changes in structural properties.

By using the foundation acceleration histories as input, and the structure acceleration histories as output, the "best-fit" parameters can be determined for each structure and each time segment. Table 3.1 summarizes the earthquake records from recent Southern California earthquakes used for identification of the three buildings.

The 1994 Northridge earthquake represents the largest amplitude excitation, to date, for the FCCF and the USCUH. Unfortunately, those data were not yet available from the California Division of Mines and Geology (CDMG) for analysis when this study was made.

The program MODE-ID is adept at identifying the best-fit modal periods. The identified equivalent modal viscous damping tends to vary considerably more and is generally less reliable. In some cases, this is a problem with the inadequate viscous damping model in the program used to model the hysteretic structure. For these reasons, more emphasis is placed on the identified modal periods.

EARTHQUAKE	FCLJC		FCCF		USCUH	
	Epicentral Distance (km)	Accel. F,B,R * (% of g.)	Epicentral Distance (km)	Accel. F,B,R * (% of g.)	Epicentral Distance (km)	Accel. F,B,R * (% of g.)
'85 Redlands M_L 4.8	30	4, 1, 3				
'86 Palm Springs M_L 5.9	90	2, 2, 4				
'87 Whittier M_L 6.1	47	3, 3, 6				
'90 Upland M_L 5.5	12	14, 5, 16				
'91 Sierra Madre M_L 5.8			28	8, 9, 11		
'92 Landers M_S 7.5	106	11, 9, 19	161	5, 8, 12	163	4, 4, 9

* F,B,R represents peak horizontal acceleration at the Foundation (below isolators), Base (above the isolators), and Roof.

TABLE 3.1 Summary of earthquakes, epicentral distances, and peak accelerations for the three studied buildings in Southern California.

3.2.1 The FCLJC

The FCLJC was instrumented by the California Division of Mines and Geology (CDMG), Strong Motion Instrumentation Program, in 1985. Since that time the instruments have recorded several events. Figure 3.5 shows an overall building elevation and the layout of the sensors. Also included are the building dimensions, the floor dead weights and mass moments of inertia. The records which have been released in a digitized form are from the 1985 Redlands [Huang *et al.*, 1986a], the 1986 Palm Springs [CSMIP, 1991], the 1987 Whittier [CSMIP, 1993a], the 1990 Upland [Huang *et al.*, 1990], and the 1992 Landers [CSMIP, 1993b] earthquakes. Other records for this building which have not been released in a digitized form at this time include the 1991 Sierra Madre, 1992 Big Bear, and the 1994 Northridge earthquakes.

Table 3.2 shows the identified equivalent linear periods and damping for the first five modes using MODE-ID. The recorded time histories have been divided into ten-second segments and the identification performed in each segment to demonstrate the variations in the identified properties as the amplitudes of the excitation and of the response change.

Figures 3.6 and 3.7 show the foundation motions from the Upland earthquake transverse (channel 12a, v, d) and longitudinal (channel 16a, v, d) directions, respectively. The Upland event, as well as the Redlands and Whittier events, contain the largest amplitude motions in the first ten seconds of the record. Figures 3.8 and 3.9 show the foundation motions from the 1992 Landers transverse (channel 12a, v, d) and longitudinal (channel 16a, v, d) directions, respectively. The Landers event and Palm Springs event contain the largest amplitude motions in the 30-40 second segment and the 20-30 sec segments, respectively. The system identification clearly shows the connection between the length of the periods of vibration and the intensity of shaking, a result of the nonlinearity of these structures.

EARTHQUAKE	Transverse				Longitudinal				Torsional	
	Mode 1		Mode 2		Mode 1		Mode 2		Mode 1	
time segment (sec)	per (sec)	damp (%)	per (sec)	damp (%)	per (sec)	damp (%)	per (sec)	damp (%)	per (sec)	damp (%)
1985 Redlands										
0- 10	.61	4.3	.28	9.9	.61	7.5	.27	7.5		
10- 20	.60	4.6	.26	13.0	.60	3.8	.27	4.9		
1986 Palm Springs										
0- 10	.63	8.2	.30	12.0	.60	6.0	.28	9.1		
10- 20	.65	4.8	.30	11.1	.65	6.3	.29	6.5		
20- 30	.64	6.5	.31.	10.0	.65	5.6	.29	4.7		
30- 40	.63	4.4	.32	12.6	.62	6.0	.27	9.8		
1987 Whittier										
0- 10	.65	4.6	.29	9.1	.66	5.1	.29	5.4		
10- 20	.63	5.1	.31	12.3	.66	6.9	.30	6.7		
20- 30	.64	5.5	.28	8.3	.65	6.7	.29	7.3		
30- 40	.61	6.0	.27	7.4	.62	5.8	.28	6.6		
1990 Upland										
0- 10	.79	6.9	.36	12.9	.80	6.3	.33	8.5	.80	11.
10- 20	.76	7.3	.34	17.3	.76	5.2	.32	7.8	.73	4.1
20- 30	.71	6.5	.33	17.1	.71	5.7	.31	6.8	.72	0.1
30- 40	.69	7.3	.28	9.5	.69	4.8	.28	6.1	.65	13.
1992 Landers										
0- 10	.69	4.5	.29	11.2	.71	8.2	.29	6.6	.67	5.1
10- 20	.77	6.6	.33	13.7	.78	7.2	.33	11.0	.75	2.1
20- 30	1.03	19.0	.40	9.9	.96	20.5	.38	14.2	-	-
30- 40	1.04	25.6	.39	3.7	1.04	20.1	.45	-	.89	14.
40- 50	.86	16.7	.39	4.4	.84	13.2	.36	9.6	.90	15.
50- 60	.79	8.2	.34	13.9	.79	8.6	.35	9.0	.79	4.1
Fixed Base										
Chapter 4 model	.62				.72				.51	
[Huang *et al.*, 1993]	.57				.61				.49	
[Kelly *et al.*, 1991]	.62				.72				-	
Design Isolated										
[Huang *et al.*, 1993]	2.0				2.0				-	
Identified, Upland										
[Huang *et al.*, 1993]	.75				.74				-	
Identified, Landers										
[Huang *et al.*, 1993]	.73				.76				-	

TABLE 3.2 FCLJC identified modal periods and equivalent viscous damping values.

The input and output channels used to identify the first two modes in the transverse direction are channel 12a for input, and channels 9a, 7a, and 6a for output.

The notation for response records is the station, followed by an a, v, or d for acceleration, velocity, or displacement, respectively. The input and output channels used to identify the first two modes in the longitudinal direction are channel 16a for input, and channels 15a and 14a for output. The input and output channels used to identify the first torsional mode are channels (13a-11a)/2 for input, and channels (10a-8a)/2 and 6a-5a for output.

Also given in table 3.2 are values for the structure-modeled fixed-base period, modeled base-isolated period, and determined modal periods [Huang *et al.*, 1993] from spectral analysis. The fixed-base model values from chapter 4 of this study are in good agreement with those of other studies. The identified period of the structure for the Upland earthquake is also in reasonable agreement with the identified period from Huang *et al.*. [1993], however, the periods identified here for the Landers event are significantly longer than those reported by Huang *et al.*. [1993] for this event.

For the Redlands, Whittier, and Upland earthquakes, both the transverse and longitudinal first modes show several trends. The periods begin slightly longer than the building fixed base period, and then as the excitation subsides, the period decreases toward the fixed base period of the structure. The damping tends to be essentially constant for these events. The second modal periods for both the transverse and longitudinal directions tend to be essentially constant. For the Palm Springs and Landers earthquakes, which have significantly larger epicentral distances (see table 3.1), the first modal periods in both directions lengthens, and then shortens again at the end of the record. Also of note is the modal damping for the transverse and longitudinal directions first mode during the Landers event. The damping increases to 25.6% and 20.5% of critical damping in the transverse and longitudinal directions, respectively, and then decreases. For the small-strain range, the equivalent viscous damping for the isolators actually can get quite large, possibly into this range.

Figure 3.10 shows the identified first transverse, longitudinal and torsional mode shapes from different segments of the time histories. In this figure, discounting the anomalous torsional Landers 0-10 second curve, as the amplitude of excitation increases, the displacement across the isolator bearings becomes a larger portion of the first modal response. Figures 3.11 and 3.12 show the roof and base displacements for the Upland and Landers events. Included on these plots are the displacements at the edge of the building floors as a result of torsion. Figure 3.11(a) consists of channels 6d-12d for the solid curve, and (6d-5d)-(13d-11d)/2 for the dashed curve. Figure 3.11(b) consists of channels 9d-12d for the solid curve, and (10d-8d)/2 - (13d-11d)/2 for the dashed curve. Figure 3.12 is plotted using the same channels as figure 3.11.

3.2.2 The FCCF

The FCCF was instrumented by CDMG in 1989. Figure 3.13 shows an overall building elevation, the layout of the sensors, dimensions, floor weights, and mass moments of inertia. The records which have been released in digitized form are those from the preliminary releases of the 1991 Sierra Madre [CSMIP, 1994a] and the 1992 Landers earthquake [CSMIP, 1994b]. Other records which have not been released in a digitized form at the time of this study include the 1992 Big Bear, and the 1994 Northridge earthquakes.

Table 3.3 shows the identified equivalent linear periods and damping for the first three modes using MODE-ID. The identification is again performed in ten-second segments in order to demonstrate the variations in the identified properties as the amplitudes of the excitation and of the response change.

Figures 3.14 and 3.15 show the foundation motions for the Sierra Madre transverse (channel 6a, v, d) and longitudinal (channel 5a, v, d) directions, respectively. Figures 3.16 and 3.17 show the foundation motions for the Landers transverse (channel

6a, v, d) and longitudinal (channel 5a, v, d) directions, respectively. The Sierra Madre record contains the largest amplitude motions in the first ten seconds of the record, whereas for the Landers event, the most intense shaking occurs in the 30-40 second segment.

EARTHQUAKE	**Transverse**				**Longitudinal**				**Torsional**	
	Mode 1		Mode 2		Mode 1		Mode 2		Mode 1	
time segment (sec)	per (sec)	damp (%)	per (sec)	damp (%)	per (sec)	damp (%)	per (sec)	damp (%)	per (sec)	damp (%)
1991 Sierra Madre										
0- 10	.77	32.5			.85	20.5			.82	-1.7
10- 20	.69	23.4			.81	21.8			.75	-
20- 30	.61	21.4			.63	23.1			.52	6.7
30- 40	.56	22.2			.55	25.0			.46	24.
40- 50	.46	37.7			.45	27.6			.36	37.
50- 60	.34	20.3			.36	20.0			.36	34.
1992 Landers										
0- 10	.47	24.7			.47	24.3			.40	23.
10- 20	.53	14.7			.54	11.2			.46	4.5
20- 30	.90	21.1			.92	19.8			.85	2.6
30- 40	1.06	17.3			1.01	15.8			1.00	7.2
40- 50	1.05	19.8			.99	20.9			.89	9.3
50- 60	.91	22.7			.87	21.6			.79	24.
60- 70	.80	21.7			.76	21.1			.70	21.
70- 80	.77	24.1			.73	22.4			.66	24.
80- 90	.67	32.5			.66	28.1			.57	21.
90- 100	.63	35.7			.60	27.3			.54	-
100- 106	.62	32.1			.55	26.3			.39	32.
Fixed Base										
Chapter 4 model	.42				.38				.23	
[Bachman *et al.*, 1990]	.40				.36				.13	
Design Isolated										
[Bachman *et al.*, 1990]	2.17				2.17				1.85	
Identified, Sierra Madre										
[Huang *et al.*, 1993]	.91				.86				-	
Identified, Landers										
[Huang *et al.*, 1993]	1.05				1.00				1.05	

TABLE 3.3 FCCF Identified modal periods and equivalent viscous damping values.

The input and output channels used to identify the first mode in the transverse direction are channels 6a+7a for input, and channels 9a+11a and 14a+16a for output. The input and output channels used to identify the first mode in the longitudinal direction are channel 5a for input, and channels 8a and 13a for output. The input and output channels used to identify the first torsional mode are channels (6a-7a) for input, and channels (9a-11a) and (14a-16a) for output.

Also included in table 3.3 are values for the structure-modeled fixed-base period, modeled base-isolated period, and determined modal periods [Huang *et al.*, 1993] from spectral analysis. The fixed-base model values from chapter 4 of this study are in good agreement with the values from Bachman *et al.* [1990]. The agreement of the identified values with those identified by Huang *et al.* [1993] is very good, except for the difference in the transverse direction from the Sierra Madre earthquake.

For both the Sierra Madre and Landers earthquakes, the first modal period for each direction significantly lengthens during the largest amplitude motions. The damping does not seem to follow a recognizable trend. Also, the 0-10 second segment of the Sierra Madre earthquake indicated a negative damping ratio for the torsional mode. This could be a result of translational input excitation adding to the torsional response output, through excitation of the fundamental transverse mode whose modeshape includes a torsional component. The torsion in the first transverse mode may also be significant despite symmetry of the building because of the "grout tile" constraint at the main entrance which will be more fully discussed in section 4.2.2.

Figure 3.18 shows the identified first transverse, longitudinal and torsional mode shapes from different segments of the time histories. In this figure, as the amplitude of excitation increases, the displacement across the isolator bearings becomes a larger portion of the first modal response. Figures 3.19 and 3.20 show the roof and base displacements for the Sierra Madre and Landers events. Included on these plots is the edge displacement of the structure due to torsion of the floor. Figure 3.19(a) consists of channels (16d+14d)/2 - (7d+6d)/2 for the solid curve, and (16d-14d)/2 - (7d-6d)/2 for the dashed curve. Figure 3.19(b) consists of channels (11d+9d)/2 - (7d+6d)/2 for the solid curve, and (11d-9d)/2 - (7d-9d)/2 for the dashed curve. Figure 3.20 is plotted using the same channels as figure 3.19.

The torsional response is a significant fraction of the overall displacements, particularly in the Sierra Madre earthquake (figure 3.19). This is particularly interesting, since the FCCF building has the most symmetric lateral force resistance system of the three buildings studied. Additional discussion regarding this torsional response can be found in section 4.2.2.

3.2.3 The USCUH

The USCUH was also instrumented by CDMG in 1989. Figure 3.21 shows an overall building elevation, the layout of the sensors, the building dimensions, the floor weights, and floor mass moments of inertia. The only record which has been released in digitized form is the preliminary release of the 1992 Landers [CSMIP, 1994c] earthquake. Other records which were not released in a digitized form at the time of this study include the 1991 Sierra Madre, 1992 Big Bear, and the 1994 Northridge earthquakes.

Table 3.4 shows the identified equivalent linear periods and damping for the first five modes using MODE-ID. The recorded time history has been divided into ten-second segments and the identification performed in each segment to demonstrate the variations in the identified properties as the amplitude of the excitation and of the response change. Figures 3.22 and 3.23 show the foundation excitation from the 1992 Landers transverse (channel 7a, v, d) and longitudinal (channel 5a, v, d) directions, respectively. The 30-40 sec segment of the Landers event contains the most intense motions for that record.

EARTHQUAKE	**Transverse**				**Longitudinal**				**Torsional**	
	Mode 1		Mode 2		Mode 1		Mode 2		Mode 1	
time segment (sec)	per (sec)	damp (%)	per (sec)	damp (%)	per (sec)	damp (%)	per (sec)	damp (%)	per (sec)	damp (%)
1992 Landers										
0- 10	.89	3.5	.40	12.3	.86	8.1	.36	7.5	.74	-1.5
10- 20	1.16	10.9	.43	9.1	.97	13.1	.44	14.1	.71	0.4
20- 30	1.19	8.1	.51	7.1	1.13	12.0	.48	9.8	1.09	3.6
30- 40	1.22	11.4	.50	10.3	1.16	12.3	.48	9.7	.90	-6.0
40- 50	1.20	8.8	.51	5.6	1.13	10.1	.46	9.0	1.01	-9.2
50- 60	1.16	7.4	.49	9.3	1.11	12.5	.44	9.0	.97	2.3
60- 70	1.10	10.7	.44	10.2	1.05	12.8	.41	9.6	.80	2.1
70- 80	1.08	7.4	.45	9.2	1.05	11.9	.44	6.8	1.04	6.5
80- 90	1.00	10.7	.42	8.0	.96	13.0	.41	9.8	1.03	-0.6
Fixed Base										
Chapter 4 Model	1.35				1.13				0.84	
[Huang *et al.*, 1993]	1.00				1.00				-	
Design Isolated										
[Huang *et al.*, 1993]	2.21				2.30				1.92	
Identified (Landers)										
[Huang *et al.*, 1993]	1.28				1.24				-	

TABLE 3.4 USCUH Identified modal periods and equivalent viscous damping values.

The input and output channels for the transverse direction are channels (6a+8a)/2 for input, and channels (10a+12a)/2, (14a+16a)/2, (18a+20a)/2, and (22a+24a)/2 for output. The input and output channels for the longitudinal direction are channels 5a for input, and channels 9a, 13a, 17a, and 21a for output. In the torsional direction, the inputs and outputs are channels (8a-6a)/2 for input, and channels (12a-10a)/2, (16a-14a)/2, (20a-18a)/2, and (24a-22a)/2 for output.

The identified modal periods indicate that the fixed-base periods of the models from chapter 4 as well as those reported by Huang *et al.* [1993] may be higher than the actual fixed-base period of the structure. The torsional mode exhibits negative damping in several segments of the Landers earthquake. Again, this is probably the result of translational excitation producing a torsional response through excitation of the fundamental transverse mode whose modeshape includes a torsional component.. Due to the very non-regular shape of this building in both plan and elevation, some torsional response is expected. The identified periods are slightly lower than those identified by Huang *et al.* [1993] for the Landers earthquake.

Again, as noted with the FCLJC and the FCCF structures, the first transverse and longitudinal modal periods begin low, increase, and then decrease again during the Landers event. However, the damping does not follow a similar trend.

Figure 3.24 shows the identified first transverse, longitudinal and torsional mode shapes from different segments of the time histories. In this figure, as the amplitude of excitation increases, the displacement across the isolator bearings becomes a larger portion of the first modal response. Figure 3.25 shows the roof and base displacements for the Landers events. Included on these plots is the displacement at the edge of the structure which can be attributed to torsion. Figure 3.25(a) consists of channels (22d+24d)/2 - (6d+8d)/2 for the solid curve, and (24d-22d)/2 - (8d-6d)/2 for the dashed curve. Figure 3.25(b) consists of channels (10d+12d)/2 - (6d+8d)/2 for the solid curve, and (12d-10d)/2 - (8d-6d)/2 for the dashed curve. The displacement of the edge of the building due to torsion is nominal, and accounts for only a small percentage of the transverse response of the building at both the base and the roof.

Conclusions will be given in chapter 5.

4. Numerical Models

This chapter is dedicated to obtaining numerical models for each of the three existing buildings. These models consist of three-dimensional linear-elastic superstructure models (models of the complete structure above the isolation system) which are analyzed using the program ETABS [Habibullah, 1992] as if they were fixed-base structures. From this analysis, the low mode (any number desired, usually between 9 and 15 modes) periods and mode shapes are obtained and input to the program 3D-BASIS [Nagarajaiah *et al.*, 1991]. Obtaining the required information for input into 3D-BASIS can be as simple as determining the masses, stiffnesses, and eccentricities for a shear structure with the eigenvalues and eigenvectors determined by any chosen method, or can involve the use of a linear-elastic program, such as ETABS, to analyze a complex structure. The program 3D-BASIS utilizes a bi-linear force-displacement curve to idealize the nonlinearity of each of the high-damping rubber or lead / rubber isolation bearings. The isolation components are assumed to all be at the same level of the structure. The isolation system is also assumed rigid in the vertical direction, and torque resistance of individual bearings is neglected [Nagarajaiah *et al.*, 1991]. The assumption of a vertically rigid isolation system is commonly made in analysis for simplicity since the isolation bearings are several orders of magnitude stiffer in the vertical direction than in the horizontal directions. The program utilizes the simplified information obtained from the superstructure analysis and combines it with a complete nonlinear time history analysis incorporating the force-displacement curve information for each isolation unit. However, due to the limitations in the bi-linear force-displacement idealization, both a small-strain and a large-strain isolation bearing relationship are constructed for each model. That is, for the FCLJC model, there is both a small-strain version and a large-strain version. Similarly for the FCCF and the USCUH models. In this chapter, the small-strain models are used. In chapter 6, the large-strain models are used. For both the small and large-strain models, the same properties of the superstructure (the ETABS portion of the analysis) are maintained.

For the base-isolation system, the idealized bearing force-displacement curves attempt to follow the hysteretic curves for each bearing type which were determined from bearing testing prior to installation. During the verification section of this chapter, the stiffness values determined from the force-displacement curves are adjusted (for the small-strain model only) using the information taken from the actual structures during past earthquakes. The adjustment of the small-strain models is needed because of the large variability of the properties of the isolation bearings under small strains. At larger strains, the force-displacement curves tend to be more predictable. Since the models consist of two parts, the superstructure and the isolation system, the verification of the small-strain models is also important for the large-strain modeling of chapter 6.

4.1 Structural Models

3D-BASIS is a program used in conjunction with a linear-elastic analysis of the superstructure. 3D-BASIS is capable of explicitly modeling isolation systems which consist of combinations of hysteretic, frictional, and viscous devices, and linear springs. The nonlinear force-displacement characteristics of the isolation components are modeled explicitly. In the following sub-sections, the details of the modeling of each structure are given.

4.1.1 The FCLJC Structural Model

The FCLJC was modeled in ETABS using rigid-in-plane diaphragms, 30.5 cm (12 in.) and 35.6 cm (14 in.) concrete shear walls, and steel concentrically-braced frames as the primary lateral load carrying system. All dimensions, members, materials, and details were taken from the structural drawings provided by Mr. William Taylor, the structural engineer of record for this building, of Taylor and Gains Associates, Pasadena, California. Estimated structural weights were taken from Maison and Ventura [1992]. Figure 4.1 shows the wire frame model used in the analysis of the superstructure.

As noted previously, the linearly modeled superstructure is mounted on 98 nonlinear isolation bearings. Seven types of bearings were used to accommodate the wide range of vertical loads and horizontal stiffness requirements. These seven types were achieved using two different high-damping rubber compounds and four rubber thickness-steel shim combinations [Kelly and Celebi, 1984]. However, all the bearings had consistent overall dimensions of 76.2 cm (30 in) in diameter and 38.1 cm (15 in) in height.

Since the seven different bearing types are well distributed at the base of the structure, it was decided to use averaging to model the bearings. This was based on experimental test results for each bearing when strained to 2% shear strain, 10% shear strain, and 50% shear strain, and averaging the lateral force required to achieve each of these strain levels for all 98 bearings. The isolation system was then modeled using 98 of the "average" bearings, one located at the base of each column. Figure 4.2 shows the average test results for the stiffest and the softest bearing types. The open dots from the tests are plotted at 2%, 10%, and 50% shear strain locations. Figure 4.2 also shows the bi-linear small-strain model and the bi-linear large-strain model (used only in Part Two) for an "average" bearing.

4.1.2 The FCCF Structural Model

The FCCF was modeled using ETABS as a two-story structure with rigid-in-plane diaphragms, and concentrically-braced perimeter frames as the primary lateral load carrying system. All dimensions, members, materials, and details were taken from structural drawings provided by Mr. Robert Bachman of Fluor Daniel, Inc., of Irvine California. Fluor Daniel is the firm responsible for the structural design of the building. Estimated structure dead weights and other information were obtained from a design fact sheet provided by Fluor Daniel, Inc. Figure 4.3 shows the ETABS wire frame model used in the superstructure analysis.

The FCCF was modeled using 32 nonlinear high-damping rubber isolators. Two types of isolators were used in this building and both types were tested prior to installation. Twenty exterior units, placed around the perimeter of the structure and each containing a steel chain, are represented by the bi-linear small-strain and large-strain models shown in figure 4.4. Also included in this figure is a hysteresis curve taken from actual exterior bearing tests [Seible and Priestley, 1989]. These laminated rubber bearings contain a vertical cylindrical hole in the center of the isolation units. The steel chain is attached to the top and bottom steel base plates, with the links remaining slack inside the bearings. As mentioned previously, at approximately 31.8 cm (12.5 in), the links become fully extended and exert a tensile force to resist further lateral displacements. It should be noted that the increased stiffness when the chain engages is not considered in this analysis. Twelve units, listed as interior bearings do not contain the restraining chain and have shearing properties which are different from the exterior bearings. The small-strain and large-strain models for the interior bearings are shown in figure 4.5. Also included in this figure is a hysteresis curve taken from actual interior bearing tests [Seible and Priestley, 1989]. The large-strain bearing models are only used in Part Two.

4.1.3 The USCUH Structural Model

The USCUH was modeled as an eight-story structure with rigid-in-plane diaphragms, and concentrically-braced perimeter frames as the primary lateral load carrying system. All dimensions, members, materials, weights, and details were taken from structural drawings, structural calculations, and a previous model provided by Mr. Jefferson Asher, the structural engineer of record for this building, and Mr. Saif Hussain of KPFF Consulting Structural Engineers in Santa Monica, California. Figure 4.6 shows the ETABS wire frame model used in the superstructure analysis.

The USCUH is mounted on 149 nonlinear isolation bearings. Four different types of bearings were utilized with varying vertical load carrying capacities, shear stiffness, and equivalent damping ratios. Type 1 bearings are 55.9 cm (22 in.) square, with a 14.0 cm (5.5 in.) lead core in the center. There are 59 type 1 bearings installed and figure 4.7 shows the actual test results of the bearing [KPFF, 1988], and the bi-linear small-strain and large-strain representations used for this type bearing. Type 2 bearings are 55.9 cm (22 in.) square, with no plug in the center. There are 8 of these installed. The displacement and force coordinates are given here for type 2 and type 3 bearings since no figure is included for these two bearing types. The five displacement and force coordinates (given in cm and kN) which define the force-displacement loop for the bi-linear small-strain model of the type 2 bearings are (.56, 14.7), (1.27, 31.8), (.15, 2.4), (-1.27, -31.8), and (-.15, -2.4). The coordinates for the large-strain force-displacement loop are (1.27, 31.8), (26.0, 278), (23.5, 215), (-26.0, -278), and (-23.5, -215). Type 3 bearings are 66.0 cm (26 in.) square, with a 14.0 cm (5.5 in.) lead core in the center. There are 9 of these installed. The five displacement and force coordinates (given in cm and kN) which define the force-displacement loop for the bi-linear small-strain model of the type 3 bearings are (.14, 66.4), (.96, 123), (.67, -9.9), (-.96, -123), and (-.67, 9.9). The coordinates for the large-strain force-displacement loop are (.96, 123), (26.0, 444), (24.1, 198), (-26.0, -444), and (-24.1, -198). Type 4 bearings are 66.0 cm (26 in.) square, with no plug in the center. There are 73 type 4 bearings and figure 4.8 shows an actual testing hysteresis loop [KPFF, 1988] plotted with the bi-linear small-strain and large-strain representations used for this type bearing. Since 89% of the bearings were either type 1 or type 4, they were the types used in the prototype testing. The properties of type 2 and type 3 bearings were inferred from the prototype test results of types 1 and 4 bearings [KPFF, 1988]. Each of the 149 bearings was individually represented in 3D-BASIS and located with its proper coordinates. The lead / rubber bearings are generally located at the building perimeter, with the elastomeric bearings located at the interior columns. The large-strain bearing models are used only in Part Two.

4.2 Verification of Models

Since each of the three structures in this study has been subjected to actual ground motions, and the structural response recorded, this information can be utilized to verify the numerical models. This recorded data can be considered as a full-scale dynamic test. It should be noted that the amplitude of response from these past earthquakes is very small, and the model verification is primarily validated for the small-strain models. Additionally, accurate modeling of the nonlinear behavior can be difficult to capture at small strains due to the extreme changes in stiffness at small strains, as well as unintended motion restraints at small displacements. These restraints are a result of structural details that tend to resist motion at the isolation plane, especially at very small displacement levels. For example, all these base-isolated structures have some details which are designed to release when motion occurs. These include such things as pop-out floor sections at entrances, sliding details at elevators and other utility connections, and locations of unintended friction which resist small levels of motion. However, achieving some level of correlation between actual motions and modeled (predicted) motions is a valuable starting point for predictive modeling.

For all models, 4% of critical damping was used for the superstructure. The small-strain nonlinear hysteresis in the bearings was adjusted as necessary and 2% equivalent viscous damping was included in the isolation system to approach a more realistic decaying response with time. Adjustments in stiffness were used in an attempt to find a balance in calibrating the peak model bearing displacements, the peak first-story shear, and the peak roof acceleration to the actual recorded quantities. This calibrating was done for the Landers earthquake only. The foundation motions for the two horizontal directions were applied simultaneously in the model. The three mentioned peak quantities were monitored for each direction to give 6 peak quantities, as the stiffness of the small-strain bearing model was adjusted. The ratio of secondary stiffness to initial stiffness (α) was maintained. This process was continued until the differences in the modeled quantities and recorded quantities were minimized. There were two reasons for using the Landers earthquake motion for this calibration. One, the recorded motions were available for all three structures; and two, the recorded motions from the Landers event are the largest amplitude motions available in most cases and carry a significant long-period content even at the large epicenter-to-site distances.

All model response quantities are taken at the center of mass for the floor level in question. For torsional responses, the rotation calculated is then multiplied by one half of the length, L of the particular building. This "torsional displacement" can, therefore, be thought of as the displacement of the edge of the floor diaphragm due to rotation of that diaphragm. The recorded response quantities are the processed acceleration, a, the velocity, v, and the displacement, d, taken from the digitized records as referenced in section 3.2. The California Division of Mines and Geology (CDMG) Strong Motion Instrumentation Program (CSMIP) staff processed and integrated the acceleration records to achieve the velocity and displacement histories.

The following correlative studies verify that the models developed for the existing buildings can reasonably produce the real structures' response quantities when excited by the given ground excitations.

4.2.1 Verification of the FCLJC Model

The small-strain average isolator model used to verify the model of the FCLJC was stiffened in order to reduce the model bearing displacements and to increase the roof accelerations to more closely approximate the actual recorded displacements and accelerations. The average isolation bearing model shown in figure 4.2 shows a yield force of 53.8 kN (12,100 lbs), a yield displacement of .61 cm (.24 in), and a ratio of secondary stiffness to initial stiffness of 0.327. The modified model maintains the same yield force and ratio, but with a yield displacement of 0.38 cm (.15 in.). Since the Redlands, the Palm Springs, and the Whittier earthquakes are all of considerably smaller amplitude than the Upland and Landers events (see table 3.1), only the latter two will be considered here.

The resulting comparisons of displacements across the isolation bearings are given in figure 4.9 for the Upland earthquake, figure 4.10 for the Landers earthquake, and figure 4.11 for the torsional response from both the Upland and Landers earthquakes. The channels used for these plots are tabulated in table 4.1. The summary of structure peak displacements is given in figure 4.12. The channels used to determine these peaks are also given in table 4.1.

	BASE	2nd Floor	Roof
Recorded			
Transverse	(10d+8d)/2 - (13d+11d)/2	7d - (13d+11d)/2	6d - (13d+11d)/2
Longitudinal	15d - 16d		14d - 16d
Torsional	(10d-8d)/2 - (13d-11d)/2		(6d-5d) - (13d-11d)/2
Modeled			
Transverse	Tran. Base Disp	Tran. 2nd Disp	Tran. Roof Disp
Longitudinal	Long. Base Disp	Long. 2nd Disp	Long Roof Disp
Torsional	Base Rotation x L/2	2nd Rotation x L/2	Roof Rotation x L/2

TABLE 4.1 FCLJC station channels used to determine relative displacements for figures 4.9 to 4.12.

The base shear comparisons are given in figures 4.13 and 4.14, with the summary of structural story shears given in figure 4.15. The recorded base shears were calculated by multiplying each story mass by the interpolated story acceleration and summed from roof to base. All base shear plots are divided by the total structure weight and given as a fraction of the building weight. Specifically, the transverse (F_T), longitudinal (F_L), and torsional (F_{Tor}) base shears are given by,

$$F_T = \frac{6a\left(M_R + \frac{2}{3}M_4 + \frac{1}{3}M_3\right) + 7a\left(\frac{1}{3}M_4 + \frac{2}{3}M_3 + M_2\right) + 9a\left(M_1 + M_B\right)}{W_{total}} \qquad 4.1$$

$$F_L = \frac{14a\left(M_R + \frac{3}{4}M_4 + \frac{1}{2}M_3 + \frac{1}{4}M_2\right) + 15a\left(\frac{1}{4}M_4 + \frac{1}{2}M_3 + \frac{3}{4}M_2 + M_1 + M_B\right)}{W_{total}} \qquad 4.2$$

$$F_{Tor} = \frac{(6a-5a)\left(MI_R + \frac{3}{4}MI_4 + \frac{1}{2}MI_3 + \frac{1}{4}MI_2\right) + \left(\frac{10a-8a}{2}\right)\left(\frac{1}{4}MI_4 + \frac{1}{2}MI_3 + \frac{3}{4}MI_2 + MI_1 + MI_B\right)}{MI_{total}(g)}$$

4.3

where M_i are the masses for each floor (R, 4, 3, 2, 1, B), MI_i are the mass moment of inertia quantities for each floor, W_{total} is the total weight of the building, and MI_{total} is the sum of all the mass moment of inertia quantities for the building. The shear quantities at any floor can be calculated using this formula considering the appropriate mass terms for the floor in question and those floors above that floor. For the FCLJC building, since the basement level is extremely stiff compared to the rest of the superstructure, the horizontal motions at the first-floor level are assumed to be the same as the motions at the base, rather than interpolating between the motions at the base and those at the second floor.

Recorded base shear vs. recorded isolation-level displacement plots are shown in figures 4.16 and 4.18 for each earthquake in the transverse direction only. Similar plots are included in figures 4.17 and 4.19 for the complete modeled structure. The trend of the loops tends to soften and to get significantly wider with larger amplitude motions. This is consistent with the models. Figure 4.18 has been plotted in time windows to more clearly show the changes in the hysteresis loops through the duration of the strong motion. Although the force-displacement curve for a single isolator is bi-linear, the model hysteresis loops are not bi-linear because of the interaction of all the isolators. The general shape and size of the loops reasonably match the loops determined from the recorded motions, keeping in mind that the double integration and subtraction involved in obtaining the recorded motions introduces some error.

Also included for comparison are the first-story shears (the story shear for the level just above the base level) in figures 4.20 and 4.21, calculated using the appropriate terms from equations 4.1, 4.2, and 4.3. The roof accelerations are plotted in figures 4.22 and 4.23. These are plots of channel 6a for figure 4.22(a) and 4.23(a), and channel 14a for figure 4.22(b) and 4.23(b).

As can be seen, the general fit of the recorded response quantities to the modeled quantities is very good which implies that the model is accurate in capturing the behavior of the actual structure.

4.2.2 Verification of the FCCF Model

Both the exterior and the interior isolating bearings were stiffened in order to more closely approximate the actual recorded response accelerations, shears, and displacements of this structure for the 1992 Landers earthquake. The process of modification was identical to that used for the FCLJC and described earlier. The exterior bearing model shown in figure 4.4 was modified from a yield displacement of 0.89 cm (.35 in.) to a yield displacement of 0.43 cm (.17 in.) to increase the initial stiffness. The interior bearing model shown in figure 4.5 was changed from a yield displacement of 1.02 cm (.40 in.) to a yield displacement of 0.51 cm (.20 in.) to also increase the initial stiffness. The ratio of the initial stiffness to the secondary stiffness remained unchanged.

The resulting comparisons of displacements across the isolation bearings are given in figure 4.24 for the Sierra Madre earthquake, figure 4.25 for the Landers earthquake, and figure 4.26 for the torsional response from both the Sierra Madre and the Landers earthquakes. The summary of structure peak displacements is given in figure 4.27. The channels used for these plots are tabulated in table 4.2.

	BASE / 1st	2nd Floor	Roof
Recorded			
Transverse	(11d+9d)/2 - (7d+6d)/2		(16d+14d)/2 - (7d+6d)/2
Longitudinal	8d - 5d		13d - 5d
Torsional	(11d-9d)/2 - (7d-6d)/2		(16d-14d)/2 - (7d-6d)/2
Modeled			
Transverse	Tran. Base Disp	Tran. 2nd Disp	Tran. Roof Disp
Longitudinal	Long. Base Disp	Long. 2nd Disp	Long Roof Disp
Torsional	Base Rotation x L/2	2nd Rotation x L/2	Roof Rotation x L/2

TABLE 4.2 FCCF station channels used to determine relative displacements for figures 4.24 to 4.27.

The base shear comparisons are given in figures 4.28 and 4.29, with the summary of structural story shears given in figure 4.30. The recorded base shears were calculated by multiplying the story masses by the interpolated story acceleration and summed from the roof to base. For this structure, the shear in the transverse (F_T), longitudinal (F_L), and the torsional (F_{Tor}) directions are given by;

$$F_T = \frac{\frac{14a+16a}{2}\left(M_R + \left(\frac{4.89}{9.98}\right)M_2\right) + \frac{9a+11a}{2}\left(\frac{5.09}{9.98}M_2 + M_B\right)}{W_{total}} \qquad 4.4$$

$$F_L = \frac{13a\left(M_R + \frac{4.89}{9.98}M_2\right) + 8a\left(\frac{5.09}{9.98}M_2 + M_B\right)}{W_{total}} \qquad 4.5$$

$$F_{Tor} = \frac{\frac{16a-14a}{2}\left(MI_R + \frac{4.89}{9.98}MI_2\right) + \frac{11a-9a}{2}\left(\frac{5.09}{9.98}MI_2 + MI_B\right)}{MI_{total}(g)} \qquad 4.6$$

where M_i are the masses for each floor (R, 2, B), MI_i are the mass moment of inertia quantities for each floor, W_{total} is the total weight of the building, and MI_{total} is the sum of all the mass moment of inertia quantities for the building. The shear quantities at any floor can be calculated using this formula considering the appropriate mass terms for the floor in question and those floors above that floor.

Recorded base shear vs. recorded isolation level displacement plots are shown in figures 4.31 and 4.33 for each earthquake in the transverse direction only. Similar plots are included in figures 4.32 and 4.34 for the complete modeled structure. The trend of the loops tends to soften and to get significantly wider with larger amplitude motions. This is consistent with the models. Figure 4.33 has been plotted in time windows to more clearly show the changes in the hysteresis loops through the duration of the strong motion. The general shape and size of the loops generally match the loops of the recorded motions.

The correlation of the recorded response quantities to the modeled quantities is not as good as in the FCLJC structure. Although the building is very uniform in both elevation and plan, the recorded motion demonstrates a much larger than predicted torsional response. Additional studies showed that even with the floor centers of mass offset to 5% of the building length, the model torsional response was still less than the actual recorded torsional response. A possible explanation is given in the following paragraphs.

Also of interest is the comparison of figure 4.31 with figure 4.32 and figure 4.33 with figure 4.34. Figures 4.31 and 4.33 (20-30 second segment) demonstrate a possible displacement restraint in several of the loops which tend to drop down on one side only, showing a reduced isolation-level displacement for the given shear value.

This is also consistent with figure 4.26 which shows the recorded isolation-level rotation much greater than the modeled rotation.

The 1994 Northridge earthquake demonstrated that a significant displacement restraint in the transverse direction existed in the form of the grouted tile at the main entrance to this facility. The compression damage (crushing) of this tile and grout indicated that impact had occurred during the earthquake. This entrance is located on the east side of the building near the north end. It was reported that this same tile required replacement after both the Sierra Madre and the Landers events. It is probable that this same entrance hindered the free transverse motion of this structure in both of these events, and this could also account for the larger than predicted torsional motion. Unfortunately, the current version of 3D-BASIS is unable to model this effect.

Figure 4.35 is included to further demonstrate this torsional and impacting behavior of the FCCF during the Landers earthquake. Plot (a) is the recorded transverse bearing displacement (cm) at the south end of the building (channels 9d-6d). Plot (b) is the recorded transverse bearing displacement (cm) at the north end of the building (channels 11d-7d). Plot (c) is the transverse acceleration (m/sec/sec) of the base level (just above the isolators) at the north end of the building (channel 11a). Firstly, the displacements at the south end are generally larger than at the north end. Secondly, one-sided acceleration spikes occur in the west direction (plot c) at locations which coincide with maxima of bearing displacements (plot b) toward the east. These acceleration spikes must have been produced by impacts between the building and the grouted tile. This episode illustrates the importance of minor details in affecting the overall dynamic response of base-isolated buildings.

Also included for comparison are the first-story shears (the story shear for the level just above the isolator level) in figures 4.36 and 4.37, plotted using the appropriate terms from equations 4.4, 4.5, and 4.6. The roof accelerations are plotted in figures

4.38 and 4.39. These are plots of channel (14a+16a)/2 for figure 4.38(a) and 4.39(a), and channel 13a for figure 4.38(b) and 4.39(b).

4.2.3 Verification of the USCUH Model

The type 1 and type 3 isolators which contain the lead core were softened in the models in order to more closely match the response of the actual structure in the 1992 Landers earthquake. The procedures used were described earlier. The small-strain model for type 1 bearings was softened by modifying the yield displacement from .21 cm (.082 in.) to .30 cm (.12 in.). The bearing type 3 model was modified by adjusting the yield displacement of .14 cm (.057 in.) to .23 cm (.090 in.). All verification for the USCUH is done using the records from the Landers earthquake.

The resulting comparisons of displacements across the isolation bearings are given in figures 4.40 and 4.41. The summary of structure peak displacements is given in figure 4.42. Table 4.3 contains the channels used for the plots in figures 4.40 through 4.42.

	BASE	2nd Floor	4th Floor	6th Floor	Roof
Recorded					
Transverse	(12d+10d)/2 - (8d+6d)/2		(16d+14d)/2 - (8d+6d)/2	(20d+18d)/2 - (8d+6d)/2	(24d+22d)/2 - (8d+6d)/2
Long.	9d - 5d		13d - 5d	17d - 5d	21d - 5d
Torsional	(12d-10d)/2 - (8d-6d)/2				(24d-22d)/2 - (8d-6d)/2
Modeled					
Transverse	Tran. Base Disp	Tran. 2nd Disp			Tran. Roof Disp
Long.	Long. Base Disp	Long. 2nd Disp			Long Roof Disp
Torsional	Base Rotation x L/2	2nd Rotation x L/2			Roof Rotation x L/2

TABLE 4.3 USCUH station channels used to determine relative displacements for figures 4.40 to 4.42.

The base shear comparisons are given in figure 4.43, with the summary of structural story shears given in figure 4.44. The recorded base shears were calculated by multiplying the story masses by the interpolated story acceleration and summed from the roof to base. For this structure, the shear in the transverse (F_T), longitudinal (F_L), and the torsional (F_{Tor}) directions are given by;

$$F_T = \frac{\frac{24a+22a}{2}\left(M_R+\frac{1}{2}M_7\right)+\frac{20a+18a}{2}\left(\frac{1}{2}M_7+M_6+\frac{1}{2}M_5\right)+\frac{16a+14a}{2}\left(\frac{1}{2}M_5+M_4+\frac{3}{4}M_3+\frac{1}{2}M_2+\frac{1}{4}M_1\right)+\frac{12a+10a}{2}\left(\frac{1}{4}M_3+\frac{1}{2}M_2+\frac{3}{4}M_1+M_B\right)}{W_{total}} \tag{4.7}$$

$$F_L = \frac{21a\left(M_R + \frac{1}{2}M_7\right) + 17a\left(\frac{1}{2}M_7 + M_6 + \frac{1}{2}M_5\right) + 13a\left(\frac{1}{2}M_5 + M_4 + \frac{3}{4}M_3 + \frac{1}{2}M_2 + \frac{1}{4}M_1\right) + 9a\left(\frac{1}{4}M_3 + \frac{1}{2}M_2 + \frac{3}{4}M_1 + M_B\right)}{W_{total}} \tag{4.8}$$

$$F_{Tor} = \frac{\frac{24a - 22a}{2}\left(MI_R + \frac{1}{2}MI_7\right) + \frac{20a - 18a}{2}\left(\frac{1}{2}MI_7 + MI_6 + \frac{1}{2}MI_5\right) + \frac{16a - 14a}{2}\left(\frac{1}{2}MI_5 + MI_4 + \frac{3}{4}MI_3 + \frac{1}{2}MI_2 + \frac{1}{4}MI_1\right) + \frac{12a - 10a}{2}\left(\frac{1}{4}MI_3 + \frac{1}{2}MI_2 + \frac{3}{4}MI_1 + MI_B\right)}{MI_{total}(g)} \tag{4.9}$$

where M_i are the masses for each floor (R, 7, 6, 5, 4, 3, 2, 1, B), MI_i are the mass moment of inertia quantities for each floor, W_{total} is the total weight of the building, and MI_{total} is the sum of all the mass moment of inertia quantities for the building. The shear quantities at any floor can be calculated using this formula considering the appropriate terms for the floor in question and those floors above that floor.

The recorded base shear vs. recorded isolation level displacement plot is shown in figure 4.45 for the Landers earthquake in the transverse direction only. A similar plot is shown in figure 4.46 for the modeled structure. The trend of the loops tends to soften and to get significantly wider with larger amplitude motions. This is consistent with the models. Figure 4.45 has been plotted in time windows to more clearly show the changes in the hysteresis loops through the duration of the strong motion.

Also included for comparison are the first-story shears (the story shear for the level just above the base level) in figure 4.47, calculated using the appropriate terms from equations 4.7, 4.8, and 4.9. The roof accelerations are plotted in figure 4.48. These are plots of channel (24a+22a)/2 and channel 21a for figures 4.48(a) and 4.48(b), respectively.

The correlation of the recorded response quantities to the modeled quantities for this structure is not very good; however, the model does demonstrate many of the time history characteristics exhibited by the actual structure. The analysis indicates that the modes are coupled translation and torsional modes. Figure 4.42 indicates that the actual superstructure is considerably stiffer than the model, at least for these small displacements. This conclusion can also be made from the system identification natural period information from chapter 3. The response quantities of the model tend to more closely match the recorded quantities in the longitudinal direction than in the transverse direction. This could be a result of less contribution due to torsion in the longitudinal direction.

5. Conclusions to Part One

Several observations and conclusions can be drawn from the chapters in Part One of this thesis.

Base-isolated structures can be modeled using bi-linear force-displacement relationships in the small-strain range of the isolation bearings. However, bi-linear relationships for small strains must be adjusted to account for additional sources of stiffness and damping which have a considerable effect in this range. The use of tri-linear force-displacement relationships could be useful to more accurately capture the small strain behavior. If using a bi-linear model, it is difficult to determine the accuracy of the model in this small strain range. Therefore, for design under moderate excitation, it might be prudent to use a suitable range of stiffness values as an effort to envelope the actual anticipated response. The bearing stiffnesses in this study were varied in order to achieve a better match between the modeled structures and the actual recorded responses. These adjustment factors may be useful for determining a reasonable range of values for design. Verification of full scale base-isolated buildings responding to large earthquake input is currently unavailable.

Period and damping vary with amplitude of excitation. Since the bearings form a softening and hysteretic system, under increased excitation, the fundamental period of the structures increases and the equivalent viscous damping increases. These two effects were illustrated in the system identification results.

Seemingly minor details can significantly alter the overall structural response of a base-isolated structure. This was demonstrated by the increased torsional response which occurred in the FCCF during the Sierra Madre and Landers earthquakes due to the grouted entrance of the structure near the north end of the building.

All the earthquakes investigated in Part One resulted in very small displacements, and accelerations. Although the structures responded in a nonlinear fashion, the recent earthquakes have clearly resulted in low levels of response in these three base-isolated buildings.

PART TWO

6. Long-Period Ground Motion

Earthquake ground motions vary tremendously from earthquake to earthquake and from site to site. These variations are the result of many factors. Researchers for years have attempted to identify what factors contribute to actual motions. Bolt has strongly linked our knowledge of earthquake ground motions with advances in the number of recording devices. He says, "Knowledge of strong ground shaking is now advancing rapidly, largely because of the growth of appropriately sited strong-motion accelerographs in seismic areas of the world [in Naeim, ed., 1989]." Bolt also notes, however, that there are still no clear recordings of ground motion in the near-source area from earthquakes with surface wave magnitude greater than M 7.5.

This lack of data creates large uncertainties in determining precise ground motions, especially near the source of large events. These uncertainties can be extremely important for structures located close to possible earthquake sources.

Because of the many identified and unidentified faults and folds in complicated tectonic settings such as Southern California, in many instances sites which were considered distant from possible seismic sources turn out to be in the near-source area (considered here to be within approximately the distance of the dimensions of the fault rupture). Recent examples in Southern California include the M 6.1 1987 Whittier earthquake and the M 6.7 1994 Northridge earthquake.

The uncertainties involved in development of site-specific design spectra are large. The uncertainties include the difficulty in identifying sources, and even if identified, the very sparse data set available to characterize near-source motions from these sources.

The purpose of this chapter is to illustrate the characteristics of ground motions resulting from moderate to large seismic events (M≥6.5) which are recorded at sites near the seismic sources.

With the continuing development of the earthquake engineering field, accepted design levels are continually being altered. This chapter illustrates ground motion levels which are significantly higher than many currently accepted levels. For specialty structures such as base-isolated buildings, these higher levels of excitation, should be considered as infrequent, but possible ground motions for many seismic areas of the world.

In the previous chapters, the FCLJC, FCCF, and USCUH have been analyzed using the recorded motions from past earthquakes. These motions have had small amplitudes, generally, at the building sites and have demonstrated the small-strain behavior of the buildings.

As we are interested in the behavior of these structures under more severe excitation, computer simulations will be employed.

The input motions for the forthcoming simulations are of two types. The first type is the collection of recorded near-source ground motions from moderate to large events. These will be further discussed in section 6.1. Chen [1995] has demonstrated that standard processing techniques, including high-pass filtering, can result in significantly reduced velocities and displacements. This is particularly true for stations which are affected by source directivity. An example, taken from Chen [1995], is the transverse component of a record from the Lucerne Valley site from the 1992 Landers earthquake. Standard baseline correction and filtering, with band pass limits of 0.2-0.4 Hz and 22.0-25.0 Hz, were applied to the record. The resulting peak acceleration, velocity, and displacement are 621 cm/sec/sec, 48.9 cm/sec, and 9.1 cm, respectively. In contrast, by using processing techniques to preserve the long-period motion in the record, Chen shows the peak acceleration, velocity, and displacement to be 720 cm/sec/sec, 146 cm/sec, and 260 cm, respectively. This record is shown in figure 6.2 and will be discussed in section 6.1. Since strong-motion records must be integrated to acquire a velocity record and integrated again to acquire a displacement record, effects of processing become more pronounced for velocities and displacements. The critical point here is simply that for longer-period structures, such as base-isolated structures, the application of high pass filtering and some types of base-line correction to records to be used in analysis can significantly reduce the computed structural response.

The second type of motion to be examined is synthetic motion, generated using a hypothetical source and propagated to the surface. Synthetic motions are used in this study because of their usefulness in producing consistent time histories of ground motion at any desired location. That is, an answer to the following question is available using synthetic motions: If a model structure performs in a certain way located at point 'x' relative to the causative fault, how would it perform in the same event if it were located 10 km from point 'x'? The techniques utilized to generate these motions will be explained in section 6.2. The synthetic motions used in this study were provided by D. Wald and T. Heaton of the USGS, and are similar to those used by Heaton *et al.*, [1994]. Many other researchers have also developed estimated motions for both real and hypothesized earthquakes. These studies include the ones by Saikia [1992], Kanamori *et al.* [1993], Kanamori [1979], Butler and Kanamori [1980], Hadley and Helmberger [1980], Hanks [1976], and Aki [1982], as well as others. Hartzell and Heaton [1983] employed a methodology known as a constrained, damped, least-squares inversion of wave-form data for the retrieval of faulting history of the 1979 Imperial Valley, California, earthquake. This same methodology was used by Wald *et al.* [1990]

for the 1987 Superstition Hills earthquake, by Wald *et al.* [1991] for the 1989 Loma Prieta earthquake, by Wald [1992] for the 1991 Sierra Madre earthquake, by Wald and Heaton [1994] for the 1992 Landers earthquake, and by Wald and Heaton [1994] for the 1994 Northridge earthquake. The extensive use of these inversion techniques to retrieve faulting parameters continues to improve the techniques and increases confidence in the strong motions generated from these models. These studies utilize available strong-motion, teleseismic, and geodetic data at given points to retrieve an estimated faulting history. Once the estimated faulting history is determined, the long-period portion of ground motions can be estimated at any site.

Both the recorded near-source motions and the synthetic motions show pronounced directivity effects. This directivity results as a physical phenomenon of energy radiating from a moving source. It is directly comparable with the familiar Doppler effect when dealing with sound waves. Since the typical fault rupture velocity is approximately 80-85% of the shear wave velocity, the resulting velocity wave form at a site in the direction of propagation is very compressed and results in large pulse-like motion [Heaton, 1990].

Using a modified faulting history of the Homestead Valley segment of the fault which ruptured in the 1992 Landers event, a forward calculation [Heaton *et al.*, 1994] has given the various ground motions for a hypothesized M 7.0 blind thrust fault which will be discussed in section 6.2.

6.1 Recorded Near-Source Ground Motions

One type of motion that could be critical for long-period structures (T>2.0 sec) would be motions with significant long-period velocity pulses. This type of motion is prevalent in the small sampling of records collected from sites near the source of energy release. Anderson and Bertero [1987] point out the significant variations in dynamic characteristics of ground motions recorded at two sites in the same area, particularly for recording stations located near the epicentral region. One reason for the rapid variations in motions near the epicenter is the strong directivity in that region.

The significance of these near-source motions, which are heavily affected by fault directivity effects, began to be appreciated after the 1966 Parkfield earthquake [Anderson and Bertero, 1987]. Since then, several records have been obtained from near-source sites from moderate-sized events. Anderson and Bertero [1987], Hudson [1977; 1988], Heaton [1994], and others have compiled data from near-source ground motions in recent years. Table 6.1 summarizes some of these earthquakes, their properties, and their peak values. In this table, the distances given are distances from the site to the nearest point on the surface projection of the fault. That is, the vertical projection of the actual rupture patch to the earth's surface. The records shown in table 6.1 have been processed by many different techniques and by different researchers. As mentioned previously, the processing has its greatest effects on velocity and displacement, since they involve integrations of the acceleration history. Therefore, the peak values are listed to demonstrate the significant amplitudes of this sampling of near-source records and not for direct comparison. The Lucerne Valley record was processed by Chen [1995] and its peak displacement value is quite large, reflecting the significant contribution of long period motion to peak displacement, and to a lesser extent, to peak velocity.

				Peak Values		
	Mag.	Station	DIST. (km)	ACC. (g)	VEL. (cm/s)	DIS. (cm)
Dip-Slip Events						
71 San Fernando	M 6.7	Pacoima Dam	0	1.12	113	38
78 Tabas, Iran	M 7.4	Tabas	3	0.92	125	106
85 Nahanni, Canada	M 6.8	Site 1	0	>2.0	39	36
		Site 2	0	0.50	31	31
92 Petrolia	M 7.0	Cape Mendocino	0	>1.8	126	67
		Petrolia	5	0.69	90	31
94 Northridge	M 6.7	Rinaldi (LADWP)	0	0.85	177	50
		Sylmar, County Hos.	2	0.91	134	44
		Jensen Filt. Plant	0	0.85	103	38
		Newhall Fire Sta.	5	0.63	101	36
Strike Slip Events						
79 Imperial Valley	M 6.5	El Centro Array # 7	1	0.65	110	41
		El Centro Array # 6	1	1.74	110	55
87 Superstition Hills	M 6.6	Parachute Test Site	0	0.53	138	60
		Superstition Mount.	6	0.91	44	15
92 Erzincan, Turkey	M 6.8	Erzincan	2	0.50	105	40
92 Landers	M 7.2	Lucerne Valley(SCE)	1	0.73	146	260

TABLE 6.1 Near-source ground motions from large earthquakes [from Heaton *et al.*, 1994].

In this study, three records have been selected as a sampling of actual recorded ground motions. The first is the El Centro N-S component from the 1940 Imperial Valley earthquake [Hudson *et al.*, 1976] (figure 6.1). This record has been processed using standard processing techniques and used extensively for analysis and design of many structures and has traditionally represented a severe earthquake ground motion. The second is the Lucerne Valley transverse component from the 1992 Landers earthquake (figure 6.2). The time history used for analysis is the version corrected by Chen [1995]. The third is the Sylmar County Hospital free-field record from the 1994 Northridge earthquake [Darragh *et al.*, 1994], also processed using standard processing techniques. The component used is the N43E component, which is obtained by rotation of the two orthogonal components to the angle which maximizes the displacement of a

SDOF oscillator with a period of 2.5 sec. and 15% damping (figure 6.3). This is done to partially compensate for the fact that only one component of motion will be utilized in the forthcoming analyses.

The 15% damped acceleration, velocity, and displacement response spectra for each of these records are plotted in figure 6.4. Also included in figure 6.4, for comparison, are the spectra from the recorded transverse foundation motion at the FCLJC from the 1992 Landers earthquake. This motion is the largest motion which any of the base-isolated structures had experienced from the earthquakes in this study.

6.2 Synthetic Near-Source Ground Motions

As outlined in section 6.1, a set of strong-motion records was developed for a hypothetical magnitude M 7.0 dip-slip event by D. Wald and T. Heaton of the USGS which is similar to those used by Heaton *et al.* [1994], where a complete discussion can be found. This represents a plausible event in many populated areas of the world including the Los Angeles metropolitan area [Dolan *et al.*, 1994; Davis *et al.*, 1989; Hauksson and Jones, 1989].

The calculated strong ground motions are within the frequency bandwidth of 0.0 to 10.0 Hz. for a hypothetical energy magnitude M_W 7.0 earthquake on a blind thrust fault. Figure 6.5 shows a diagram of the blind thrust fault, the slip distribution on the fault, and the locations of stations at a 5 km grid spacing at the ground surface. Ground motions are deterministically calculated at frequencies lower than 1 Hz. assuming a 35 km. long by 18 km. fault which dips 28 degrees northward beneath a horizontally-stratified sedimentary basin. The hypocenter is at the lower center area of the fault. The rupture velocity is assumed to be 2.9 km/sec. The fault model used is a modified slip distribution taken from the Homestead Valley segment of the M 7.2 1992 Landers earthquake. The peak slip in this model is reduced to 5.1 meters with an average slip of

2.17 meters. At frequencies greater than 1 Hz., ground motions are approximated by actual records from the Sylmar County Hospital free-field site [Darragh, 1994] for stations A through H and 1 through 6, and by the Stone Canyon Reservoir records [UCSB, 1994] for the remaining stations, both from the 1994 Northridge (M_W 6.7) earthquake. These records were corrected for appropriate distance, where distances were taken as the distance from the fault surface projection, using the attenuation relationships of Boore *et al.* [1993]. A matched pair of filters was used to remove periods less than 1 second from the deterministically calculated motions and to remove periods greater than 1 second from the actual recorded ground motion records. The filtered actual ground motion and the deterministically calculated motion were then summed to form the final ground motions.

It should be emphasized that the estimated motions used here are not an attempt to find the maximum credible motions for a near-source event. Instead, the estimated motions are a result of choosing parameters considered typical for a M_W 7.0 earthquake. These parameters include such parameters as the peak slip on the fault, the average slip on the fault, the overall fault dimensions, and the assumed rupture velocity. Two horizontal components of velocity are generated for each station.

The two horizontal components of velocity, which were provided by Wald and Heaton for each grid station, were vectorially combined at the angle which resulted in the maximum spectral displacement of a 15% damped, oscillator with a period of 2.5 seconds. A period of 2.5 seconds and 15% damping, close to the properties of a typical base-isolated building oscillating under large ground motions, were selected as the basis for rotation to partially compensate for the fact that in the analysis, only one component of motion will be utilized. This determined angle varies from station to station. Having done this, single components of acceleration, velocity, and displacement were calculated at each station. Figures 6.6(a), (b), and (c) show contours of peak displacement, velocity, and acceleration in the calculated direction, respectively. Figures 6.7(a), (b), (c), and (d) show contours of peak single-degree-of-freedom oscillator displacements for periods and damping ratios of 2.2 sec and 10% damping, 2.2 sec and 20% damping, 1.4 sec and 20% damping, and 3.0 sec and 20% damping, respectively. These are also calculated for the single component of motion as described above. Tables of the actual numerical results used to generate figures 6.6 and 6.7 are included in appendix A.

A comparison of the 2.2 second oscillator with 10% damping with the oscillator with 20% damping shows only a slight change in the extent of displacement contours. However, by maintaining the 20% damping, changing the period to 1.4 seconds decreases the spectral displacements considerably. Additionally, by changing the period to 3.0 seconds, the spectral displacements increase considerably. These plots illustrate the substantial region which would experience very large spectral displacements in a M 7.0 event.

Three stations were selected as a sampling of these synthetic ground motions. Station D05 exhibits the maximum displacement of a 2.5 sec, 15% damped oscillator of all of the stations. Stations B06 and H04 are examples of two moderate motions, with B06 being located approximately 20 km south of the fault surface projection, and station H04 being located on the fault surface projection, but away from the direction of fault rupture. Refer to figure 6.5 for station locations.

Figures 6.8, 6.9, and 6.10 show the acceleration, velocity, and displacement time histories for station B06, D05, and H04, respectively. Figure 6.11 contains plots of spectral acceleration, spectral velocity and spectral displacement for the synthetic motions shown in figures 6.8-6.10. These spectra tend to have moderate acceleration values, but large velocity and displacement values.

6.3 Response of Structural Models to Near-Source Ground Motions

The focus of this section is to reanalyze each of the models of chapter 4, again using the identical ETABS superstructure, but now using the large-strain force-displacement relationships for the isolation bearings in 3D-BASIS. The large-strain relationships will be used since the bearing displacements expected are larger than 3 to 4 cm. These large-strain relationships are taken from the bearing test data for the bearings prior to installation as described in chapter 4. Each model is subjected to only one component of motion, applied in the transverse direction of each building model. Therefore, the contribution due to bi-directional loading is neglected. The reported displacements are those for the bearing displacements (base displacement - foundation displacement) and the roof displacements (roof displacement - foundation displacement) for the floor center of mass in the transverse direction.

Each of the three buildings has an isolation gap of width D_{TM}. This value is established during the design of the building, and is reflected in the detailing at the isolation level. The value for D_{TM} is usually obtained by multiplying the maximum corner bearing displacement obtained from analysis by a safety factor (often 1.5). Obviously, D_{TM} is different for each building. For the FCLJC, D_{TM} is 41 cm. The concrete retaining wall at the perimeter of the building is located at this distance from both the base level and first floor level of the building. For the FCCF, D_{TM} is 32 cm. At this distance, the ultimate restraint chain in the perimeter isolation bearings begins to engage, and all structural, architectural, and utility components are designed for a displacement of 39 cm [Anderson, 1990]. For the USCUH, D_{TM} is 26 cm. Concrete pedestals near each isolation bearing, cantilevering up from the foundation, are located at a distance, D_{TM}, from the column extensions beneath the base slab. The perimeter concrete retaining wall is located at a distance of 34 cm from both the concrete base slab and the first floor slab [Asher *et al.*, 1990].

The acceleration time histories used for foundation excitation for each model are those described in section 6.1 and 6.2, namely, the N-S El Centro component from the 1940 Imperial Valley earthquake [Hudson *et al.*, 1976], the transverse Lucerne Valley component from the 1992 Landers earthquake [Chen, 1995], the Sylmar County Hospital free-field N43E component from the 1994 Northridge earthquake [Darragh *et al.*, 1994], as well as three stations from the synthetic motions, namely B06, D05, and H04 [Heaton *et al.*, 1994].

Figures 6.12, 6.13, and 6.14 are plots of the peak displacements of the base center-of-mass and roof center-of-mass, relative to the foundation, for the FCLJC, the FCCF, and the USCUH, respectively. For the FCLJC (figure 6.12), three of the acceleration histories lead to peak bearing displacements greater than D_{TM}. These are the synthetic H04, Sylmar, and synthetic D05. For the FCCF (figure 6.13), all the described motions except the El Centro acceleration lead to peak bearing displacements greater than D_{TM}. For the USCUH (figure 6.14), also all the described motions, except the El Centro record, lead to peak bearing displacements greater than D_{TM}. These bearing displacements are very large. In some cases, up to approximately 4 times the D_{TM} values.

These models analyzed using 3D-BASIS in conjunction with ETABS do not include the displacement barriers, i.e., the perimeter walls, chains, and pedestals. The large amplitudes of the bearing displacements, greatly exceeding D_{TM} for the stronger ground motions, indicate that the actual impacts between the buildings and the displacement barriers could be strong enough to damage the buildings. Effects of such impacts are considered in Chapter 7 for a typical base-isolated building (TBIB).

7. Typical Base-Isolated Building (TBIB)

In order to further evaluate the response of base-isolated structures to the near-source motions presented in chapter 6, including impacts between the building and its displacement barrier, a typical three-story base-isolated structural model will be utilized.

7.1 The TBIB Structural Model

A typical base-isolated building (TBIB) was designed to conform to the provisions of the 1991 Uniform Building Code [ICBO, 1991]. The design is intended to be representative of a structure founded on high-damping rubber bearings or a combination of lead / rubber and elastomeric bearings.

The design displacement of the bearings for this structure is calculated using the following formula from the 1991 Uniform Building Code [ICBO, 1991]:

$$D = \frac{10ZNS_I T_I}{B}, \text{ inches} \tag{7.1}$$

where,

Z = zone factor=0.4 (seismic zone 4),
N = near-field factor=1.5 (sites closer than 5 km to an active fault),
S_I = soil factor=1.0 (soil type 1: rock and stiff soil),
T_I = effective isolated period of vibration at D, taken to be 2.2 sec,
B = damping factor=1.35 (ς_I = 0.15, ς_I is the effective viscous damping ratio of bearings at displacement, D).

Values of T_I and ς_I are based on a rigid superstructure. For this structure the basic design displacement, D, is 24.8 cm (9.78 in.). The total displacement, including effects of accidental torsion, D_T = 1.1 D = 27.3 cm (10.8 in.), and the total maximum displacement, $D_{TM} = 1.5 D_T = 41.0$ cm (16.1 in). D_{TM} is the distance to the displacement barrier and is used for design of the flexible connections [ICBO, 1991].

The TBIB is modeled as a three-story shear building (planar model) with floor masses and story stiffnesses selected to give a fixed-base period of 0.5 seconds (figure 7.1). The values of floor masses and story stiffnesses are representative of a real structure. A bi-linear relation is taken for the isolation system force-displacement curve (figure 7.1). The ratio of secondary bearing stiffness to initial bearing stiffness, α_P, is taken as 0.15. From the values of D, T_I, ς_I, and α_P, the initial stiffness, k_p, and yield force, F_{py}, for all the bearings as a group can be calculated. The relevant formulas are:

$$T_I = 2\pi\sqrt{M/k_I} \qquad 7.2$$

$$\zeta_I = \frac{2}{\pi}\left(\frac{F_{py}}{F_p(\Delta_p)_{\Delta_p=D}} - \frac{F_{py}/k_p}{D}\right), \qquad 7.3$$

where M = total superstructure mass, k_I = secant stiffness of all the bearings together at bearing shear displacement $\Delta_p = D$, and F_p = shear force carried by bearings at displacement Δ_p. Resulting values for k_p and F_{py} are listed in figure 7.1. Note that equations 7.2 and 7.3 take the superstructure to be rigid.

Table 7.1 compares properties of the models for the three previously studied buildings with the properties of the TBIB structural model. The TBIB model compares quite closely with the FCLJC model. The main differences are that TBIB has a longer effective period, T_I, and a smaller ratio of secondary-to-initial stiffness, α_p, for the bearings. In addition TBIB has a higher effective damping ratio than does the FCLJC model. However, for acceleration histories which lead to very large bearing displacements, the longer secondary period of TBIB leads to bearing displacements more similar to those of the FCCF or USCUH. The TBIB model is, however, representative of these structural numerical models and much can be learned from the study of its response.

		FCLJC	FCCF	USCUH	TBIB
Design Disp. D (cm)		27	15	17	24
Total Design Disp. D_T (cm)		27	22	17	27
Total Max. Design Disp. D_{TM} (cm)		41	32	26	41
Fixed Base Period T (sec)	Trans.	.62	.42	1.35	.50
	Long.	.72	.38	1.13	
	Tors.	.51	.23	.84	
Effective Isolated Period * T_I @ D (sec)		1.90	1.94	2.01	2.2
Effective Damping Ratio * ζ_I @ D (% of critical)		12.5	11.2	14.3	15.0
Period based on initial bearing stiffness * T_1 (sec)		1.15	1.55	1.01	0.98
Period based on secondary bearing stiffness * T_2 (sec)		2.15	2.24	2.48	2.54
Stiffness Ratio $\alpha_p = (T_1/T_2)^2$		0.29	0.48	0.17	0.15

* Superstructure taken to be rigid.

TABLE 7.1 Properties of the FCLJC, FCCF, USCUH, and TBIB models.

Before adding the displacement barriers and some other features to the TBIB model, analyses of the model shown in figure 7.1 are made using 3D-BASIS to provide some additional comparisons with the three previously studied buildings.

Figure 7.2 shows the peak base and roof displacements relative to the foundation of the TBIB model when subjected to the El Centro, Lucerne, Sylmar, B06, D05, and H04 acceleration time histories, as computed by 3D-BASIS. Again, as noted with regard to the models of the three existing buildings, displacement barriers are not modeled and bearing displacements in excess of D_{TM} indicate that impact across the isolation gap would occur. The computed bearing displacements are large, as was the case with the FCLJC, FCCF, and USCUH models (compare to figures 6.12, 6.13, and 6.14), again indicating that severe impacts would occur. In order to conduct further analysis, TBIB will be analyzed using a program developed at Caltech and described in section 7.2.

7.2 The Program 2D-BUMP

The computer program 2D-BUMP was developed by J. F. Hall and M. W. Halling and written by J. F. Hall at Caltech. The program 2D-BUMP is used to analyze base-isolated structures in which the base of the building impacts a displacement barrier. Nonlinearity in the superstructure is also included. Figure 7.3(a) shows a diagram of the TBIB building, with figures 7.3(b), (c), and (d) showing the force-displacement models for the various components of the structure, namely, each story, the bearings (the total curve for all bearings together), and the barriers at each side of the structure. In addition, the program considers the P-Δ effects in the superstructure and added viscous damping at the isolation level.

Each story of the structure is capable of yielding at a level which is appropriate for the applied design criteria of the superstructure (figure 7.3(b)). The parameters k_i, α_i, F_{iy}, and F_{iu} are the initial story stiffness, story stiffness ratio (ratio of secondary to initial stiffness), story yield force, and story ultimate force, respectively, for each story.

The bearings are modeled as bi-linear, unless the bearing displacement exceeds the displacement corresponding to the point "2" in figure 7.3(c). In that case, the restoring force remains constant with increasing displacement. The parameters k_p, α_p, F_{py}, and F_{pu} are the initial bearing stiffness, bearing stiffness ratio, bearing yield force, and bearing ultimate force, respectively, for all the bearings together. The parameter for the amount of additional viscous damping at the bearing level is $EDAMP$, given as the percentage of critical damping. For all the models discussed, this factor is based on a period of 2.2 seconds with a rigid superstructure.

The barriers are modeled as nonlinear springs, with hysteretic damping. In each contact with a barrier, if the barrier yields, the gap becomes larger than the initial gap as shown in figure 7.3(d). The parameters k_s, F_{sy}, h, and GAP are the initial barrier stiffness, barrier yield force, hysteretic damping factor, and the initial gap, respectively, for the right and the left barriers. As can be seen in figure 7.3(d), the resisting force of the barrier resists the motion as a nonlinear spring with hysteretic damper with a factor h. The damping is proportional to the displacement and in phase with the velocity.

By setting the story yield forces, F_{iy}, the ultimate bearing force, F_{pu}, and the initial gap, GAP, to very large numbers, the structural model maximum displacements, at the roof and base for TBIB using 2D-BUMP, are essentially equivalent (within 2%, for the six near-source motions considered) to the displacements from 3D-BASIS. Therefore, figure 7.2, although plotted using the results from 3D-BASIS, would be very similar using 2D-BUMP. The purpose of this study is not to compare these programs, but it is informative to note that by assuming an elastic superstructure, no barriers included, and bi-linear hysteresis for the isolation bearings, the outputs are essentially equivalent.

7.3 2D-BUMP Results

Five sets of parameters were selected in order to investigate the response of TBIB to the selected ground motions. These are model 1, model 2, model 3, model 4, and fixed-base model (no isolation). In addition, model 2 was analyzed using various "gap" dimensions which will be referred to later in the chapter. The story heights and floor weights are as given in figure 7.1. The parameters for the various models are summarized in table 7.2. For all the models, the mass and stiffnesses are such that the fixed-base structure has a period of 0.5 seconds.

The model which is taken as the "typical" model is model 2. Models 2, 3, 4, and fixed-base each have first-story yield strengths of 0.18 times the weight of the building above the base. The yield strengths of the other stories are proportional to the story stiffnesses. This is conservative for this base-isolated building, and note that the ultimate story strengths are another 50% greater. Model 1 has a first story yield strength of 0.51 times the weight of the building above the base, with the yield strengths of the other stories in proportion to the story stiffnesses. This is an extremely conservative value for a base-isolated building. Model 3 is equivalent to model 2 except that model 3 has barrier stiffnesses and strengths of 4 times the values of the other models. The parameter $EDAMP$ is increased, from 1% in the other models, to 10% in model 4 to evaluate the effect of increased viscous damping in the isolation system. The fixed-base model has superstructure parameters similar to model 2, but without bearings.

Variable		ALL Models	Model 1	Model 2	Model 3	Model 4	Fixed Base
Parameters for Story i							
k_i (kN/cm)	i=1	6520					
	i=2	5124					
	i=3	4193					
α_i	i=1	0.1					
	i=2	0.1					
	i=3	0.1					
F_{iy} (kN)	i=1	---	11,340	4003	4003	4003	4003
	i=2	---	8911	3145	3145	3145	3145
	i=3	---	7299	2576	2576	2576	2576
F_{iu}/F_{iy}	i=1-3	1.5					
Parameters for Bearings							
k_p (kN/cm)		1331					∞
α_p		0.15					N/A
F_{py} (kN)		1948					∞
F_{pu}/F_{py}		5.05					N/A
$EDAMP$(%)		---	1.0	1.0	1.0	10.0	N/A
Parameters for Barriers							
k_s (kN/cm)		---	17,510	17,510	70,050	17,510	N/A
F_{sy} (kN)		---	22,240	22,240	88,960	22,240	N/A
h		0.6					N/A
GAP (cm)		41.0					N/A

Note: The floor weights for the 4th, 3rd, 2nd, and 1st/base floors are 6227, 8007, 8007, and 9786 kN, respectively.

TABLE 7.2 Parameters for 2D-BUMP analyses.

Each model was first subjected to the Sylmar County Hospital free-field record. The total acceleration at the second floor, the bearing displacement, and the second-floor displacement time histories are presented in figures 7.4, 7.5, 7.6, 7.7, and 7.8 for models 1 through 4 and fixed base, respectively. Also noted are the maximum striking velocity at impact with a barrier and the maximum ductility demand in the first story. The maximum ductility demand in story i is defined as

$$\text{max ductility demand } = \frac{|\Delta_i|_{\max} - \Delta_{ip}}{\Delta_{iy}} \tag{7.4}$$

where Δ_i is the lateral offset of story i,

Δ_{ip} is the permanent offset of story i, and

$\Delta_{iy} = {F_{iy}}/{k_i}$.

The total acceleration at the second floor, the bearing displacement, and the second-floor displacement time histories for model 2 are also plotted for the El Centro, Lucerne, B06, D05, and H04 ground motions in figures 7.9, 7.10, 7.11, 7.12, and 7.13, respectively. Table 7.3 contains the tabulated bearing displacements, striking velocities, ductility demands, and second floor accelerations for each of the five models when subjected to each of the six near-source ground motions.

	Max Bearing Displacement (cm)	Max Striking Velocity (cm/sec)	Max Ductility Demand	Max 2nd Floor Accel. (cm/sec^2)
El Centro, N-S Motion				
model 1	7.6	0.0	0.0	130
model 2	7.6	0.0	0.0	130
model 3	7.6	0.0	0.0	130
model 4	7.0	0.0	0.0	129
Fixed-Base	-	-	2.6	263
Lucerne Valley, Trans. Motion				
model 1	41.7	40.6	0.5	871
model 2	41.2	14.0	13.2	345
model 3	41.1	14.0	13.4	384
model 4	34.9	0.0	6.8	287
Fixed-Base	-	-	8.0	430
Sylmar County Hosp. Motion				
model 1	42.8	90.1	2.5	1266
model 2	41.8	52.6	41.4	630
model 3	41.4	52.8	41.3	758
model 4	36.4	0.0	11.9	315
Fixed-Base	-	-	12.8	450
B06 Synthetic				
model 1	41.4	26.3	0.0	662
model 2	39.0	0.0	9.1	288
model 3	39.0	0.0	9.1	288
model 4	33.9	0.0	5.4	270
Fixed-Base	-	-	3.1	314
D05 Synthetic				
model 1	46.5	165.4	8.5	1335
model 2	45.2	153.3	95.5	1117
model 3	42.4	153.2	94.8	1567
model 4	43.9	123.4	76.2	960
Fixed-Base	-	-	43.3	367
H04 Synthetic				
model 1	42.2	68.9	1.6	1076
model 2	41.9	51.6	20.6	593
model 3	41.4	51.6	20.5	761
model 4	38.9	0.0	13.0	311
Fixed-Base	-	-	8.0	747

TABLE 7.3 Tabulation of maximum bearing displacements, maximum striking velocities, maximum ductility demands, and maximum 2nd floor accelerations.

A comparison of figure 7.5 (model 2) and figure 7.6 (model 3) demonstrate the very small effect of stiffer and stronger barriers. The stiffer and stronger barriers induce slightly higher accelerations in the superstructure as expected, but have essentially no effect on the ductility demand, floor displacements, and bearing displacements. This can also be observed from table 7.3.

Figures 7.4 through 7.13 demonstrate the consequences of impacts with a displacement barrier. These consequences include yielding of the superstructure and significant high-frequency acceleration spikes in the structure. Figure 7.12 demonstrates the excessive permanent story offsets which could be expected under such severe loading as ground motion D05.

As mentioned, model 2 was analyzed using the Sylmar County Hospital ground motion by varying GAP while holding all other parameters unchanged. Table 7.4 is a summary of the maximum bearing displacement, maximum striking velocity, maximum ductility demand, and maximum 2nd floor acceleration as GAP is varied from 0 to 51 cm.

GAP (cm)	Max Bearing Displacement (cm)	Max Striking Velocity (cm/sec)	Max Ductility Demand	Max 2nd Floor Accel. (cm/sec^2)
0	0.6	0.0	15.0	473
5.1	6.7	72.3	19.9	759
10.2	12.4	101.5	21.8	795
15.2	17.3	101.0	21.4	840
20.3	22.5	100.3	24.8	926
25.4	27.8	114.8	37.5	1035
30.5	32.6	109.5	41.0	995
35.6	37.0	85.8	42.4	879
41.0	41.8	52.6	41.4	630
45.7	46.2	29.8	32.3	379
50.8	48.2	0.0	25.1	355

TABLE 7.4 Tabulation of maximum bearing displacements, maximum striking velocities, maximum ductility demands, and maximum 2nd floor accelerations from the Sylmar County Hospital motion and the model 2 structure while varying GAP .

Several observations can be made regarding table 7.4. The maximum floor accelerations tend to correspond with the maximum striking velocities. That is, the faster the base of the building is traveling at impact, the higher the acceleration spike will be in the superstructure. However, the range of gap values which result in the highest ductility demands does not correspond with the range of gap values which give the highest striking velocities and accelerations. The lowest superstructure acceleration occurs when the gap is set to 50.8 cm. At this distance, no impact occurs. However the ductility demand is moderate, indicating that significant yielding is occurring in the superstructure. For this ground motion, the model indicates that setting the gap to 0 results in relatively low ductility demands and superstructure accelerations.

Each model is subjected to the complete set of synthetic ground motions. The maximum bearing displacement, maximum striking velocity, maximum first-story ductility demand, and the maximum second-floor acceleration are plotted as contours in figures 7.14, 7.15, 7.16, 7.17, and 7.18 for the 5 models, respectively (the tabulated numerical data can be found in Appendix A). Figures 7.14 - 7.17 for maximum bearing displacements and maximum striking velocities quantifies the areal extent of the region within which the TBIB would impact its barrier. Bearing displacements above 41 cm and striking velocities above zero define this region. Variations in the apparent shape of the 41 cm contour of bearing displacement and the zero striking velocity contour are due to the coarseness of the contour interval in the plotting routine. For the typical model (model 2), this area contains approximately 300 km^2.

Comparing figures 7.15 and 7.16 shows that the bearing displacements, striking velocities, and ductility demands for models 2 and 3 are almost identical. However, model 3 (figure 7.16) with k_s and F_{sy} four times larger than model 2, induces considerably higher accelerations in the building (see second-floor acceleration plots and table 7.3). The maximum accelerations, however, are sharp, high-frequency spikes which do not substantially affect the ductility demands.

Comparing figures 7.14 and 7.15 shows that the bearing displacements and striking velocities for models 1 and 2 are very similar. However, there is a very large difference in the ductility demands and a moderate difference in structure accelerations. Model 1 (figure 7.14) has the same story stiffnesses as model 2, but its story yield levels, F_{iy}, are greater by a factor of 2.83 which reduces the ductility demand. The stronger model (model 1) also produces a moderate increase in superstructure accelerations as expected. Additional observations show that the stronger model 1 results in considerably higher bearing displacements in the areas where barrier impact does not occur. This indicates the effect of energy dissipation in the superstructure through yielding to reduce the bearing displacements.

Comparing models 2, 4, and 5 (figures 7.15, 7.17, and 7.18) allows the following observations. Model 2 is the same as model 4 except for the additional viscous damping in the isolation system for model 4. The performance of model 4 is moderately better than that of model 2. For example, taking station D05, the maximum values for bearing displacement, striking velocity, ductility demand, and second floor acceleration are 45 cm, 153 cm/sec, 96, and 1117 cm/sec/sec for model 2 and 44 cm, 123 cm/sec, 76, and 960 cm/sec/sec for model 4, respectively. The greatest difference is in the ductility demand, where the additional damping reduced the ductility demand by only 21%. On the other hand, the Lucerne, Sylmar, and H04 records (table 7.3) indicate that the additional viscous damping reduces the bearing displacements enough to avoid impacts with the barrier. In this case, the ductility demand is reduced by much more. The addition of viscous damping at the base level has been proposed as a method to control excessive bearing displacements. However, the addition of 10% viscous damping only moderately reduces the TBIB model displacement response, but in some cases, the moderate reduction can lead to avoidance of impact which then results in much lower ductility demands than if impact occurs.

The maximum ductility demand and maximum second floor acceleration for the fixed-base structure (figure 7.18) are 43 and 367 cm/sec/sec at station D05. These values are considerably less than the values of either model 2 or model 4. However, for comparison, at station F07, the maximum ductility demand and maximum second floor accelerations are 0 and 161 cm/sec/sec, 0 and 140 cm/sec/sec, and 4 and 433 cm/sec/sec for models 2, 4, and fixed-base, respectively. In other words, at the stations somewhat removed from the most pronounced directivity, the superstructure accelerations and ductility demands for the base-isolated structural models are significantly less than for the similar fixed-base structure. However, in the area of pronounced directivity, the ductility demand and the peak accelerations for the fixed-base structure are less than those for the base-isolated structures because of the effects of the barrier impacts. This puts in perspective the poor performance of a base-isolated structure if the bearing displacement exceeds the maximum total design limit. Additional conclusions can be found in chapter 8.

8. Conclusions to Part Two

As the world-wide data set of recorded near-source motion from moderate to large events grows, and with constant improvements in recording instruments and processing procedures, the nature of the waveforms is becoming better understood. Although moderate in size, the 1994 Northridge earthquake resulted in several valuable records to add to this sparse data set. In this study, recorded near-source motions, as well as the synthetic near-source ground motions, demonstrate large velocity and displacement pulses which can cause large responses in long-period structures such as base-isolated buildings. Structural models of base-isolated buildings indicate a vulnerability to these recorded near-source motions. These models indicate that impact would occur between the isolation level and the structure displacement barriers. These impacts cause inelastic deformations to occur in the superstructure which would be associated with structural damage, and in extreme cases, might cause structural instability and collapse. The impacts result in the rapid deceleration of the base level, but the upper levels of the structure continue to move.

Impact of the base with the barriers for TBIB model 2 would occur for sites located in a region near the epicenter with an areal extent of 300 km^2. This area would be expected to increase significantly for larger magnitude events. Also, due to the directivity effects, a large portion of this area is further than 5, or even 10 km from the surface projection of the fault.

Yielding in the building superstructure significantly reduces the displacements across the bearings and results in lower accelerations in the superstructure, particularly if the base impacts the barrier. Many base-isolated buildings are designed considering the superstructure to remain elastic. This type of analysis will generally result in larger bearing displacements than if the superstructure is represented as a yielding structure. This procedure is, therefore, generally a conservative approach for determining required D_{TM} distances as long as the design input motions are sufficient. This type of modeling, however, does not capture the realistic amount of structural yielding that may occur above the isolation surface.

A four-fold increase in barrier stiffness and yield force has a very small effect on the ductility demand of the superstructure, but results in larger spikes of high frequency acceleration in the superstructure at impact with the barrier. This implies that the stiffer barrier would have little effect on the damage to the actual structure, but the large acceleration could have an adverse effect on building contents.

Due to the impulsive nature of the highly directed near-source earthquake energy, increases in base viscous damping are not as effective in reducing response displacements as would be expected for a sinusoidal excitation. Additional viscous damping is currently being suggested as a way to control very large displacements at the isolation level. In order to be effective for mitigating the effects of large near-source motions (such as D05 motion), large damping values would be required. However, this would also transfer more force into the building.

In the near-source region, as long as impact with the barrier does not occur, the isolated building model behavior is preferable to that of a fixed-base model. However, if impact occurs, the behavior of the isolated structure, as measured by the story ductility demands and superstructure floor accelerations, quickly worsens. These high ductility demands indicate significant structural damage. In the region where impact occurs, the same measures of behavior indicate, in most cases, more desirable behavior from a similar fixed-base structure.

The response spectra values, of both the recorded near-source and synthetic near-source ground motions, tend to be significantly larger than those of strong-motion acceleration histories which have traditionally been considered large (e.g., El Centro, N-S, 1940). This is particularly true for spectral velocities and displacements where the differences are intensified in the period range greater than 1.5 seconds.

This study considered only a M 7.0 event, yet the surface areal extent which resulted in very large model responses was considerable. Even larger events are possible and evidence exists which indicates that unlike peak acceleration values, peak velocities and displacements do not tend to saturate in the near-source region [Heaton *et al.*, 1994]. This is particularly important for long-period structures located near possible large-magnitude earthquake sources.

Perhaps the simplest solution to the problem of impact of the base with the barrier would be to significantly increase the design displacements of base-isolated structures. This approach requires continuing advancements in the development of isolation systems. However, advances in the production of elastomeric, as well as other isolation systems, currently allow for larger displacements than were considered achievable in past years. Continuing development in these areas is required to ensure the acceptance of base isolation as an effective aseismic design technique. Allowing for larger displacements across the bearings is also recommended by Anderson *et al.* [1992] as a possible solution to extreme ground motions.

Source magnitude, orientation of the fault, proximity to the surface projection of the fault, and the type of slip on a fault should all be considered in the design of critical structures, and are possible considerations for a performance-type design criteria, not only for base-isolated structures, but for all long-period structures.

Additional studies are required in order to more thoroughly consider the response of base-isolated structures from near-source ground motions.

References

Aki, K., Strong motion prediction using mathematical modeling techniques, *Bull. Seism. Soc. Am.*, **72**, S29-41, 1982.

Anderson, J. C., and V. V. Bertero, Uncertainties in establishing design earthquakes, *J. of Structural Engineering, ASCE*, **113**, No. 8, Aug. 1987.

Anderson, T. L., Seismic isolation design and construction practice, *Proc. Fourth U. S. Nat. Conf. on Earthquake Engineering*, EERI, **3**, Palm Springs, May 1990.

Anderson, T. L., R. E. Bachman, and P. R. Grant, Base isolation response to extreme ground motions, *Proc. Tenth World Conf. on Earthquake Engineering*, Rotterdam, 1992.

Applied Technology Council, *Tentative Provisions for the Development of Seismic Regulations for Buildings*, ATC 3-06, National Bureau of Standards Special Publication 510, Washington, 1978.

Asher, J. W., D. R. Van Volkinburg, R. L. Mayes, T. Kelly, B. I. Sveinsson, and S. Hussain, Seismic isolation design of the U.S.C. University Hospital, *Proc. Fourth U. S. Nat. Conf. on Earthquake Engineering*, EERI, **3**, Palm Springs, May 1990.

Bachman, R. E., M. J. Gomez, and K. C. Chang, Verification analysis of the base-isolated Los Angeles County Fire Command and Control Facility, *Proc. Fourth U. S. Nat. Conf. on Earthquake Engineering*, EERI, **3**, Palm Springs, May 1990.

Beck, J. L., Statistical system identification of structures, *Structural Safety and Reliability*, 1395-1402, ASCE, 1989.

Beck, J. L., *Determining Models of Structures from Earthquake Records, Report No. EERL 78-01,* Earthquake Engineering Research Laboratory, California Institute of Technology, Pasadena, California, June 1978.

Boore, D., W. Joyner, and T. Fumal, Estimation of response spectra and peak accelerations from western North American earthquakes: *An Interim Report, U.S. Geological Survey Open File Report 93-509*, 1993.

Butler, R., and H. Kanamori, Long-period ground motion from a great earthquake, *Bull. Seism. Soc. Am.*, **70**, No. 4, pp. 943-961, Aug. 1980.

California State Building Standards Commission, *California State Building Code*: California Administrative Code, Title 24, Part 2, Sacramento, California, 1981.

California Strong Motion Instrumentation Program, Processed strong-motion data from the Palm Springs earthquake of 8 July 1986, California Division of Mines and Geology, Office of Strong Motion Studies, *Report No. OSMS 91-16*, 1991.

California Strong Motion Instrumentation Program, Processed strong-motion data for Rancho Cucamonga-Law and Justice Center from the Whittier earthquake of 1 October 1987, California Division of Mines and Geology, Office of Strong Motion Studies, 1993a.

California Strong Motion Instrumentation Program, Processed strong-motion data for Rancho Cucamonga-Law and Justice Center from the Landers earthquake of 28 June 1992, California Division of Mines and Geology, Office of Strong Motion Studies, 1993b.

California Strong Motion Instrumentation Program, Pre-processed strong-motion data for Los Angeles-Fire Command/Control Building from the Sierra Madre earthquake of 28 June 1991, California Division of Mines and Geology, Office of Strong Motion Studies, 1994a.

California Strong Motion Instrumentation Program, Pre-processed strong-motion data for Los Angeles-Fire Command/Control Building from the Landers earthquake of 28 June 1992, California Division of Mines and Geology, Office of Strong Motion Studies, 1994b.

California Strong Motion Instrumentation Program, Pre-processed strong-motion data for Los Angeles-University Hospital from the Landers earthquake of 28 June 1992, California Division of Mines and Geology, Office of Strong Motion Studies, 1994c.

Caughey, T. K., Nonlinear analysis, synthesis and identification theory, *Proc. Symposium on Testing and Identification of Nonlinear Systems*, California Institute of Technology, March 1975.

Chen, X., Near-Field Ground Motion from the Landers Earthquake, *Engineers Thesis*, California Institute of Technology, Pasadena, California, 1995.

Clough, R. W. and J. Penzien, *Dynamics of Structures*, McGraw-Hill, Inc., New York, 1975.

Darragh, R., T. Cao, C. Cramer, M. Huang, and A. Shakal, Processed CSMIP strong-motion records from the Northridge, California earthquake of January 17, 1994: release no. 1, California Division of Mines and Geology, Office of Strong Motion Studies, *Report No. OSMS 94-06B*, 1994.

Davis, T. L., J. Namson, and R. F. Yerkes, A cross-section of the Los Angeles area: seismically active fold and thrust belt, the 1987 Whittier Narrows earthquake and earthquake hazard, *J. Geophys. Res.* **94**, 9644-9664, 1989.

Distifano, N., and R. Todeschini, Modeling, identification and prediction of a class of nonlinear viscoelastic materials, *International Journal of Solids and Structures*, **9**, 1976.

Dolan, J., K. Sieh, T. Rockwell, R. Yeats, J. Shaw, J. Suppe, G. Huftile, and E. Gath, Plausible earthquake scenarios for the greater Los Angeles metropolitan region, submitted to *Science*, 1994.

Habibullah, A., *ETABS Three Dimensional Analysis of Building Systems*, Computers and Structures, Inc., Berkeley, California, 1992.

Hadley, D. M., and D. V. Helmberger, Simulation of strong ground motions, *Bull. Seism. Soc. Am.*, **70**, No. 2, pp. 617-630, Apr. 1980.

Hanks, T. C., Observations and estimation of long-period strong ground motion in the Los Angeles basin, *Earthquake Engineering and Structural Dynamics*, **4**, 473-488, 1976.

Hartzell, S. H., and T. H. Heaton, Inversion of strong ground motion and teleseismic waveform data for the fault rupture history of the 1979 Imperial Valley, California earthquake, *Bull. Seism. Soc. Am.*, **73**, 1553-1583, 1983.

Hauksson, E., and L. M. Jones, The 1987 Whittier Narrows earthquake sequence in Los Angeles, Southern California: seismological and tectonic analysis, *J. Geophys. Res.*, **95**, 9569-9589, 1989.

Heaton, T. H., Evidence for and implications of self healing pulses of slip in earthquake rupture, *Physics of the Earth and Planetary Interiors*, **64**, 1-20, 1990.

Heaton, T. H., J. H. Hall, D. J. Wald, and M. W. Halling, The response of high-rise and base-isolated buildings to a hypothetical M_W 7.0 blind thrust earthquake, submitted to *Science*, 1994.

Huang, M. J., T. Cao, U. Vetter, and A. Shakal, Processed strong-motion data from the base-isolated San Bernardino County Law and Justice Center for the Upland earthquake of 28 February 1990, California Division of Mines and Geology, Office of Strong Motion Studies, *Report No. OSMS 90-03*, 1990.

Huang, M. J., P. K. Malhotra, and A. F. Shakal, Analysis of records from four base-isolated buildings during low levels of ground shaking, *Proc. ATC-17-1 Seminar on Seismic Isolation, Passive Energy Dissipation, and Active Control*, Applied Technology Council, San Francisco, California, 1993.

Huang, M. J., A. Shakal, D. Parke, J. Ragsdale, and R. Sherburne, Processed data from the strong-motion record obtained at a base-isolated building in Rancho Cucamonga, California, during the Redlands earthquake of 2 October 1985, California Division of Mines and Geology, Office of Strong Motion Studies, *Report No. OSMS 86-01*, 1986.

Hudson, D. E., Strong motion earthquake measurements in epicentral regions, *Proc. Sixth World Conf. on Earthquake Engineering*, New Delhi, 1977.

Hudson, D. E., Some recent near-source strong motion accelerograms, *Proc. Ninth World Conf. on Earthquake Engineering*, Tokyo, 1988.

Hudson, D. E., M. D. Trifunac, and A. G. Brady (1969 to 1976). Analysis of strong-motion accelerograms, Vol. I, Parts A-Y, Vol. II, Parts A-Y, Vol. III, Parts A-Y, Vol. IV, Parts A-Y, Index Vol. (*EERL Report 76-02*), Earthquake Engineering Research Laboratory, California Institute of Technology, Pasadena, California, 1976.

International Conference of Building Officials, *Uniform Building Code: 1991 Edition*, International Conference of Building Officials, Whittier, California, 1991.

Kanamori, H., A semi-empirical approach to prediction of long-period ground motions from great earthquakes, *Bull. Seism. Soc. Am.*, **69**, No. 6, pp. 1645-1670, 1979.

Kanamori, H., P. C. Jennings, S. K. Singh, and L. Astiz, Estimation of strong ground motions in Mexico City expected for large earthquakes in the Guerrero seismic gap, *Bull. Seism. Soc. Am.*, **83**, No. 3, pp. 811-829, Jun. 1993.

Kelly, J. M., Aseismic base isolation: review and bibliography, *Soil Dynamics and Earthquake Engineering*, **5**, No. 3, 1986.

Kelly, J. M., I. D. Aiken, and P. W. Clark, Response of base-isolated structures in recent Californian earthquakes, *Proc. SMIP91 Seminar on Seismological and Engineering Implications of Recent Strong-Motion Data*, California Strong Motion Instrumentation Program, Sacramento, May 1991.

Kelly, J. M., and M. Celebi, Verification Testing of Prototype Bearings for a Base Isolated Building, *Report No. UCB/SESM-84/01*, University of California, Berkeley, 1984.

KPFF Consulting Engineers and Dynamic Isolation Systems, Inc., Design of USC University Hospital Using Seismic Isolation, Design, Analysis and Evaluation, Santa Monica, California, 1988.

Maison, B. F., and C. E. Ventura, Seismic analysis of base-isolated San Bernardino County building, *Earthquake Spectra*, **8**, No. 4, 1992.

Masri, S. F., H. Sassi, T. K. Caughey, Nonparametric identification of nearly arbitrary nonlinear systems, *ASME J. of Applied Mechanics*, **11**, Jan 1981.

McVerry, G. H., and J. L. Beck, Structural identification of JPL building 180 using optimally synchronized earthquake records, *Report No. EERL 83-01*, Caltech, 1983.

Naeim, F., ed., *The Seismic Design Handbook,* Van Nostrand, New York, 1989.

Nagarajaiah, S., A. M. Reinhorn, and M. C. Constantinou, 3D-BASIS Nonlinear Dynamic Analysis of Three-Dimensional Base Isolated Structures: Part II, *Technical Report NCEER-91-0005,* National Center for Earthquake Engineering Research, Buffalo, 1991.

Natke, H. G. and J. T. P. Yao, ed., *Structural Safety Evaluation Based on System Identification Approaches*, Vieweg & Sohn, Wiesbaden, 1988.

Papageorgiou, A. S., and B. C. Lin, Study of the earthquake response of the base-isolated Law and Justice Center in Rancho Cucamonga, *Earthquake Eng. and Struct. Dyn.*, **18**, 1189-1200, 1989.

Peng, C. Y., Generalized Modal Identification of Linear and Nonlinear Dynamic Systems, *Ph.D. Thesis,* California Institute of Technology, Pasadena, California, 1988.

Saikia, C. K., Estimated ground motions in Los Angeles due to M_W=7 earthquake on the Elysian thrust fault, *Bull. Seism. Soc. Am.*, **83**, No 3, pp. 780-810, 1993.

Seible, F. and M. J. N. Priestley, L. A. County Fire Control Center, Bearing Tests 1 to 4, Test Report to Fyfe and Associates, Department of Applied Mechanics and Engineering Sciences, U. C. San Diego, La Jolla, California, 1989.

Skinner, R. I., W. H. Robinson, and G. H. McVerry, *An Introduction to Seismic Isolation,* John Wiley and Sons, New York, 1993.

Söderström, T. and P. Stoica, *System Identification*, Prentice Hall International (UK) Ltd., 1989.

Stanton, J. and C. Roeder, Advantages and limitations of seismic isolation, *Earthquake Spectra,* **7**, No. 2, 1991.

Structural Engineers Association of California, Seismology Committee, *Recommended Lateral Force Requirements, 1990 Edition,* Sacramento, California, 1990.

Tarics, A. G., D. Way, and J. M. Kelly, The Implementation of Base Isolation for the Foothill Communities Law and Justice Center, *Report to the National Science Foundation and the County of San Bernardino,* Reid and Tarics Associates, San Francisco, 1984a.

Tarics, A. G., D. Way, J. M. Kelly, and R. Holland, Report on the Manufacture and Testing of Seismic Bearings for the Foothill Communities Law and Justice Center, Base Isolation Consultants, Inc., San Francisco, 1984b.

Udwadia, F. E. and C-P Kuo, Nonparametric identification of a class of nonlinear close-coupled dynamic systems, *International Journal of Earthquake Engineering and Structural Dynamics*, **9**, 1981.

University of California at Santa Barbara, Strong Motion Record from the Stone Canyon Reservoir Station, 1994 Northridge Earthquake, 1994.

Wald, D. J., Strong motion and broadband teleseismic analysis of the 1991 Sierra Madre, California, earthquake, *J. Geophys. Res.,* **97**, 11033-11046, 1992.

Wald, D. J., and T. H. Heaton, Spatial and temporal distribution of slip for the 1992 Landers, California, earthquake, *Bull. Seism. Soc. Am.*, **84**, 668-691, 1994a.

Wald, D. J., and T. H. Heaton, A dislocation model of the 1994 Northridge, California earthquake determined from strong ground motions, U. S. Geological Survey *Open-File Report 94-278,* 1994b.

Wald, D. J., T. H. Heaton, and D. V. Helmberger, Rupture model of the 1989 Loma Prieta earthquake from the inversion of strong motion and broadband teleseismic data, *Bull. Seism. Soc. Am.*, **81**, 1540-1572, 1991.

Wald, D. J., D. V. Helmberger, and S. H. Hartzell, Rupture process of the 1987 Superstition Hills earthquake from the inversion of strong-motion data, *Bull. Seism. Soc. Am.*, **80**, 1079-1098, 1990.

Werner, S. D., J. L. Beck, and M. B. Levine, Seismic response evaluation of Meloland road overpass using 1979 Imperial Valley earthquake records, *Earthquake Engineering and Structural Dynamics*, **15**, 249-274, 1987.

Woodward-Clyde Consultants, Geological and earthquake ground motion, Fire Command and Control Facility, Monterey Park, California, Project No. 8843128A, 15 March 1988.

Figures

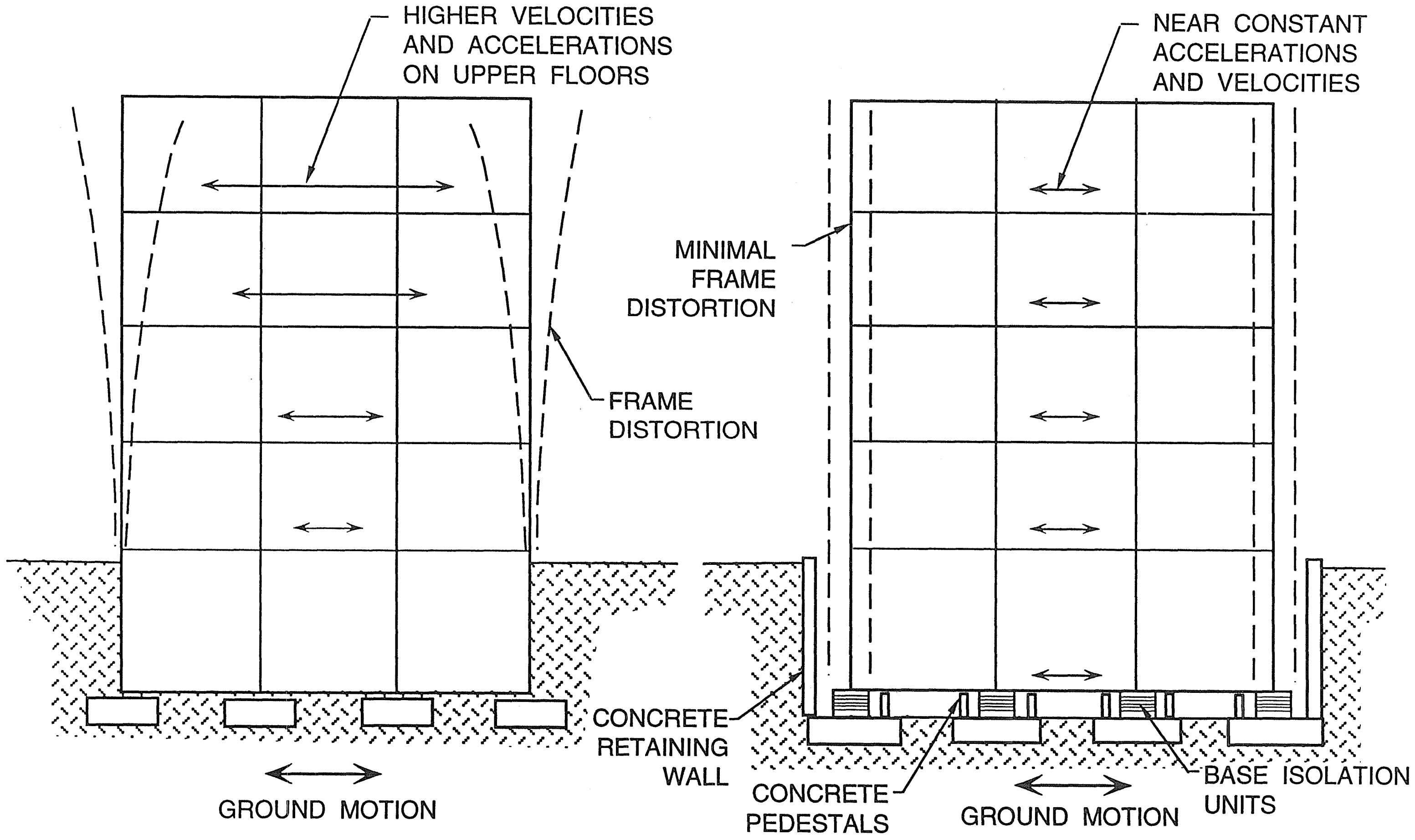

(a) Conventional Building Movement during Earthquake

(b) Base Isolated Building Movement during Earthquake

Figure 2.1 Idealized comparison of dynamic response of a conventional fixed-base building and a base-isolated building.

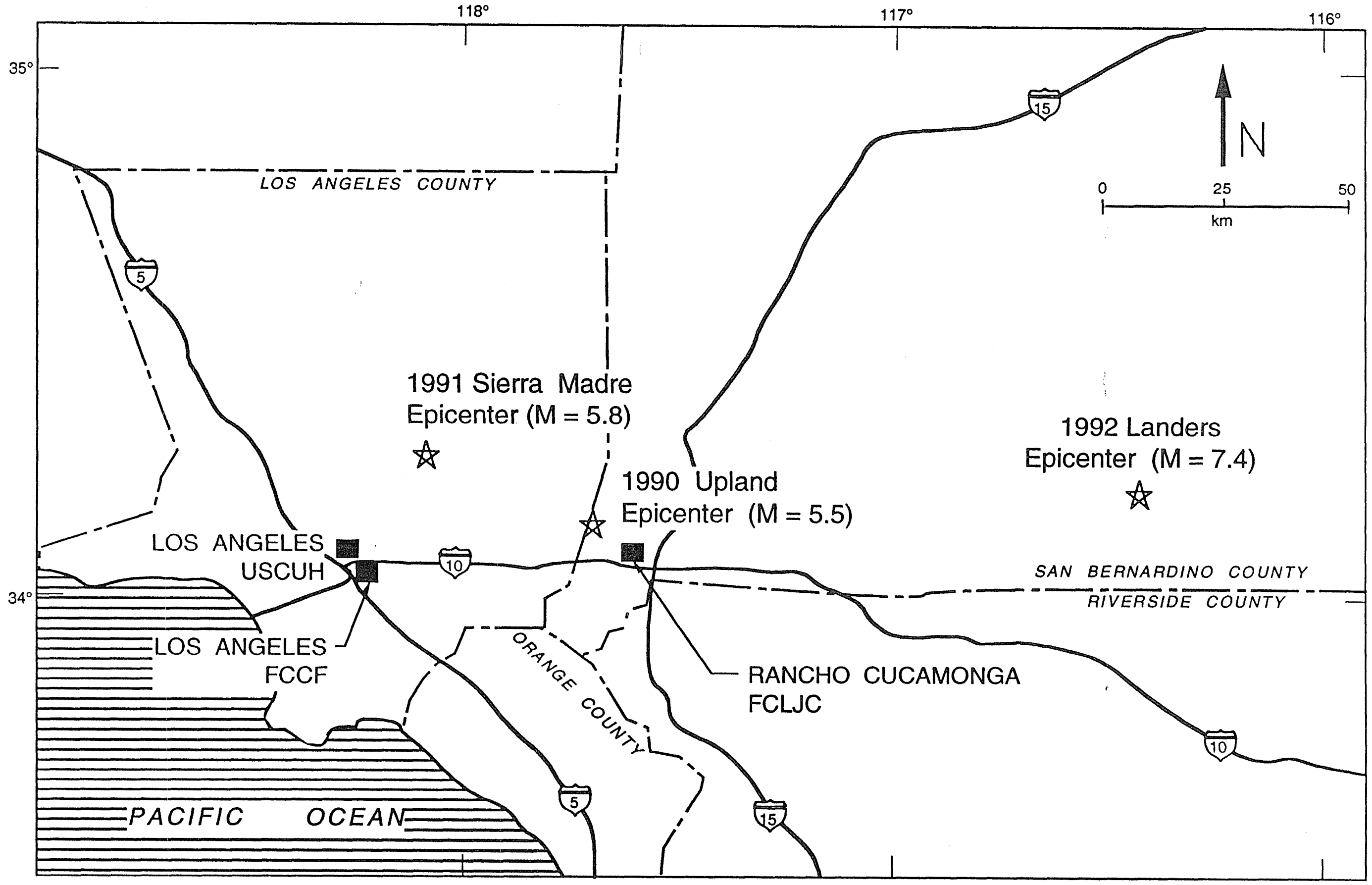

Figure 3.1 Location map of the three studied structures and epicenters of several recent Southern California earthquakes.

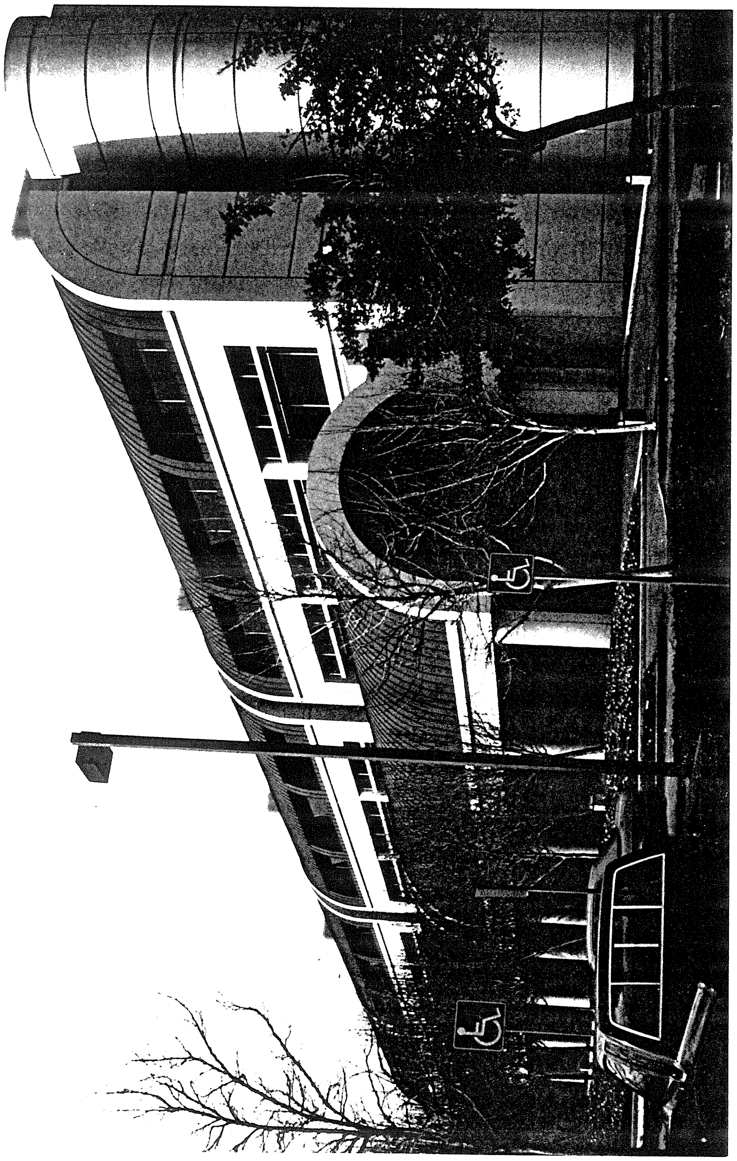

Figure 3.2 The Foothill Communities Law and Justice Center (FCLJC).

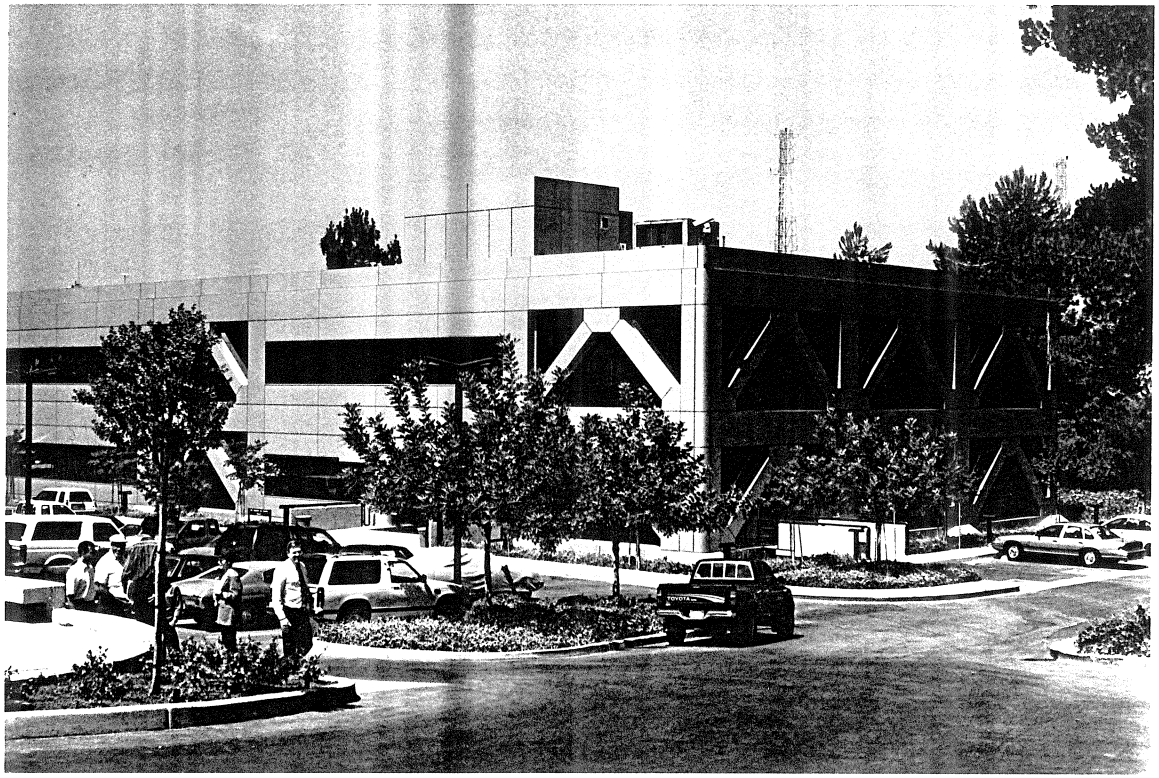

Figure 3.3 The Los Angeles County Fire Command and Control Facility (FCCF).

Figure 3.4 The University of Southern California University Hospital (USCUH).

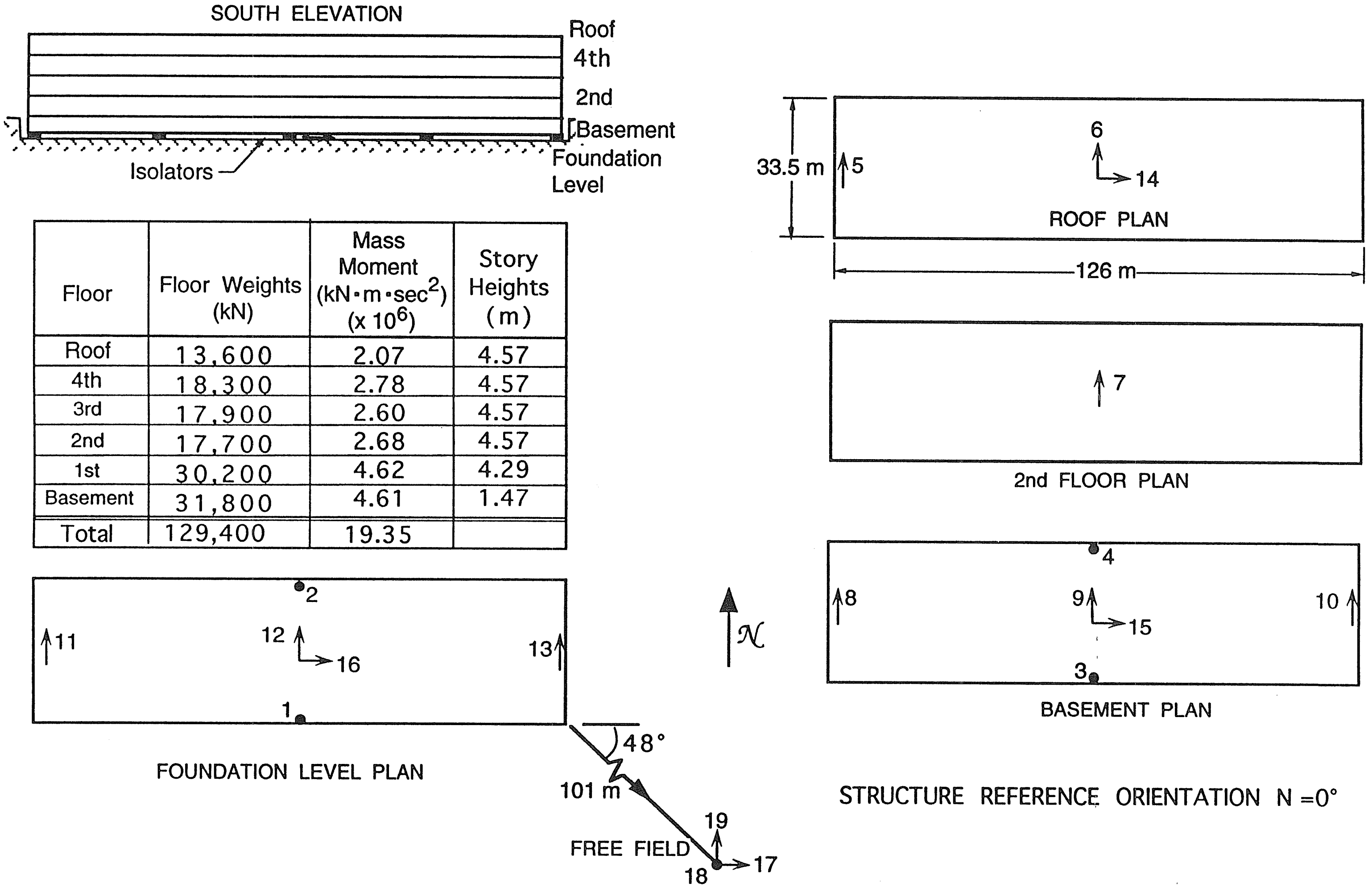

Floor	Floor Weights (kN)	Mass Moment (kN·m·sec^2) (x 10^6)	Story Heights (m)
Roof	13,600	2.07	4.57
4th	18,300	2.78	4.57
3rd	17,900	2.60	4.57
2nd	17,700	2.68	4.57
1st	30,200	4.62	4.29
Basement	31,800	4.61	1.47
Total	129,400	19.35	

Figure 3.5 FCLJC schematic diagram showing locations of accelerometers as well as properties used in analysis.

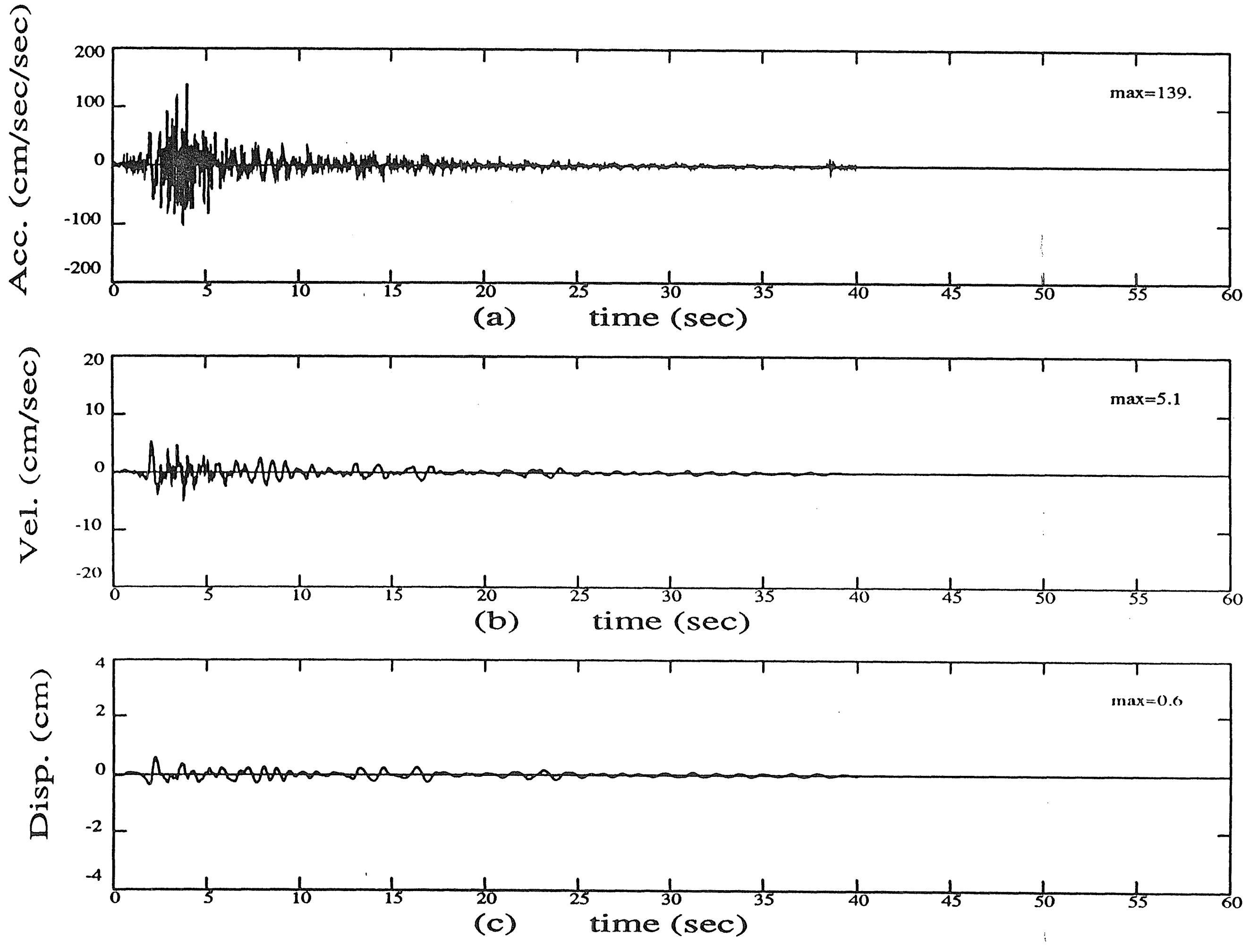

Figure 3.6 FCLJC transverse foundation motion (channel 12) from the 1990 Upland earthquake.

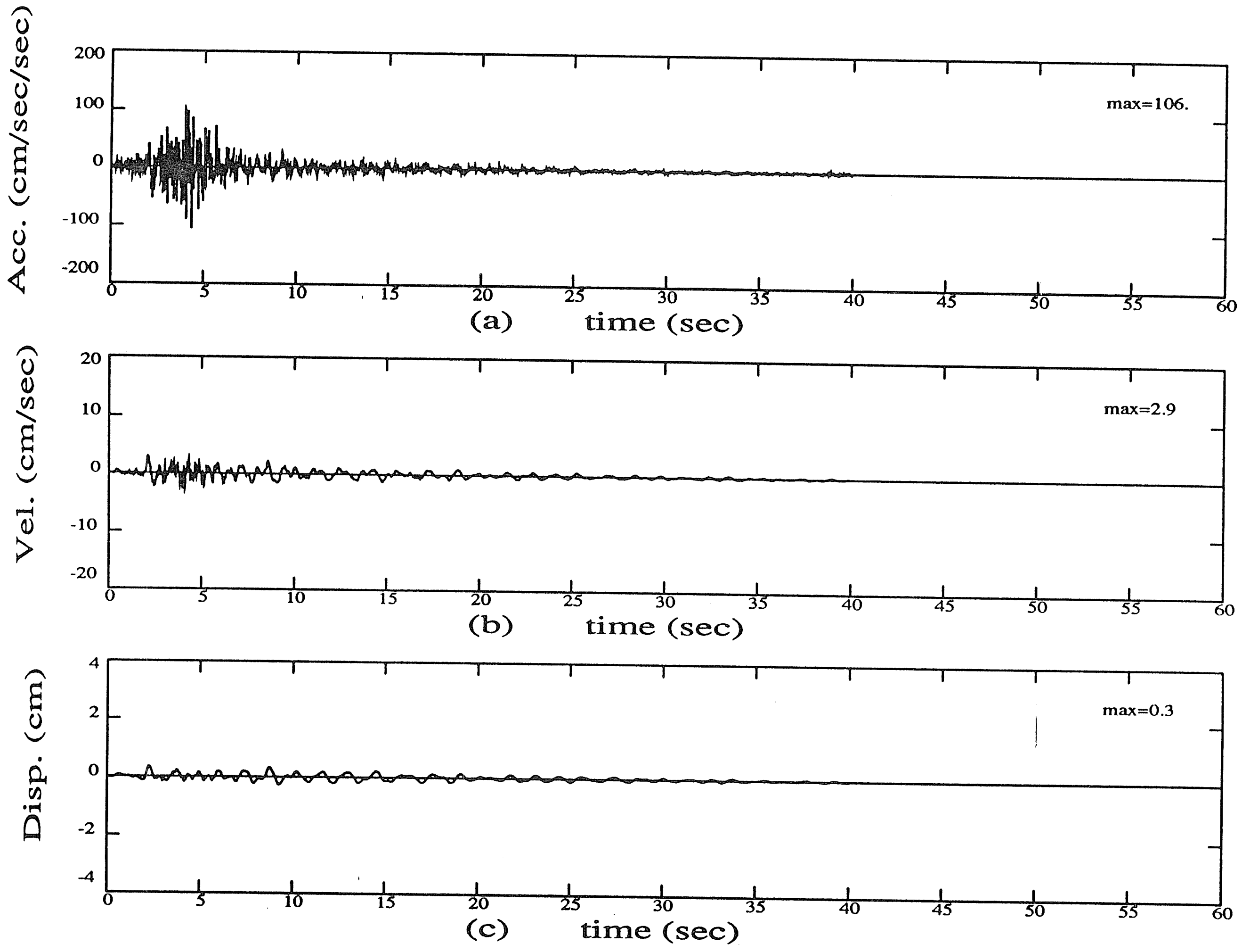

Figure 3.7 FCLJC longitudinal foundation motion (channel 16) from the 1990 Upland earthquake.

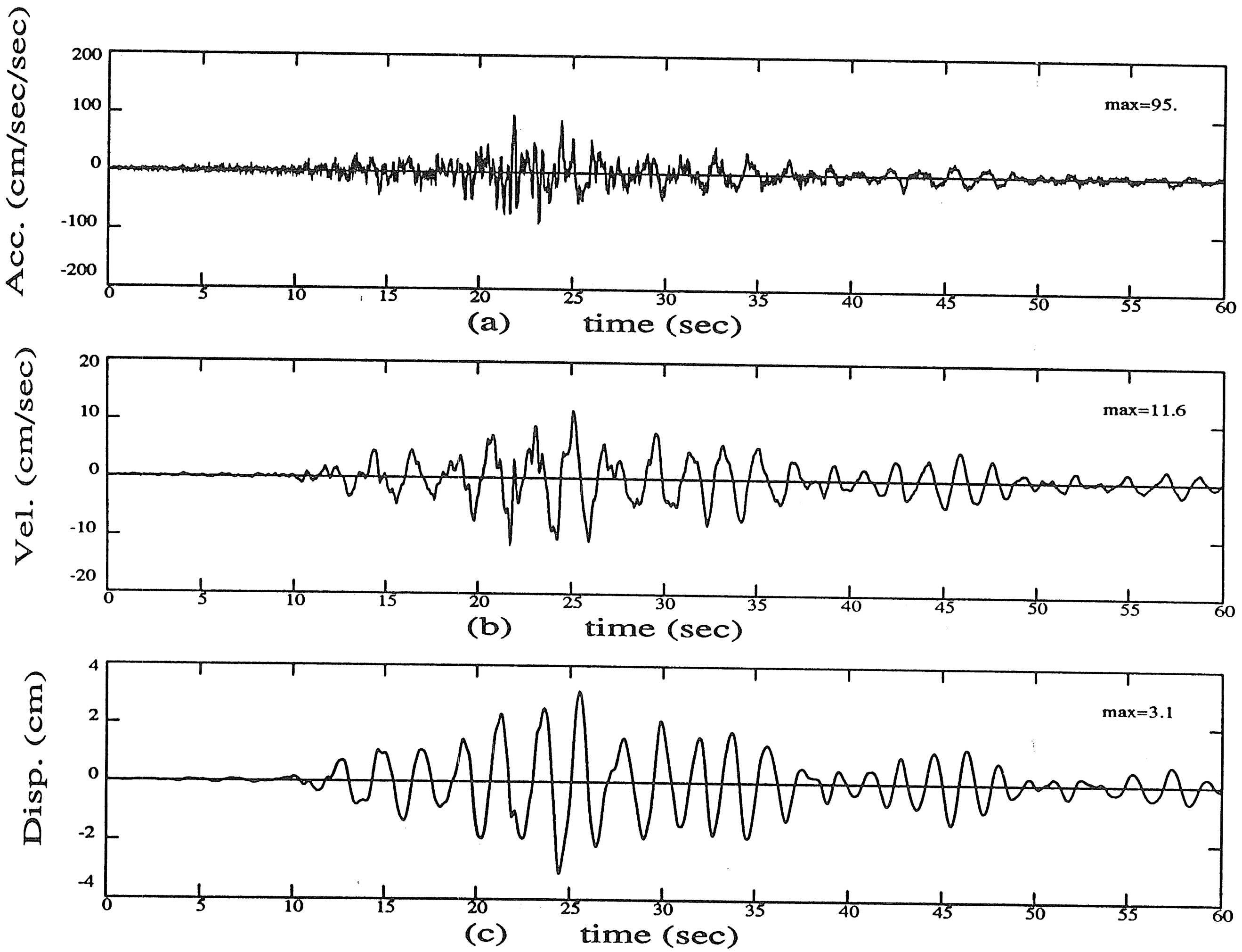

Figure 3.8 FCLJC transverse foundation motion (channel 12) from the 1992 Landers earthquake.

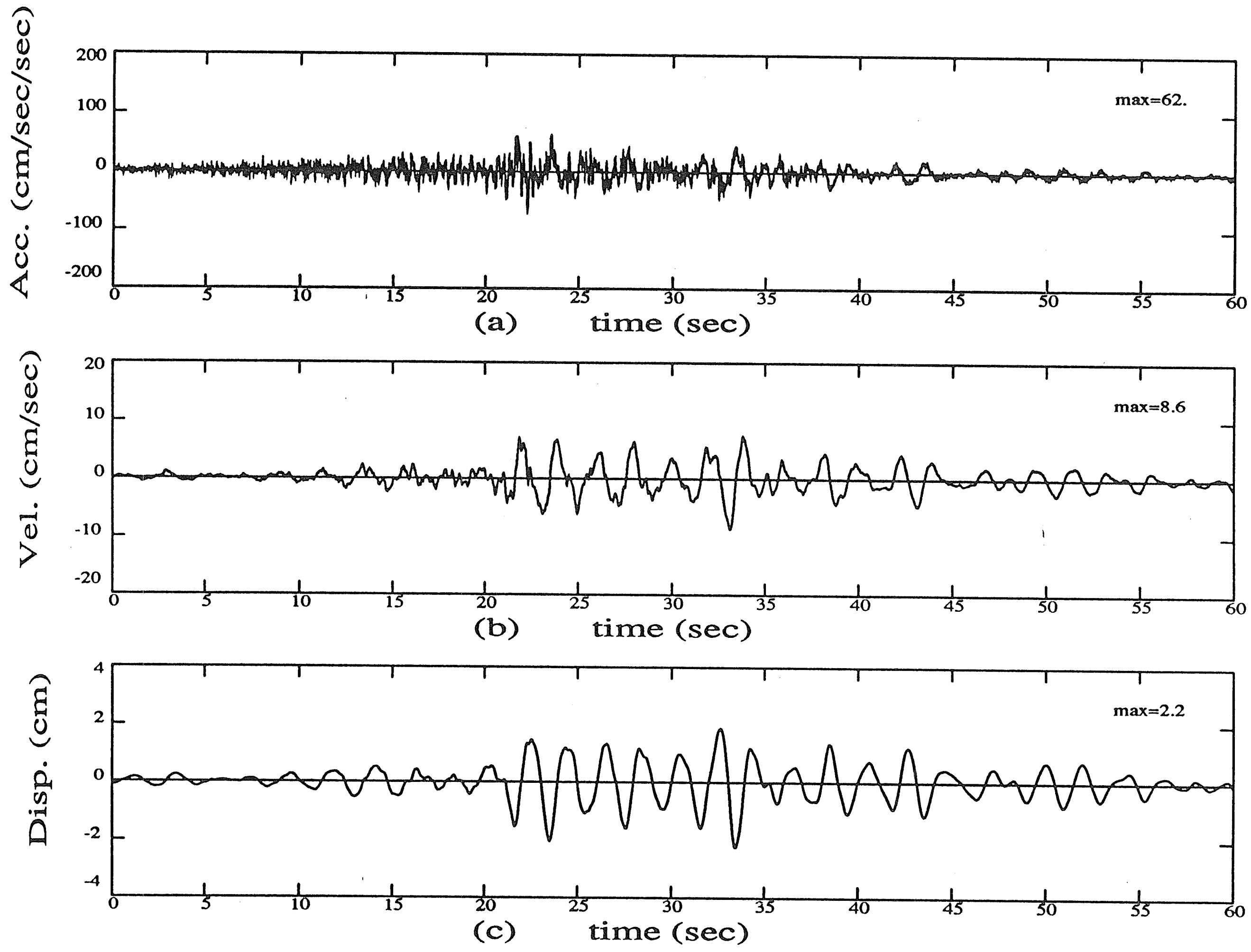

Figure 3.9 FCLJC longitudinal foundation motion (channel 16) from the 1992 Landers earthquake.

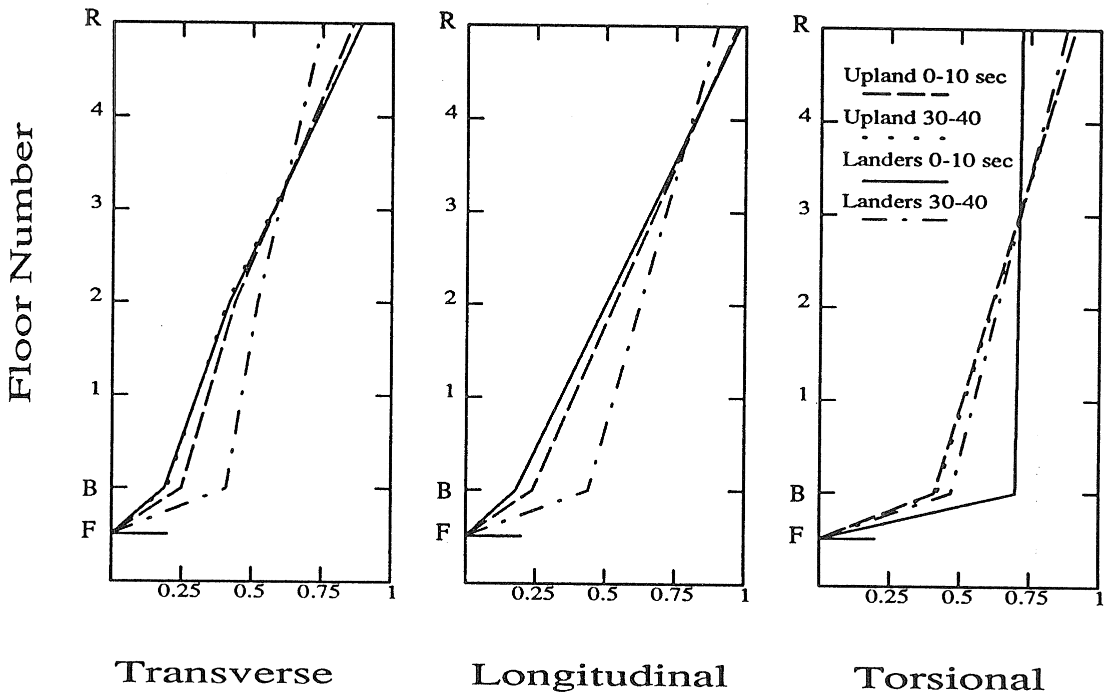

Figure 3.10 FCLJC identified first transverse, longitudinal, and torsional mode shapes from the 1990 Upland and the 1992 Landers earthquakes. Each mode shapes is normalized to a vector length of one.

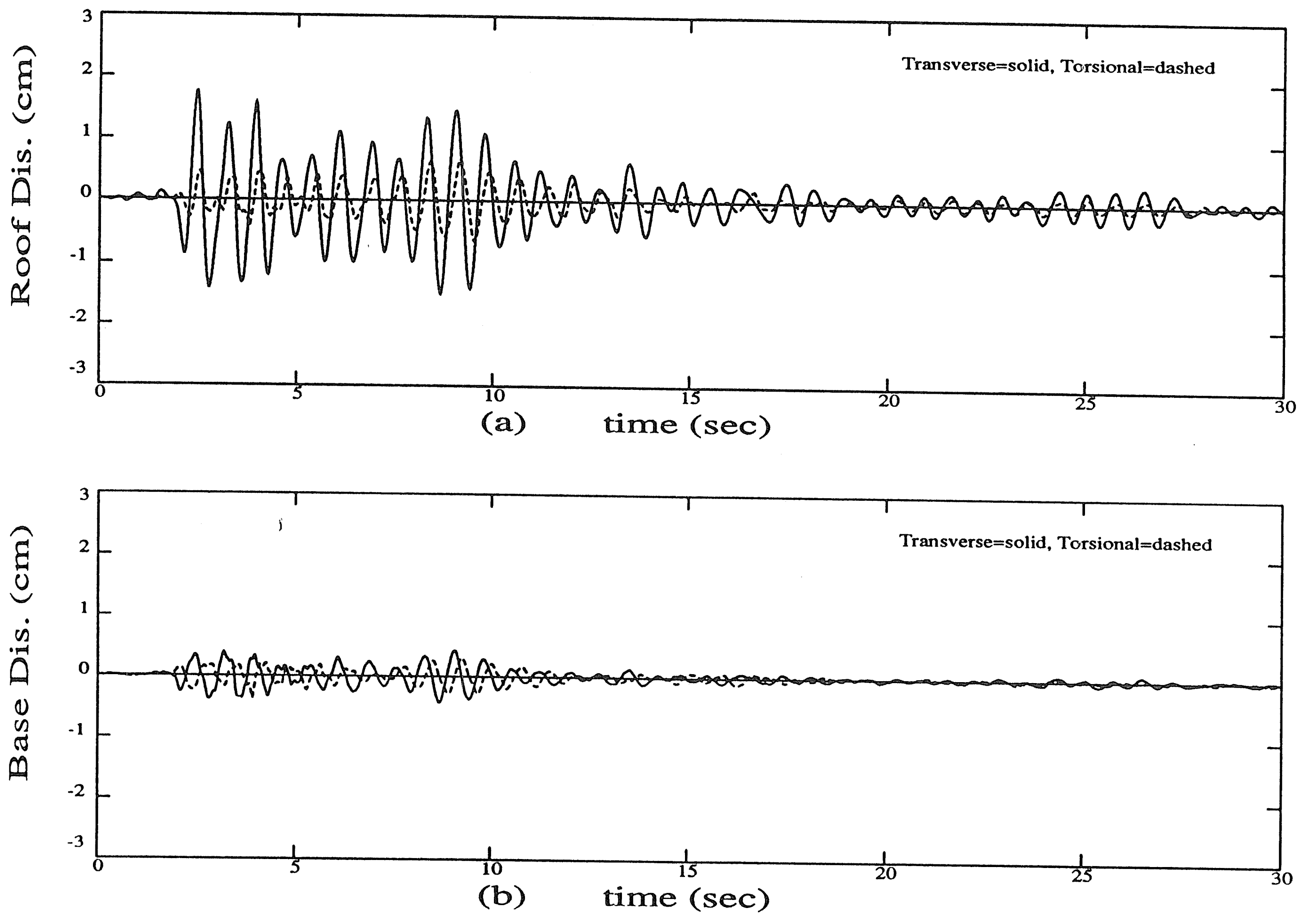

Figure 3.11 FCLJC recorded transverse response at the roof and base (relative to the foundation) including torsional response (rotation x L/2) from the 1990 Upland earthquake.

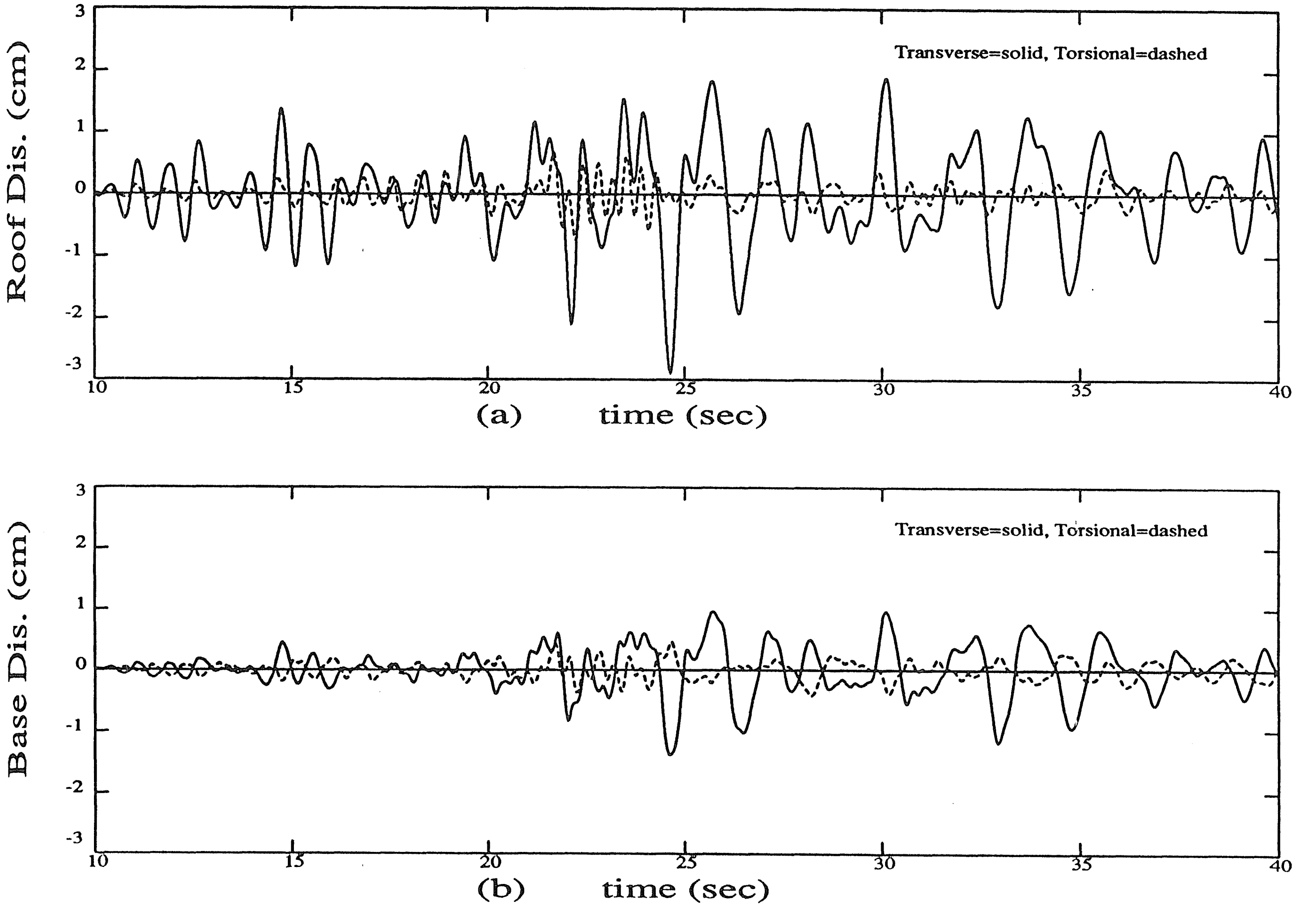

Figure 3.12 FCLJC recorded transverse response at the roof and base (relative to the foundation) including torsional response (rotation x L/2) from the 1992 Landers earthquake.

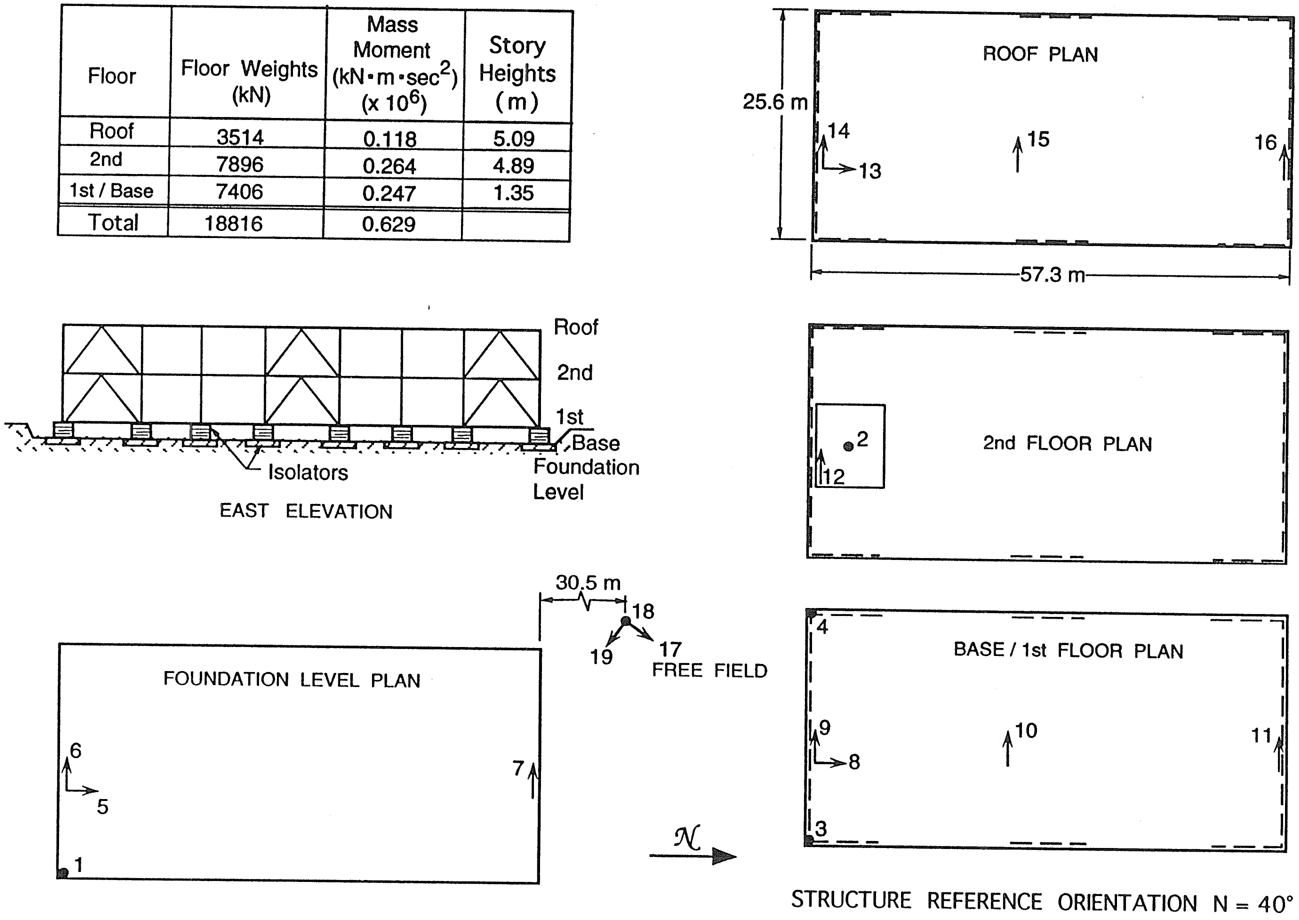

Floor	Floor Weights (kN)	Mass Moment (kN•m•sec^2) (x 10^6)	Story Heights (m)
Roof	3514	0.118	5.09
2nd	7896	0.264	4.89
1st / Base	7406	0.247	1.35
Total	18816	0.629	

STRUCTURE REFERENCE ORIENTATION N = 40°

Figure 3.13 FCCF schematic diagram showing locations of accelerometers as well as properties used in analysis.

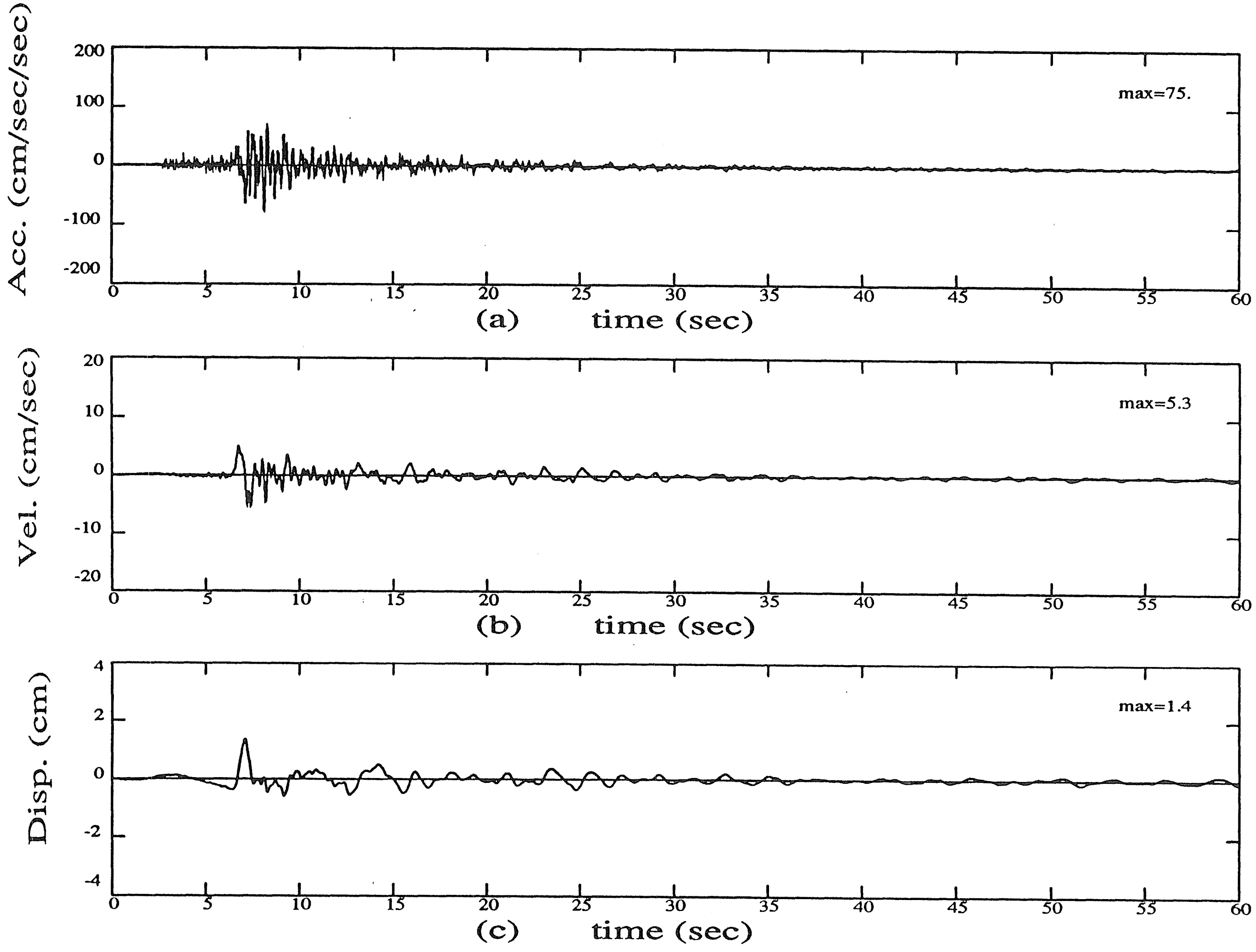

Figure 3.14 FCCF transverse foundation motion (channel 6) from the 1991 Sierra Madre earthquake.

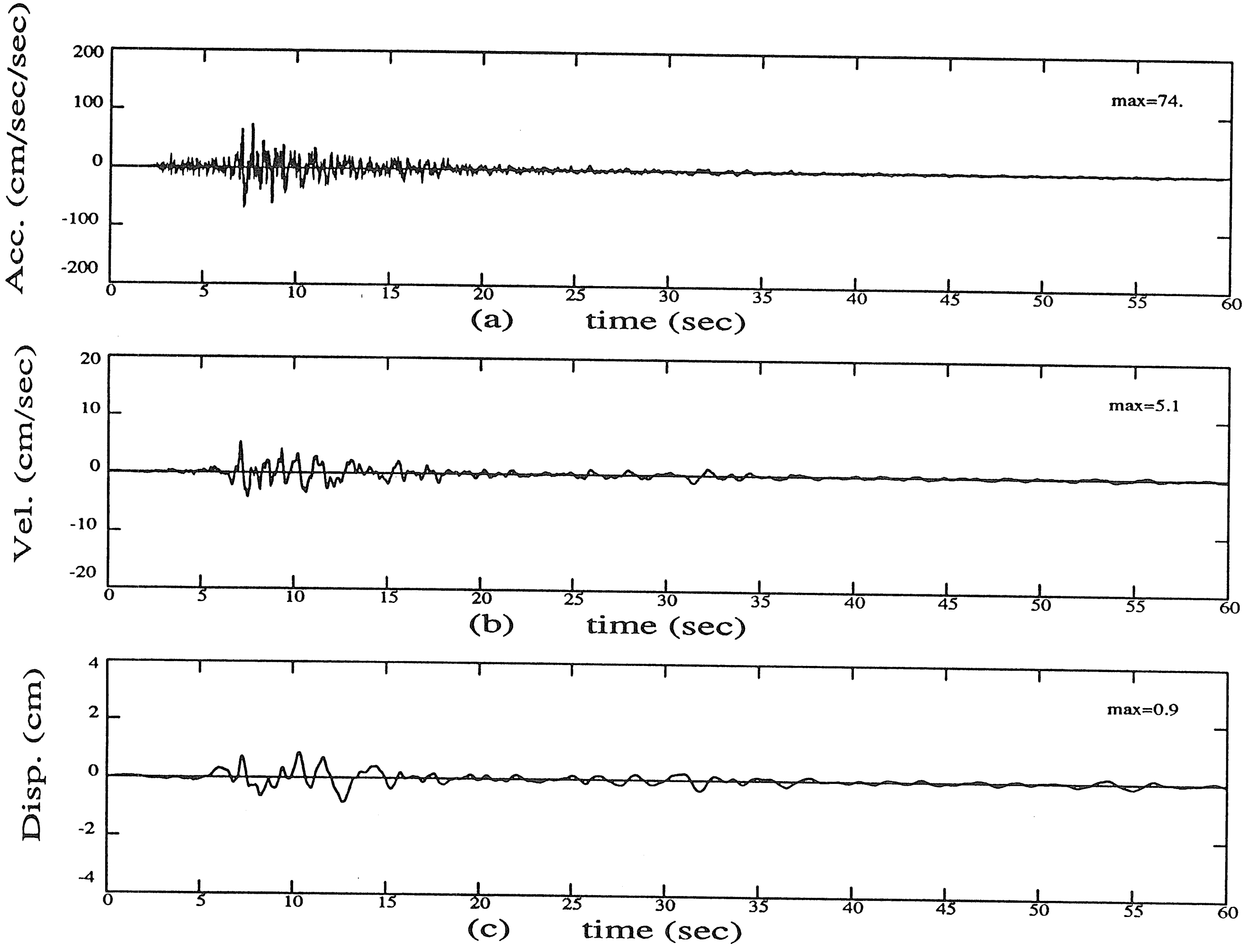

Figure 3.15 FCCF longitudinal foundation motion (channel 5) from the 1991 Sierra Madre earthquake.

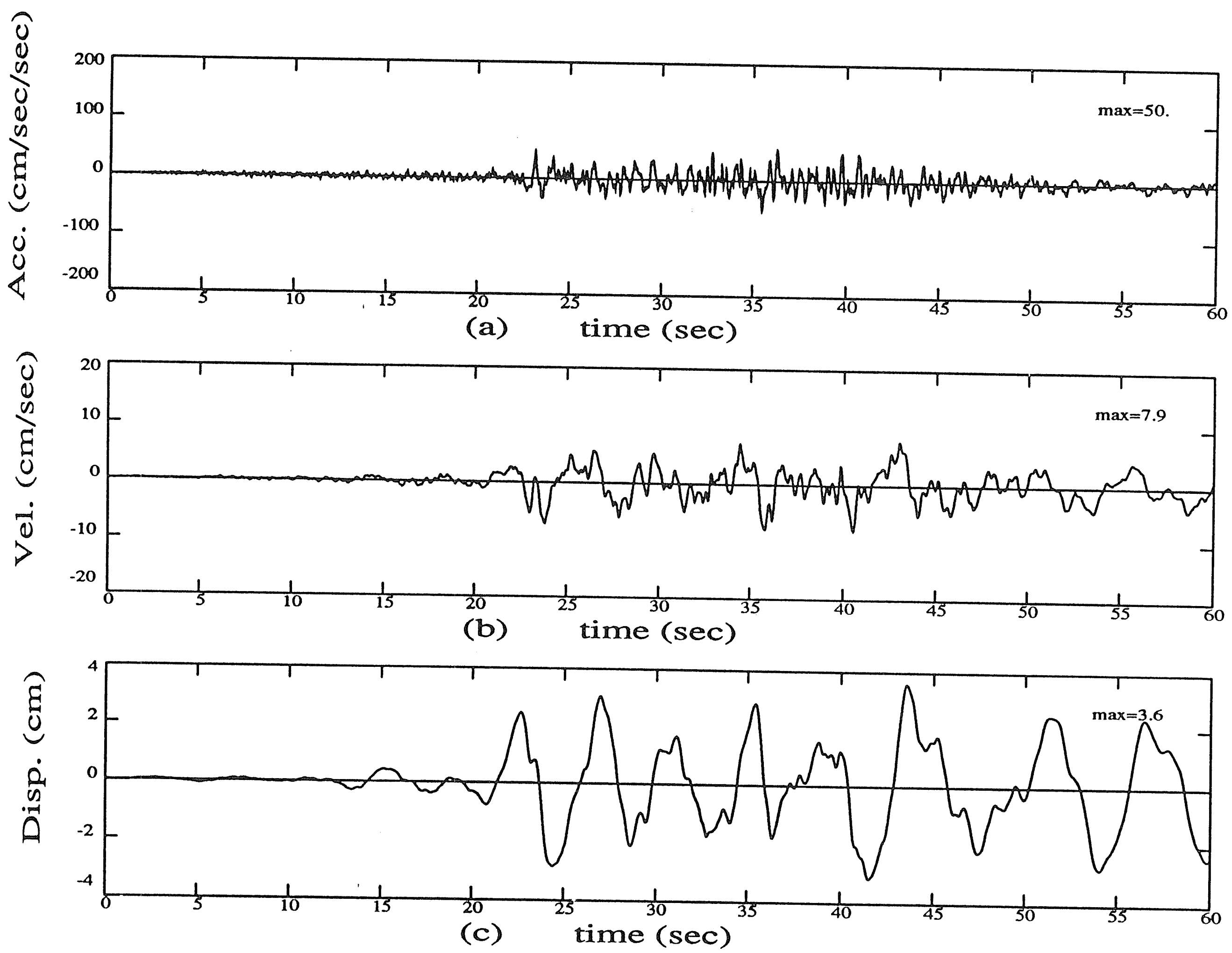

Figure 3.16 FCCF transverse foundation motion (channel 6) from the 1992 Landers earthquake.

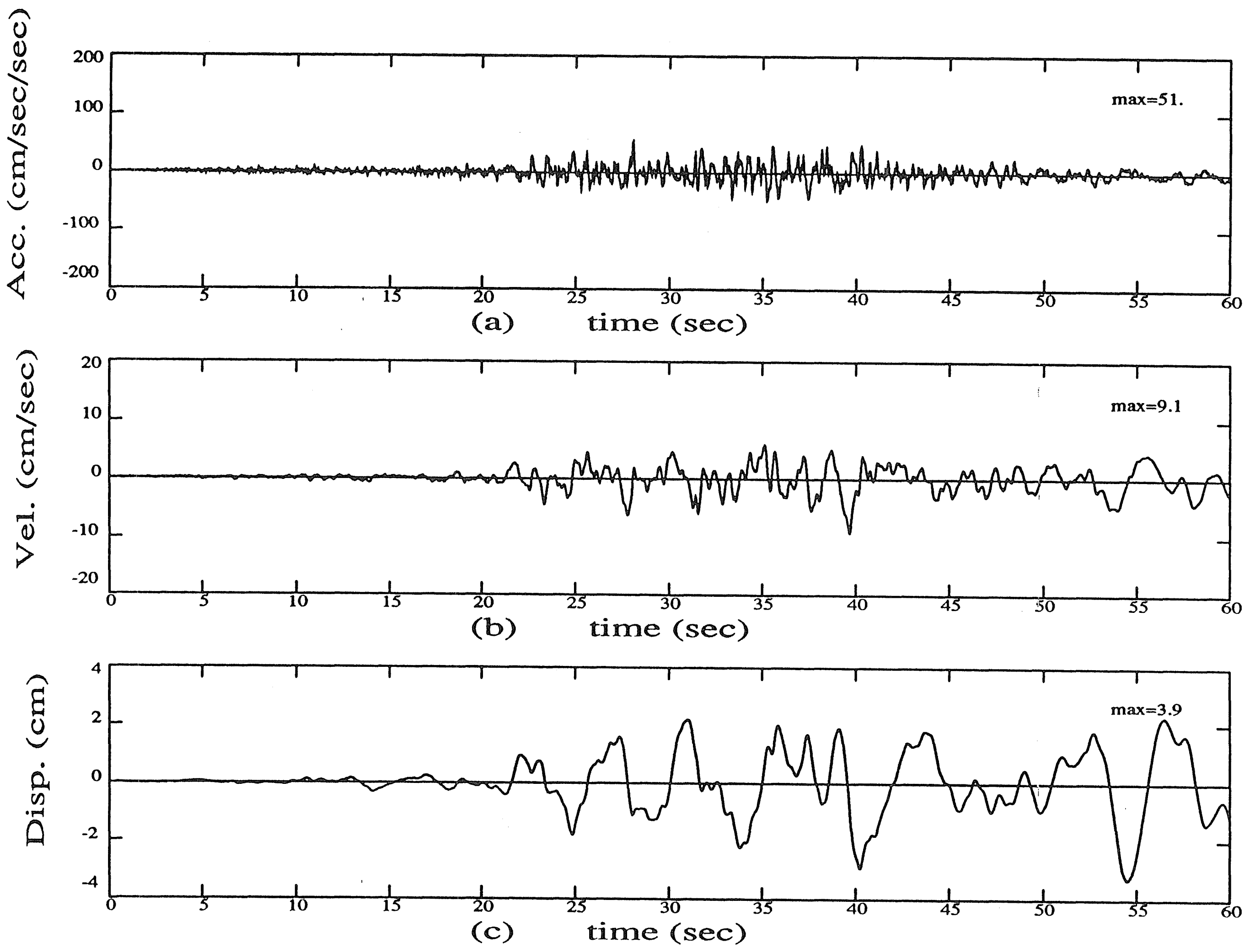

Figure 3.17 FCCF longitudinal foundation motion (channel 5) from the 1992 Landers earthquake.

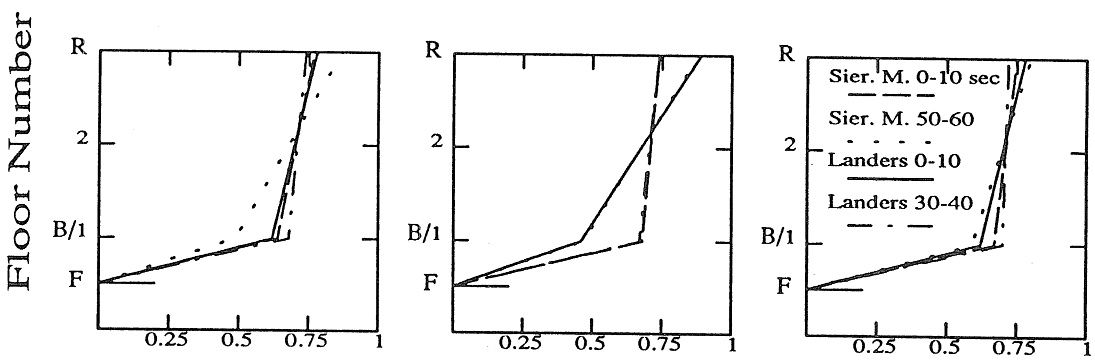

Transverse Longitudinal Torsional

Figure 3.18 FCCF identified first transverse, longitudinal, and torsional mode shapes from the 1991 Sierra Madre and the 1992 Landers earthquakes. Each mode shape is normalized to a vector length of one.

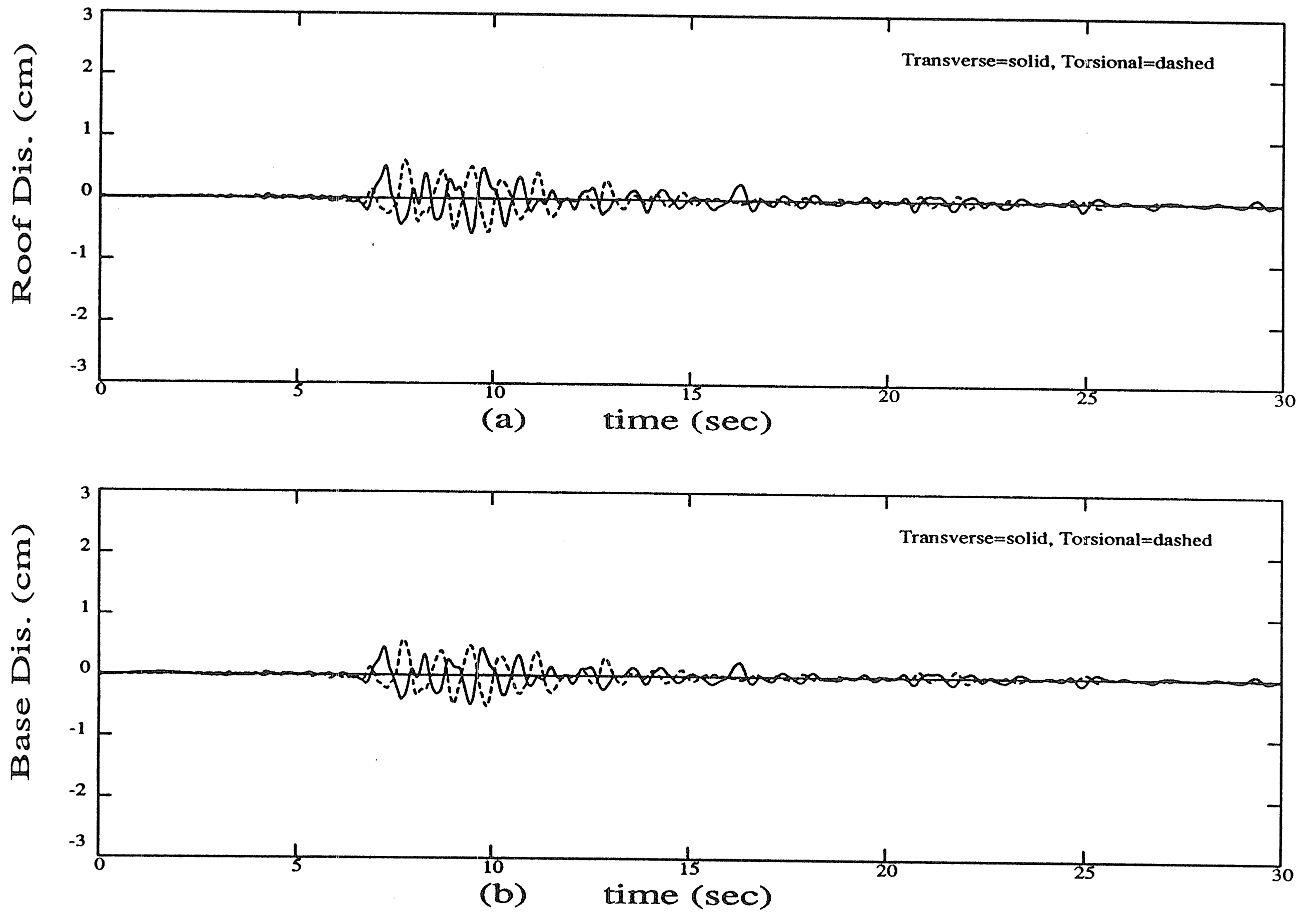

Figure 3.19 FCCF recorded transverse response at the roof and base (relative to the foundation) including torsional response (rotation x L/2) from the 1991 Sierra Madre earthquake.

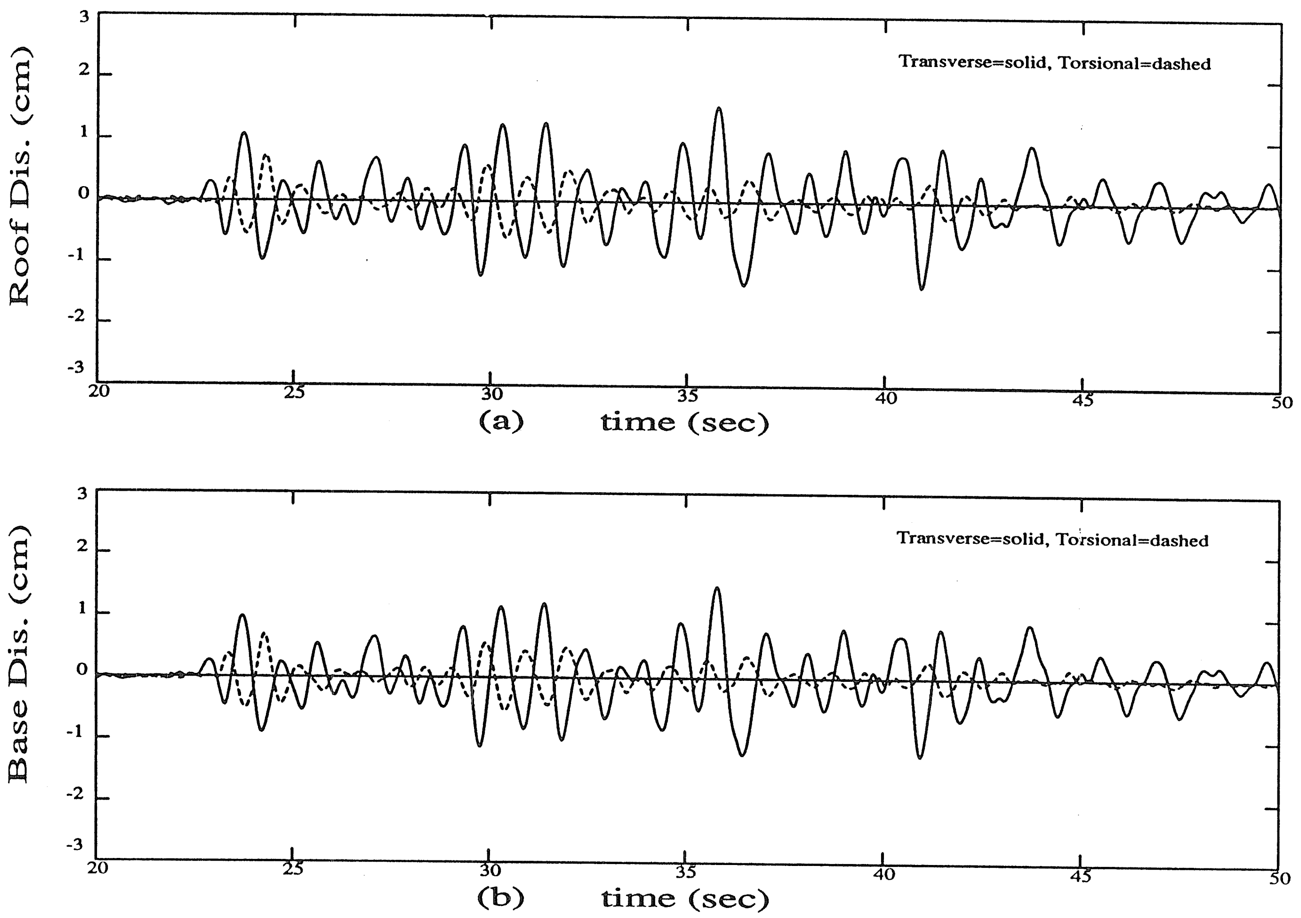

Figure 3.20 FCCF recorded transverse response at the roof and base (relative to the foundation) including torsional response (rotation x L/2) from the 1992 Landers earthquake.

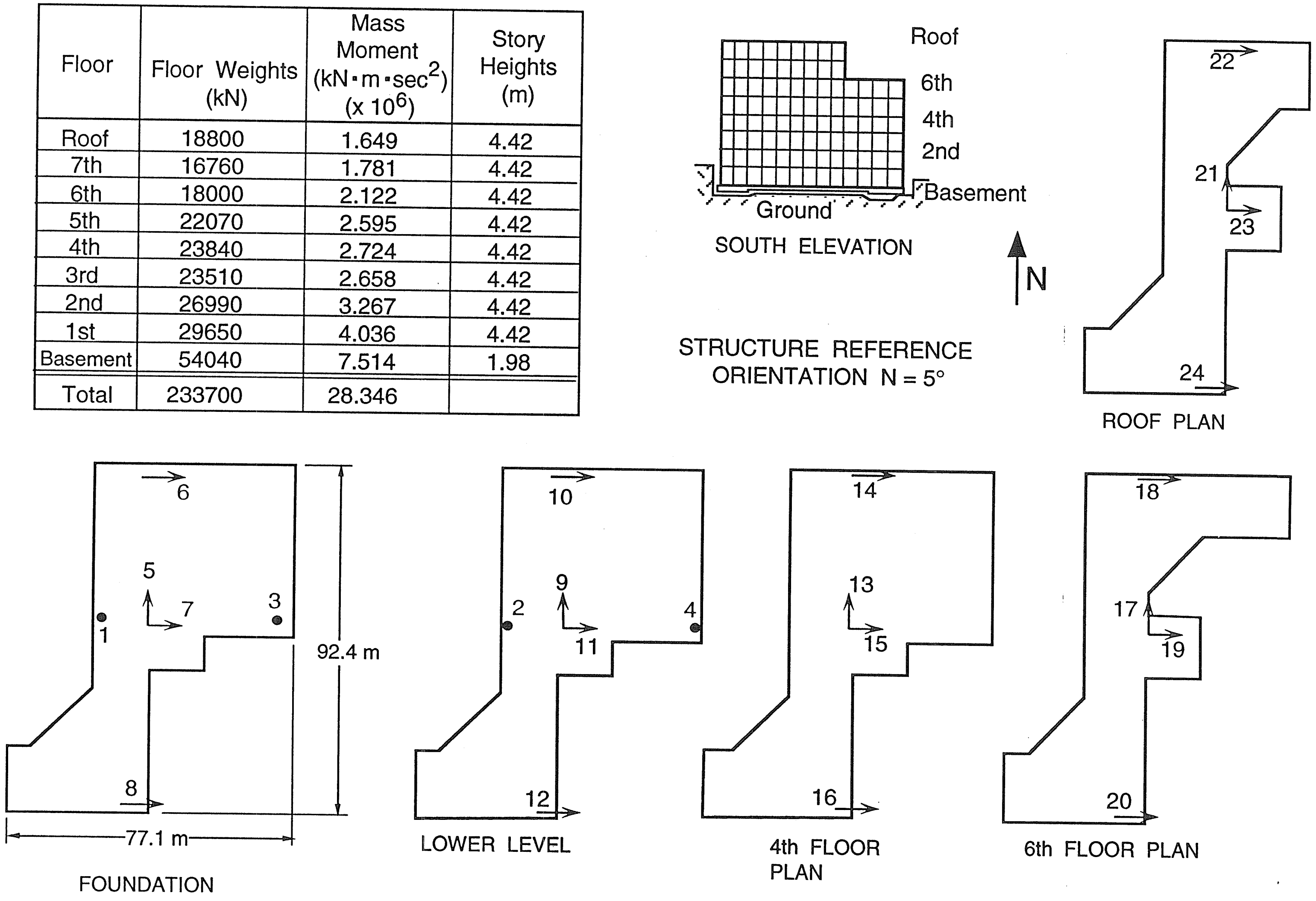

Floor	Floor Weights (kN)	Mass Moment ($kN \cdot m \cdot sec^2$) ($\times 10^6$)	Story Heights (m)
Roof	18800	1.649	4.42
7th	16760	1.781	4.42
6th	18000	2.122	4.42
5th	22070	2.595	4.42
4th	23840	2.724	4.42
3rd	23510	2.658	4.42
2nd	26990	3.267	4.42
1st	29650	4.036	4.42
Basement	54040	7.514	1.98
Total	233700	28.346	

Figure 3.21 USCUH schematic diagram showing locations of accelerometers as well as properties used in analysis.

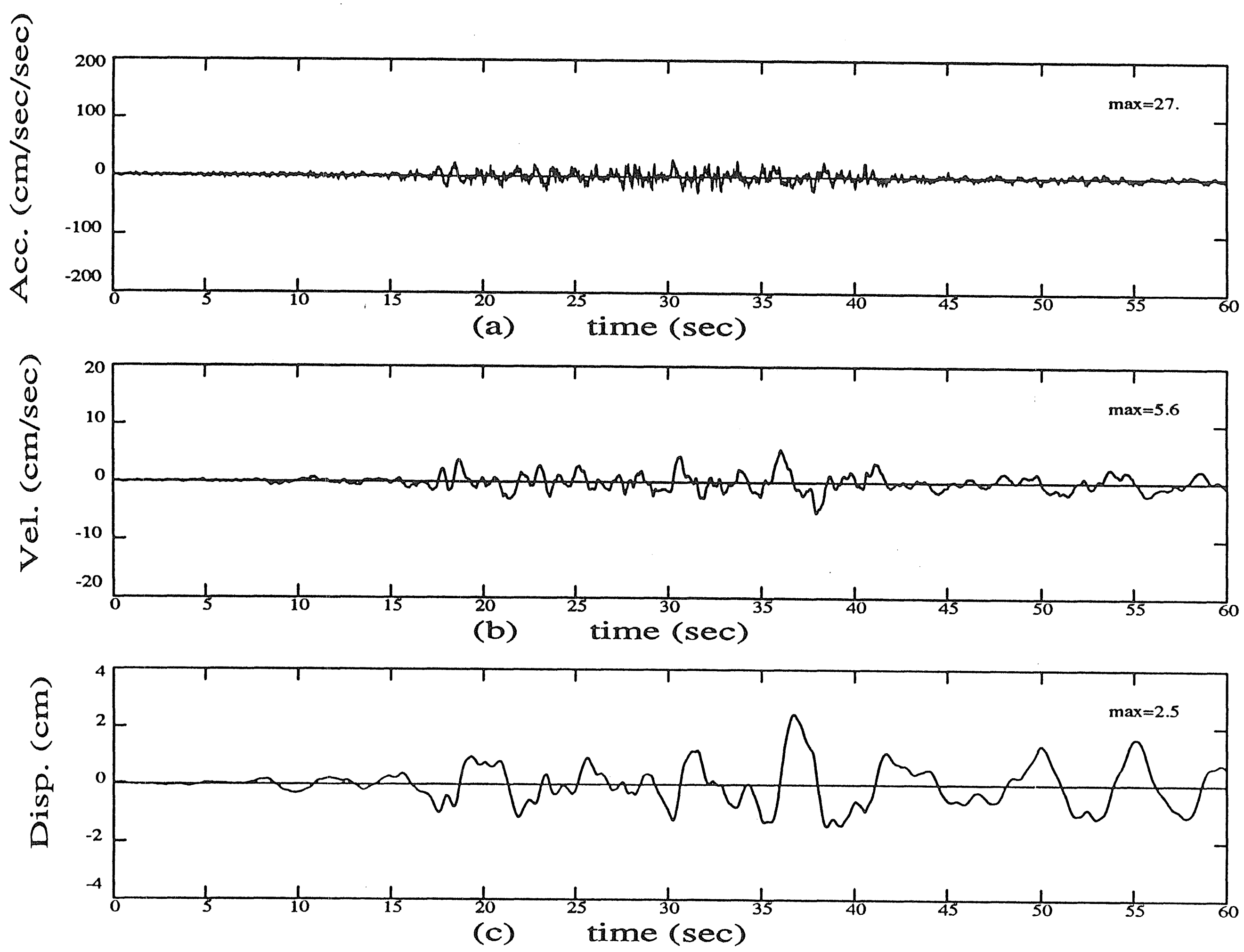

Figure 3.22 USCUH transverse foundation motion (channel 7) from the 1992 Landers earthquake.

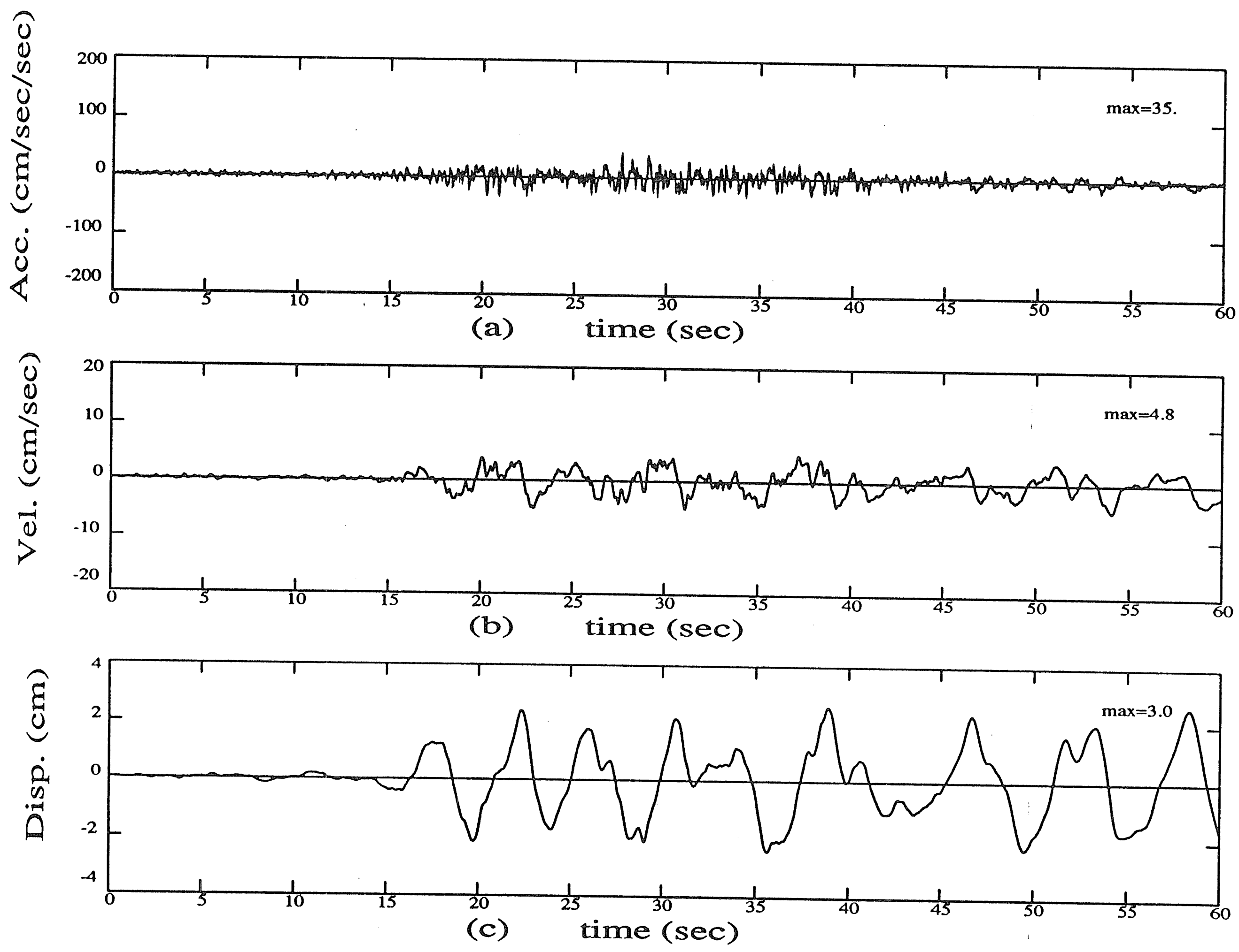

Figure 3.23 USCUH longitudinal foundation motion (channel 5) from the 1992 Landers earthquake.

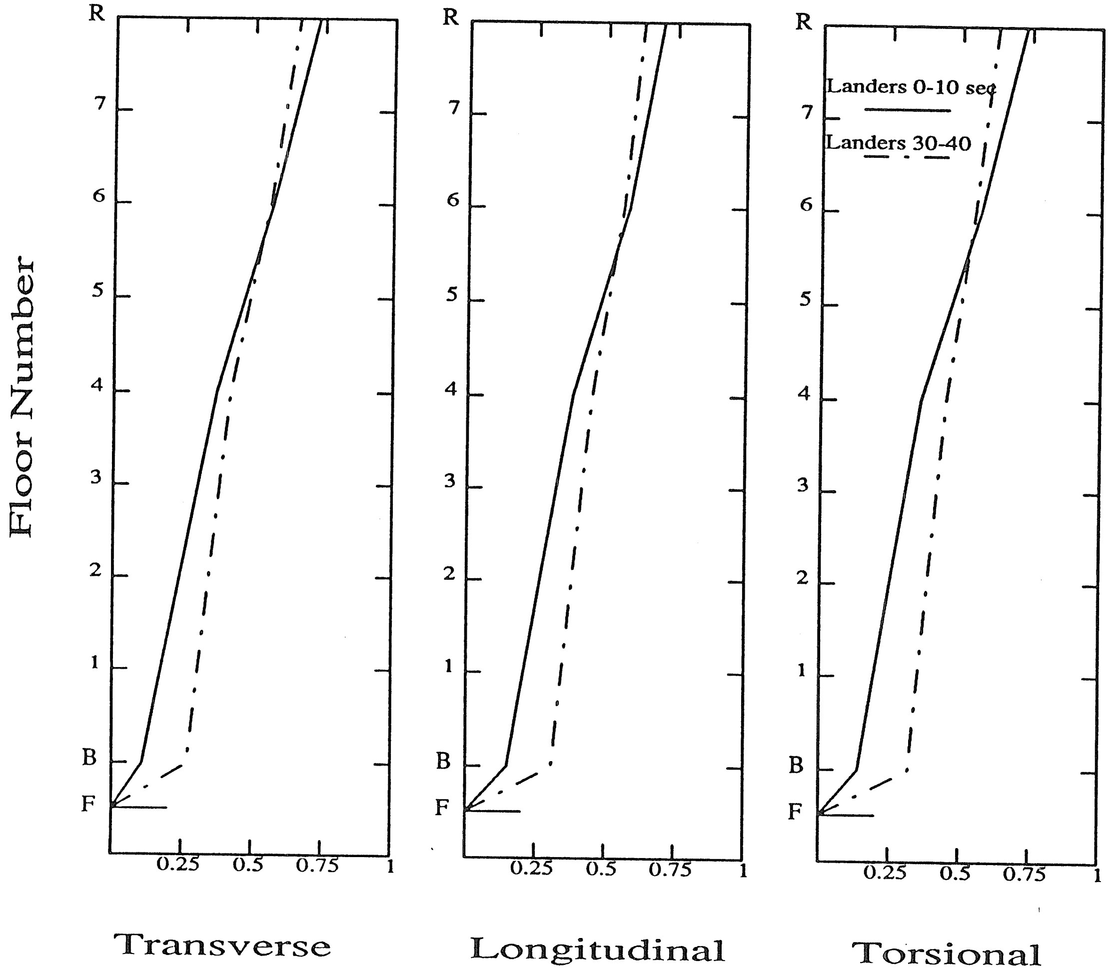

Figure 3.24 USCUH identified first transverse, longitudinal, and torsional mode shapes from the 1992 Landers earthquake. Each mode shape is normalized to a vector length of one.

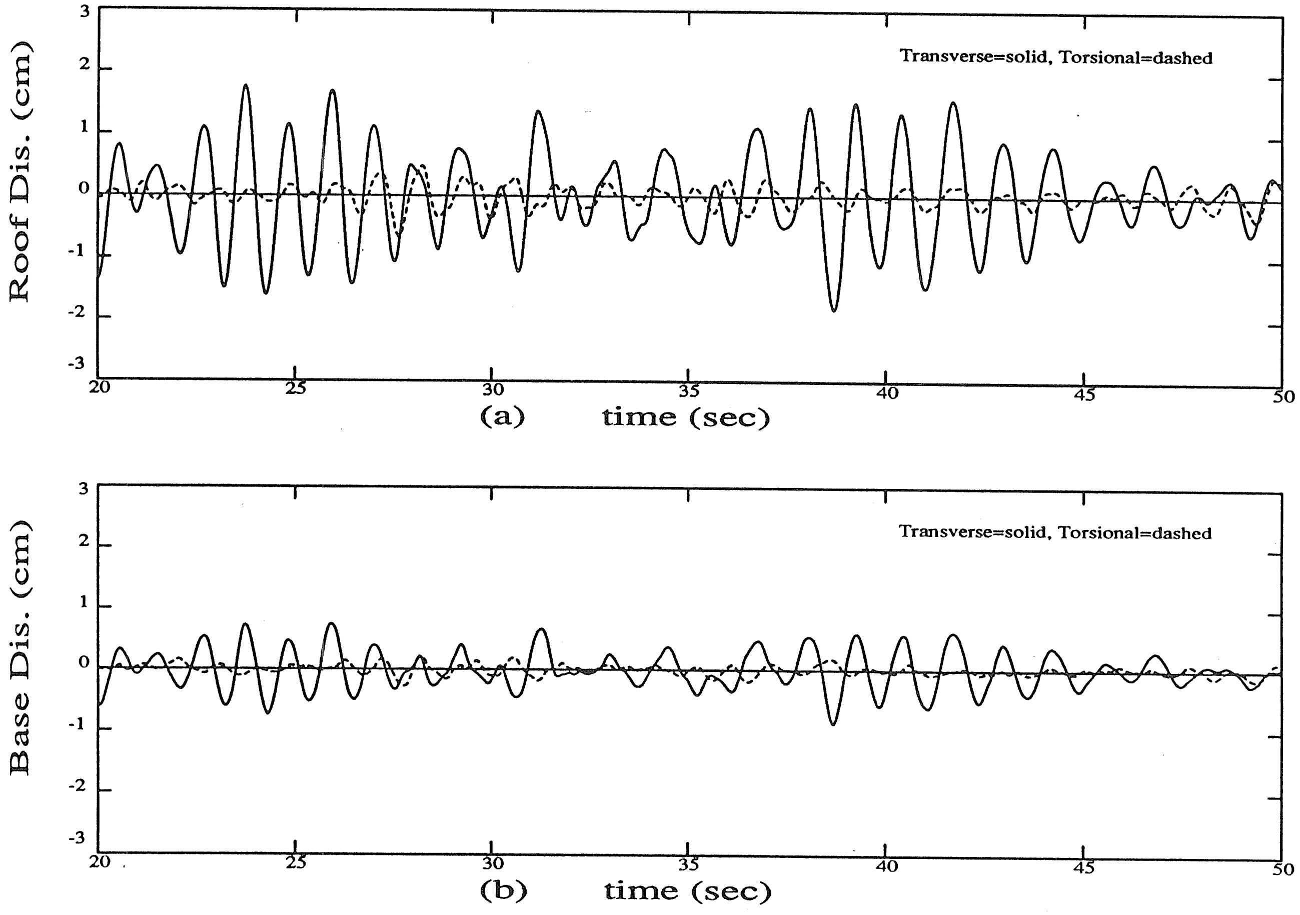

Figure 3.25 USCUH recorded transverse response at the roof and base (relative to the foundation) including torsional response (rotation x L/2) from the 1992 Landers earthquake.

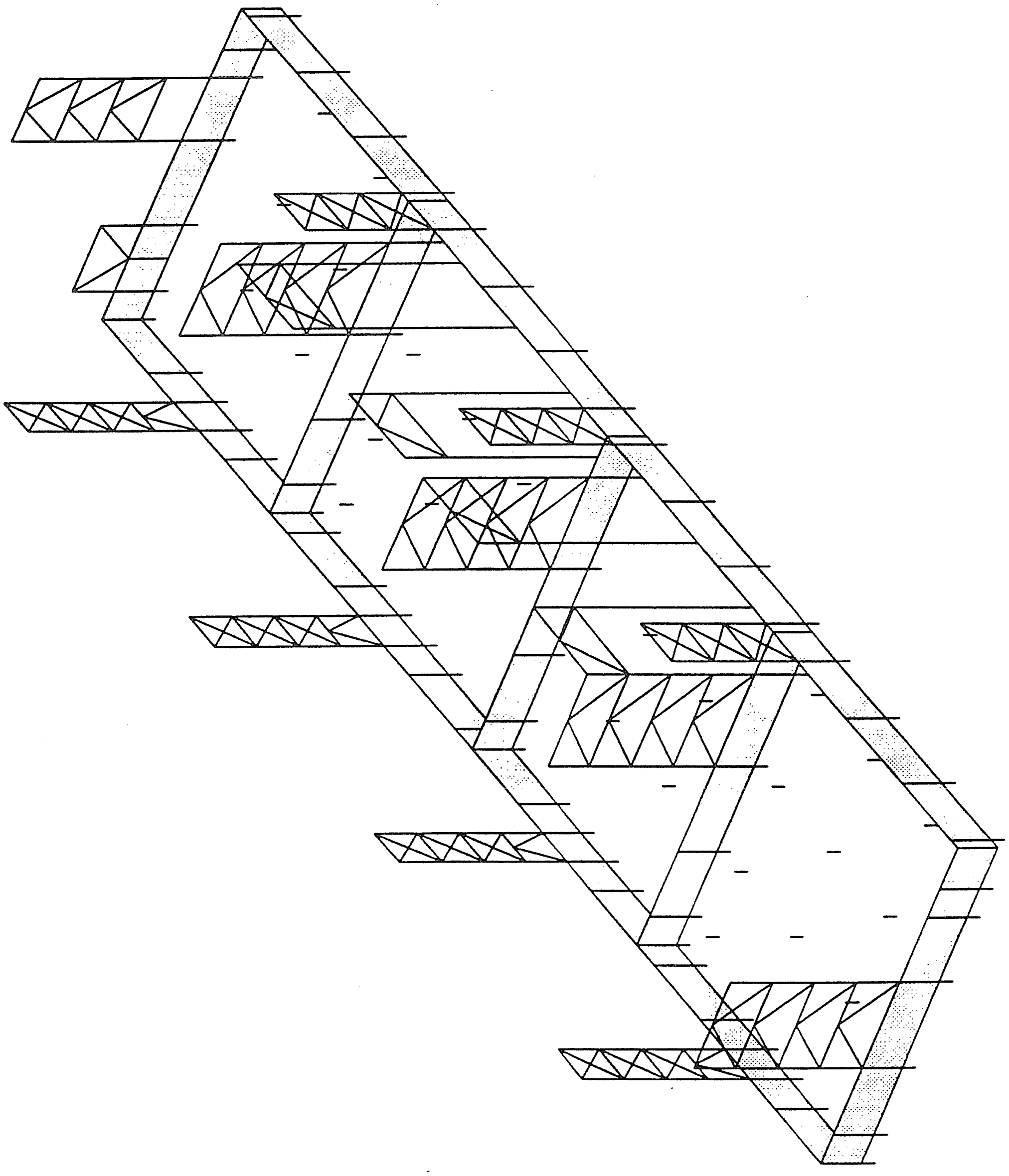

Figure 4.1 FCLJC three dimensional model. Linear-elastic superstructure model supported by 98 nonlinear isolation bearings.

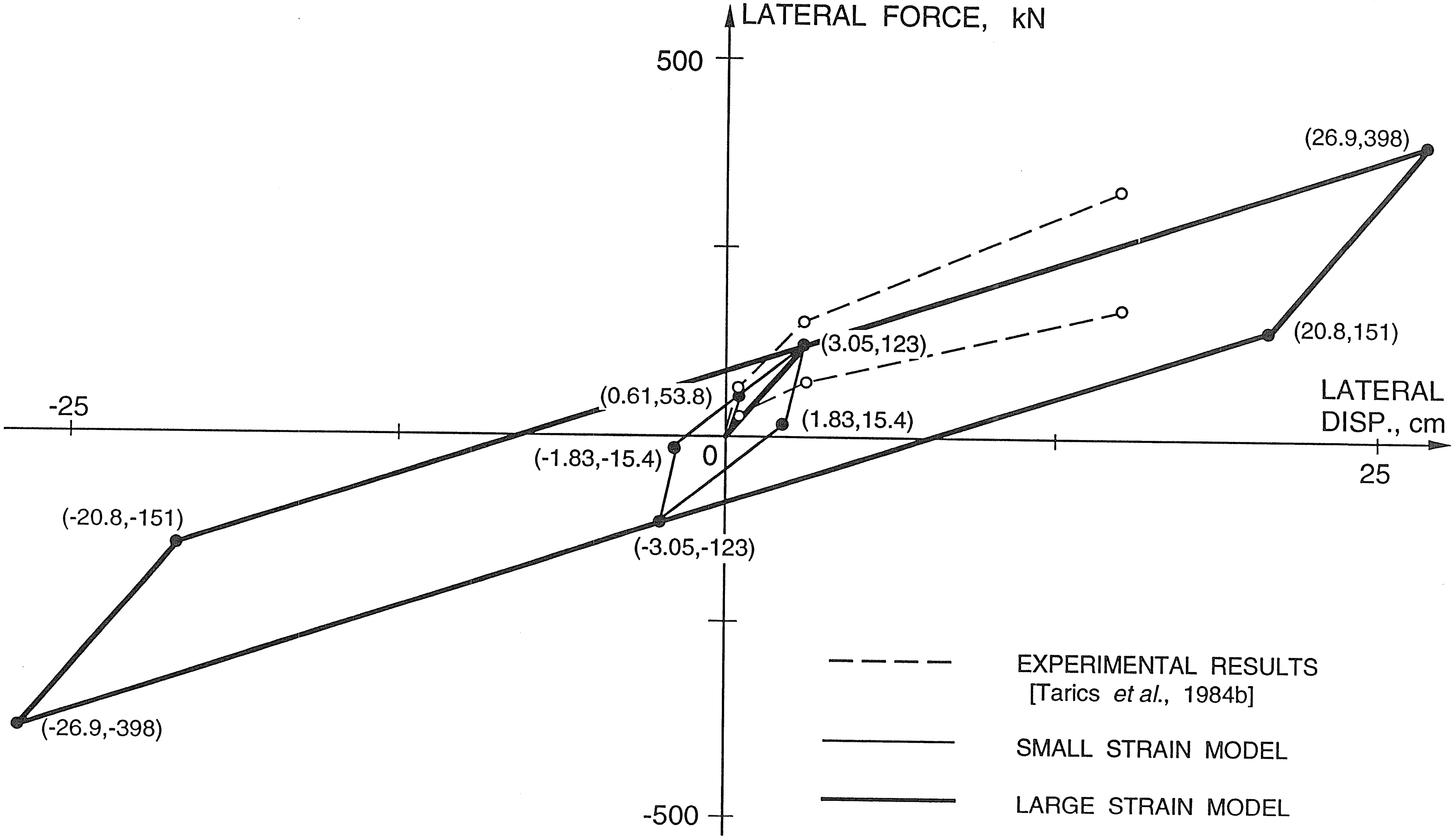

Figure 4.2 FCLJC force-displacement curve for small-strain model (Part One), large-strain model (Part Two), and the range of experimental results (points plotted at 2%, 10%, and 50% strain). The building model contains 98 of these "average" bearings.

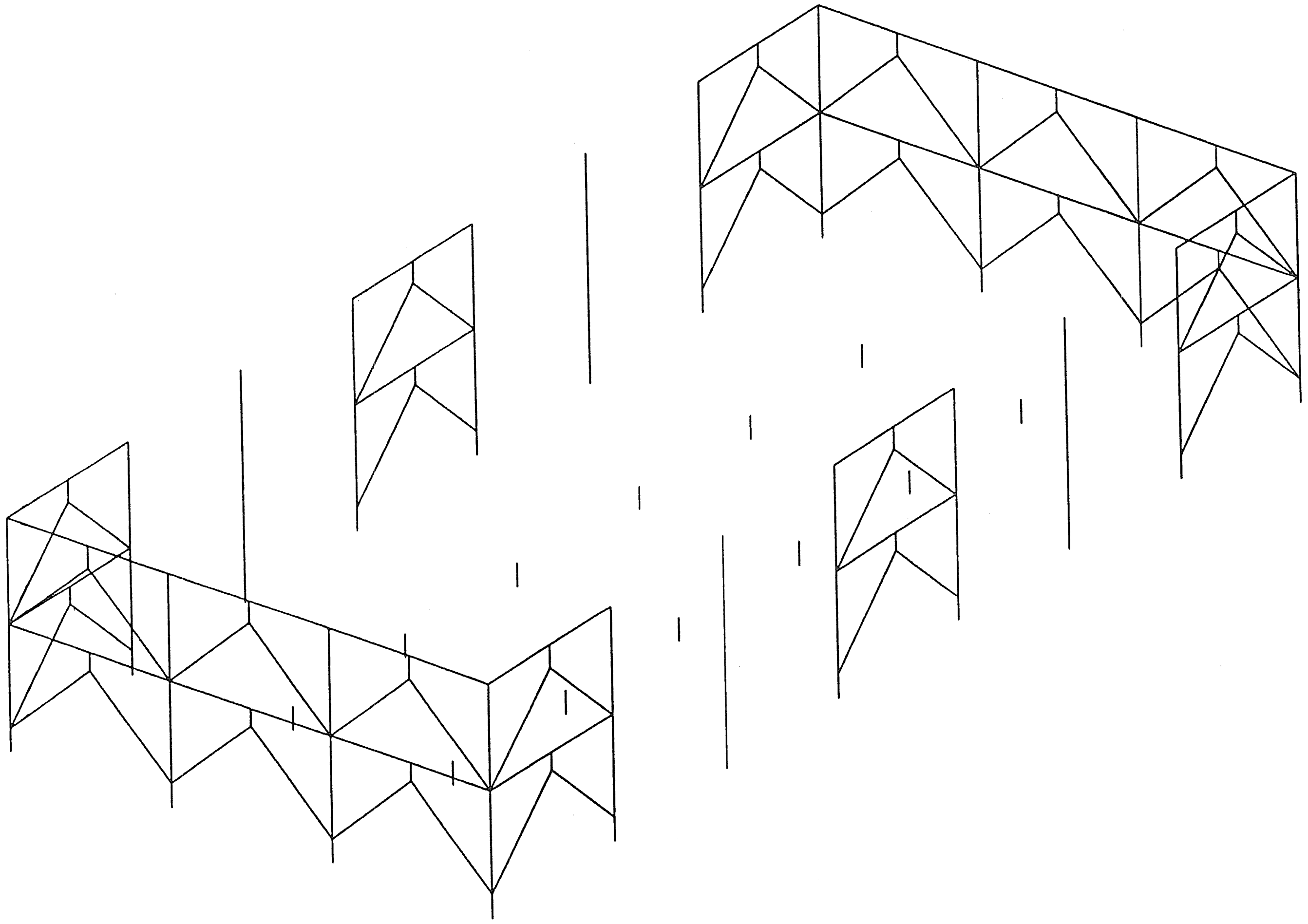

Figure 4.3 FCCF three dimensional model. Linear-elastic superstructure model supported by 32 nonlinear isolation bearings.

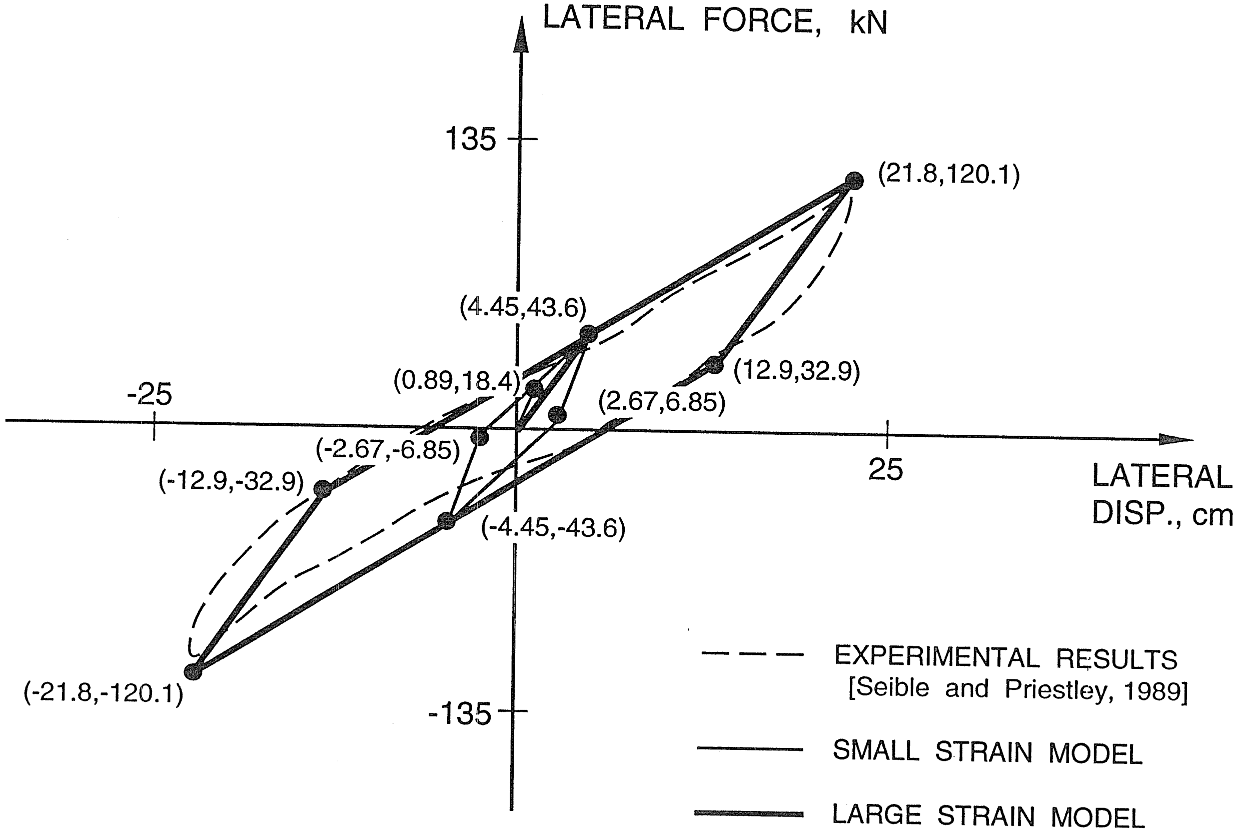

Figure 4.4 FCCF force-displacement curve for small-strain model (Part One), large-strain model (Part Two), and a hysteresis loop from a prototype bearing test. The building contains 20 of these exterior bearings.

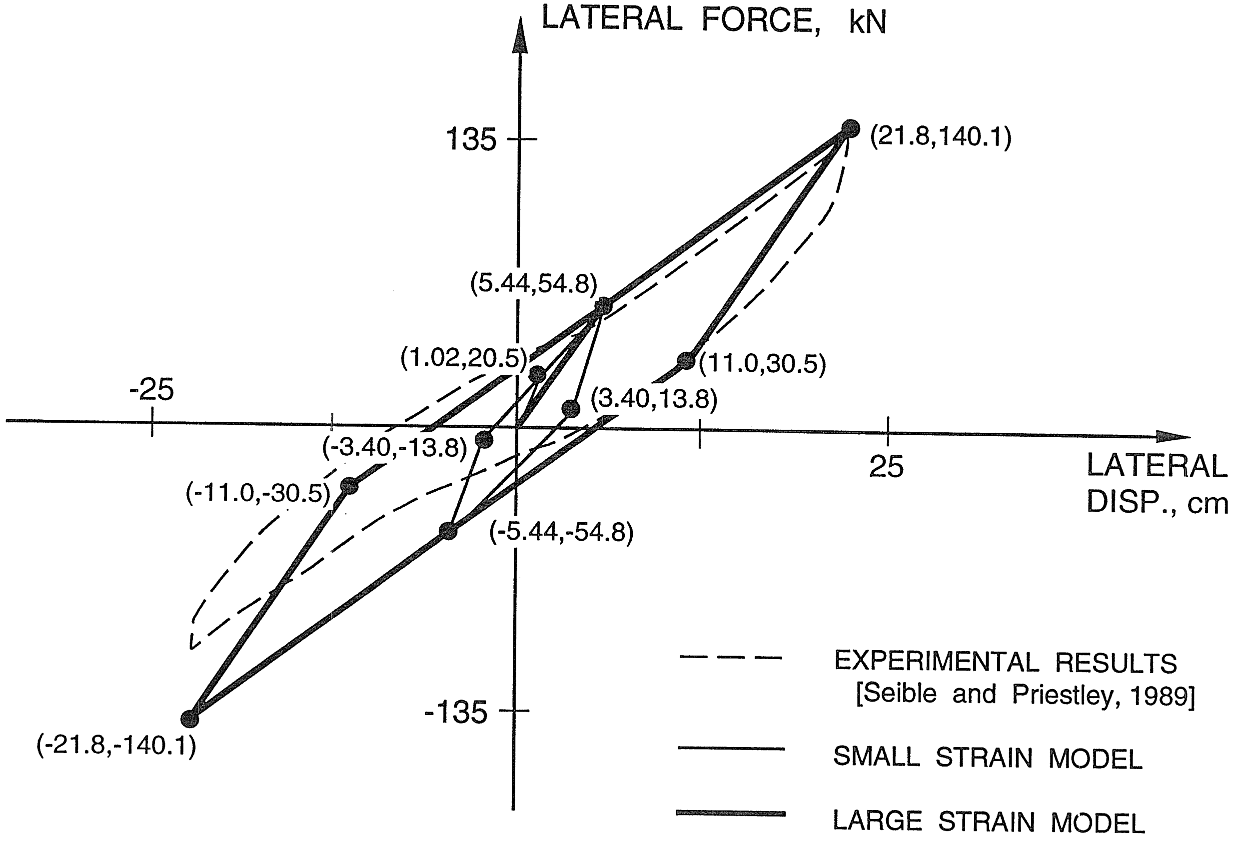

Figure 4.5 FCCF force-displacement curve for small-strain model (Part One), large-strain model (Part Two), and a hysteresis loop from a prototype bearing test. The building contains 12 of these interior bearings.

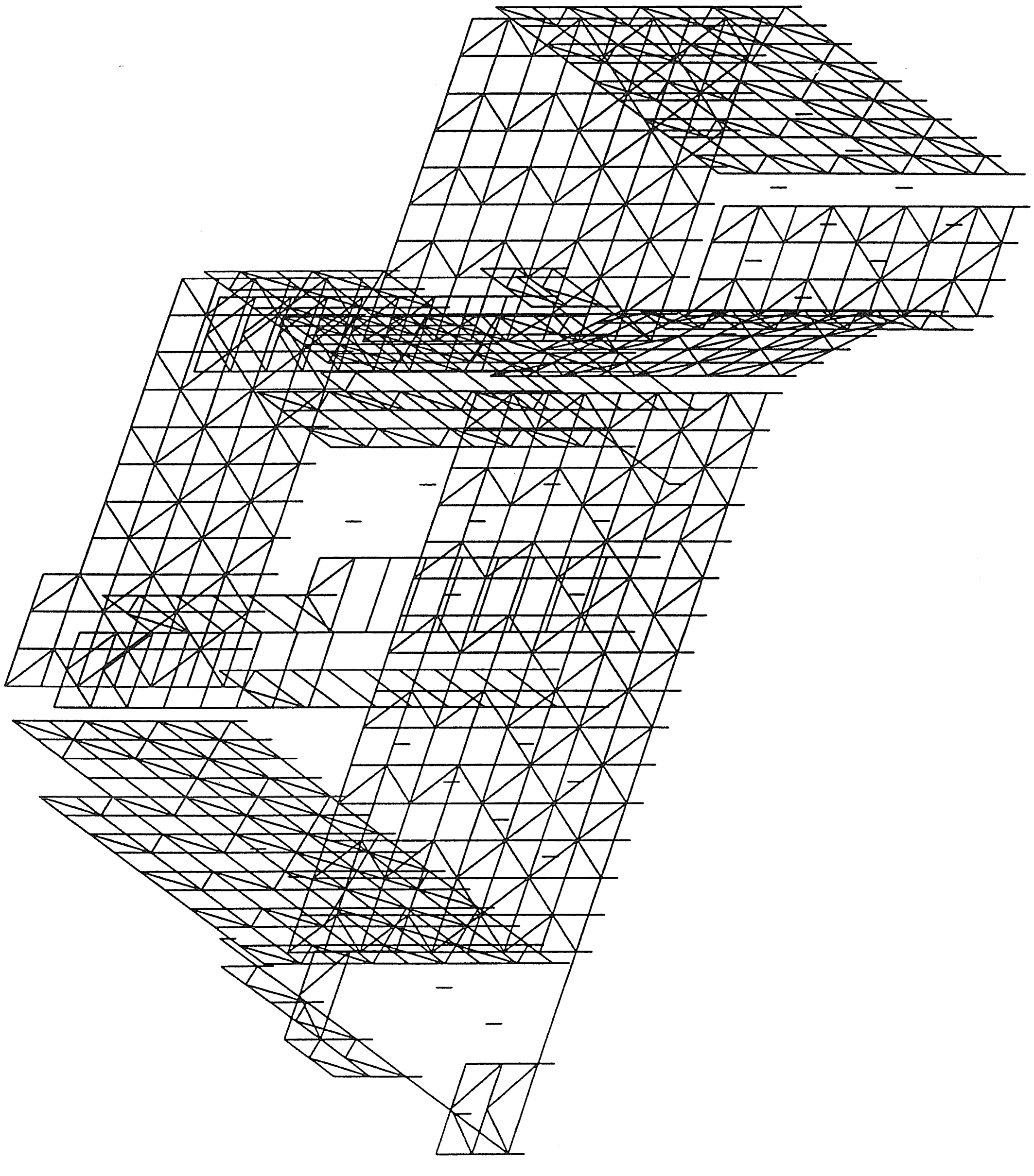

Figure 4.6 USCUH three dimensional model. Linear-elastic superstructure model supported by 149 nonlinear isolation bearings.

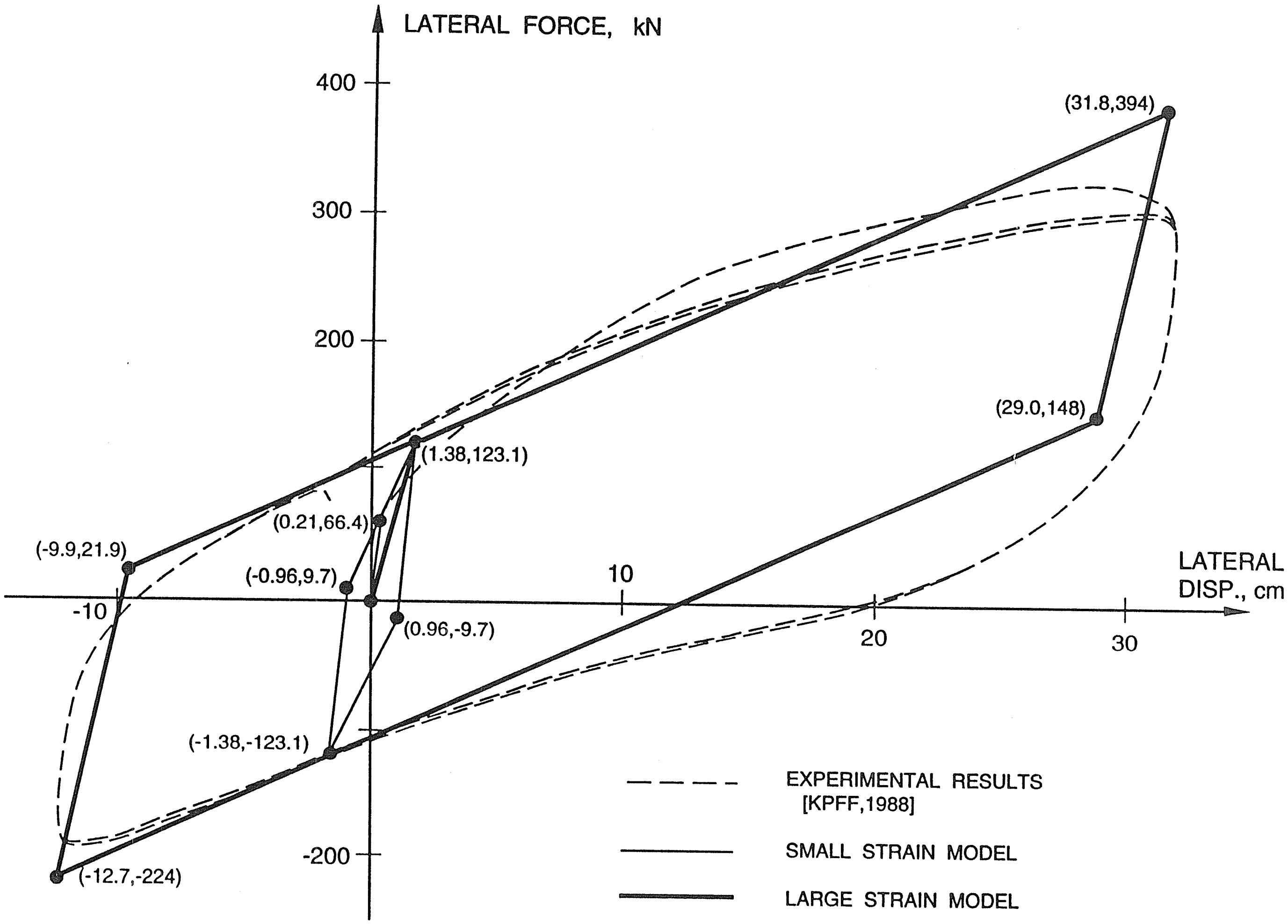

Figure 4.7 USCUH force-displacement curve for small-strain model (Part One), large-strain model (Part Two), and a hysteresis loop from a prototype bearing test. The building contains 59 of these type 1 lead / rubber bearings.

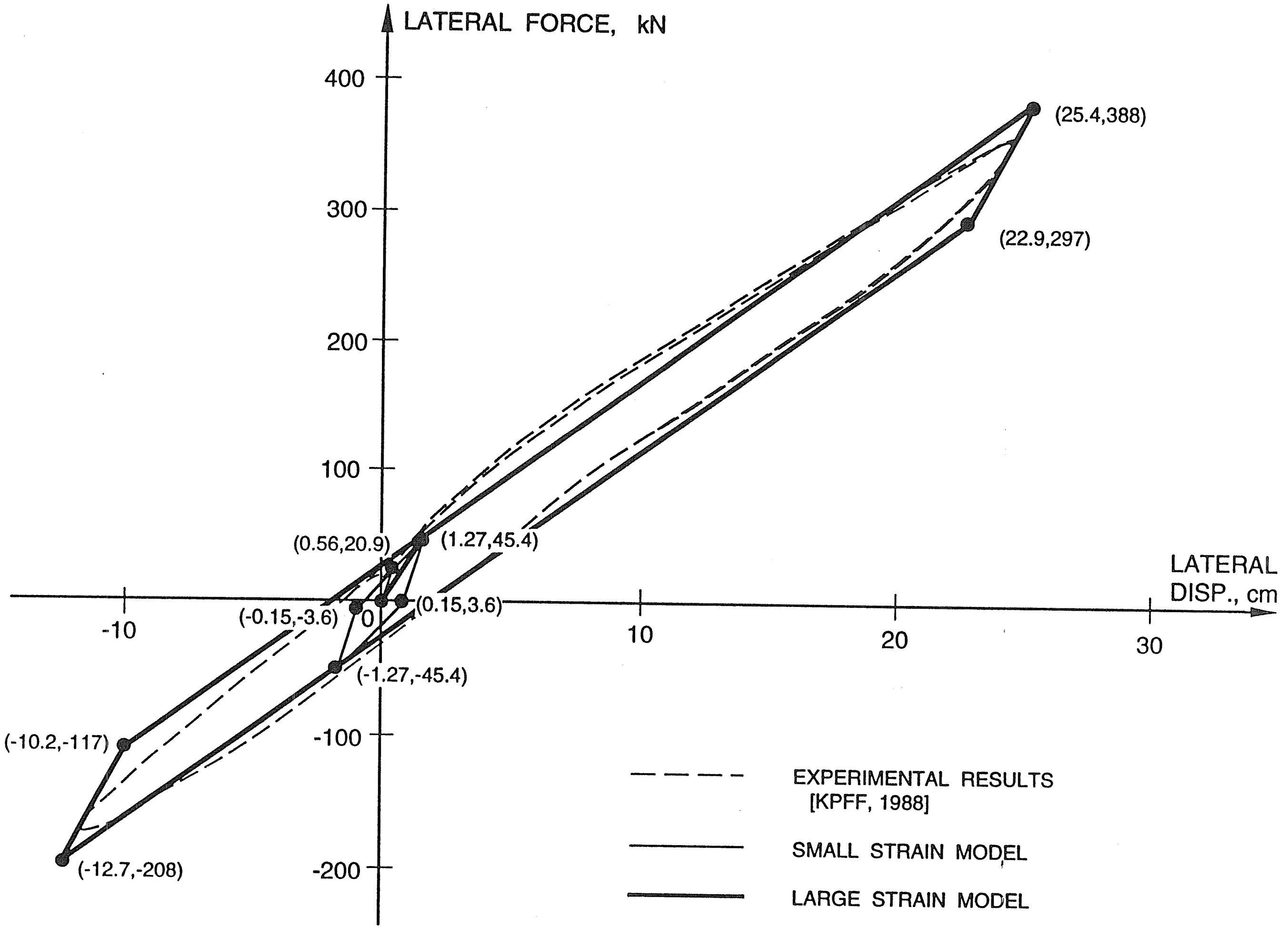

Figure 4.8 USCUH force-displacement curve for small-strain model (Part One), large-strain model (Part Two), and a hysteresis loop from a prototype bearing test. The building contains 73 of these type 4 elastomeric bearings.

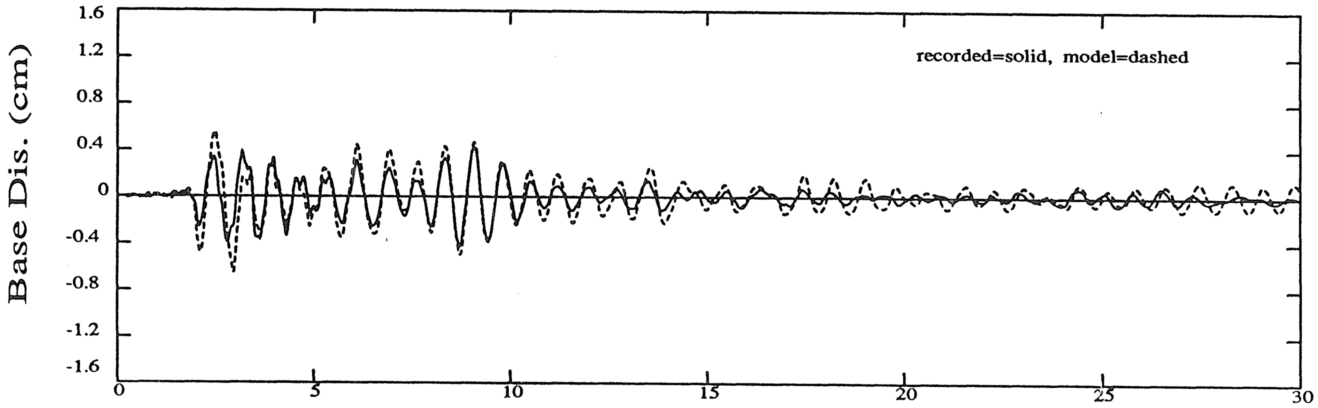

(a) Transverse

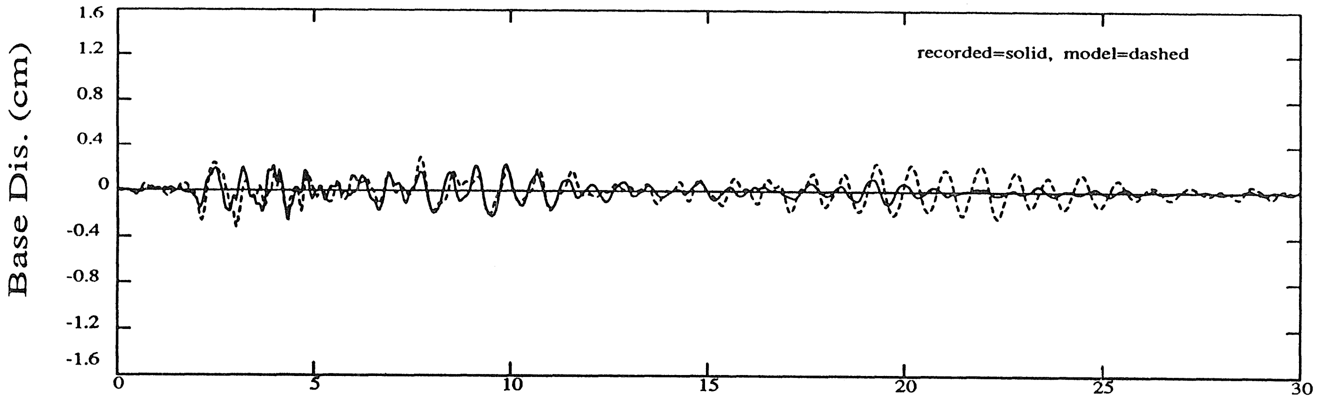

(b) Longitudinal

Figure 4.9 FCLJC recorded and modeled base displacement (relative to foundation displacement) in the transverse and longitudinal directions from the 1990 Upland earthquake.

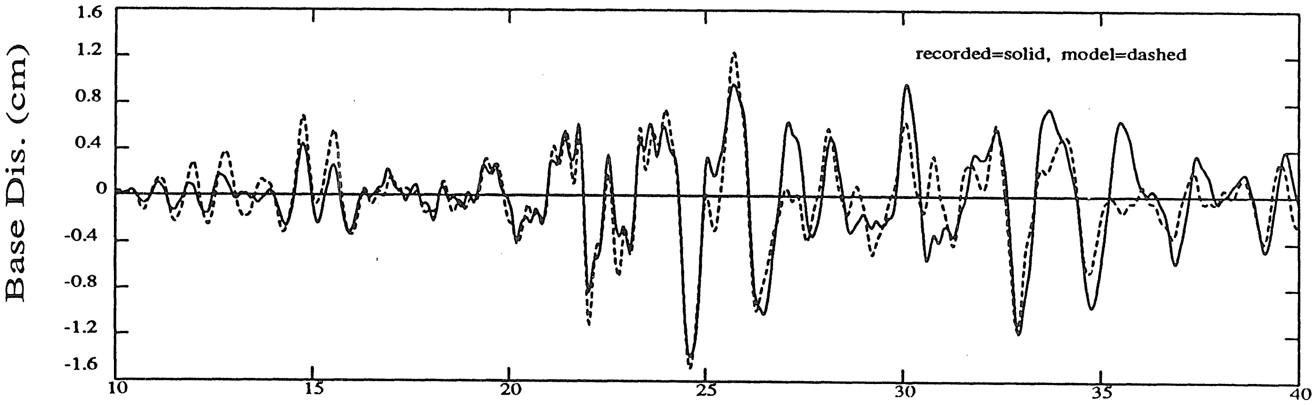

(a) Transverse

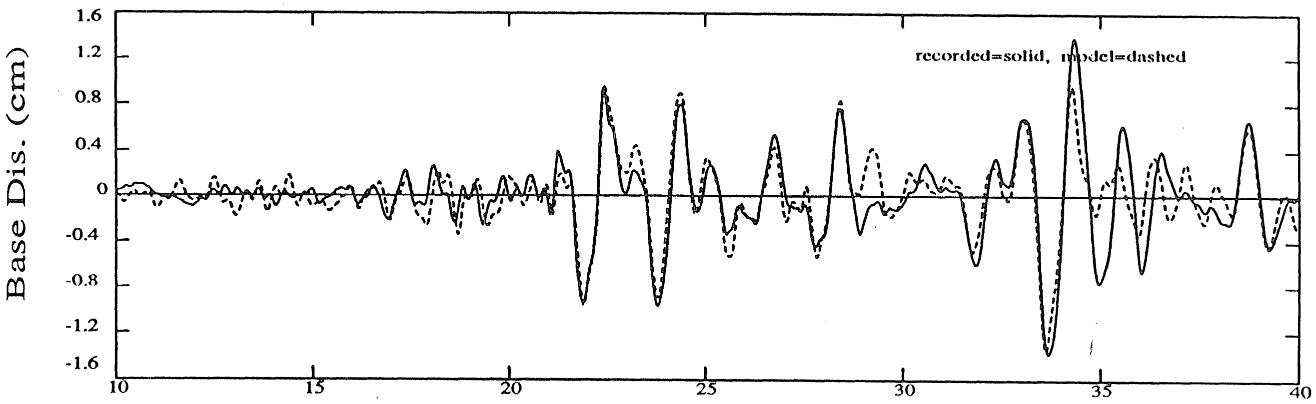

(b) Longitudinal

Figure 4.10 FCLJC recorded and modeled base displacement (relative to foundation displacement) in the transverse and longitudinal directions from the 1992 Landers earthquake.

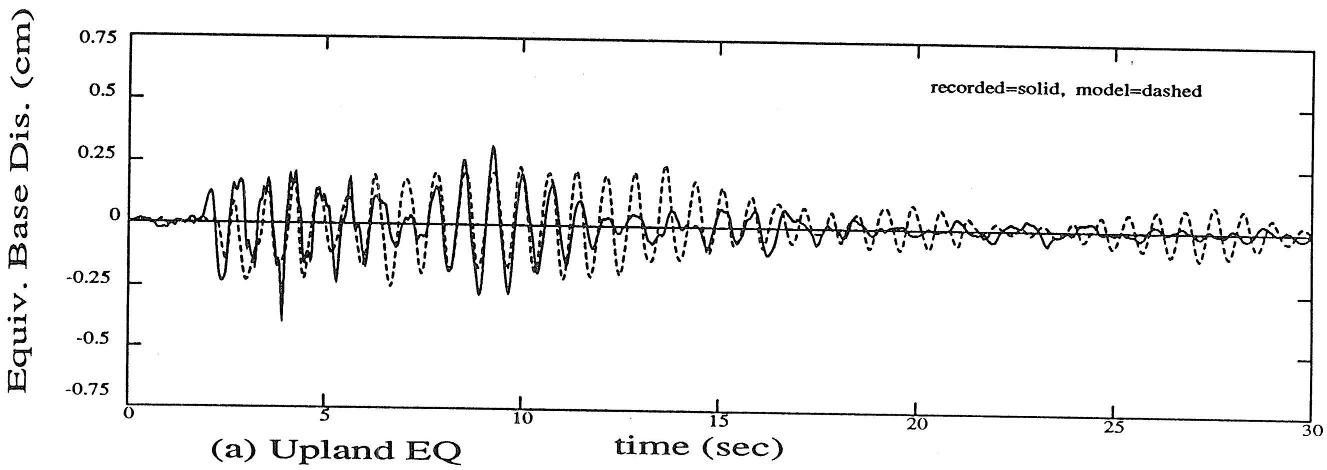

(a) Upland EQ

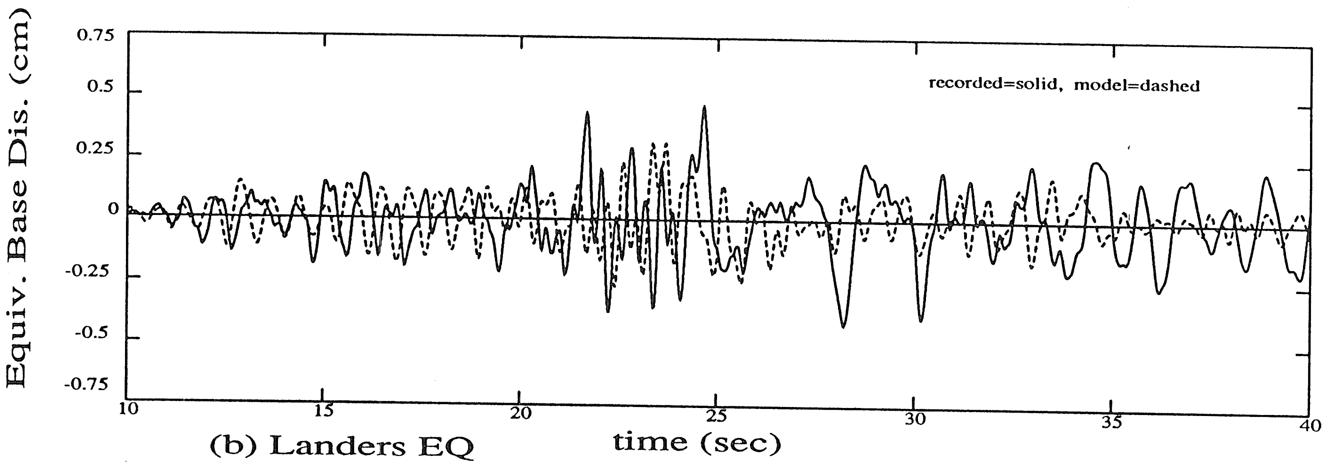

(b) Landers EQ

Figure 4.11 FCLJC recorded and modeled torsional base displacement ((base rotation relative to foundation rotation) x L/2) from the 1990 Upland and the 1992 Landers earthquakes.

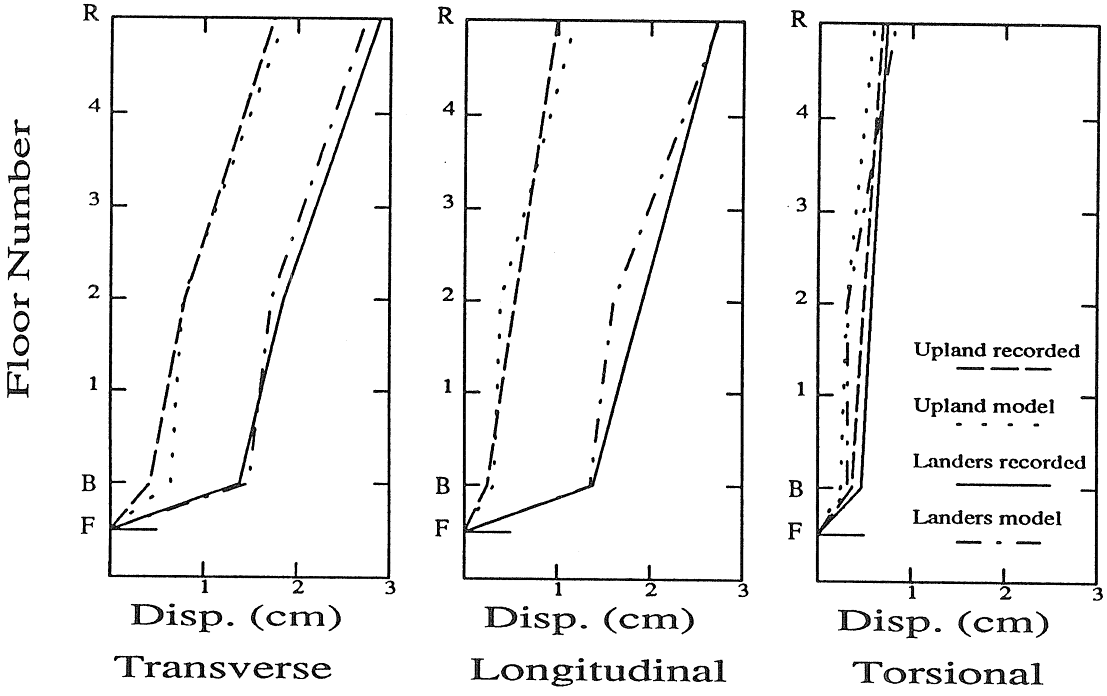

Figure 4.12 FCLJC peak floor displacements (relative to the foundation) from the 1990 Upland and 1992 Landers earthquakes. Torsional displacement is calculated as the floor rotation relative to the foundation rotation x L/2.

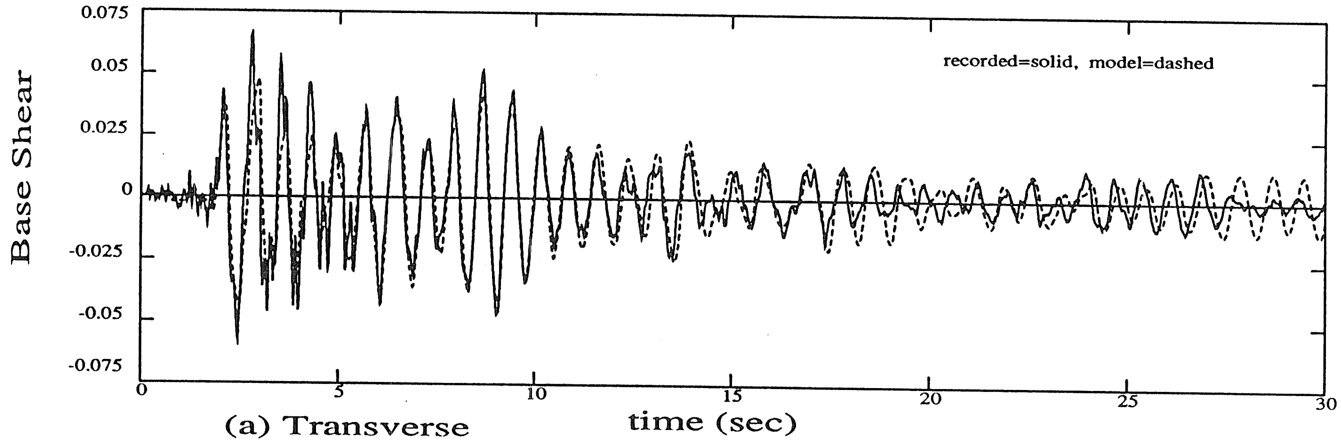

(a) Transverse

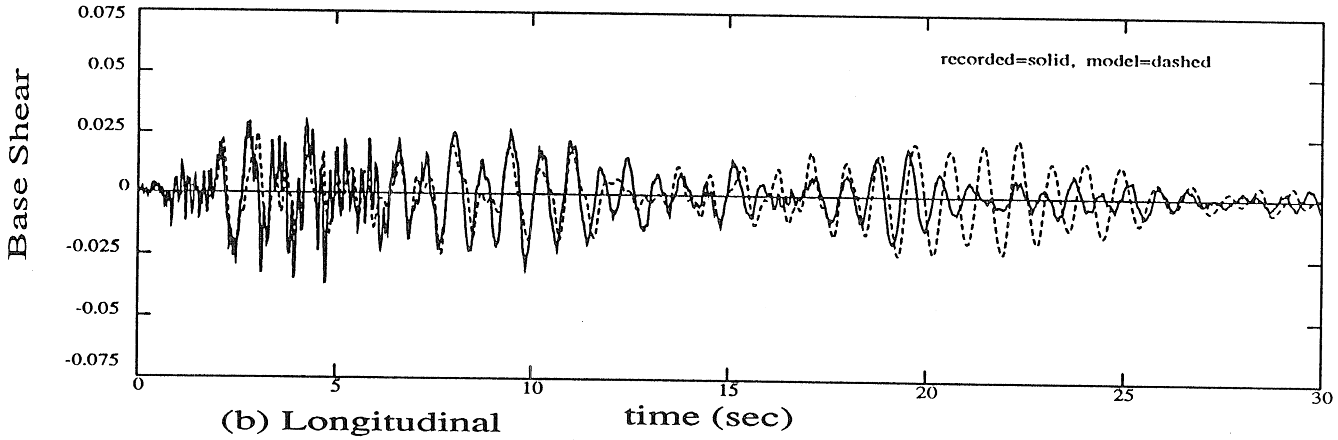

(b) Longitudinal

Figure 4.13 FCLJC recorded and modeled base shear in the transverse and longitudinal directions from the 1990 Upland earthquake (Refer to equations 4.1 and 4.2).

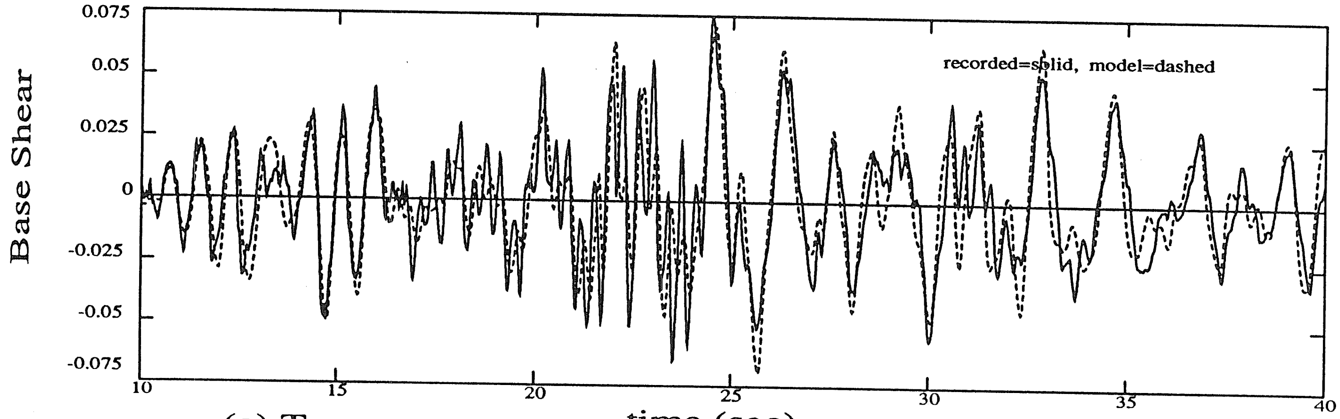

(a) Transverse

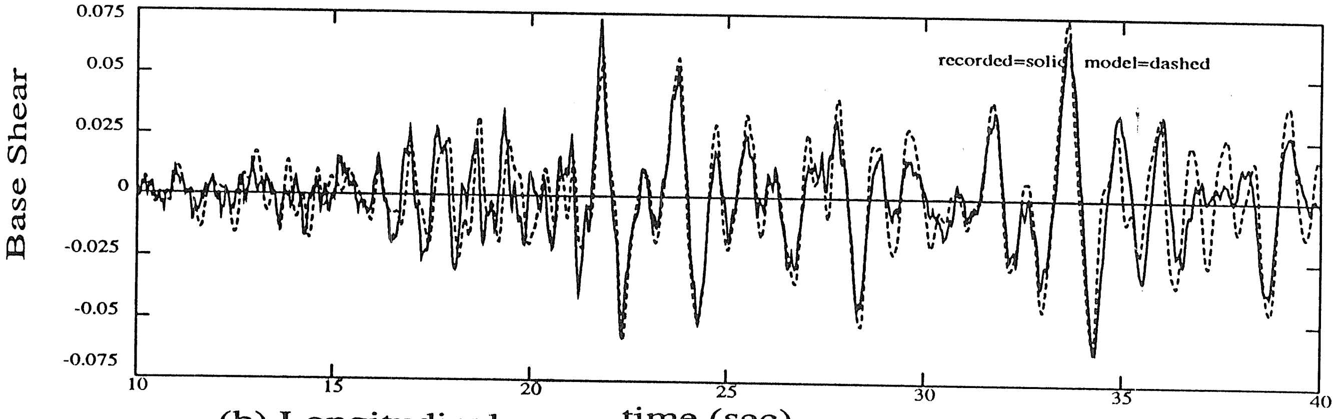

(b) Longitudinal

Figure 4.14 FCLJC recorded and modeled base shear in the transverse and longitudinal directions from the 1992 Landers earthquake (Refer to equations 4.1 and 4.2).

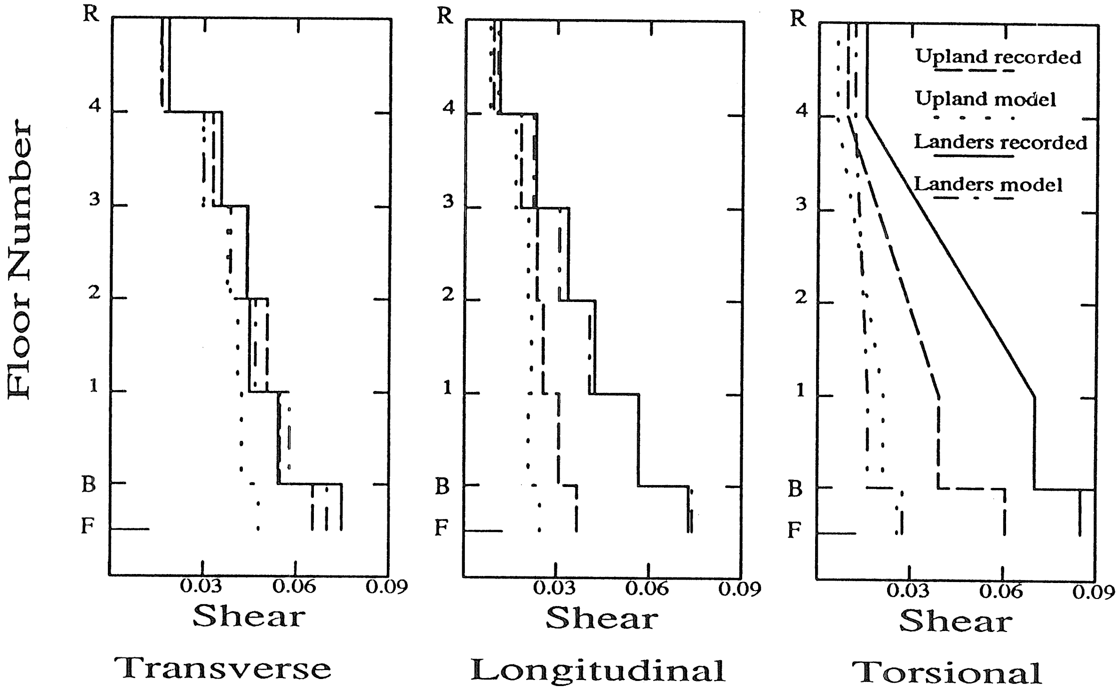

Figure 4.15 FCLJC peak story shears from the 1990 Upland and 1992 Landers earthquakes (Refer to equations 4.1, 4.2, and 4.3).

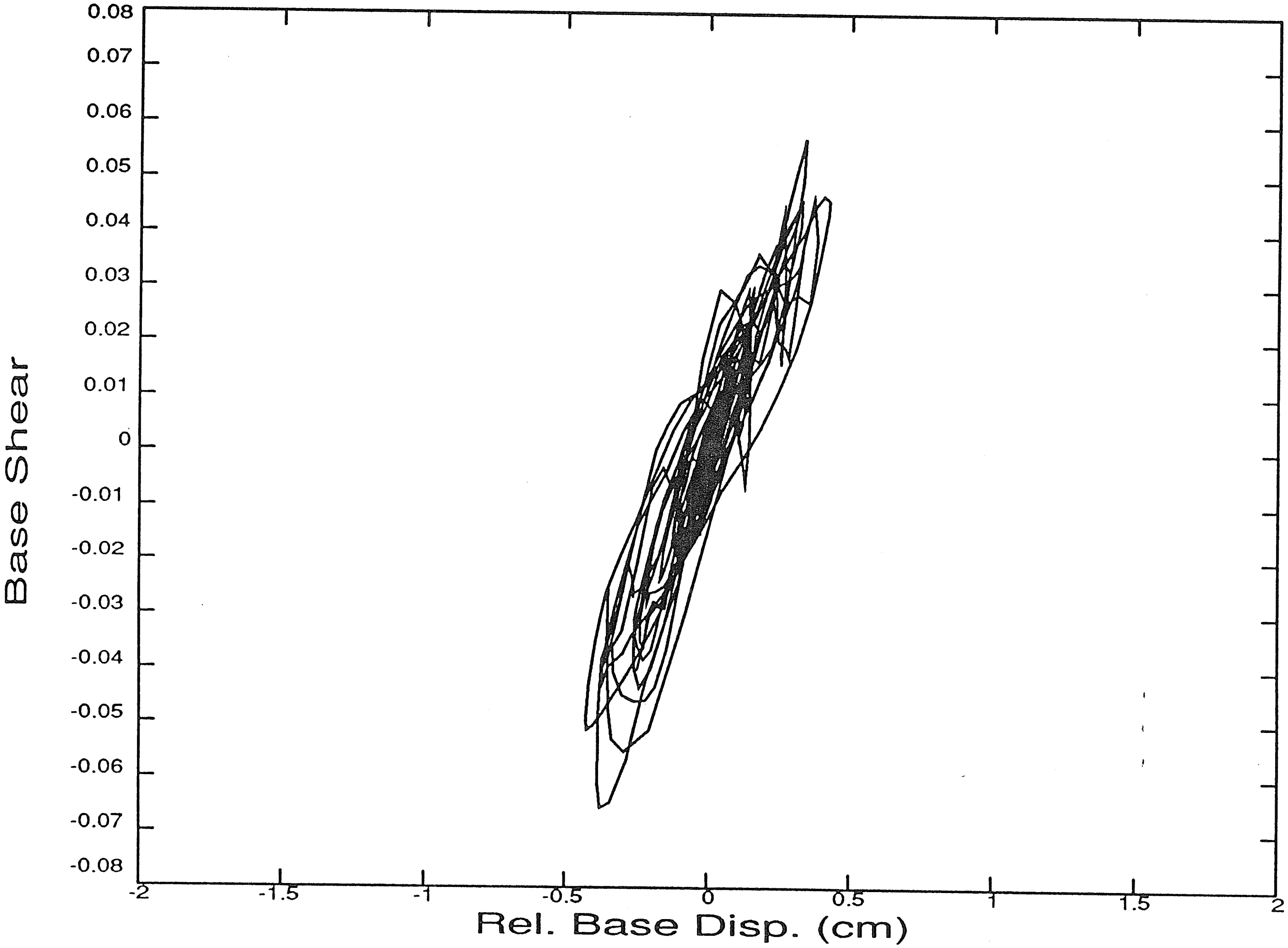

Figure 4.16 FCLJC recorded force-displacement curve for the base level (isolation bearings) in the transverse direction from the 1990 Upland earthquake (Refer to equation 4.1).

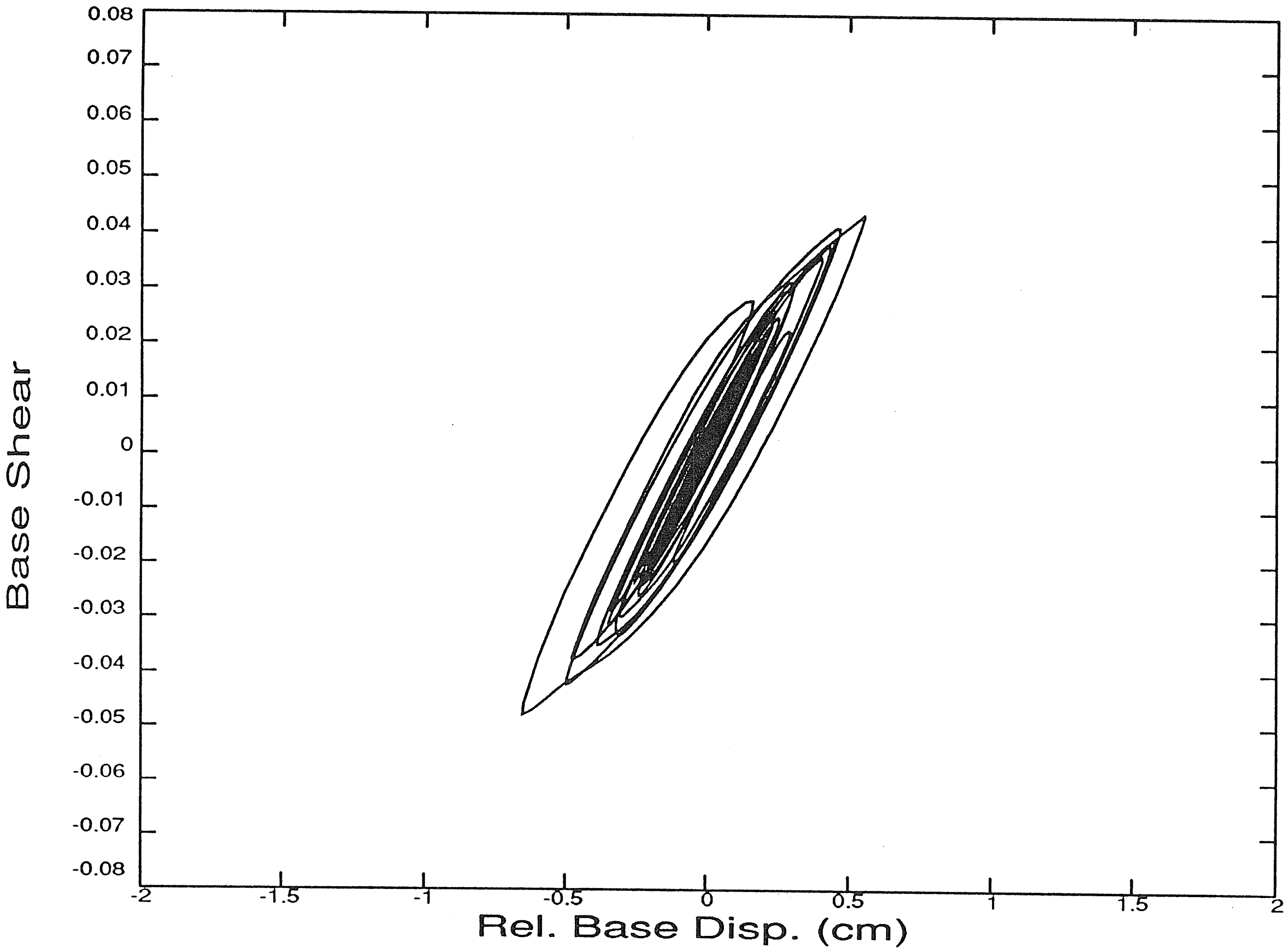

Figure 4.17 FCLJC modeled force-displacement curve for the base level (isolation bearings) in the transverse direction from the 1990 Upland earthquake.

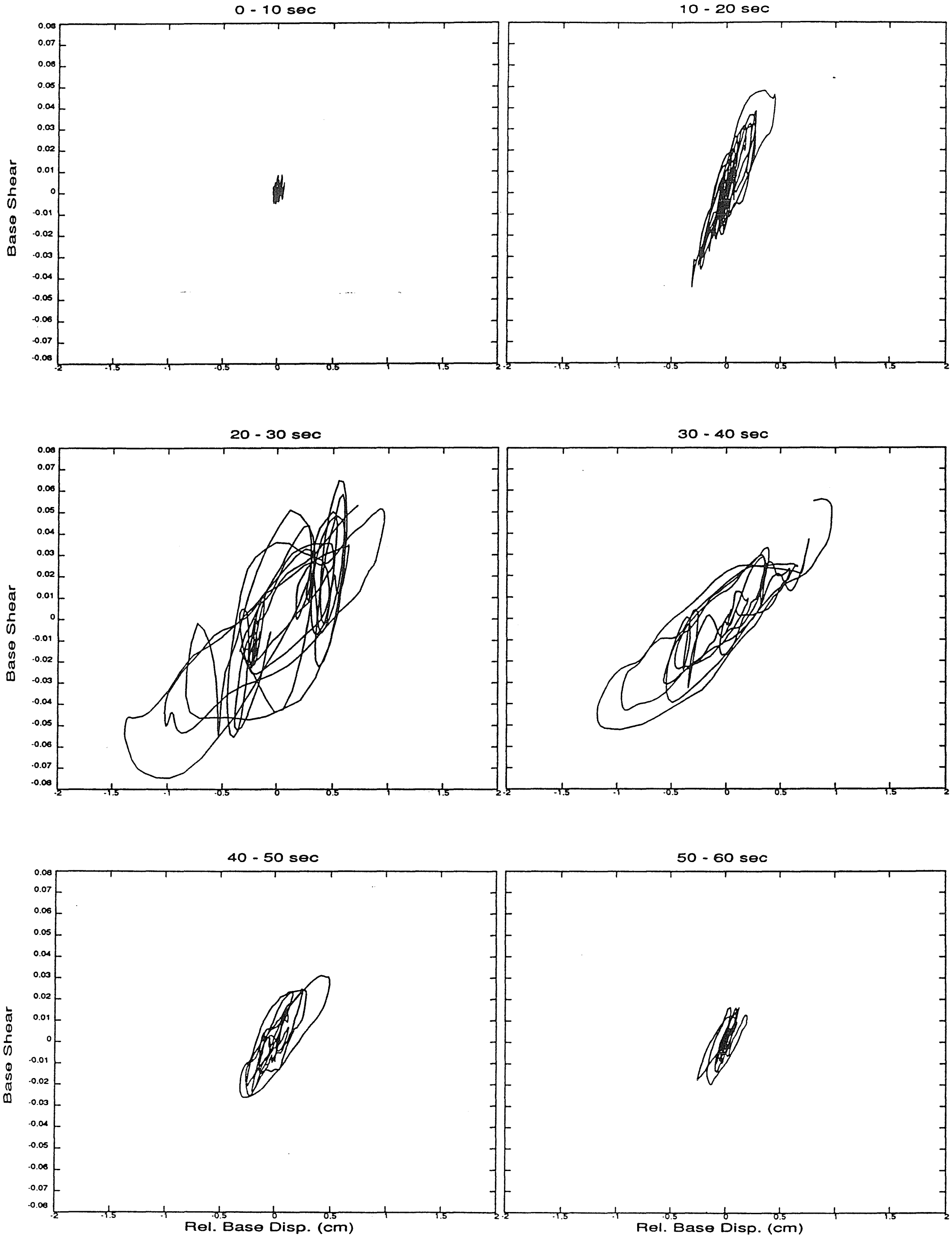

Figure 4.18 FCLJC recorded force-displacement curve for the base level (isolation bearings) in the transverse direction from the 1992 Landers earthquake which has been divided into 10 sec time segments (Refer to equation 4.1).

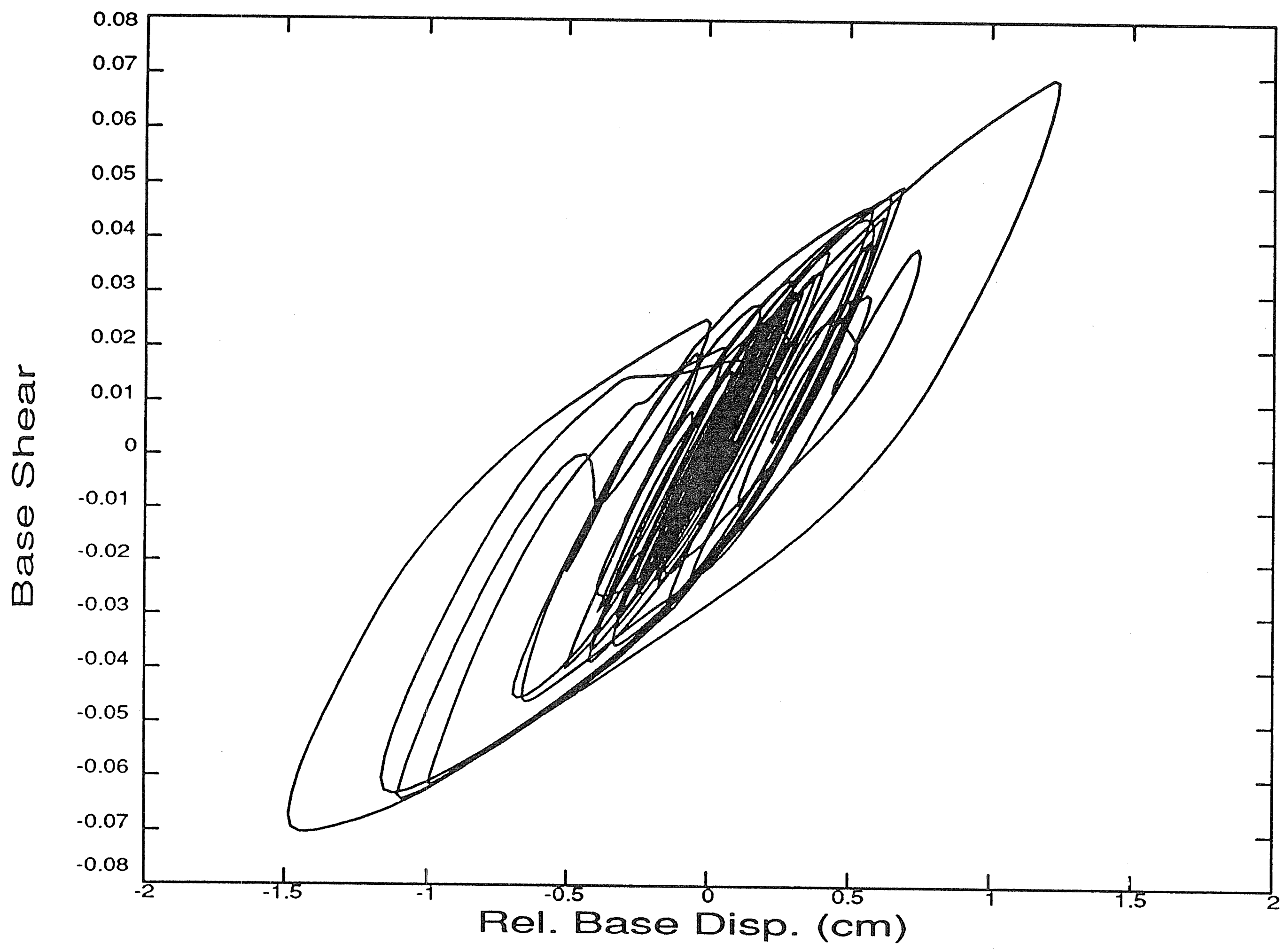

Figure 4.19 FCLJC modeled force-displacement curve for the base level (isolation bearings) in the transverse direction from the 1992 Landers earthquake.

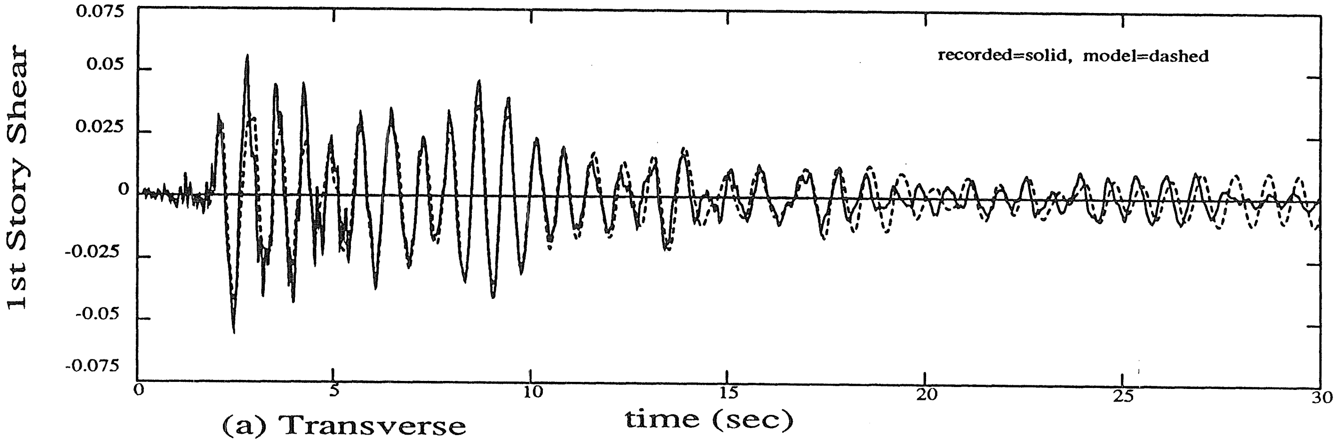

(a) Transverse

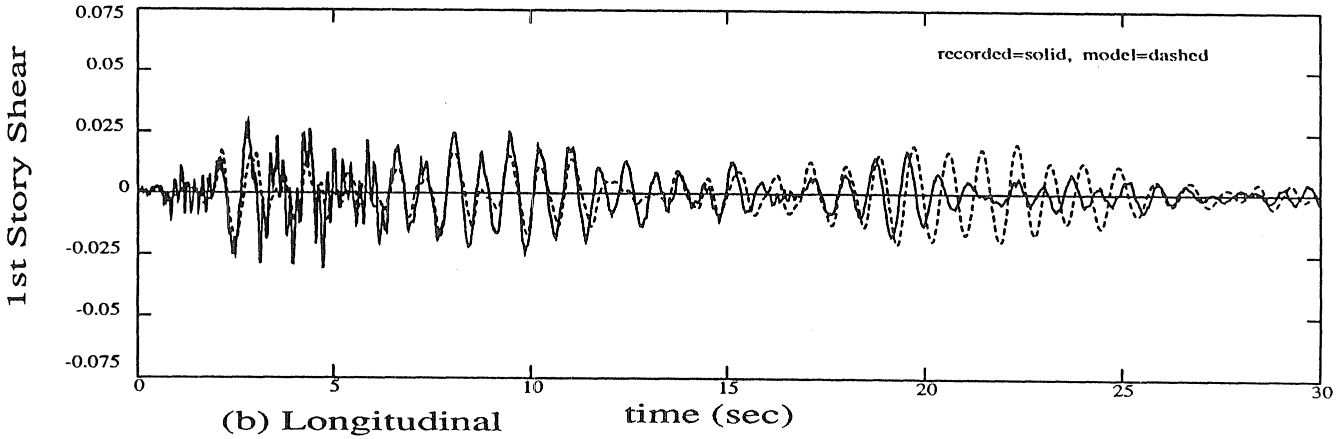

(b) Longitudinal

Figure 4.20 FCLJC recorded and modeled first story shear in the transverse and longitudinal directions from the 1990 Upland earthquake (Refer to equations 4.1 and 4.2).

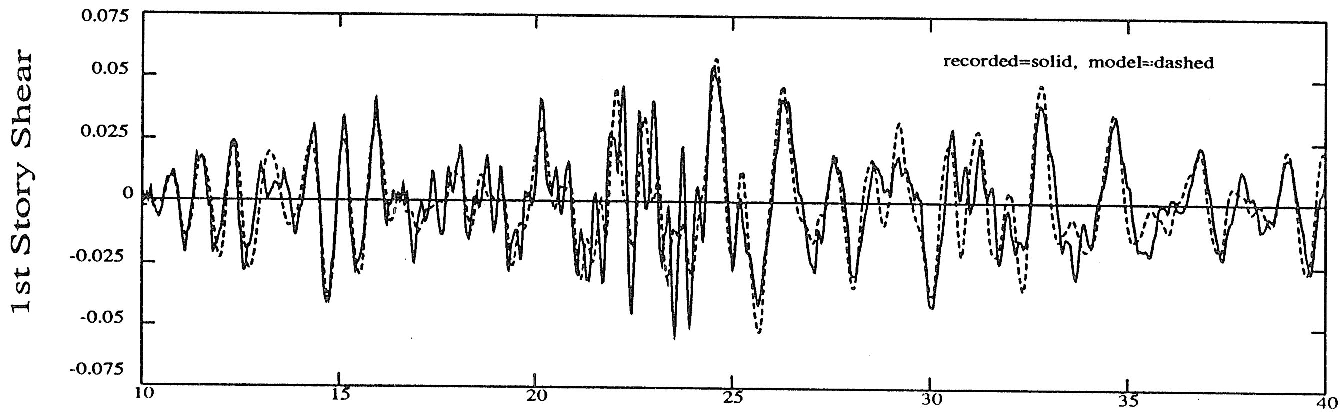

(a) Transverse

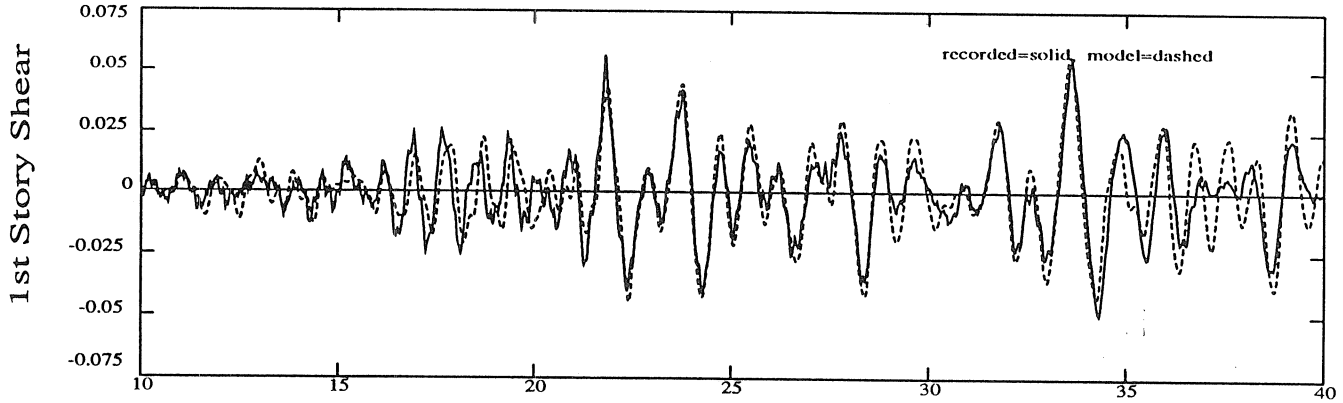

(b) Longitudinal

Figure 4.21 FCLJC recorded and modeled first story shear in the transverse and longitudinal directions from the 1992 Landers earthquake (Refer to equations 4.1 and 4.2).

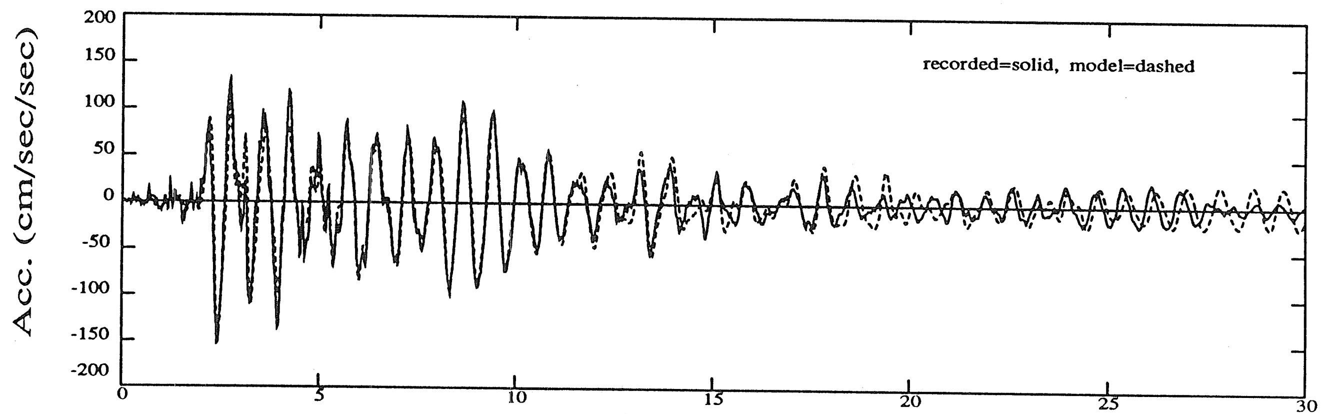

(a) Transverse

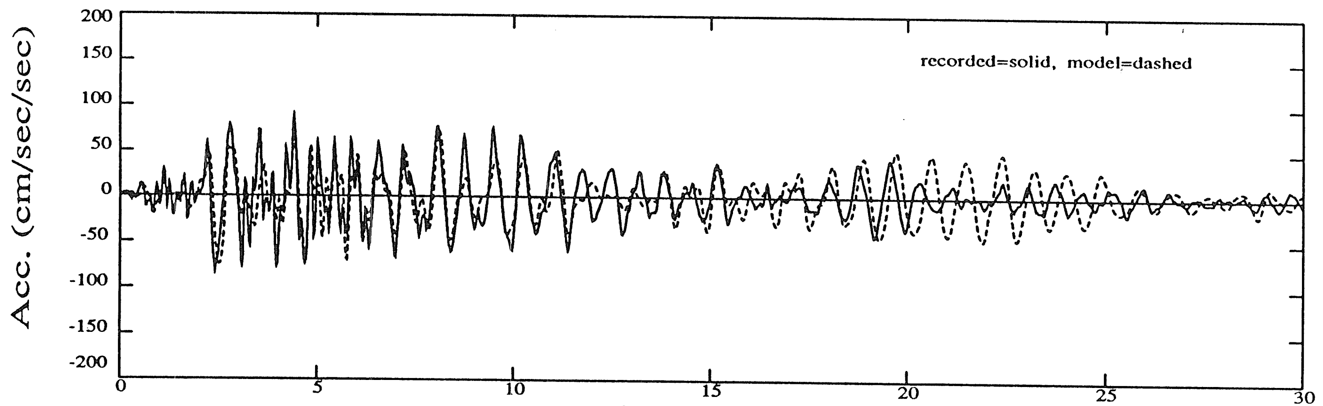

(b) Longitudinal

Figure 4.22 FCLJC recorded and modeled roof acceleration in the transverse and longitudinal directions from the 1990 Upland earthquake.

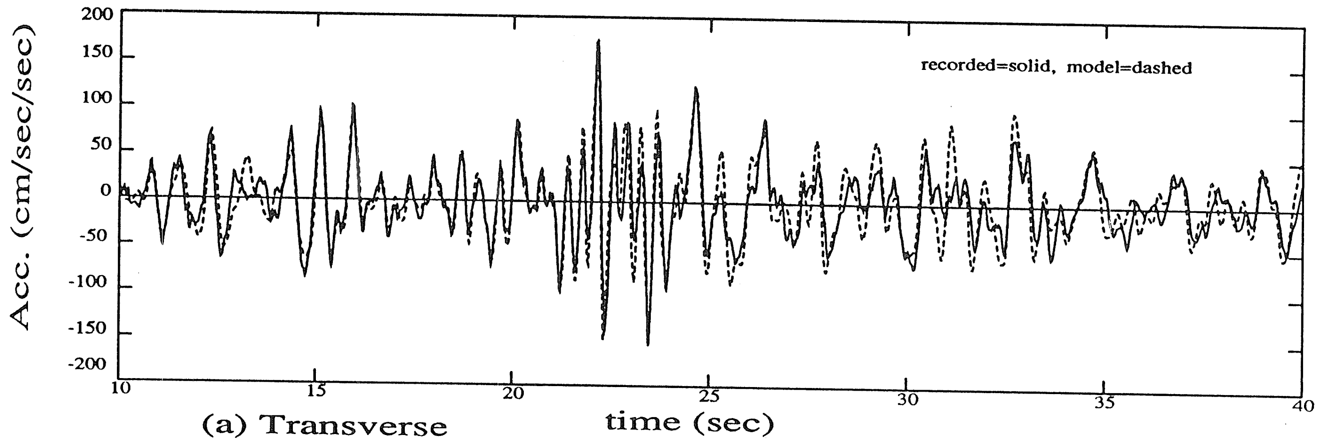

(a) Transverse

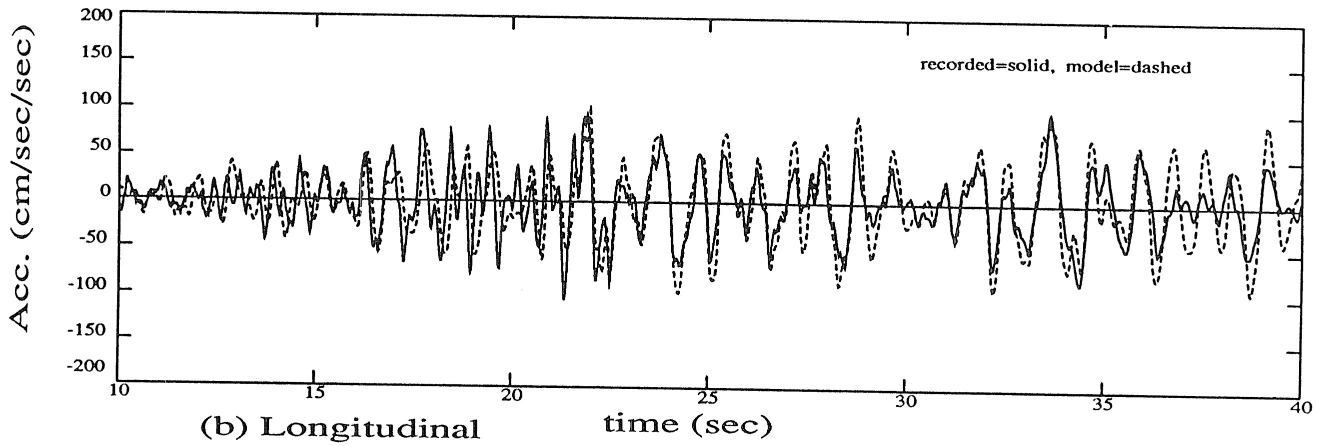

(b) Longitudinal

Figure 4.23 FCLJC recorded and modeled roof acceleration in the transverse and longitudinal directions from the 1992 Landers earthquake.

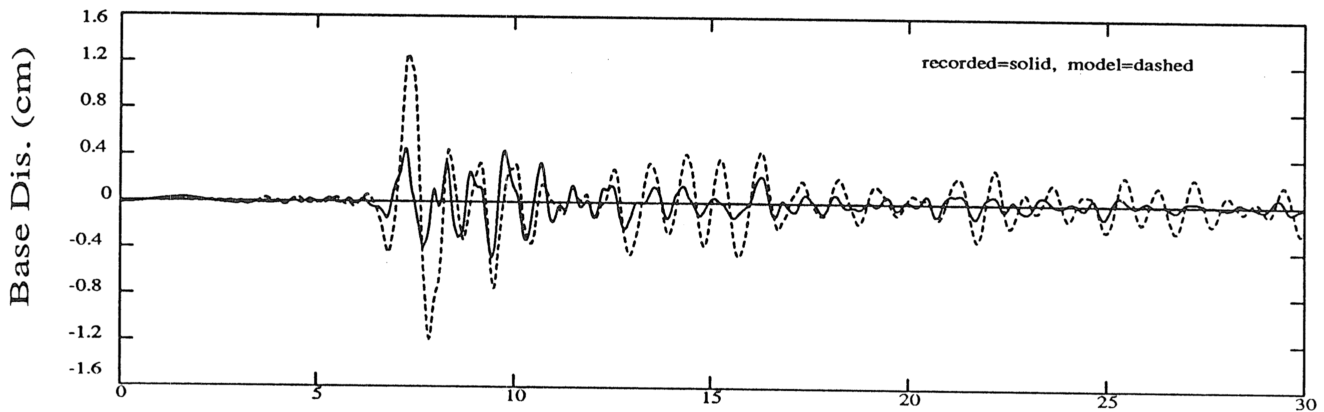

(a) Transverse

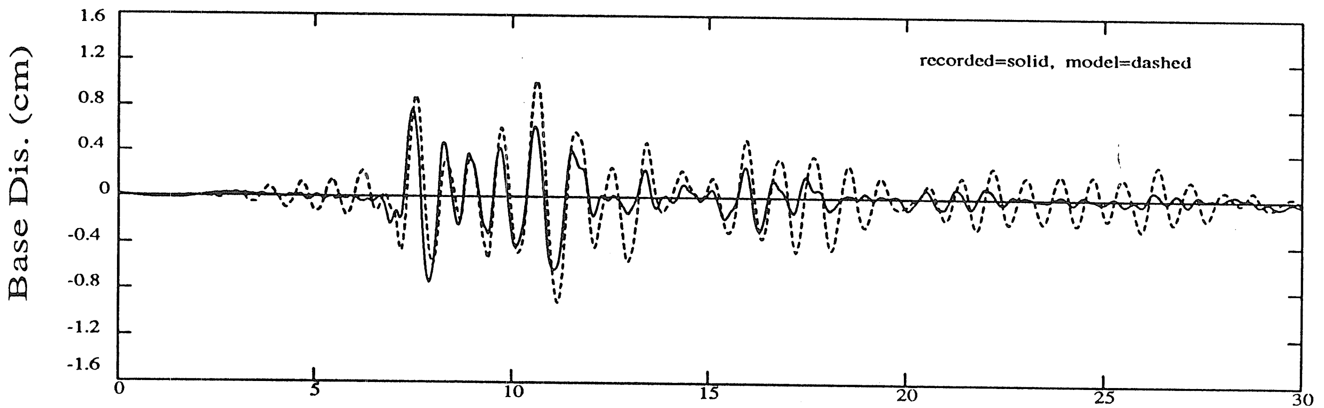

(b) Longitudinal

Figure 4.24 FCCF recorded and modeled base displacement (relative to foundation displacement) in the transverse and longitudinal directions from the 1991 Sierra Madre earthquake.

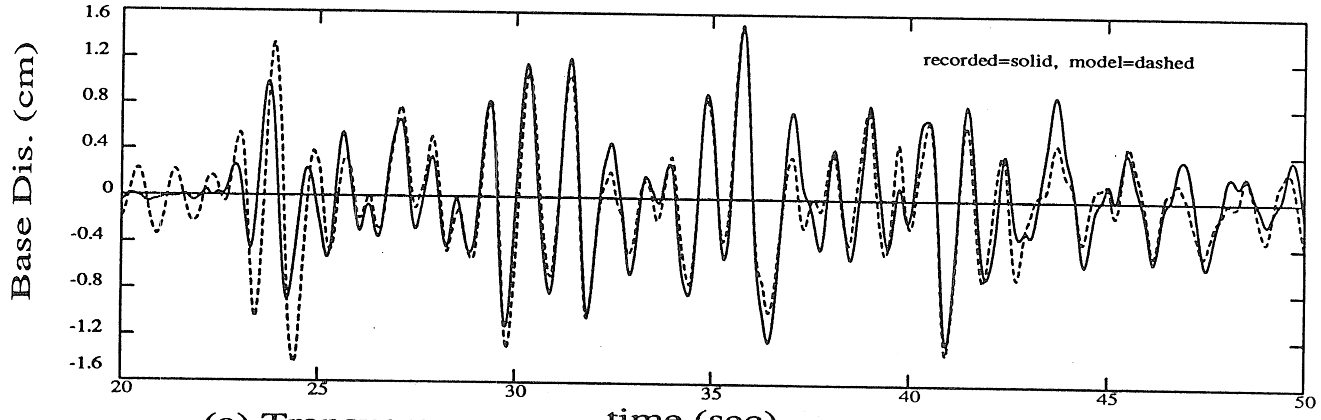

(a) Transverse

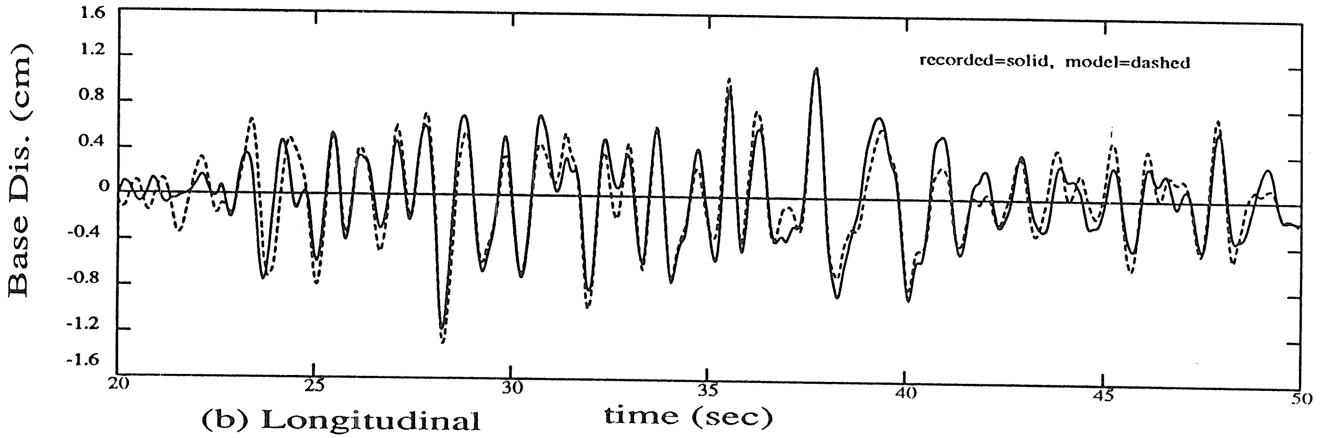

(b) Longitudinal

Figure 4.25 FCCF recorded and modeled base displacement (relative to foundation displacement) in the transverse and longitudinal directions from the 1992 Landers earthquake.

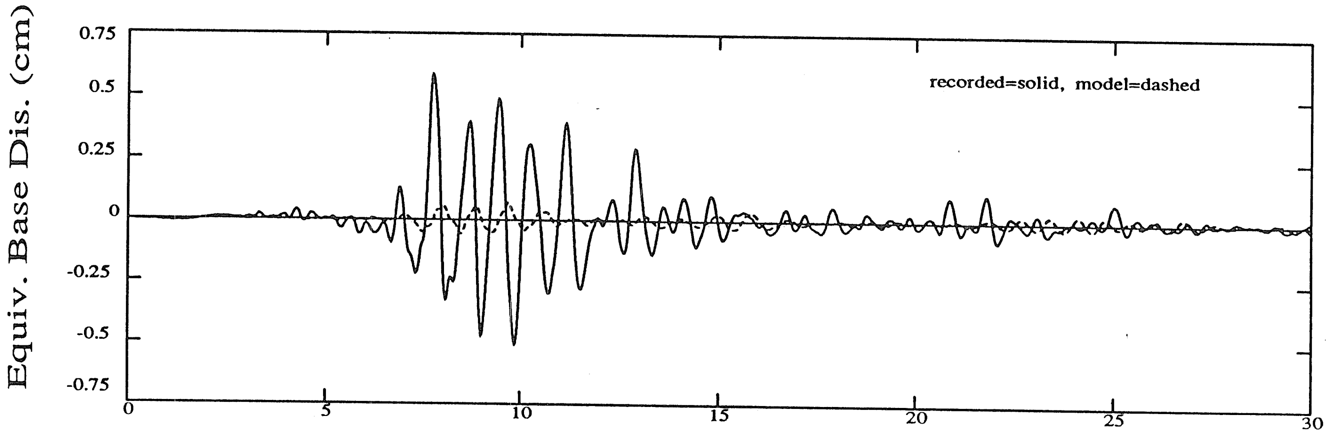

(a) Sierra Madre EQ

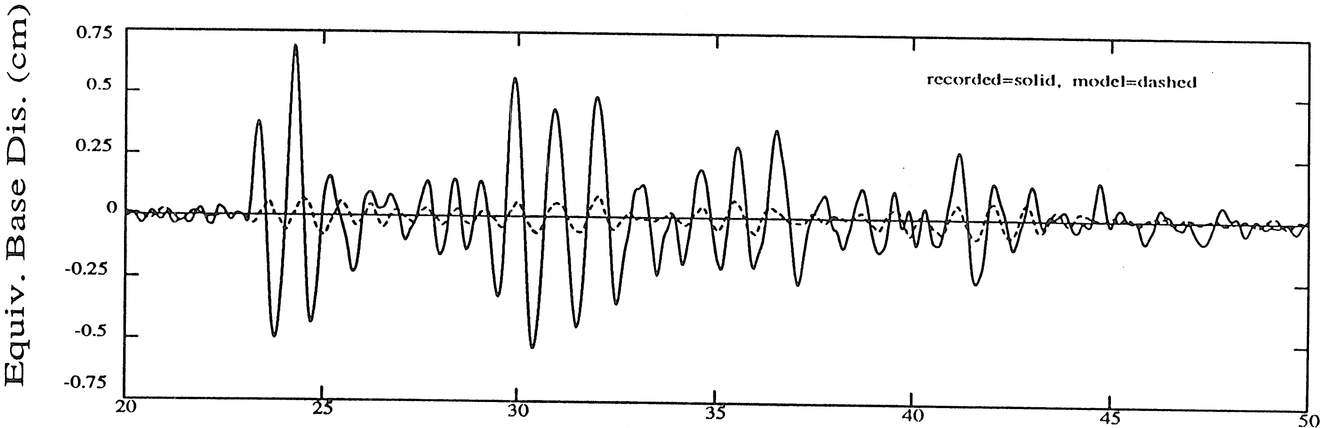

(b) Landers EQ

Figure 4.26 FCCF recorded and modeled torsional base displacement ((base rotation relative to foundation rotation) x L/2) from the 1991 Sierra Madre and the 1992 Landers earthquakes.

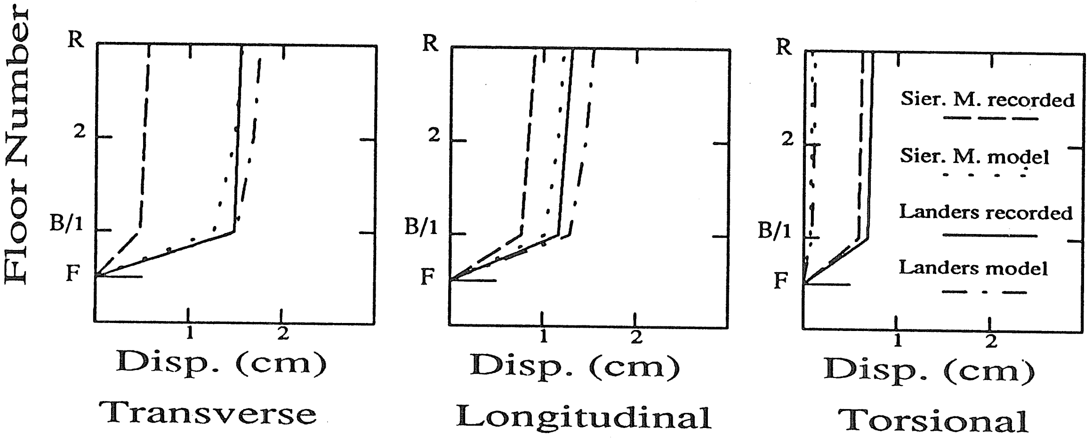

Figure 4.27 FCCF peak floor displacements (relative to the foundation) from the 1991 Sierra Madre and 1992 Landers earthquakes. Torsional displacement is calculated as the floor rotation relative to the foundation rotation x L/2.

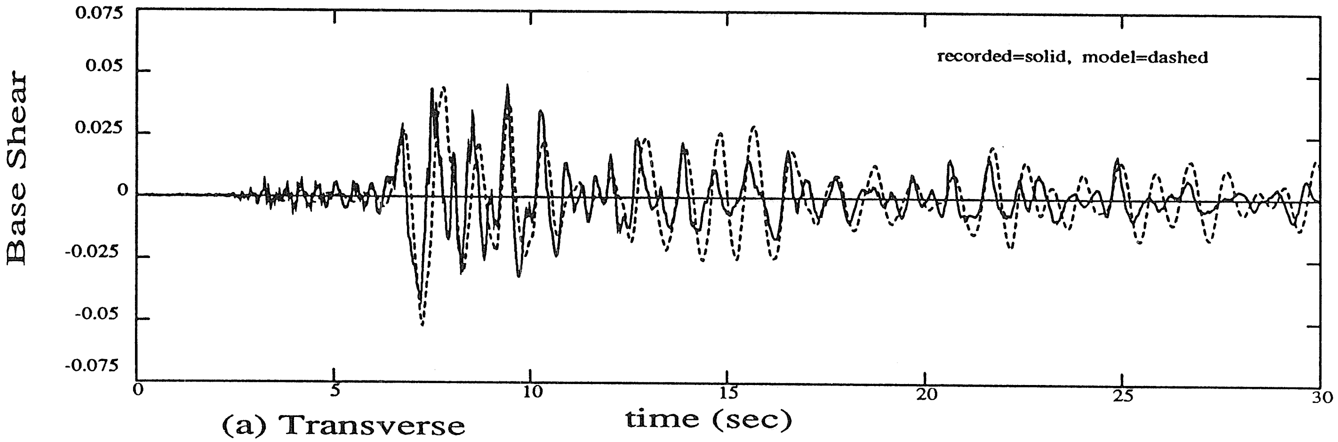

(a) Transverse

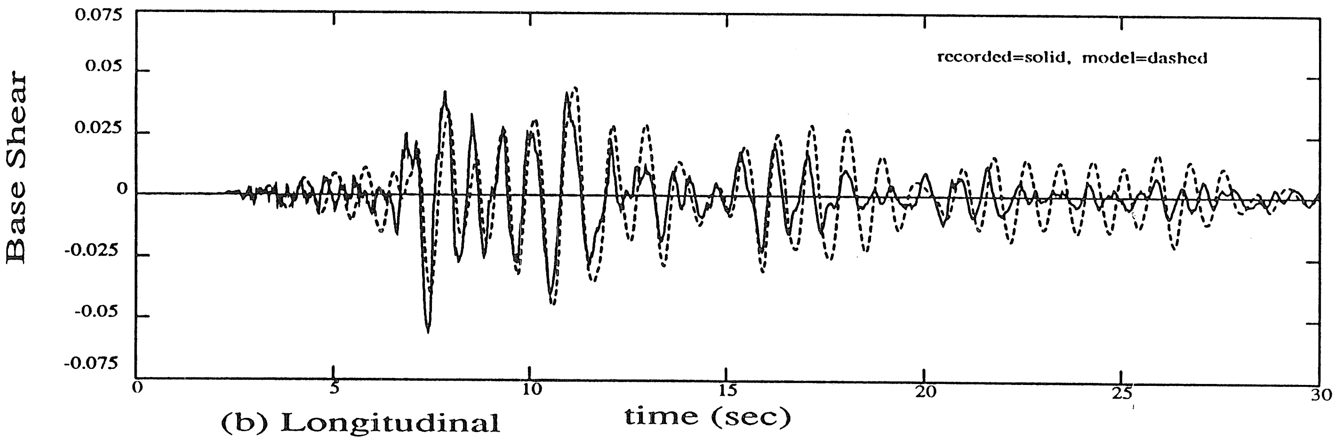

(b) Longitudinal

Figure 4.28 FCCF recorded and modeled base shear in the transverse and longitudinal directions from the 1991 Sierra Madre earthquake (Refer to equations 4.4 and 4.5).

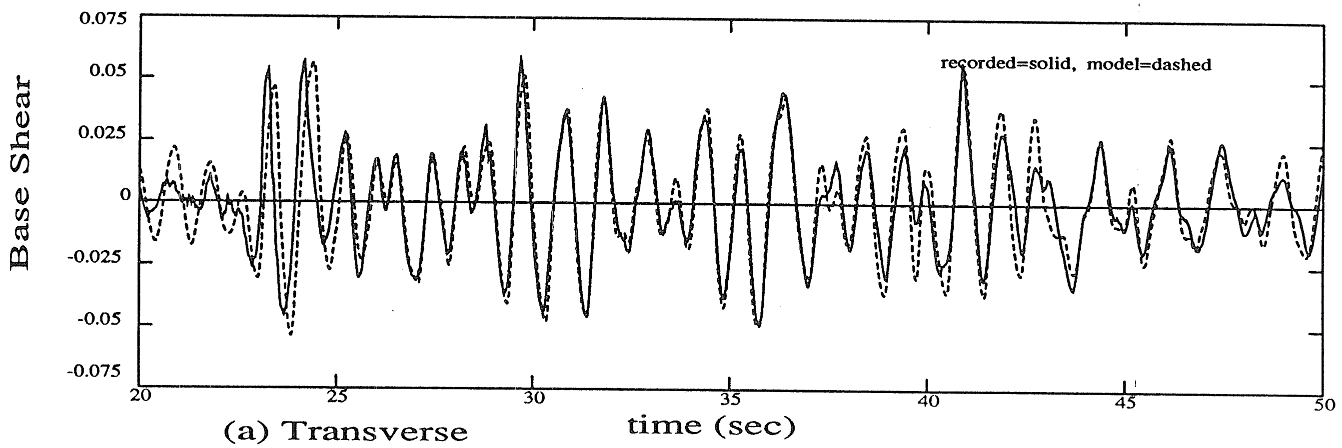

(a) Transverse

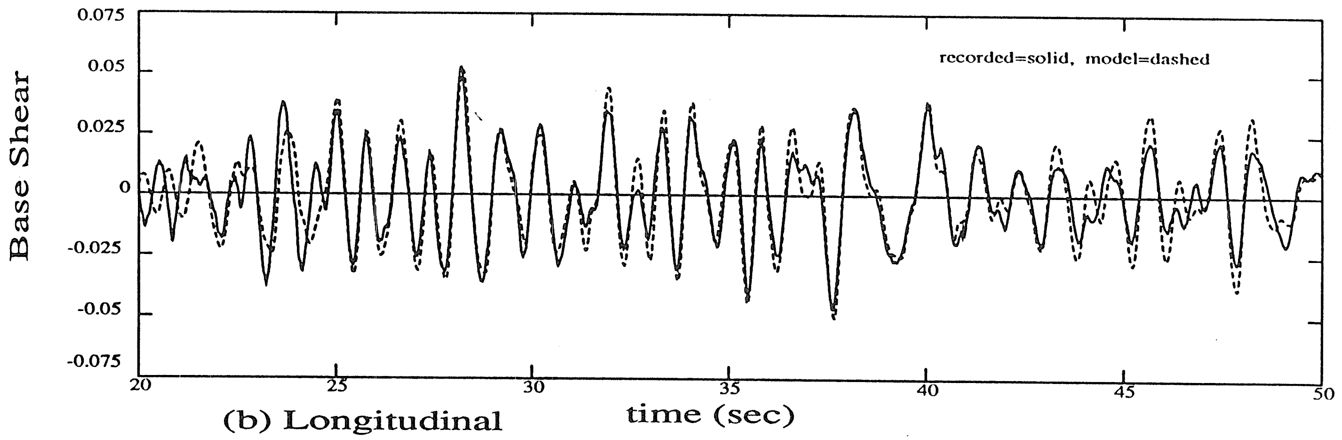

(b) Longitudinal

Figure 4.29 FCCF recorded and modeled base shear in the transverse and longitudinal directions from the 1992 Landers earthquake (Refer to equations 4.4 and 4.5).

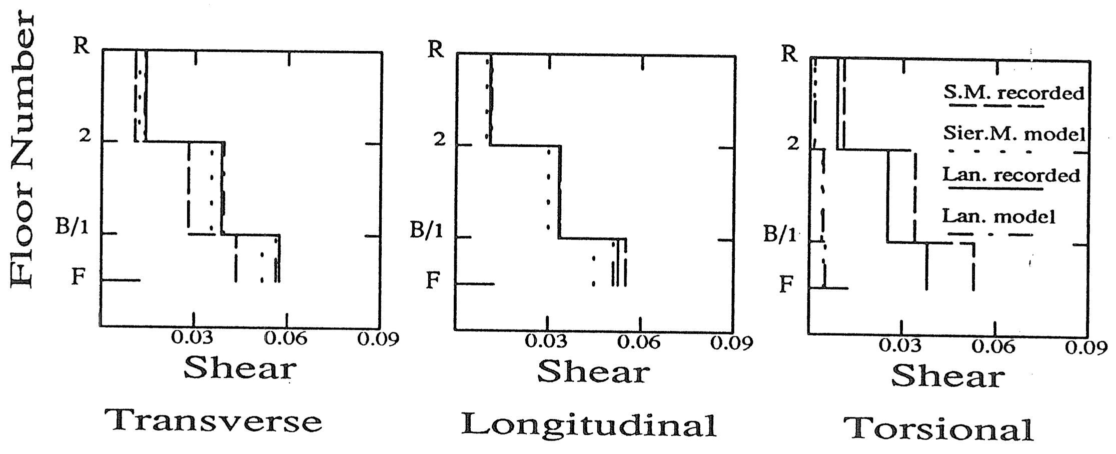

Figure 4.30 FCCF peak story shears from the 1991 Sierra Madre and 1992 Landers earthquakes (Refer to equations 4.4, 4.5, and 4.6).

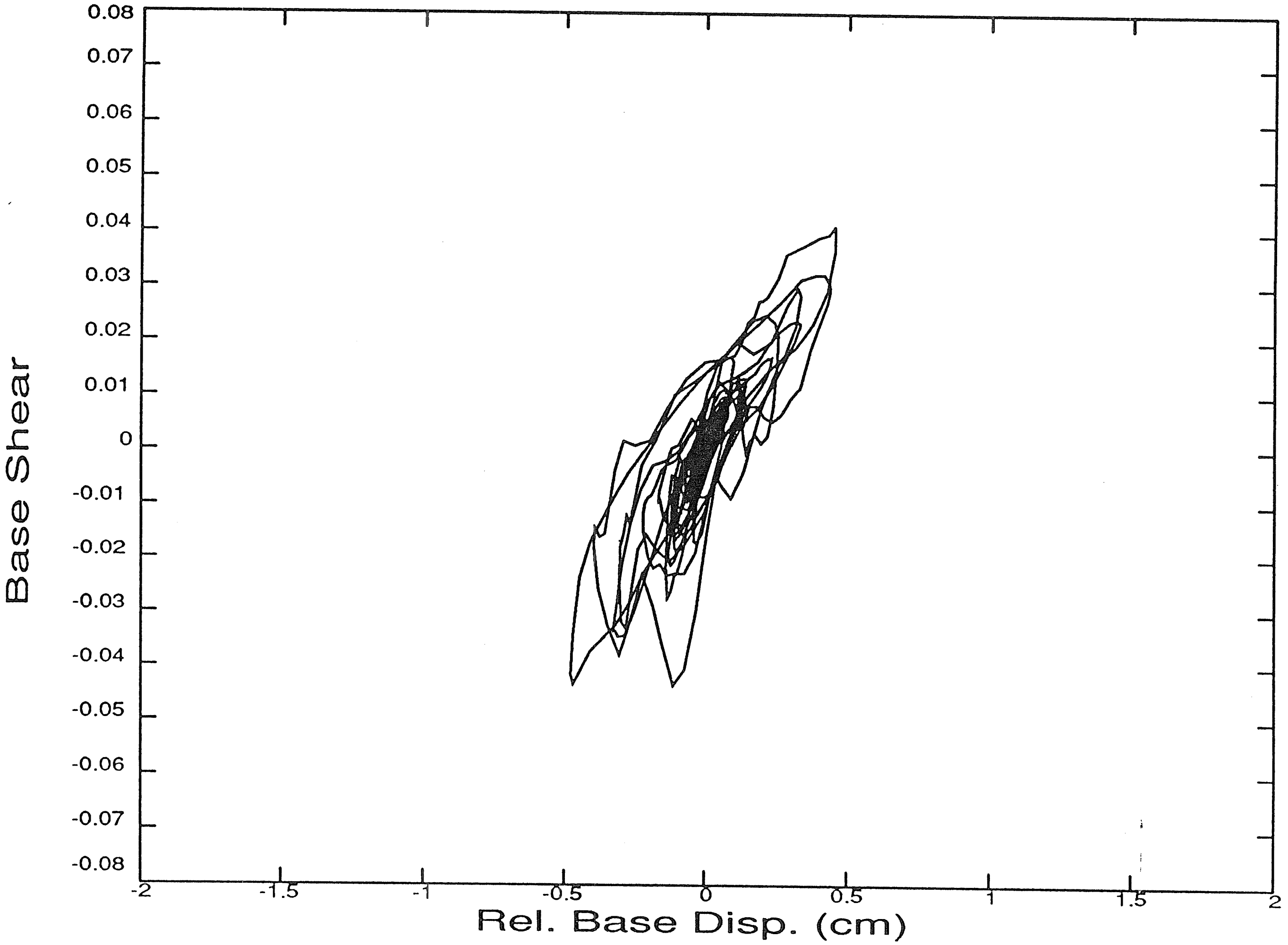

Figure 4.31 FCCF recorded force-displacement curve for the base level (isolation bearings) in the transverse direction from the 1991 Sierra Madre earthquake (Refer to equation 4.4).

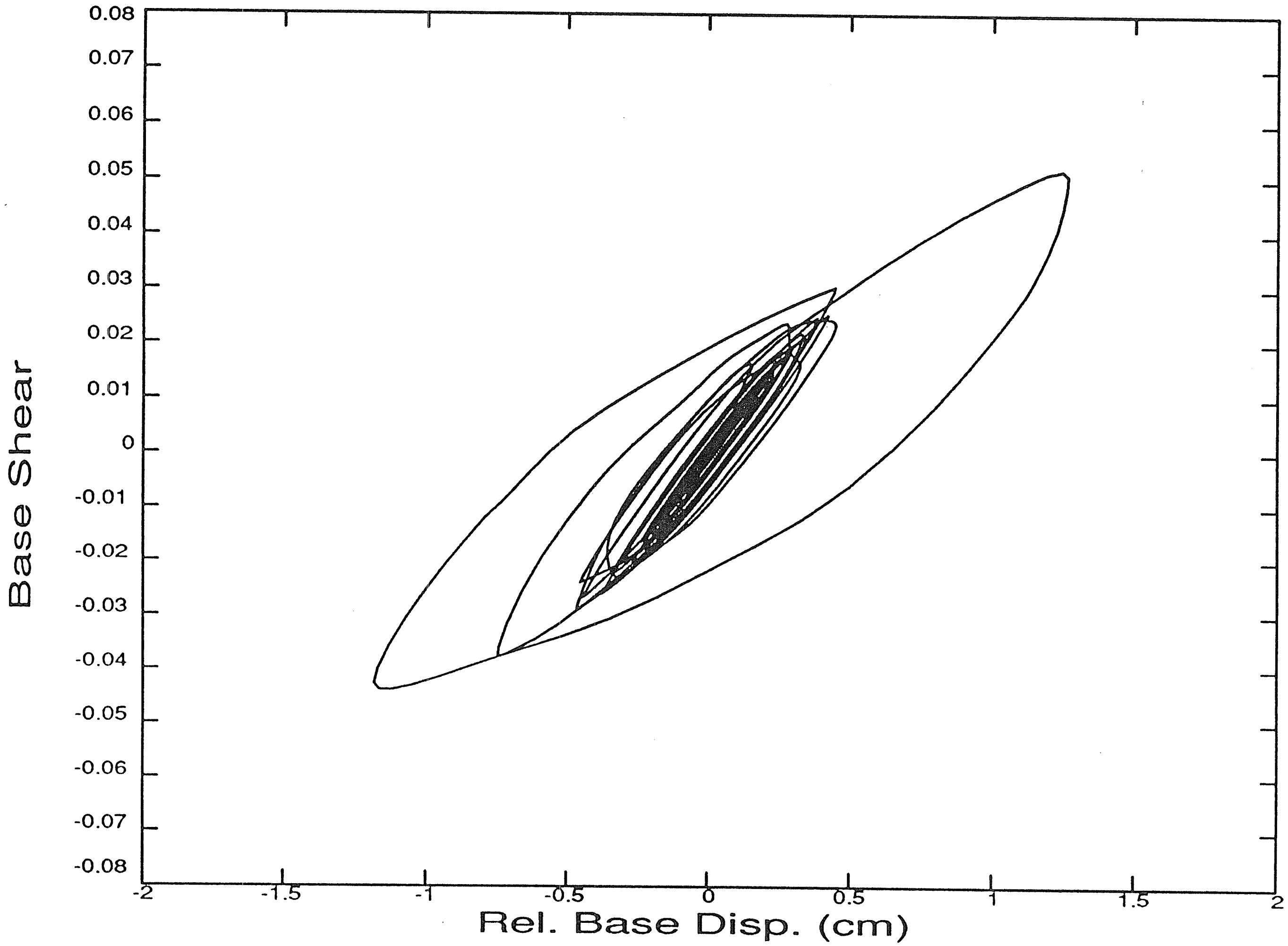

Figure 4.32 FCCF modeled force-displacement curve for the base level (isolation bearings) in the transverse direction from the 1991 Sierra Madre earthquake.

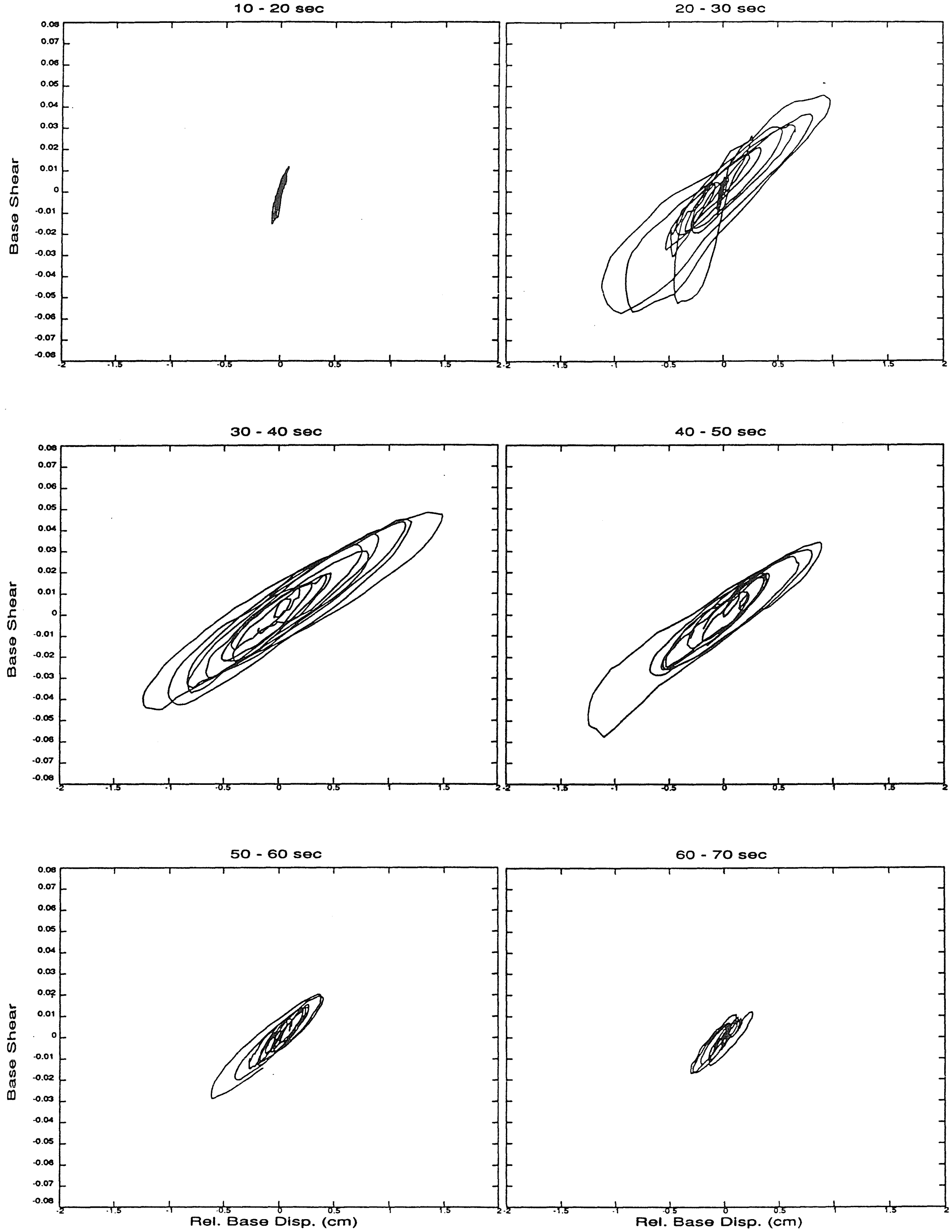
10 - 20 sec

20 - 30 sec

30 - 40 sec

40 - 50 sec

50 - 60 sec

60 - 70 sec

Figure 4.33 FCCF recorded force-displacement curve for the base level (isolation bearings) in the transverse direction from the 1992 Landers earthquake which has been divided into 10 sec time segments (Refer to equation 4.4).

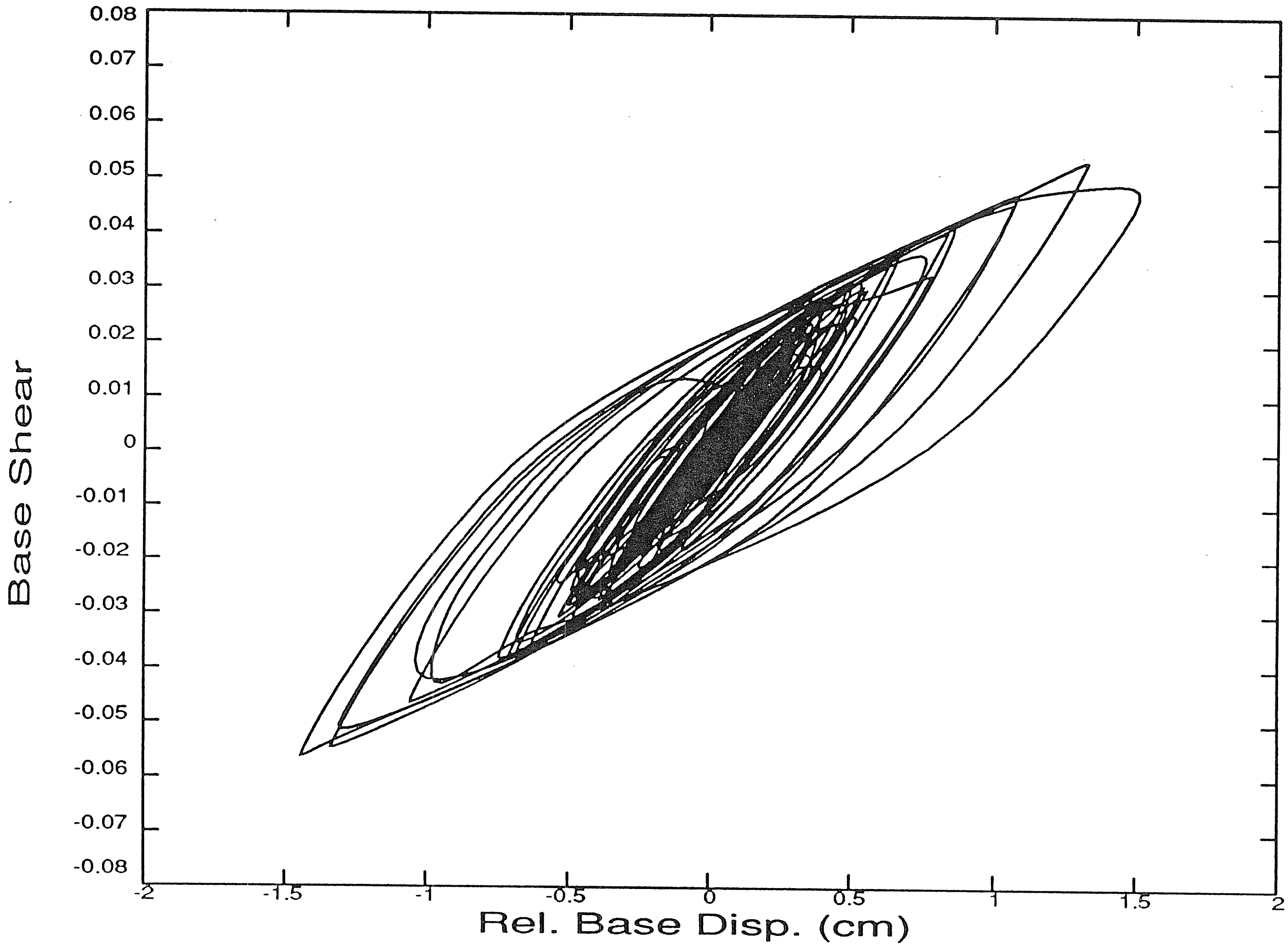

Figure 4.34 FCCF modeled force-displacement curve for the base level (isolation bearings) in the transverse direction from the 1992 Landers earthquake.

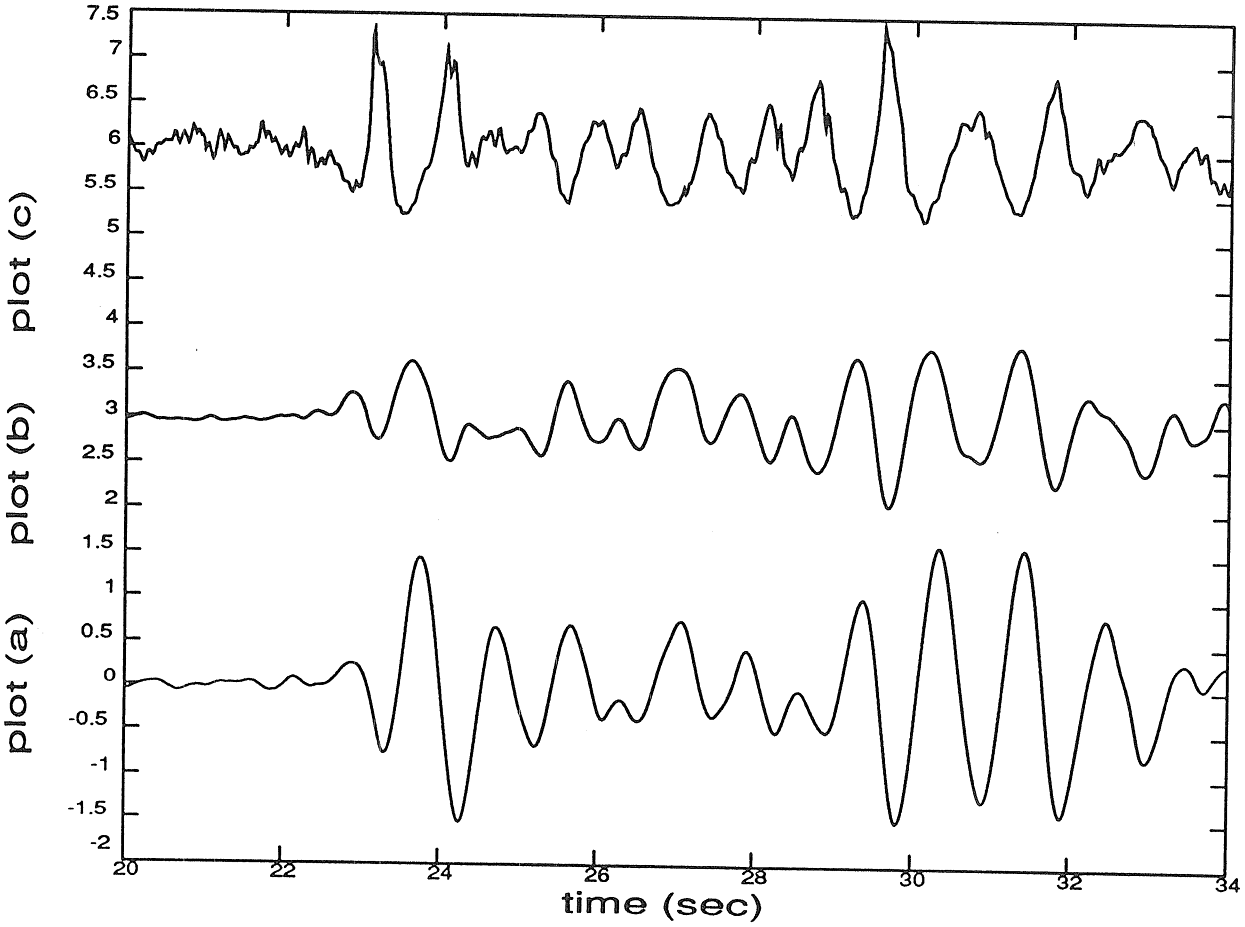

Figure 4.35 FCCF recorded transverse bearing displacement (cm) at the south end of building (plot a), recorded transverse bearing displacement (cm) at the north end of building (plot b), and recorded transverse 1st floor acceleration (m/sec/sec) at the north end of building (plot c).

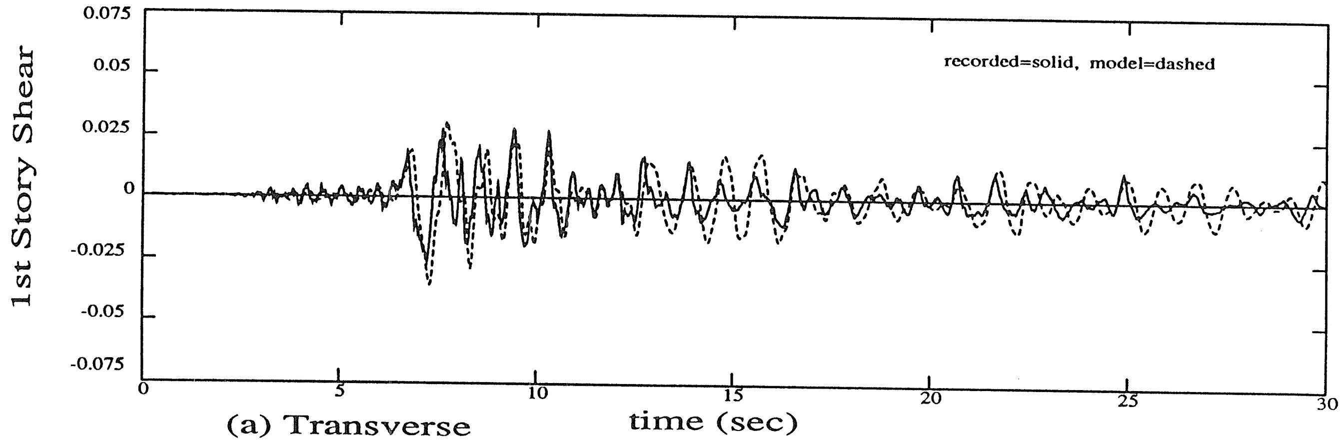

(a) Transverse

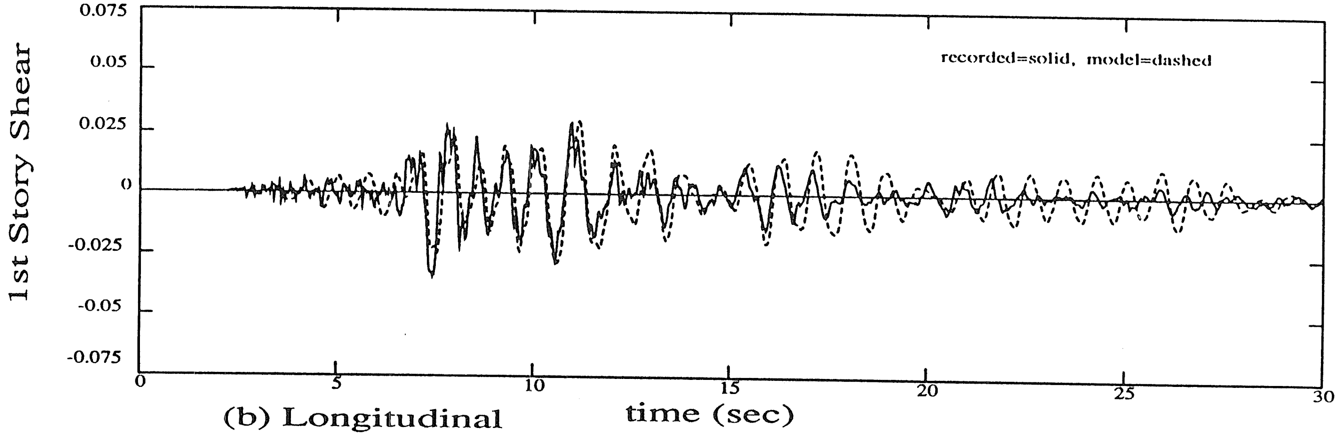

(b) Longitudinal

Figure 4.36 FCCF recorded and modeled first story shear in the transverse and longitudinal directions from the 1991 Sierra Madre earthquake (Refer to equations 4.4 and 4.5).

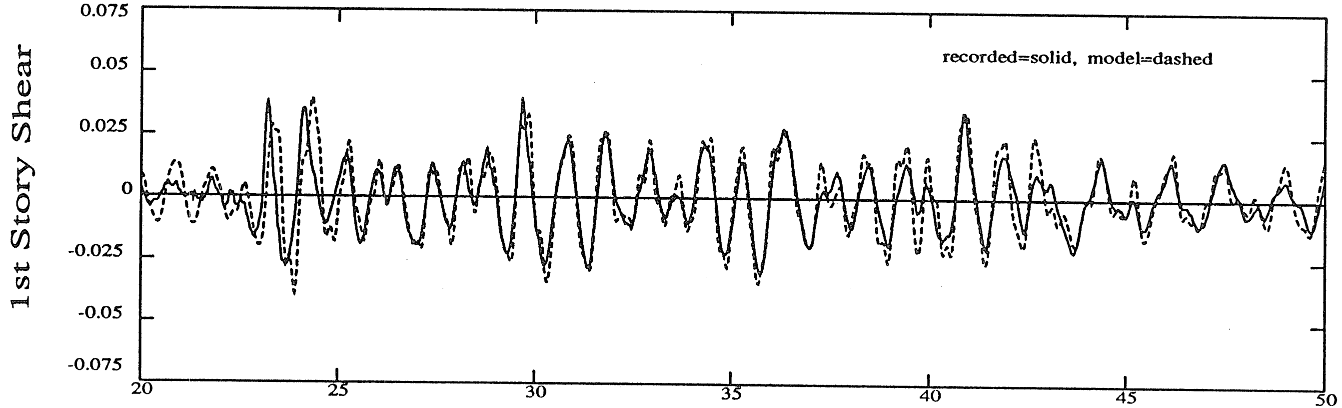

(a) Transverse

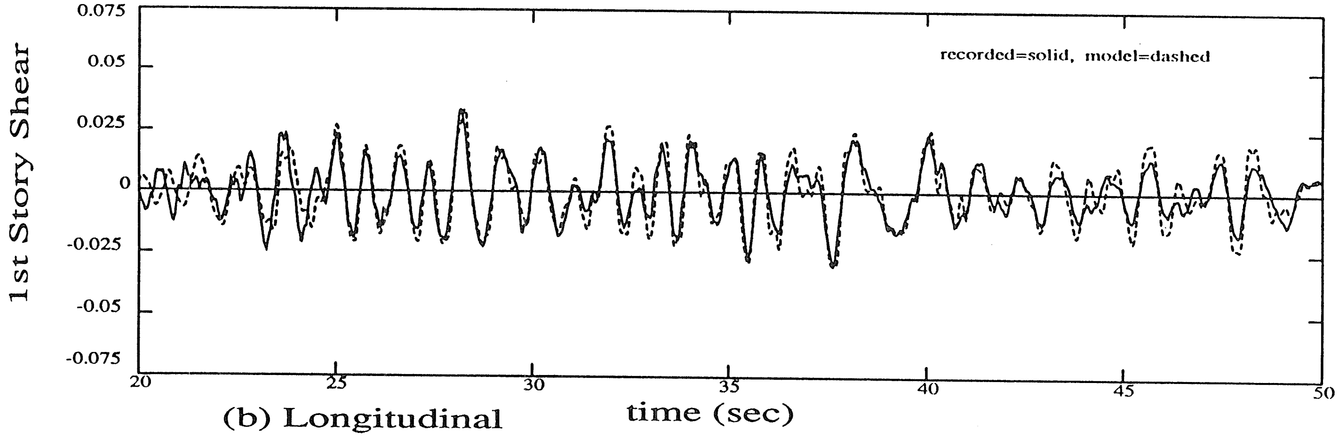

(b) Longitudinal

Figure 4.37 FCCF recorded and modeled first story shear in the transverse and longitudinal directions from the 1992 Landers earthquake (Refer to equations 4.4 and 4.5).

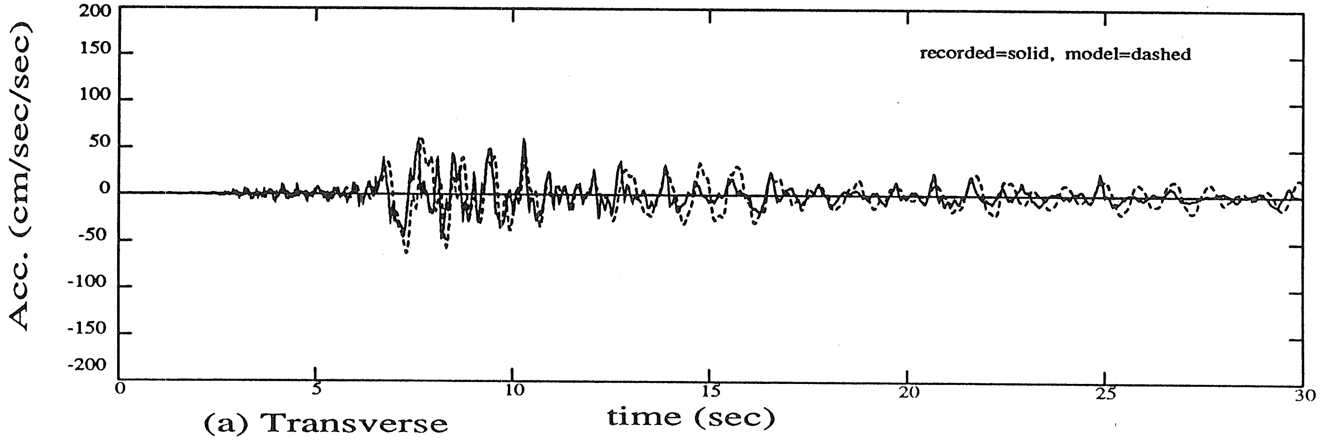

(a) Transverse

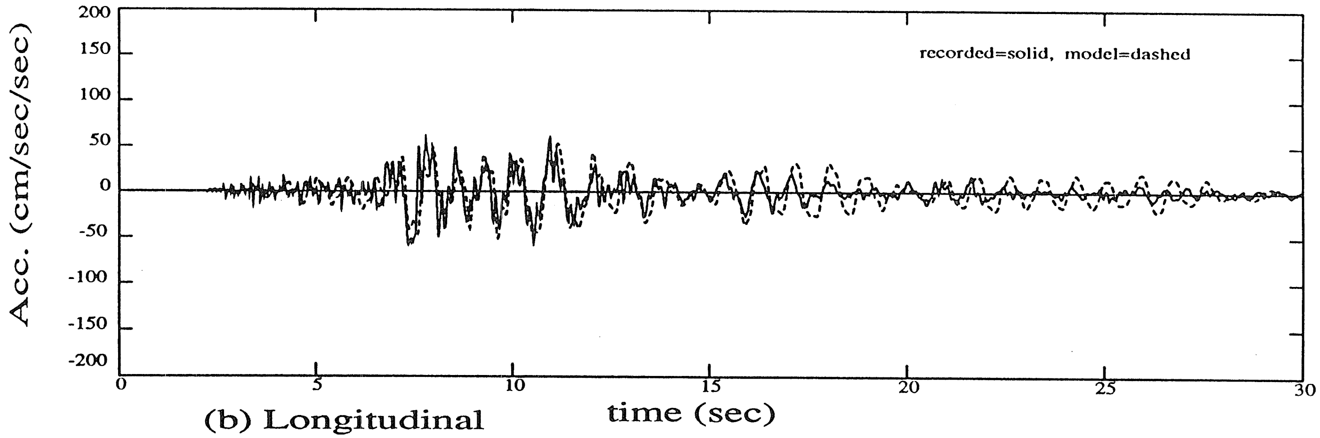

(b) Longitudinal

Figure 4.38 FCCF recorded and modeled roof acceleration in the transverse and longitudinal directions from the 1991 Sierra Madre earthquake.

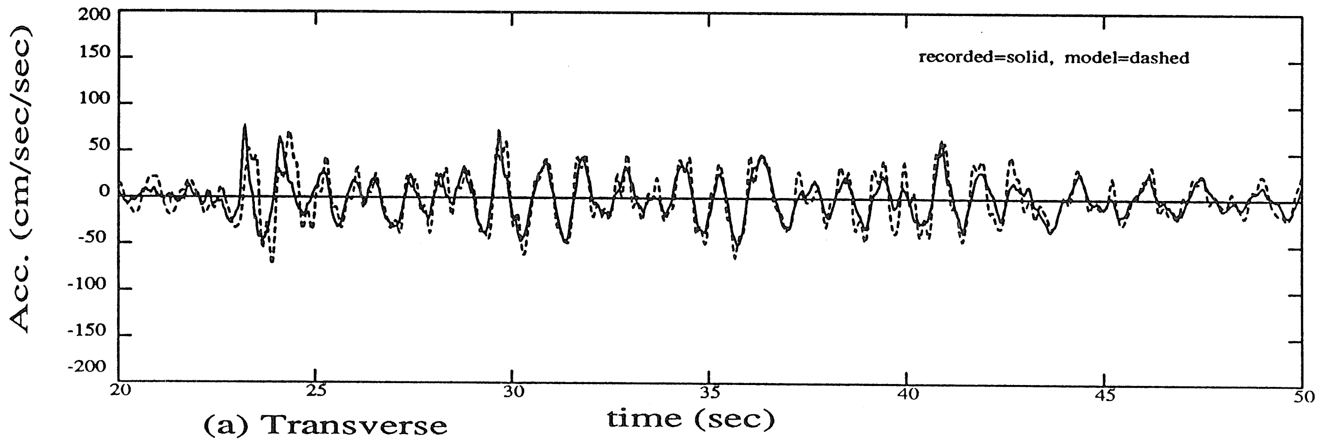

(a) Transverse

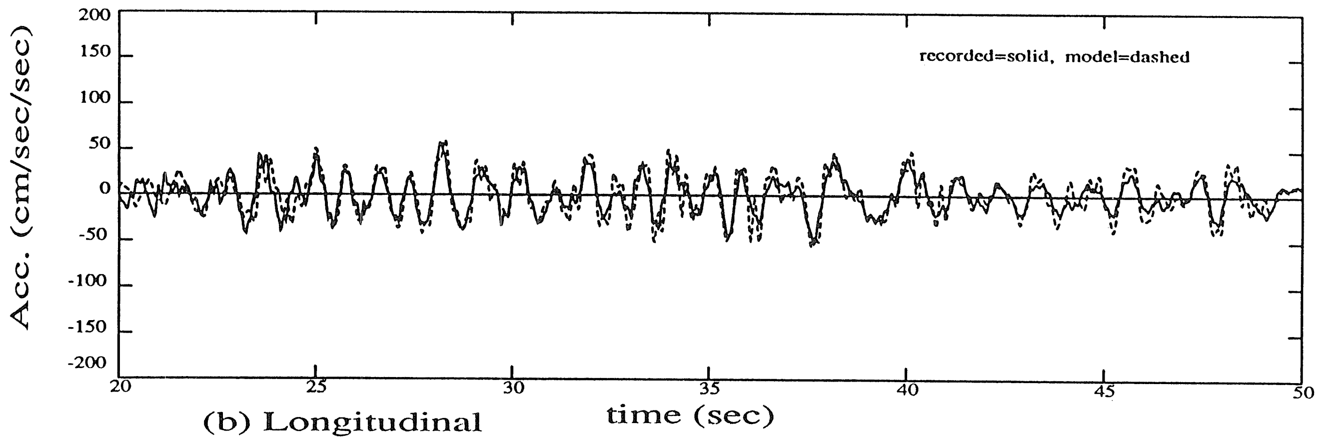

(b) Longitudinal

Figure 4.39 FCCF recorded and modeled roof acceleration in the transverse and longitudinal directions from the 1992 Landers earthquake.

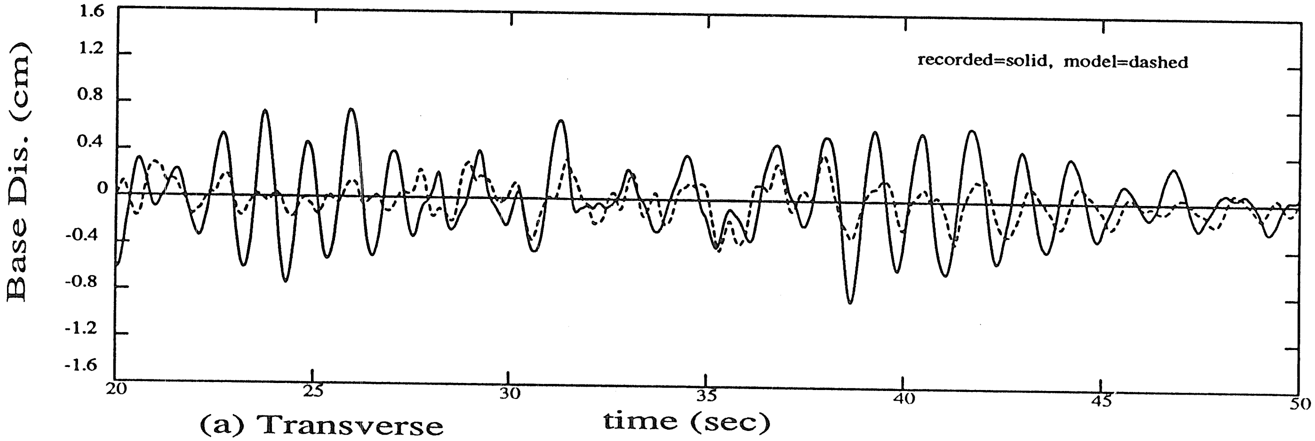

(a) Transverse

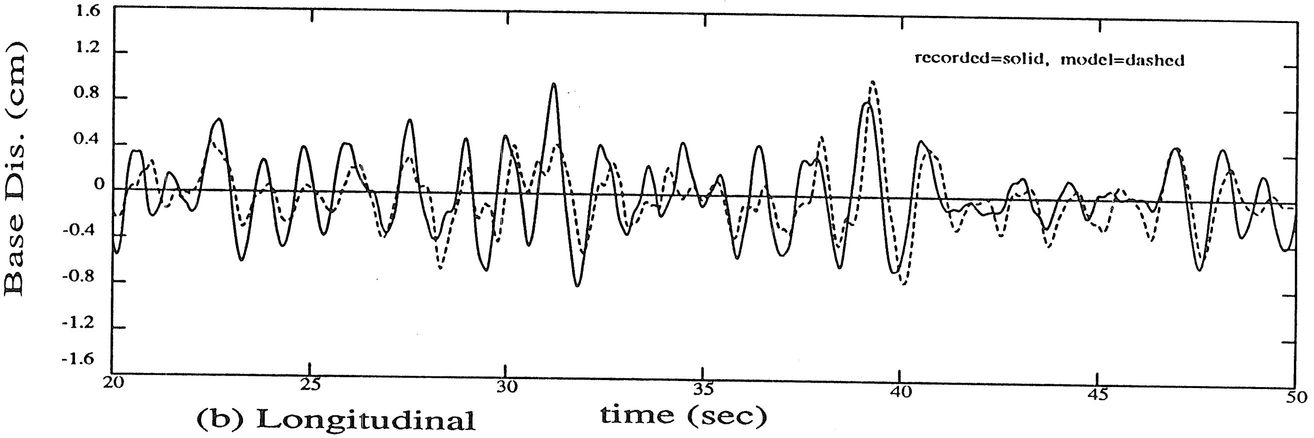

(b) Longitudinal

Figure 4.40 USCUH recorded and modeled base displacement (relative to foundation displacement) in the transverse and longitudinal directions from the 1992 Landers earthquake.

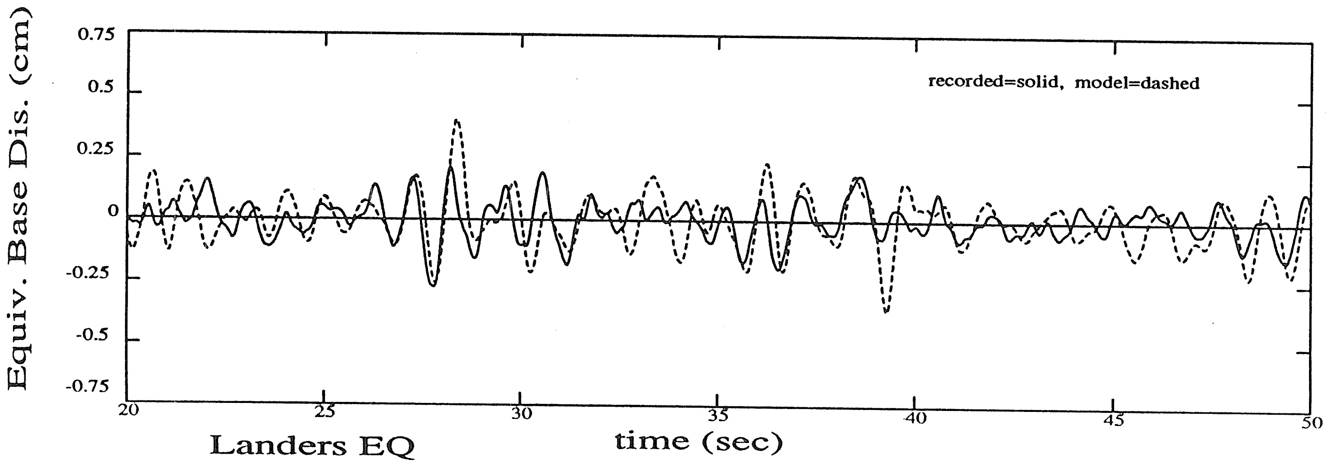

Figure 4.41 USCUH recorded and modeled torsional base displacement ((base rotation relative to foundation rotation) x L/2) from the 1992 Landers earthquake.

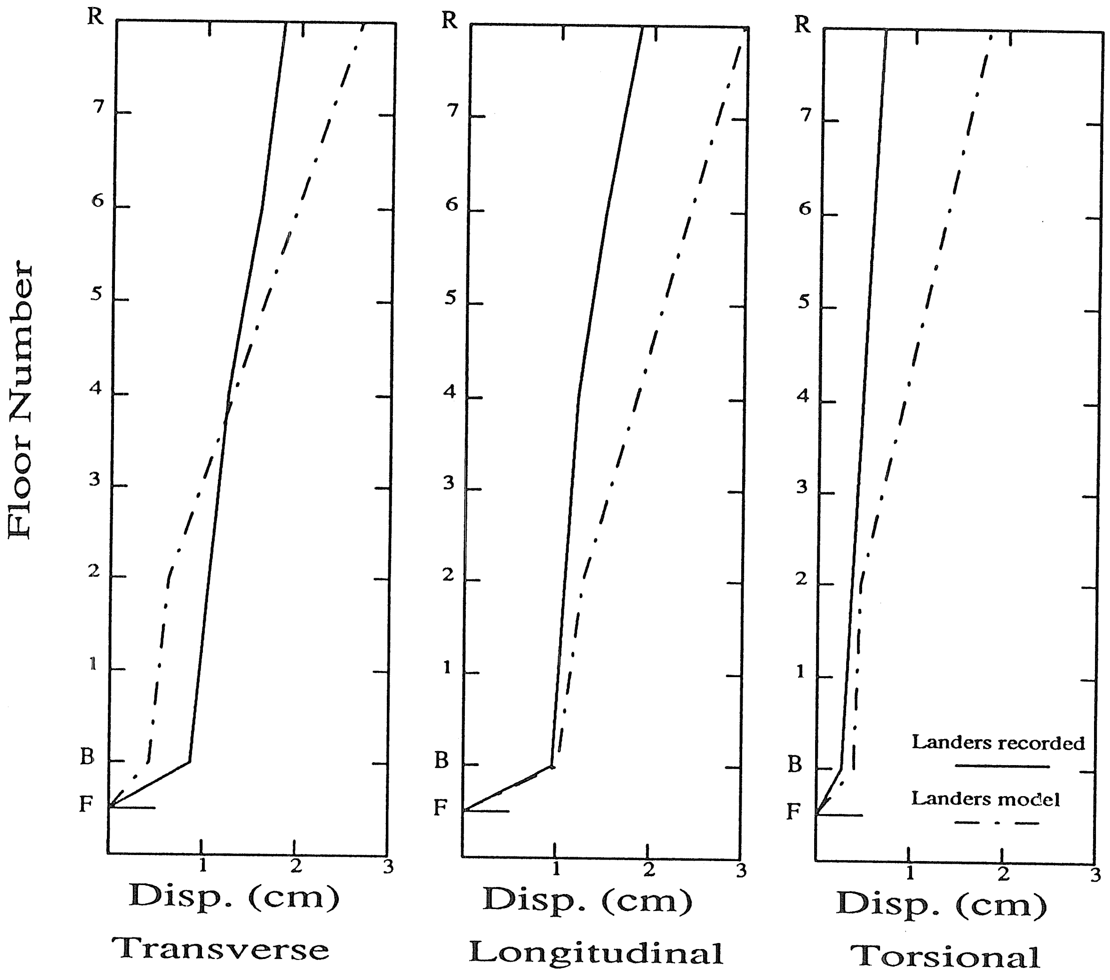

Figure 4.42 USCUH peak floor displacements (relative to the foundation) from the 1992 Landers earthquake. Torsional displacement is calculated as the floor rotation relative to the foundation rotation x L/2.

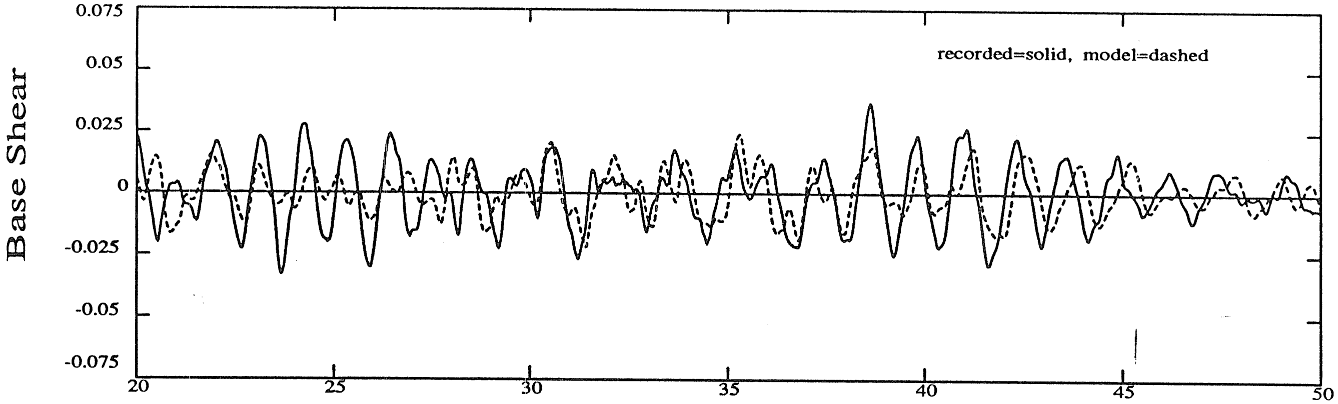

(a) Transverse

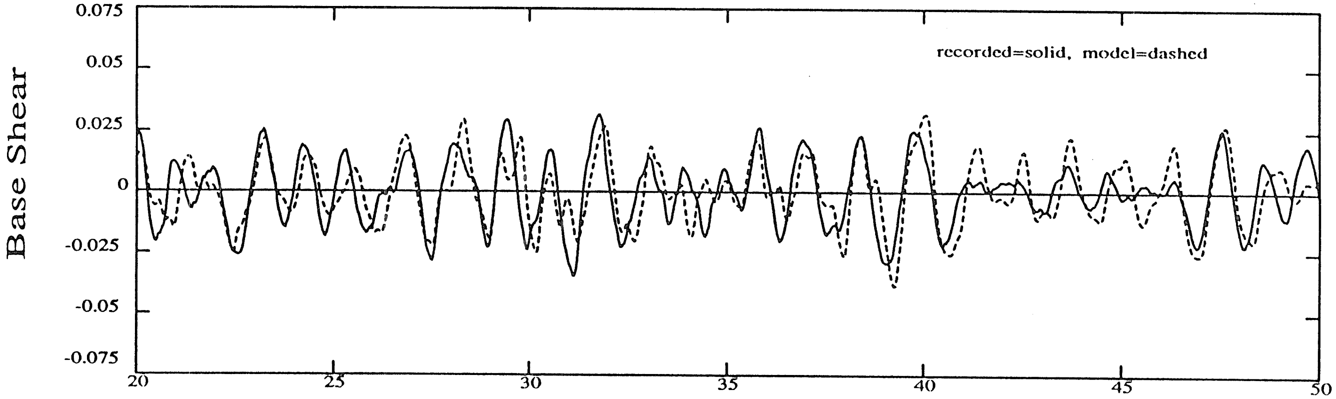

(b) Longitudinal

Figure 4.43 USCUH recorded and modeled base shear in the transverse and longitudinal directions from the 1992 Landers earthquake (Refer to equations 4.7 and 4.8).

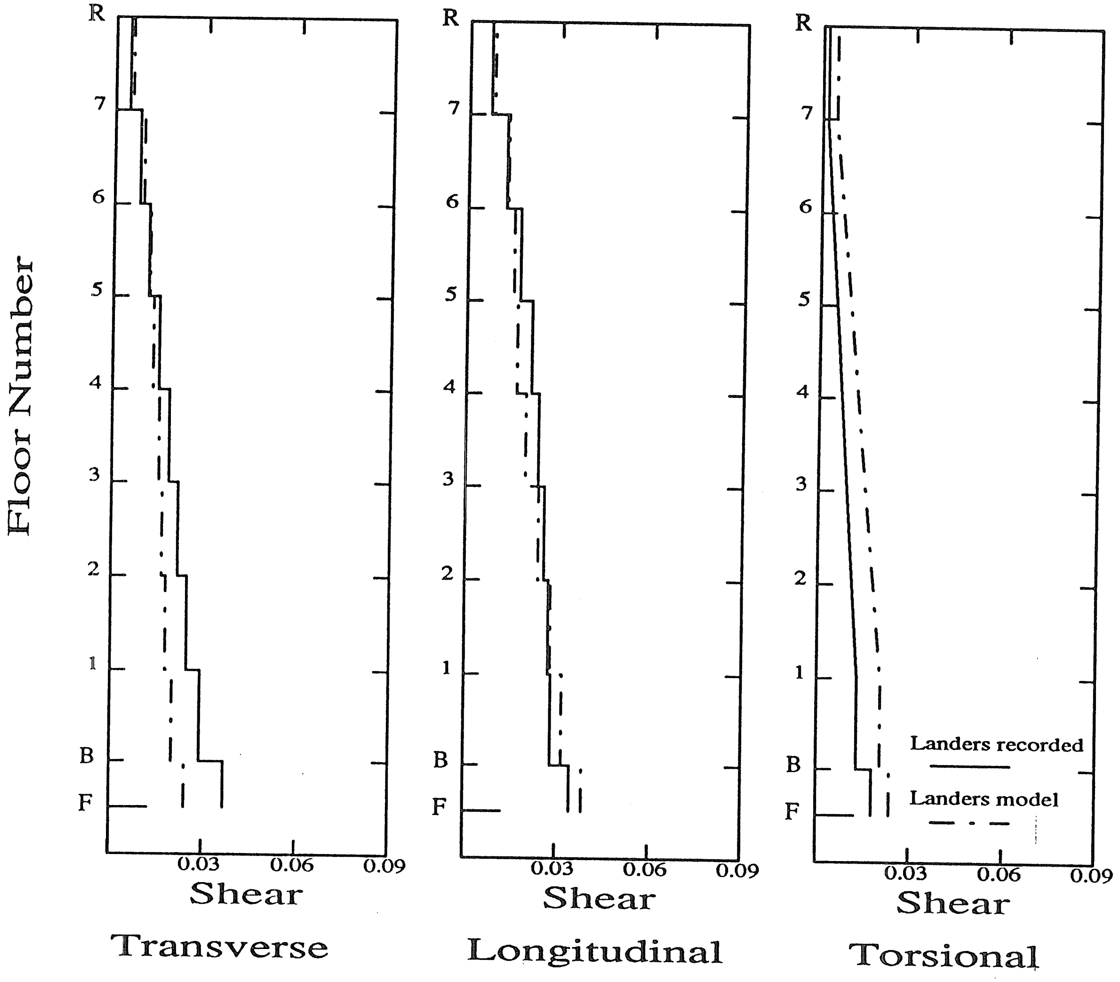

Figure 4.44 USCUH peak story shears from the 1992 Landers earthquake (Refer to equations 4.7, 4.8, and 4.9).

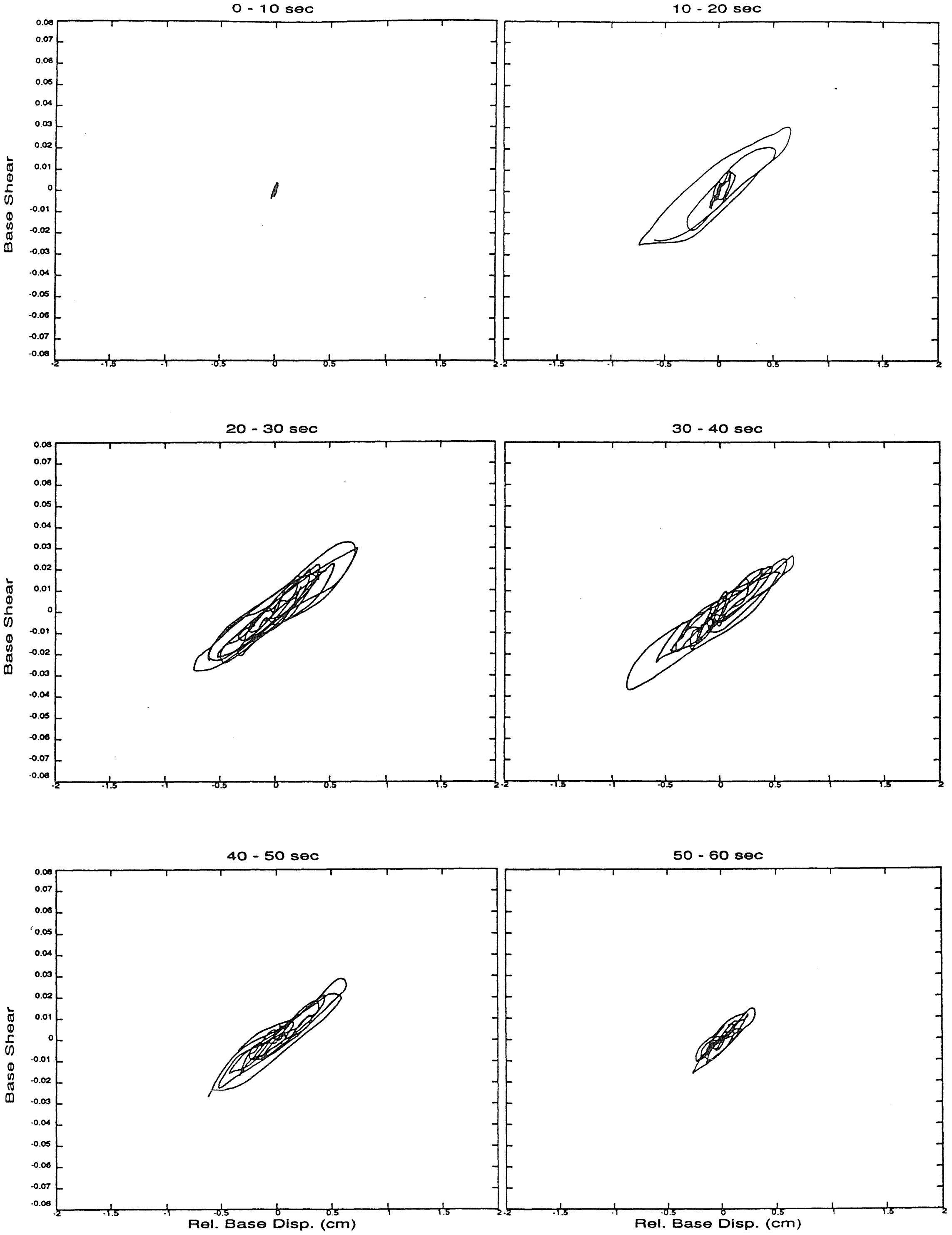

Figure 4.45 USCUH recorded force-displacement curve for the base level (isolation bearings) in the transverse direction from the 1992 Landers earthquake which has been divided into 10 sec time segments (Refer to equation 4.7).

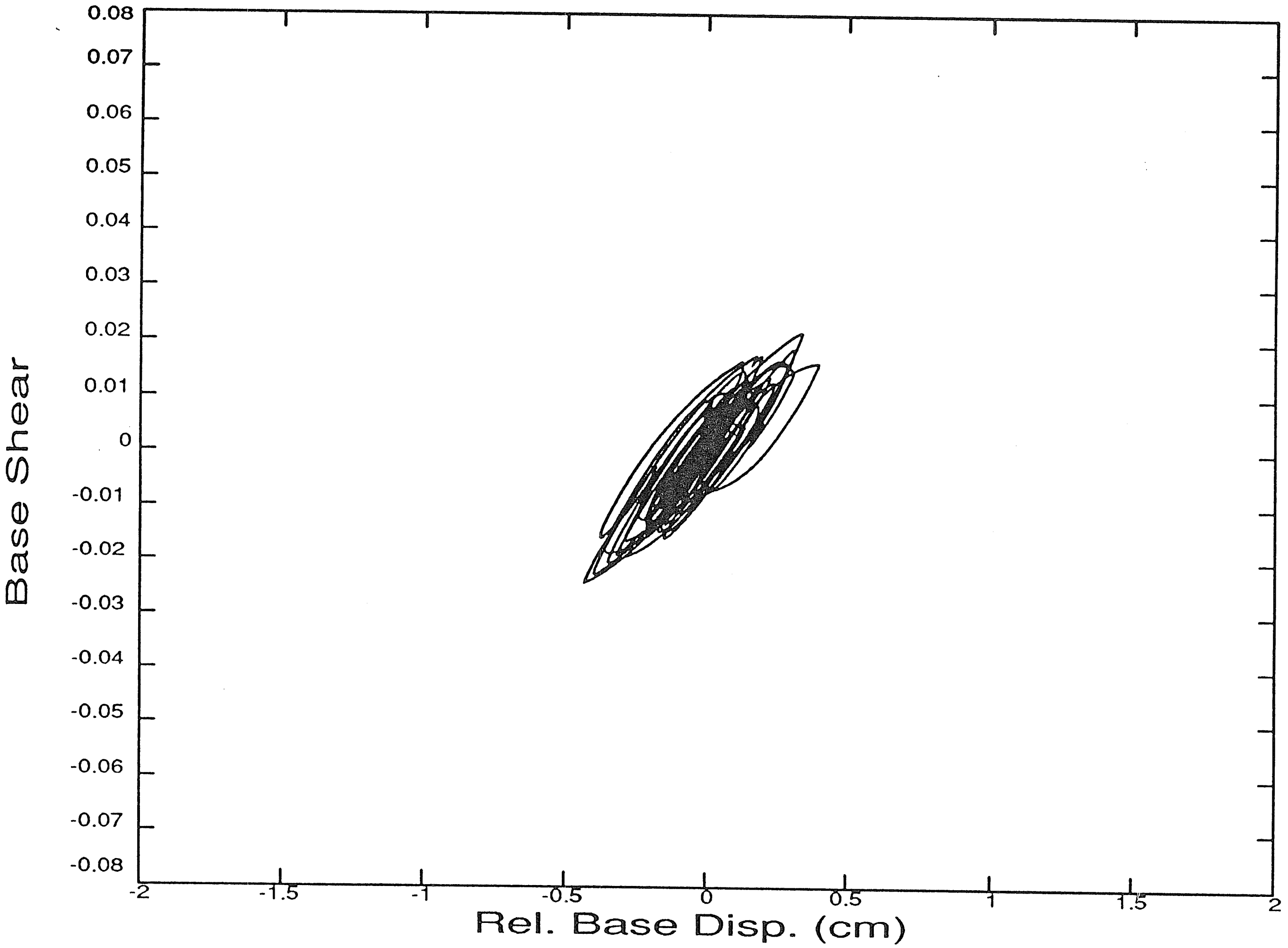

Figure 4.46 USCUH modeled force-displacement curve for the base level (isolation bearings) in the transverse direction from the 1992 Landers earthquake.

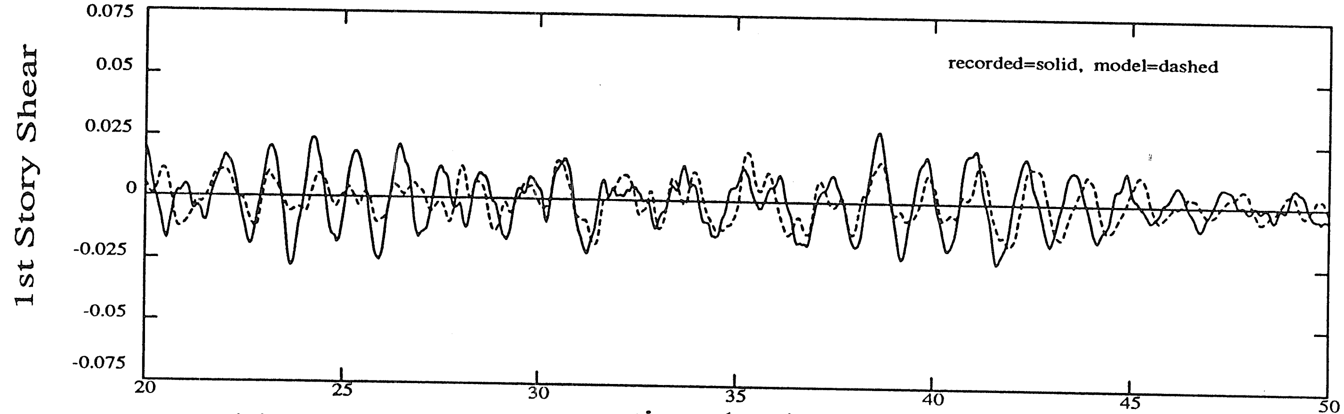

(a) Transverse

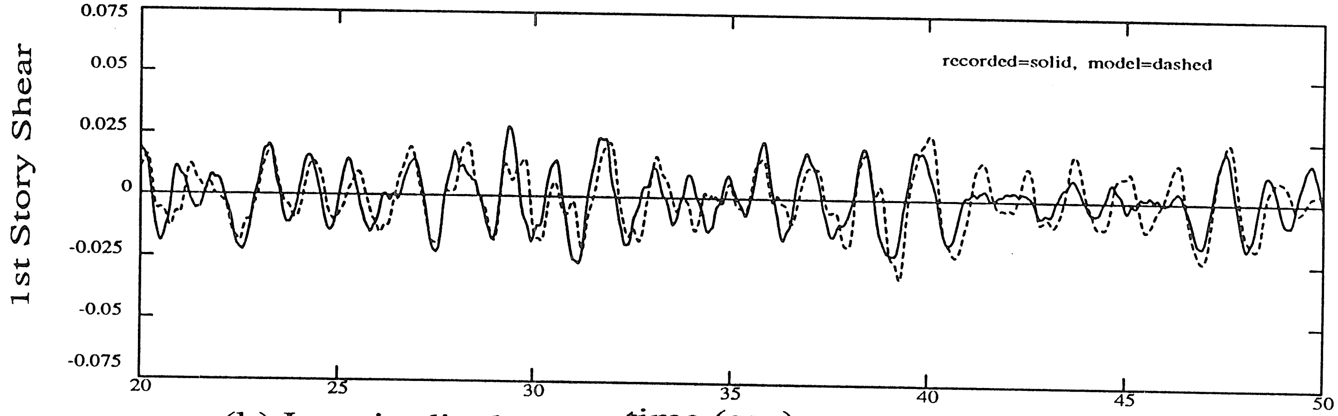

(b) Longitudinal

Figure 4.47 USCUH recorded and modeled first story shear in the transverse and longitudinal directions from the 1992 Landers earthquake (Refer to equations 4.7 and 4.8).

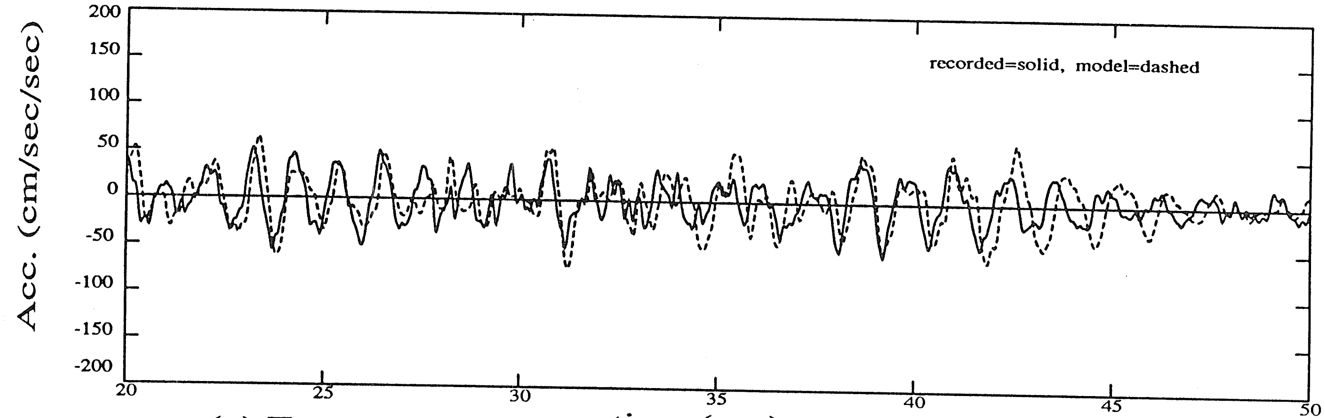

(a) Transverse

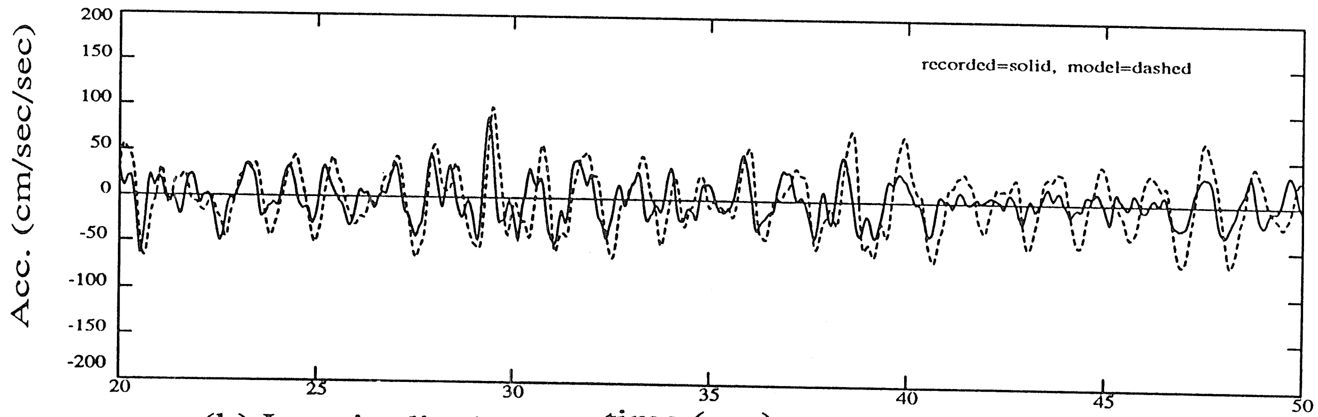

(b) Longitudinal

Figure 4.48 USCUH recorded and modeled roof acceleration in the transverse and longitudinal directions from the 1992 Landers earthquake.

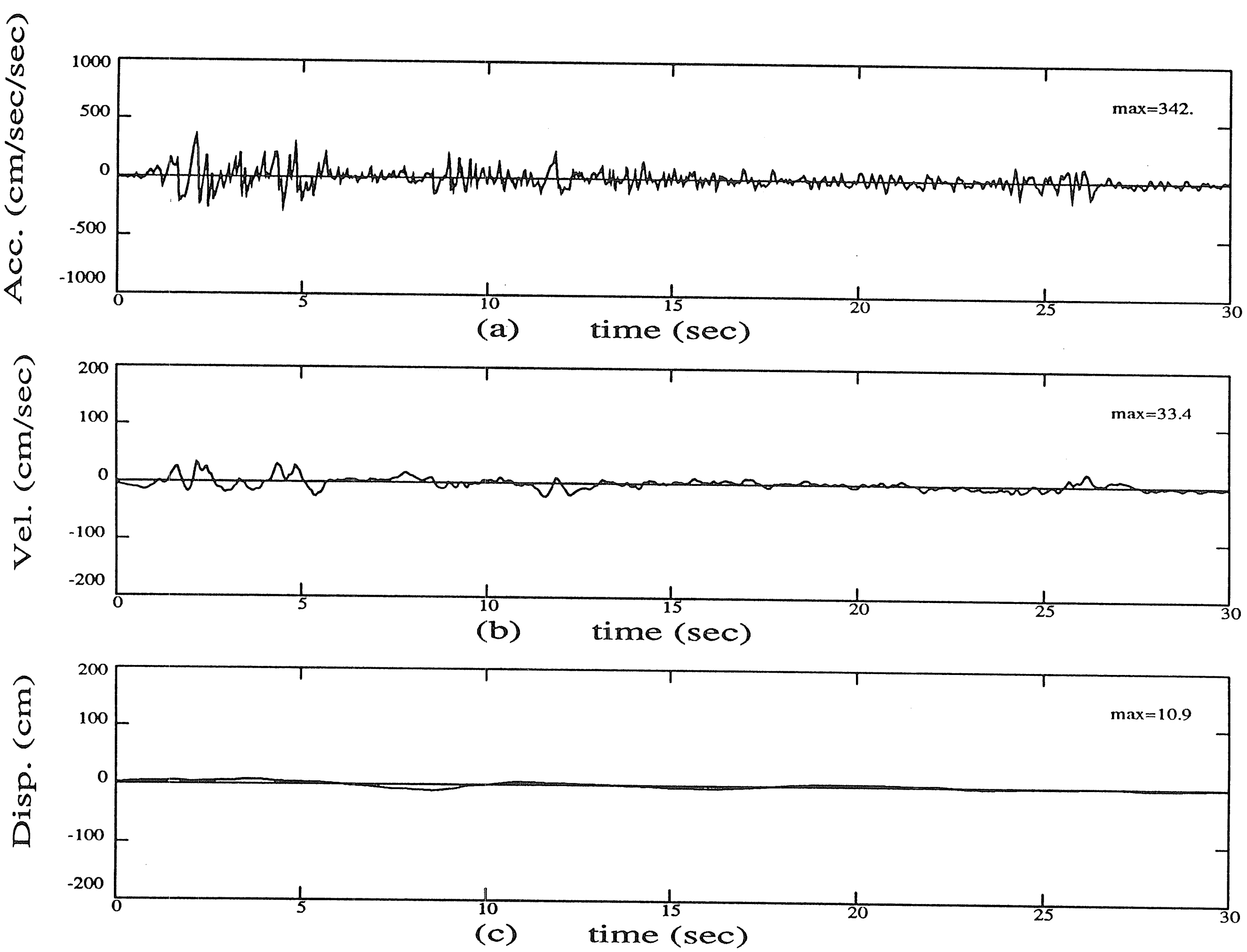

Figure 6.1 El Centro N-S component from the 1940 Imperial Valley earthquake [Hudson *et al.*, 1976].

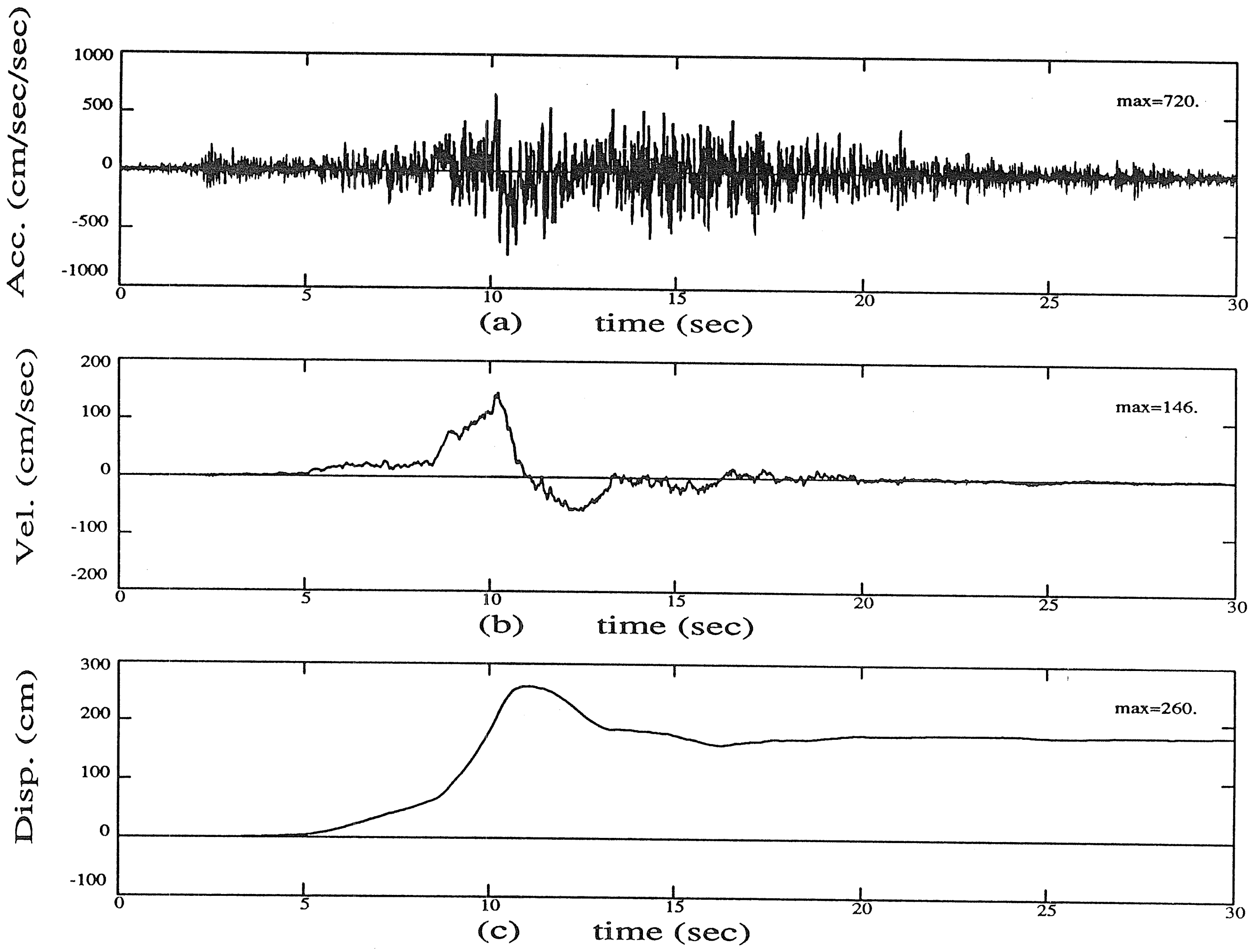

Figure 6.2 Lucerne Valley transverse (N-S) component from the 1992 Landers earthquake [Chen, 1995].

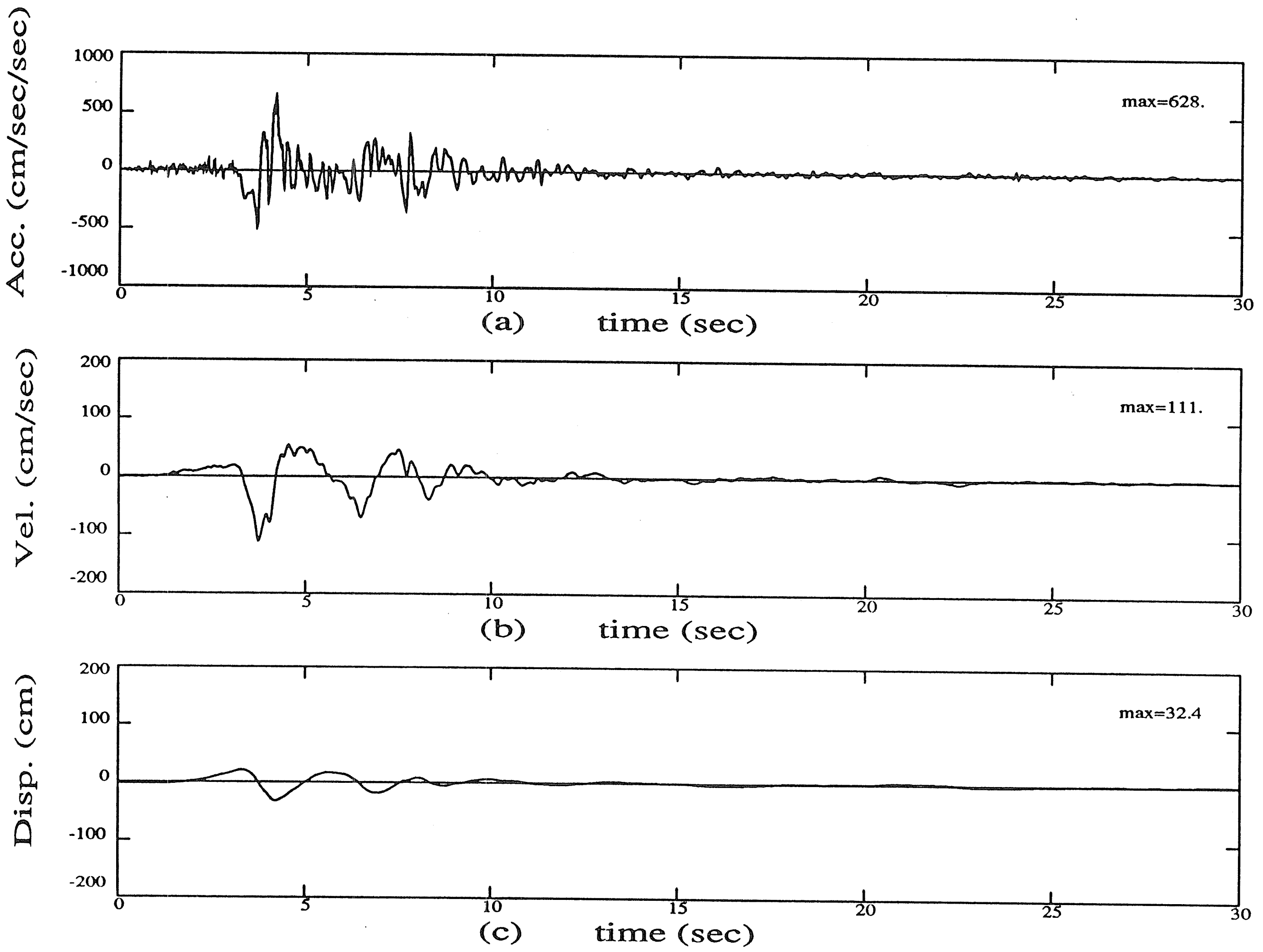

Figure 6.3 Sylmar County Hospital parking lot free field N43E component from the 1994 Northridge earthquake [Darragh *et al.*, 1994].

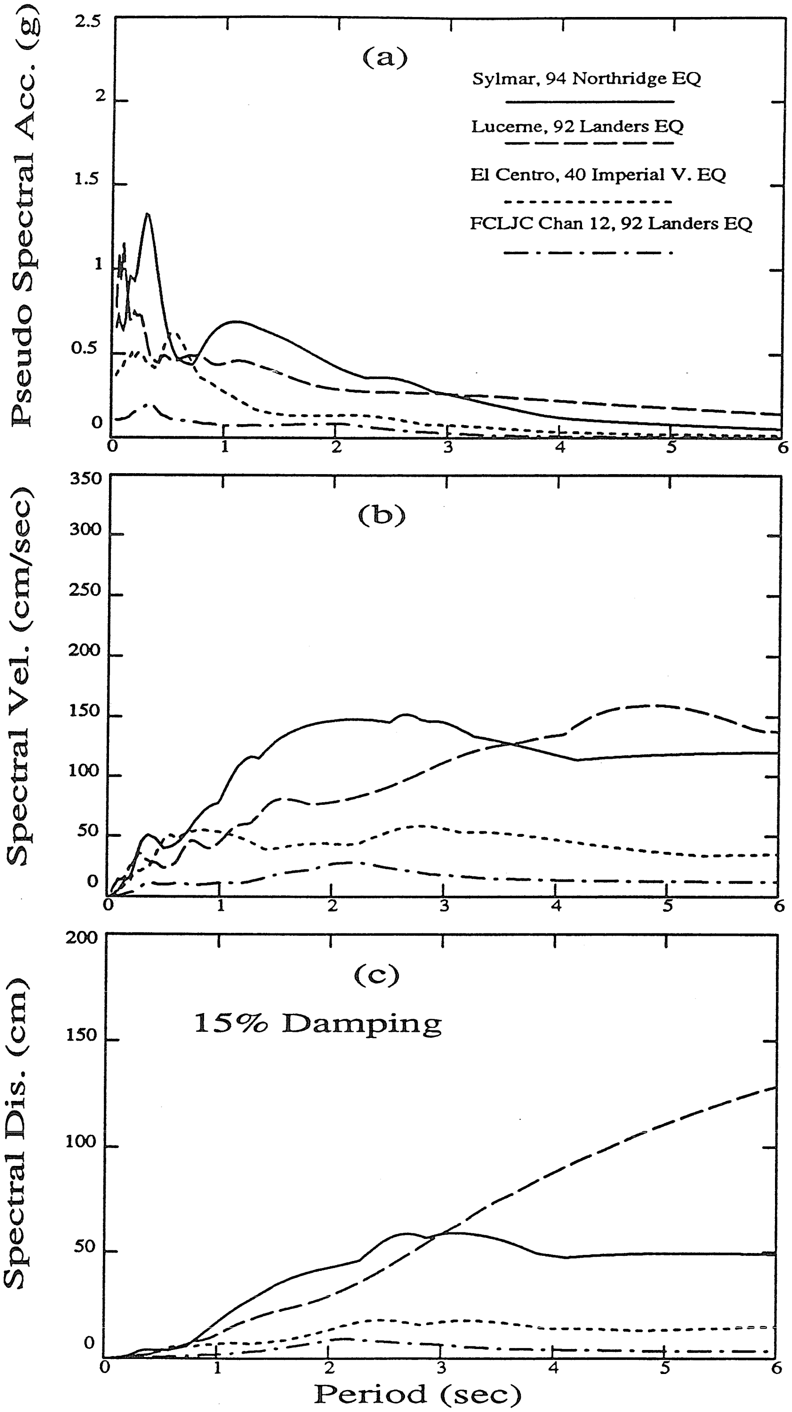

Figure 6.4 Spectral acceleration, velocity, and displacement for the El Centro, Lucerne, Sylmar County Hosp., and FCLJC transverse foundation (channel 12) record from the Landers earthquake.

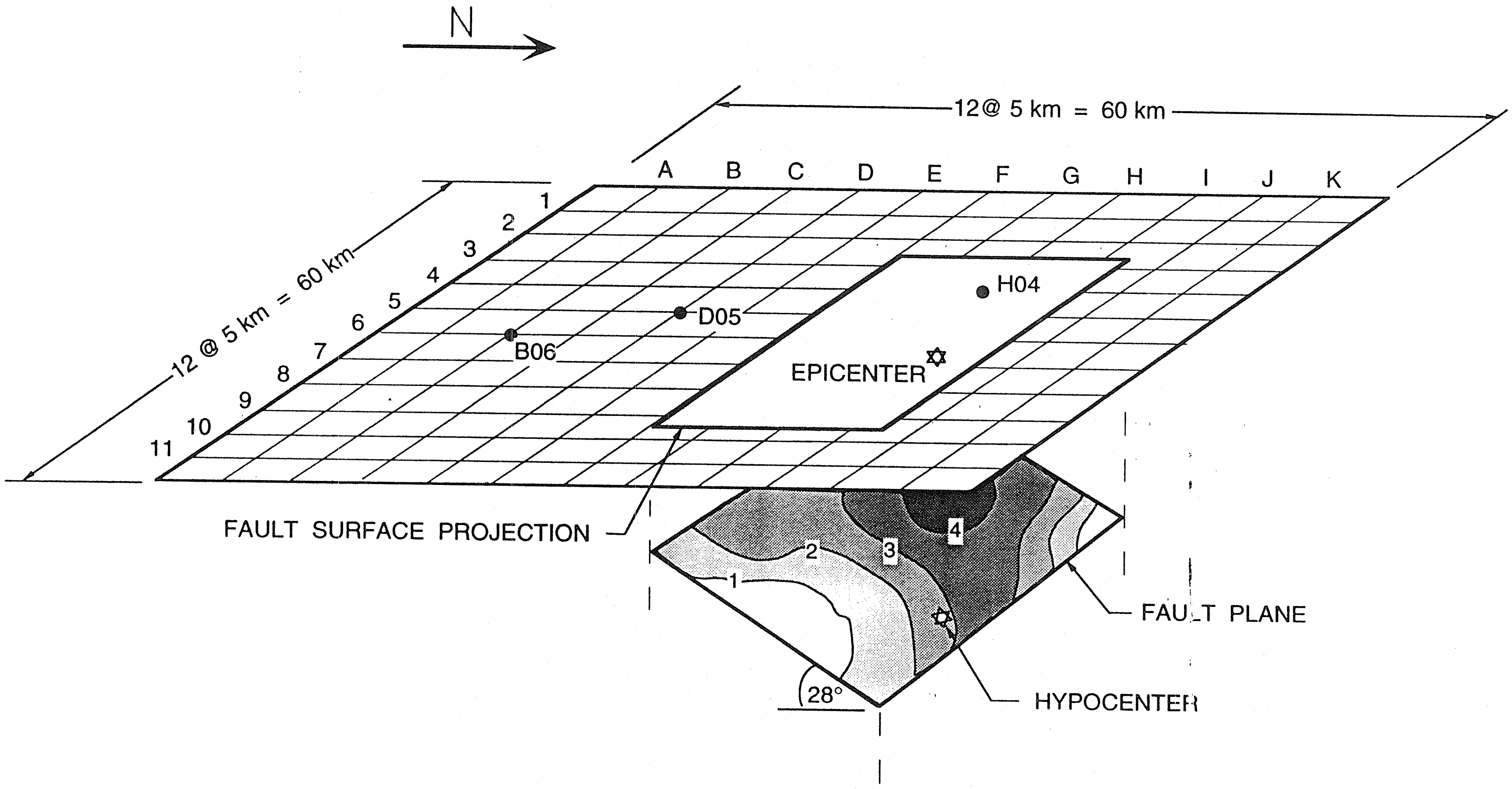

Figure 6.5 Diagram showing the hypothetical fault plane, locations of the 121 stations relative to the fault, contours of the modeled slip distribution, and the location of the hypocenter.

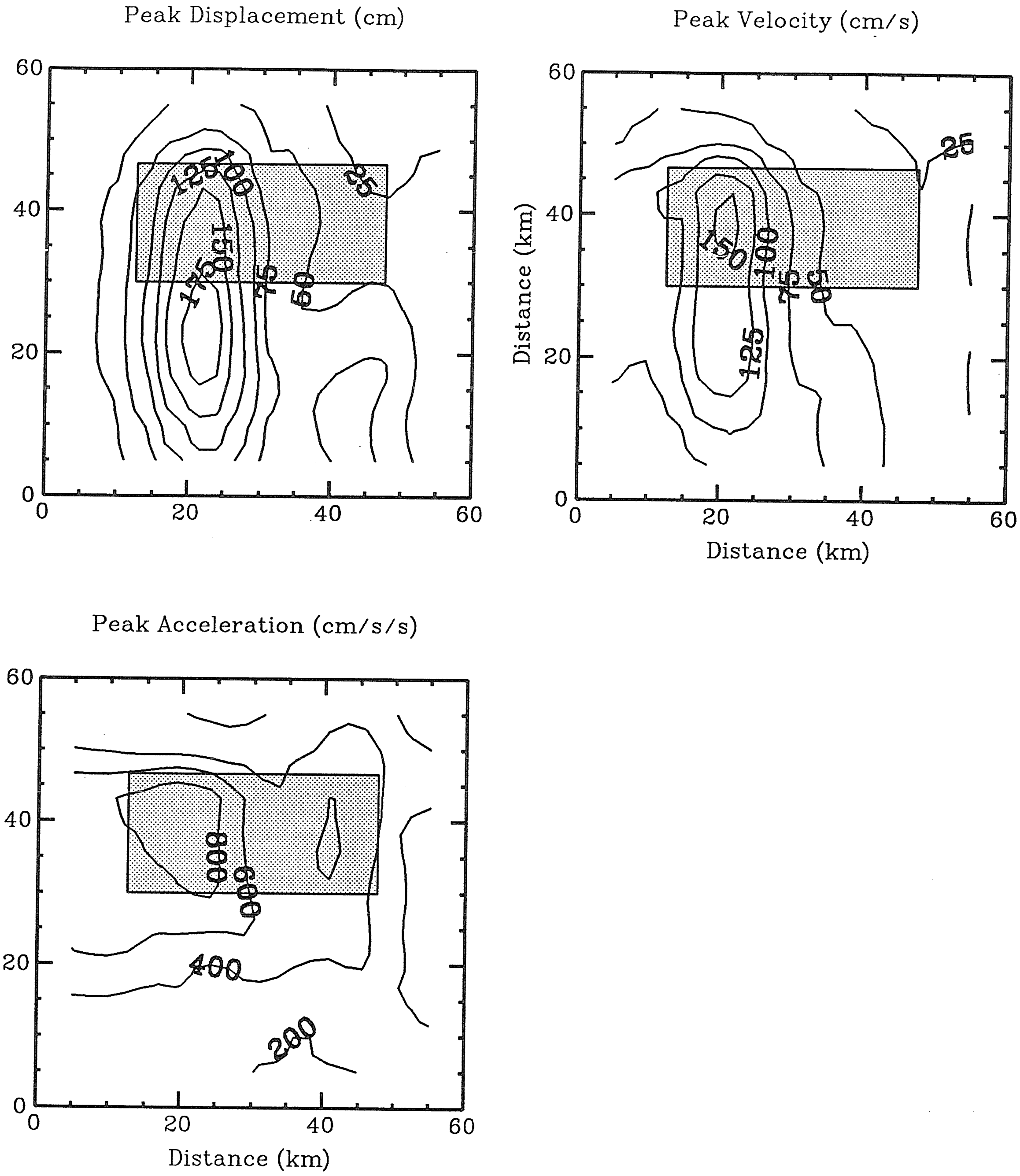

Figure 6.6 Contours of peak ground displacement, velocity, and acceleration along the rotation directions.

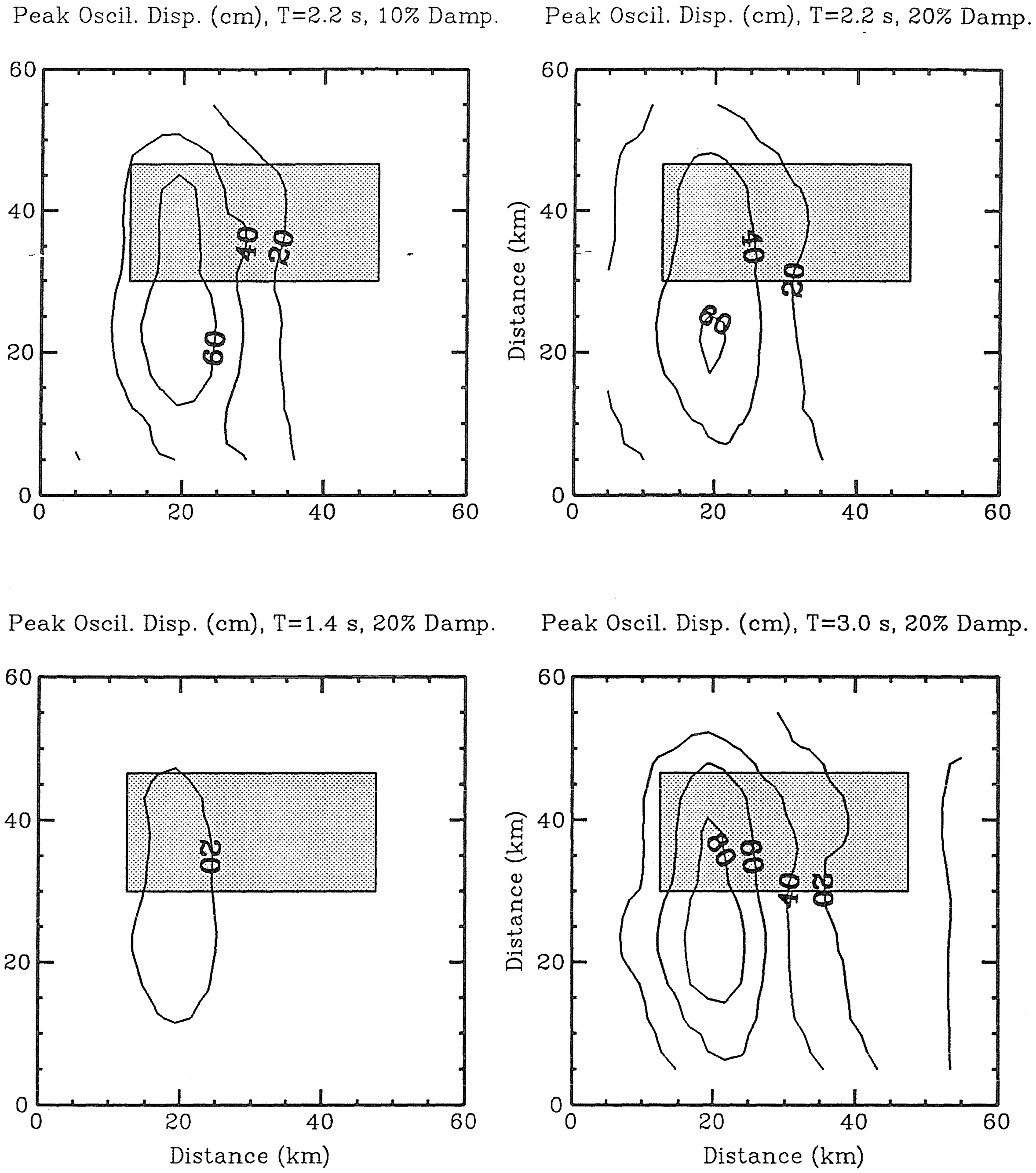
Peak Oscil. Disp. (cm), T=2.2 s, 10% Damp.

Peak Oscil. Disp. (cm), T=2.2 s, 20% Damp.

Peak Oscil. Disp. (cm), T=1.4 s, 20% Damp.

Peak Oscil. Disp. (cm), T=3.0 s, 20% Damp.

Figure 6.7 Contours of peak single-degree-of-freedom (SDOF) oscillator displacements for periods and viscous damping values of 2.2 sec and 10%, 2.2 sec and 20%, 1.4 sec and 20%, and 3.0 sec and 20% along the rotation directions.

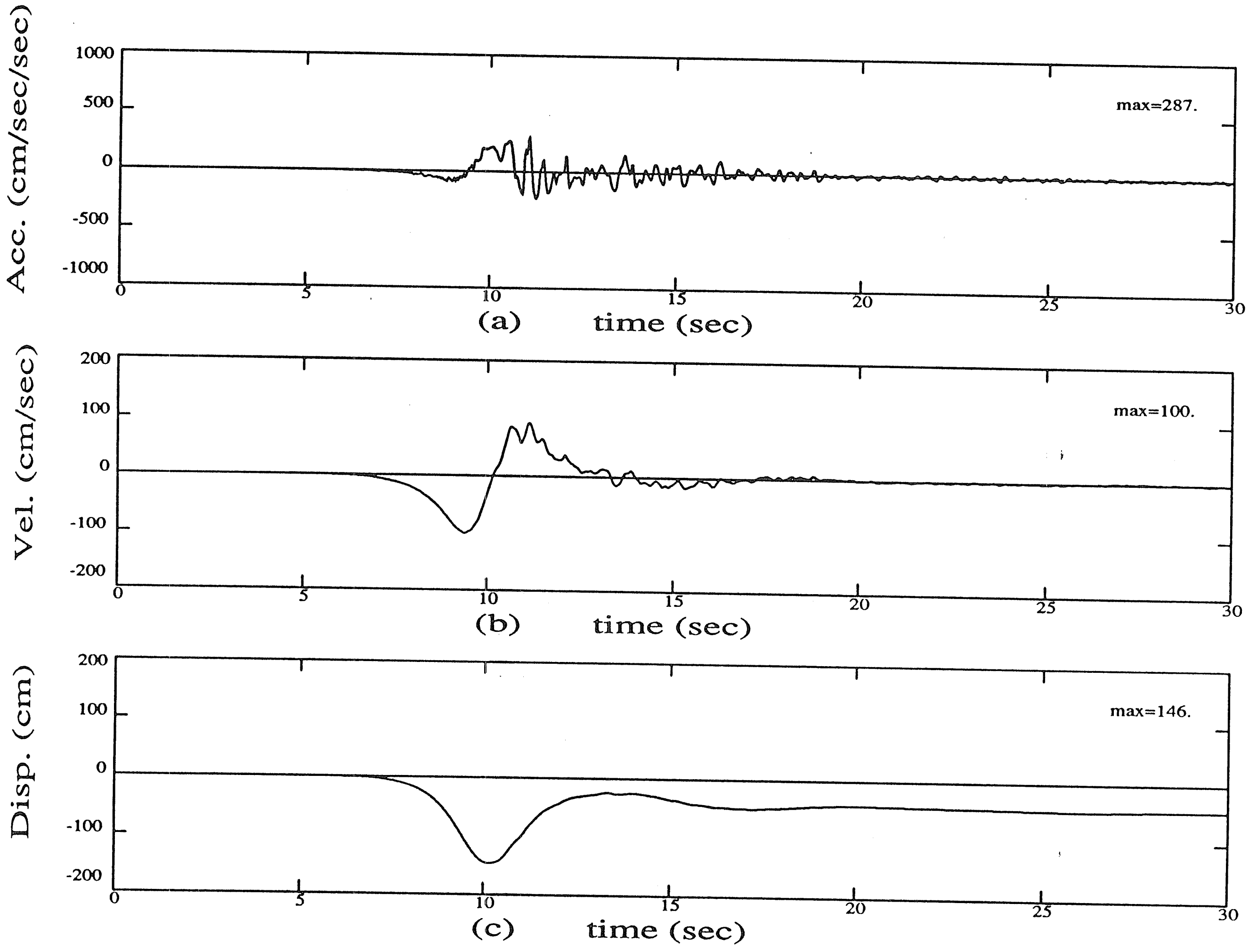

Figure 6.8 Synthetic motion B06 N69E time history.

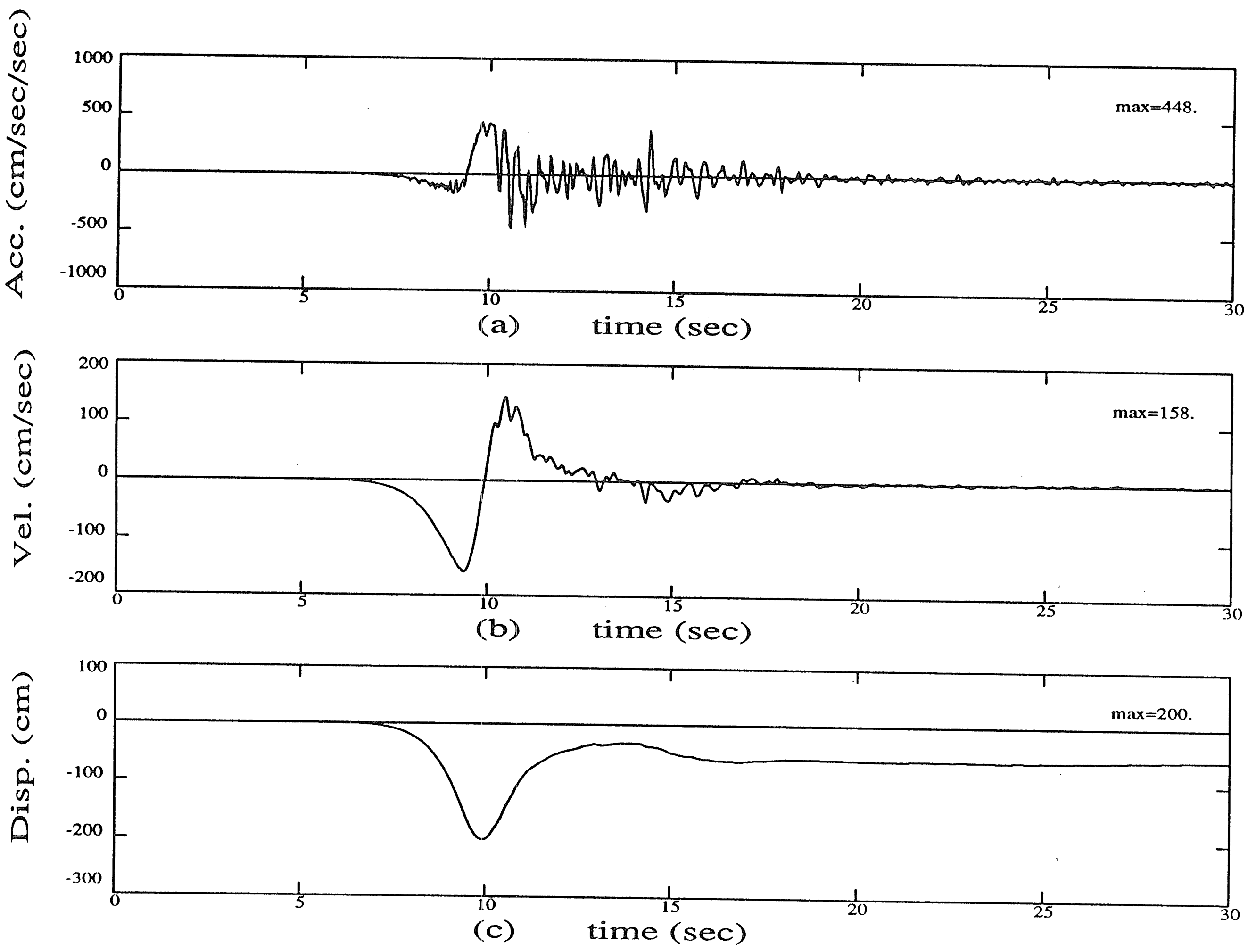

Figure 6.9 Synthetic motion D05 N17E time history.

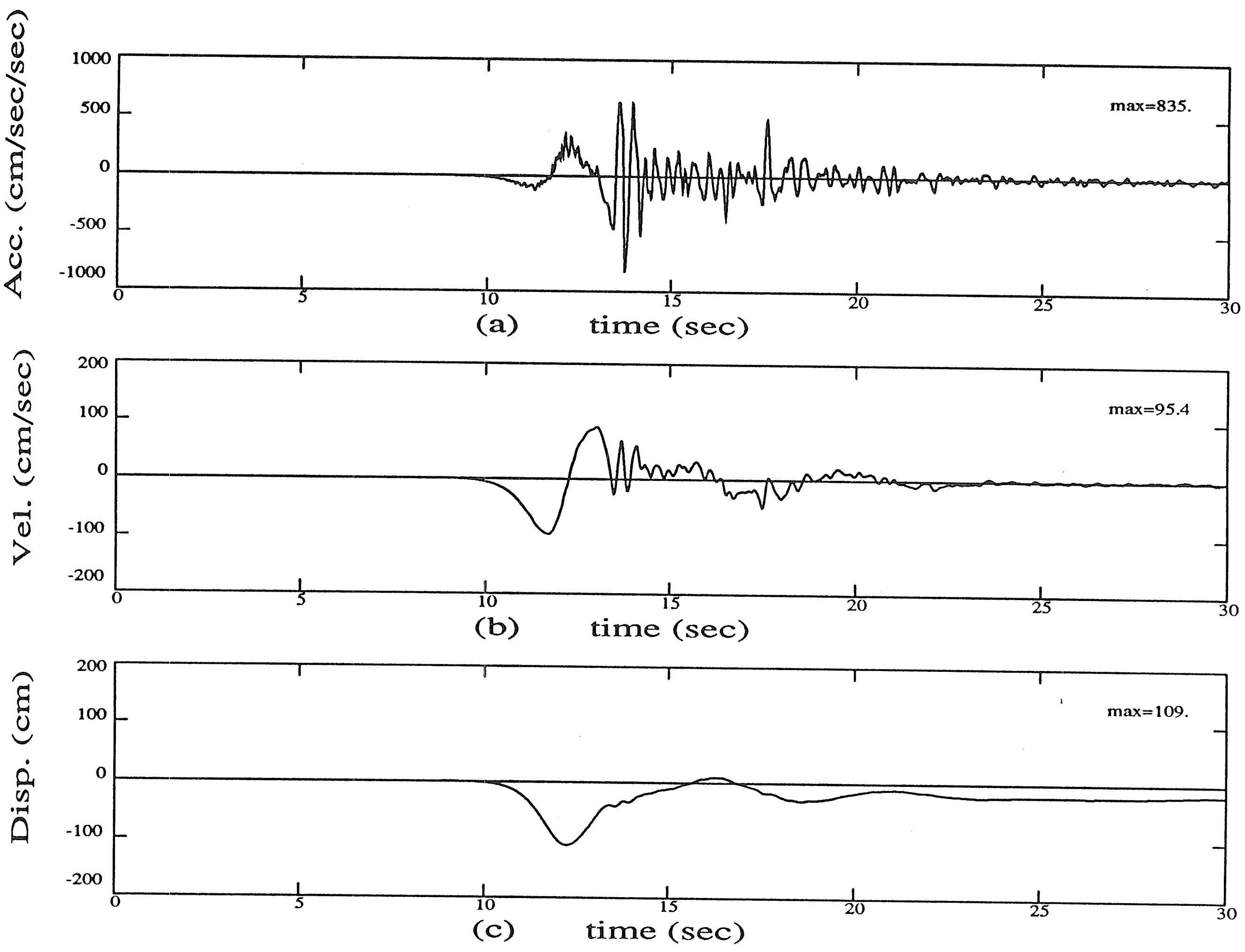

Figure 6.10 Synthetic motion H04 N24W time history.

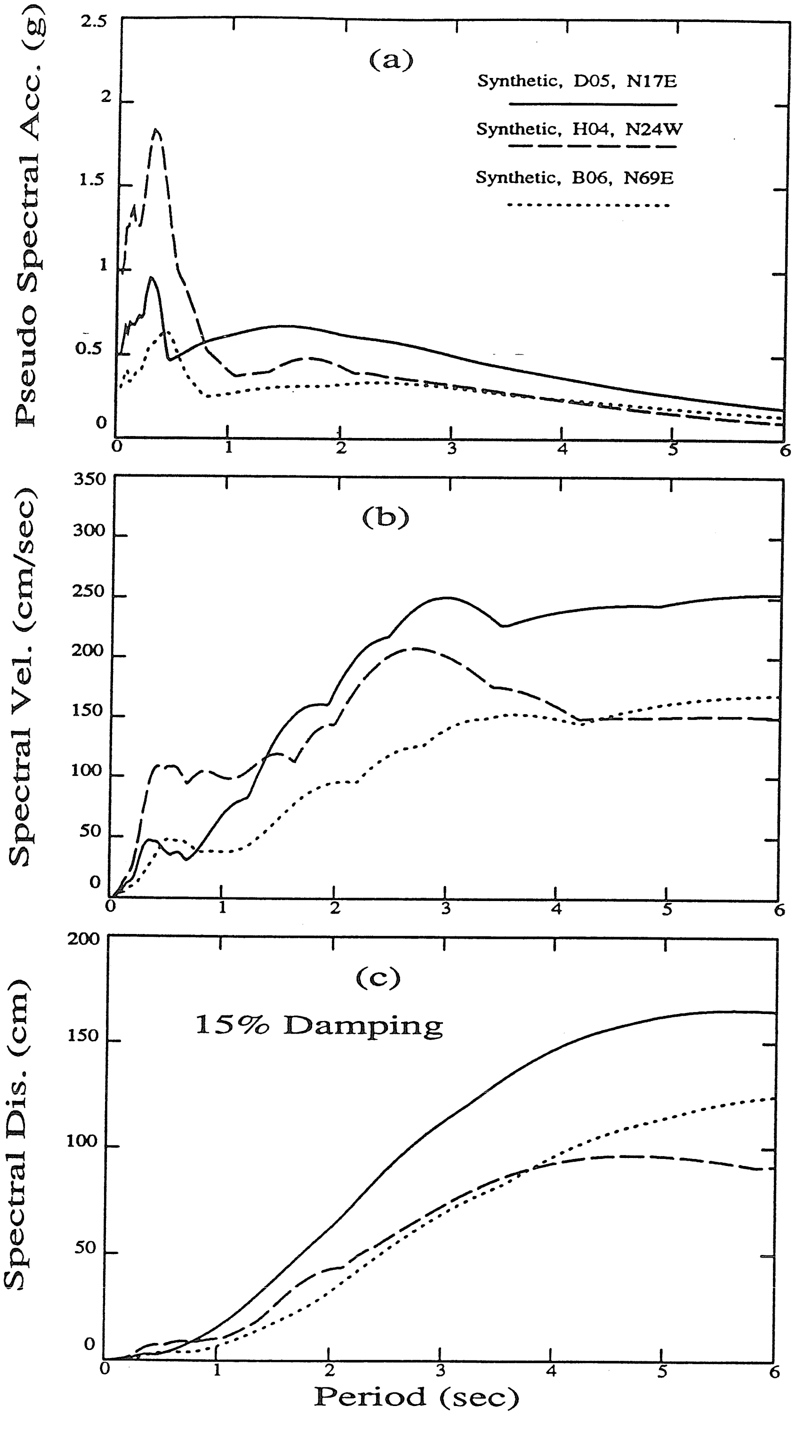

Figure 6.11 Spectral acceleration, velocity, and displacement for the B06 N69E, D05 N17E, and H04 N24W records.

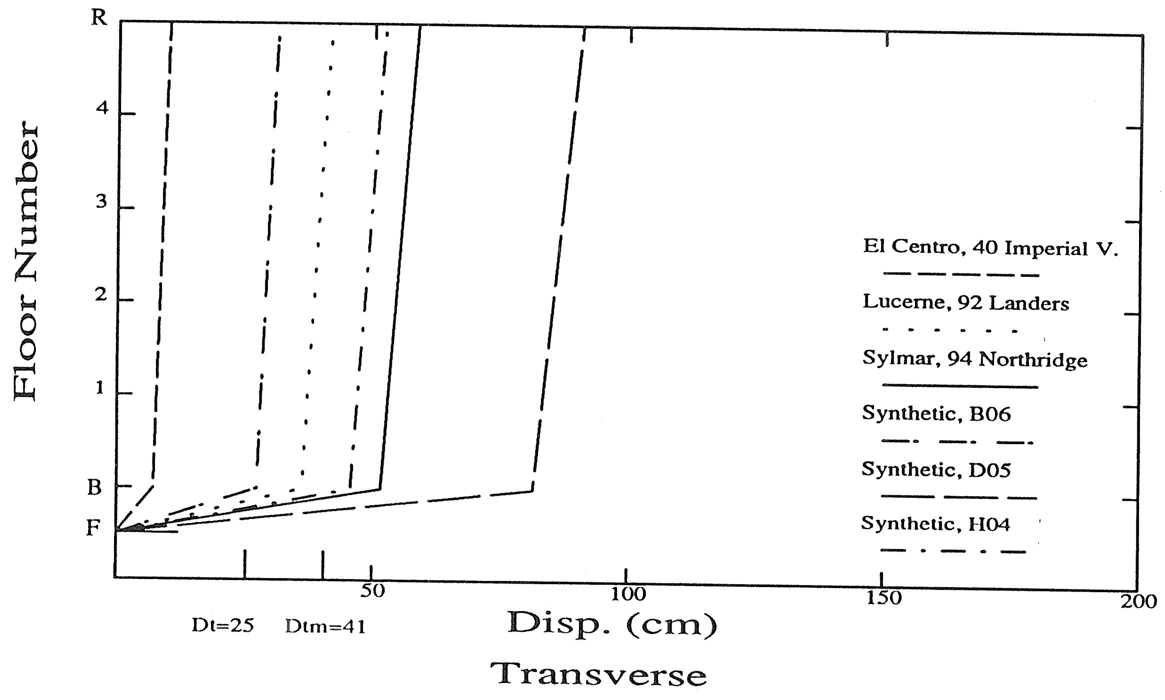

Figure 6.12 FCLJC model peak floor displacements when subjected to near-source ground motions (i.e., El Centro, Lucerne, Sylmar, B06, D05, H04).

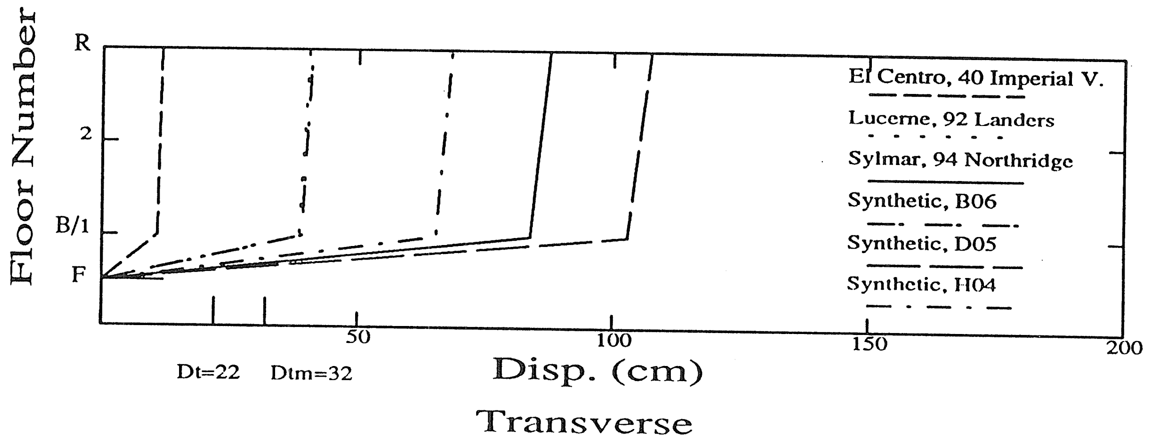

Figure 6.13 FCCF model peak floor displacements when subjected to near-source ground motions (i.e., El Centro, Lucerne, Sylmar, B06, D05, H04).

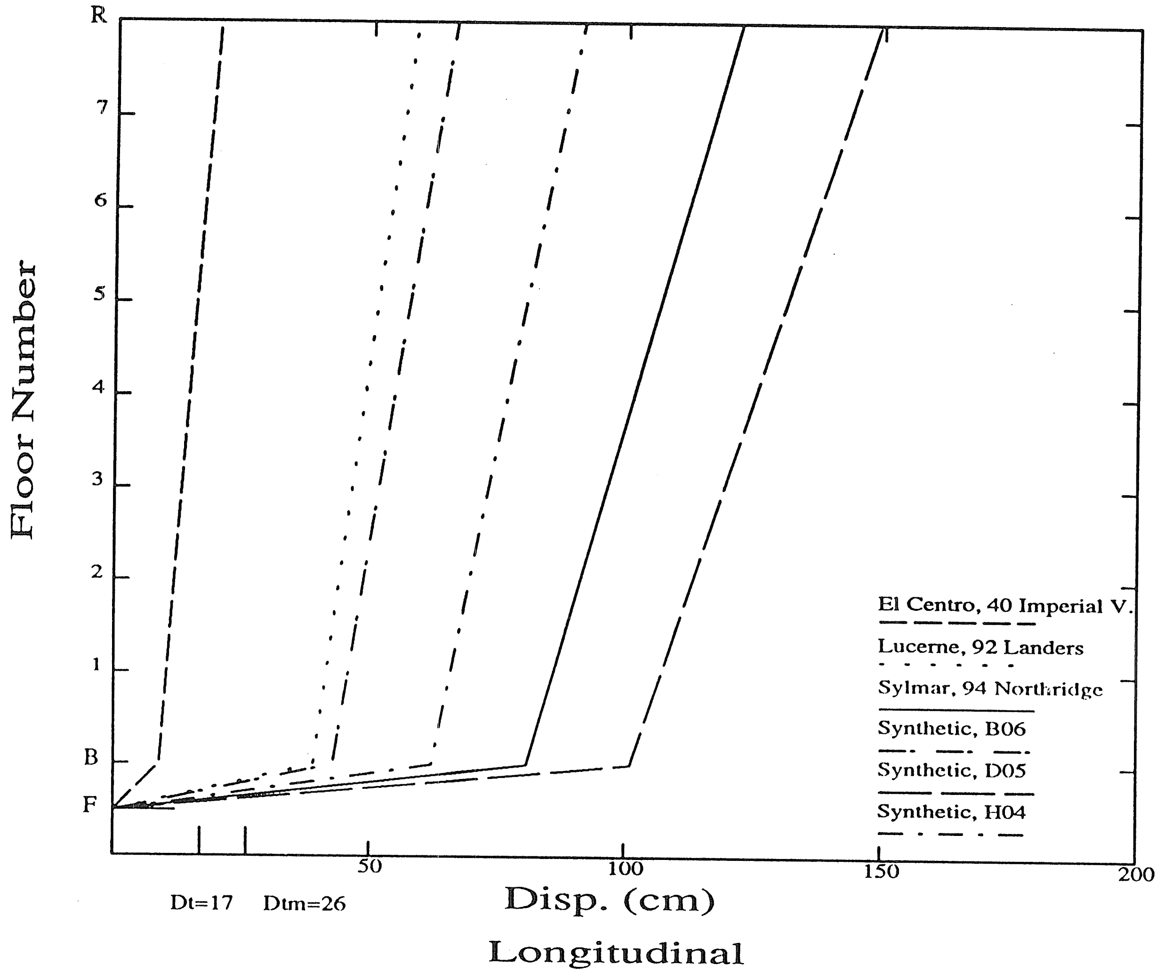

Figure 6.14 USCUH model peak floor displacements when subjected to near-source ground motions (i.e., El Centro, Lucerne, Sylmar, B06, D05, H04).

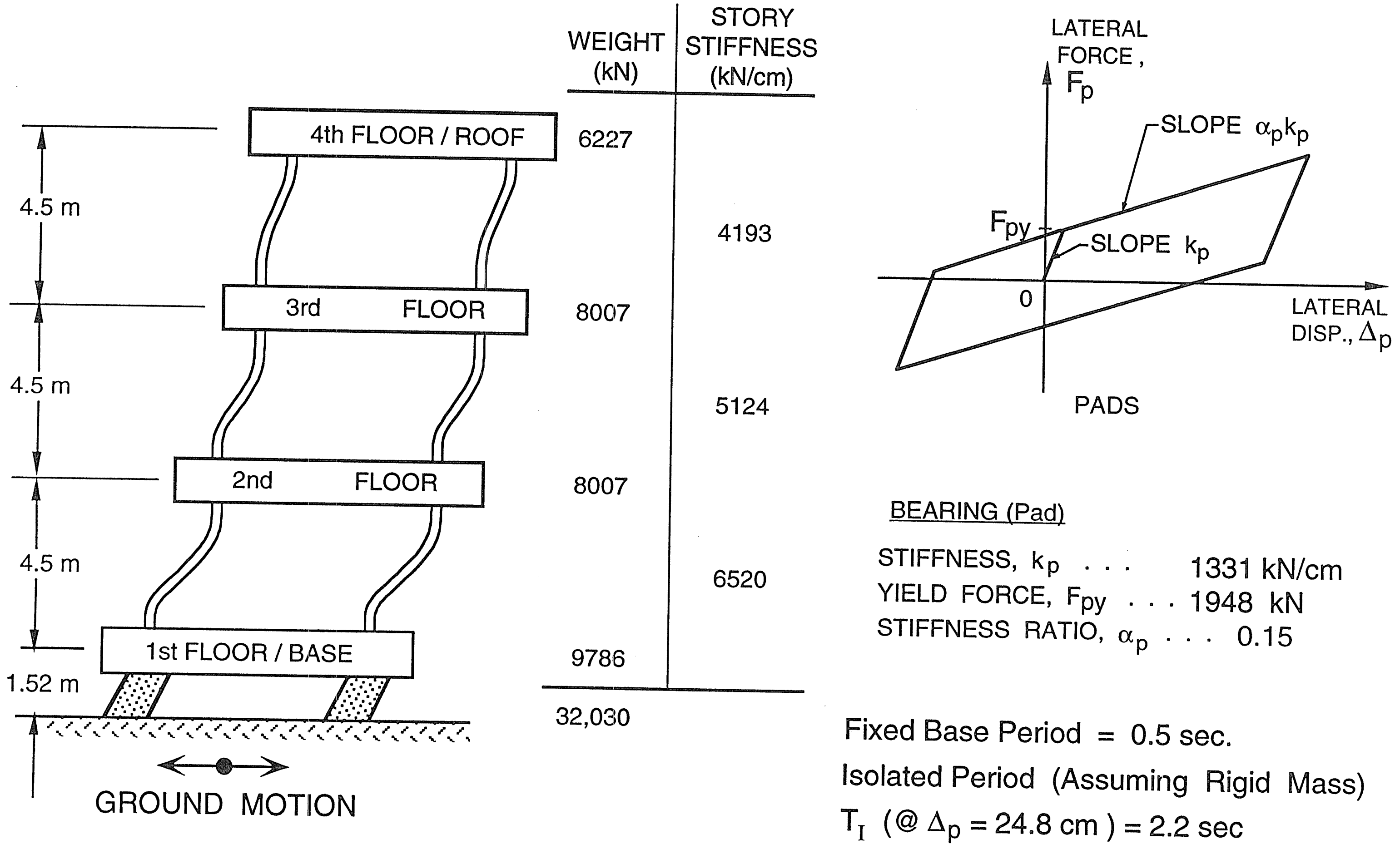

Figure 7.1 Typical base-isolated building (TBIB) model.

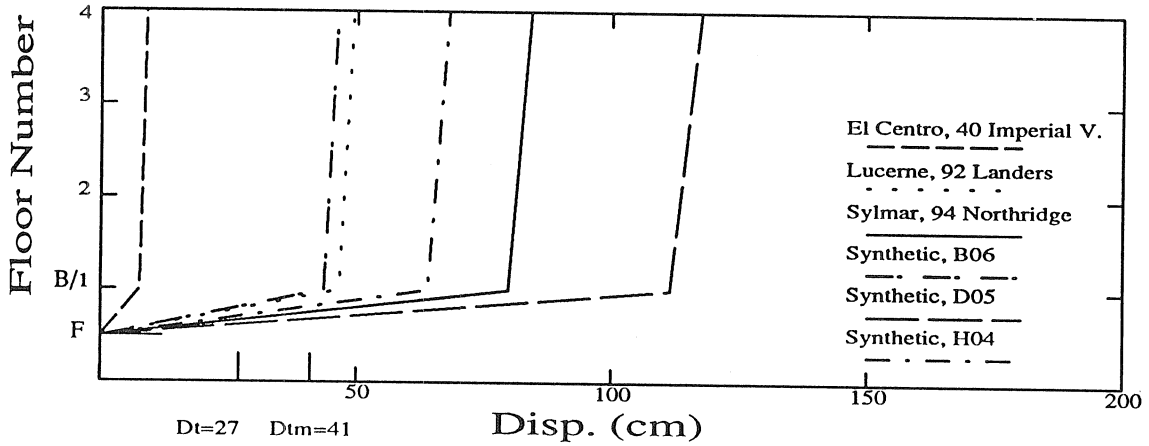

Figure 7.2 TBIB model peak floor displacements when subjected to near-source ground motions (i.e., El Centro, Lucerne, Sylmar, B06, D05, H04).

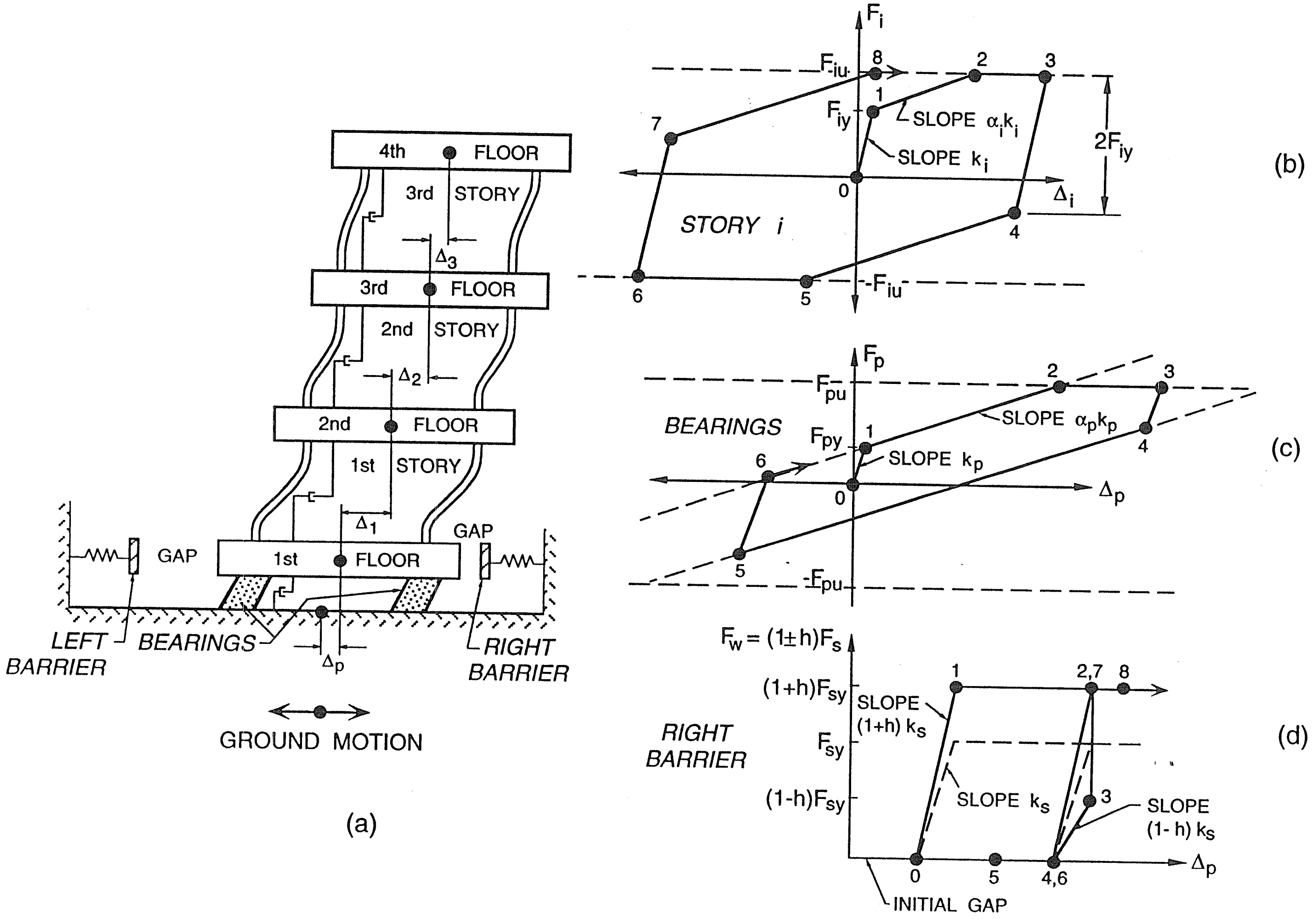

Figure 7.3 Idealized three-story building (TBIB) analyzed using 2D-BUMP (figure a). Shown are the force-displacement relationships for each story, i, of the building (figure b), for all the isolation bearings taken together (figure c), and for the right barrier (figure d). The relationship for the left barrier is similar to the right. The values for all the parameters are presented in table 7.2.

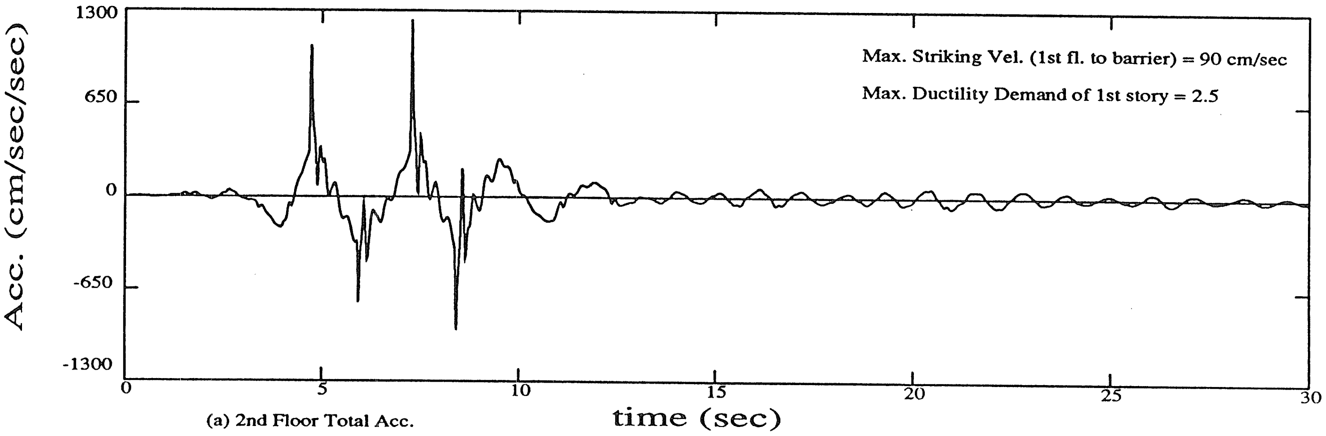

(a) 2nd Floor Total Acc.

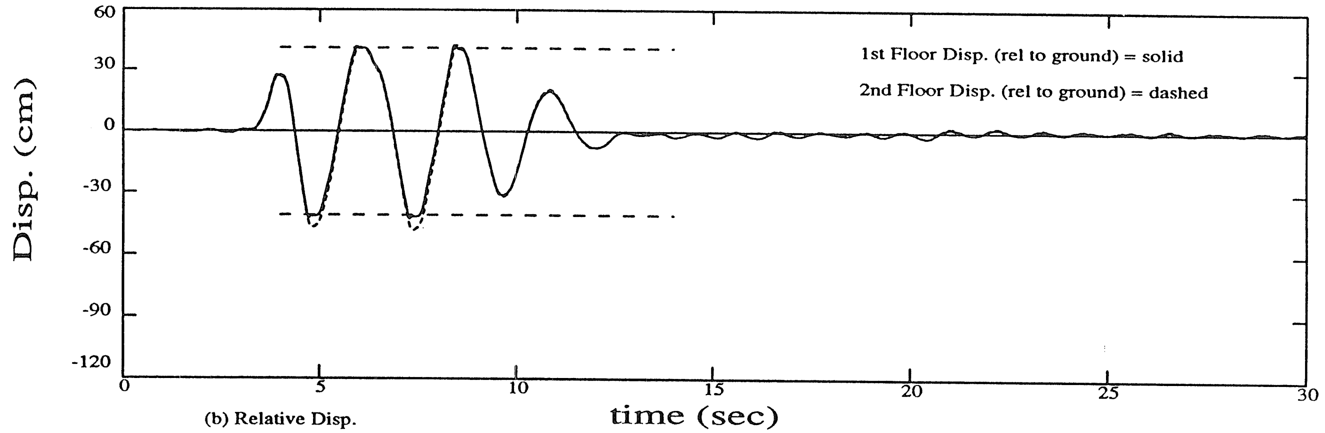

(b) Relative Disp.

Figure 7.4 **TBIB-model 1** second floor acceleration and the first and second floor displacement histories (relative to the foundation) using the **Sylmar** County Hosp. free field record as the excitation. Also given are the maximum striking velocity and the maximum ductility demand of the first story.

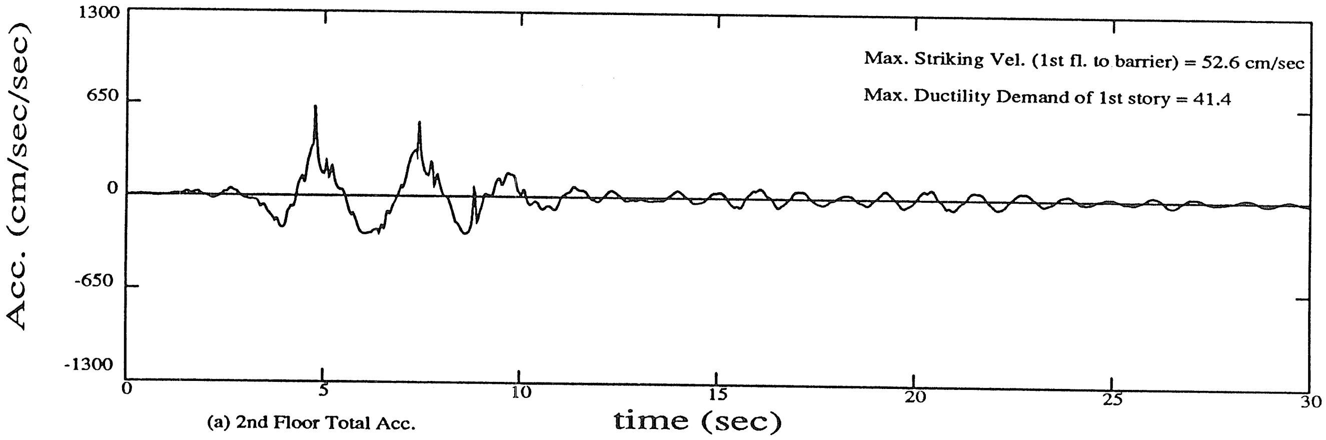

(a) 2nd Floor Total Acc.

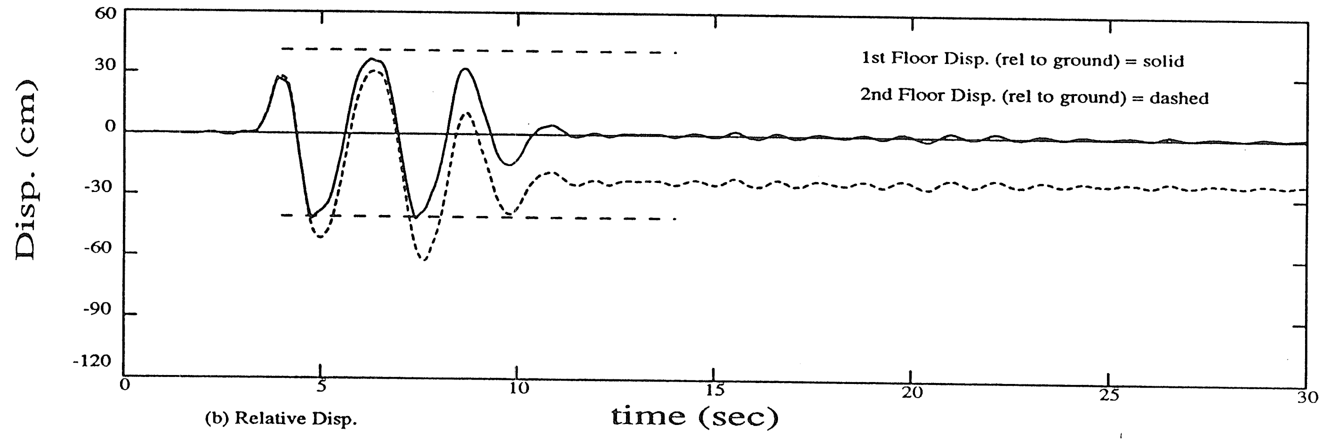

(b) Relative Disp.

Figure 7.5 **TBIB-model 2** second floor acceleration and the first and second floor displacement histories (relative to the foundation) using the **Sylmar** County Hosp. free field record as the excitation. Also given are the maximum striking velocity and the maximum ductility demand of the first story.

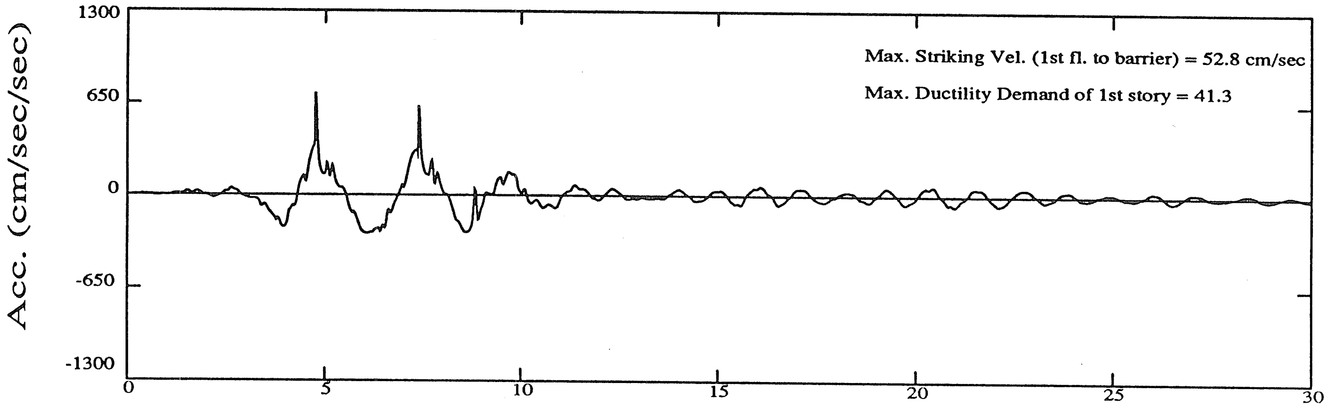

(a) 2nd Floor Total Acc.

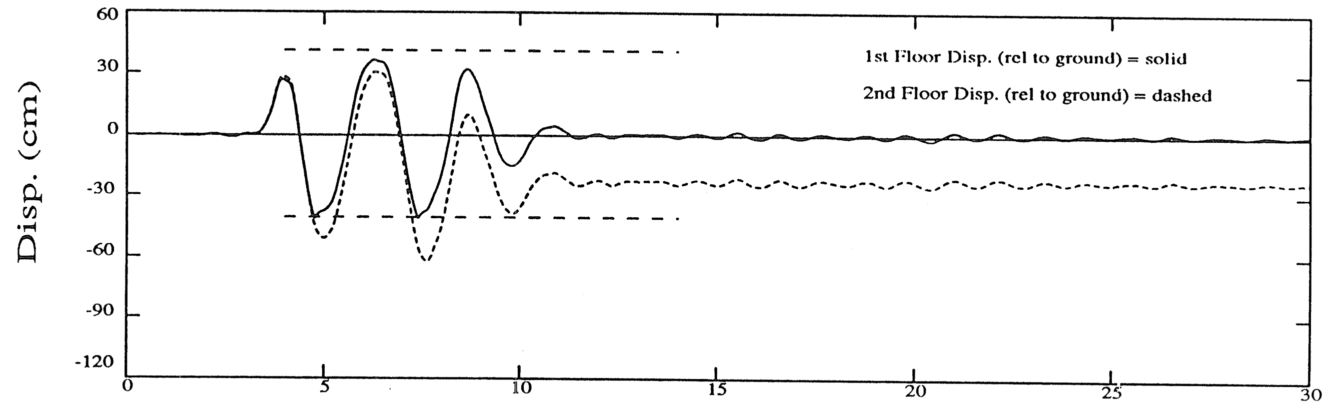

(b) Relative Disp.

Figure 7.6 TBIB-**model 3** second floor acceleration and the first and second floor displacement histories (relative to the foundation) using the **Sylmar** County Hosp. free field record as the excitation. Also given are the maximum striking velocity and the maximum ductility demand of the first story.

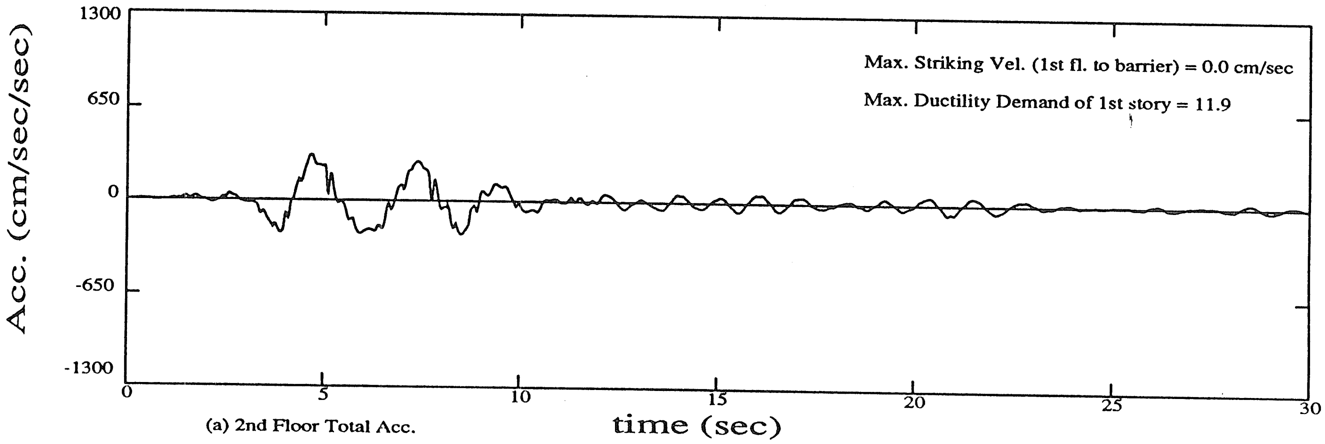

(a) 2nd Floor Total Acc.

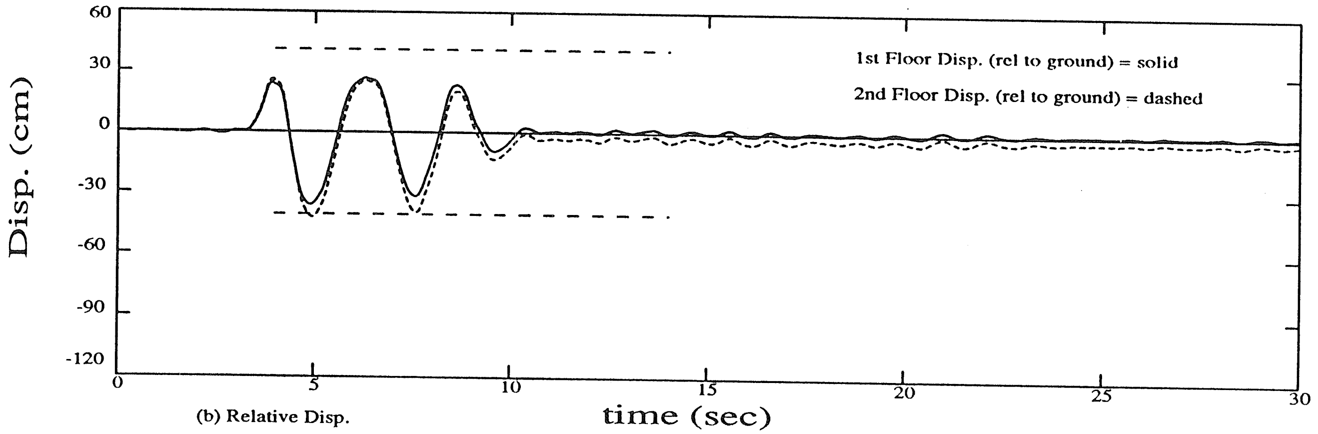

(b) Relative Disp.

Figure 7.7 **TBIB-model 4** second floor acceleration and the first and second floor displacement histories (relative to the foundation) using the **Sylmar** County Hosp. free field record as the excitation. Also given are the maximum striking velocity and the maximum ductility demand of the first story.

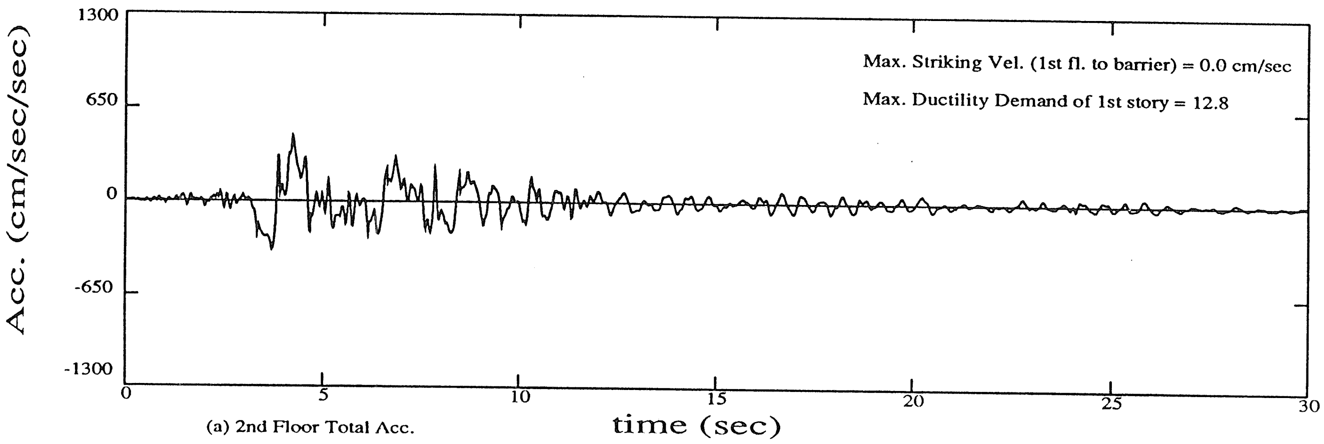

(a) 2nd Floor Total Acc.

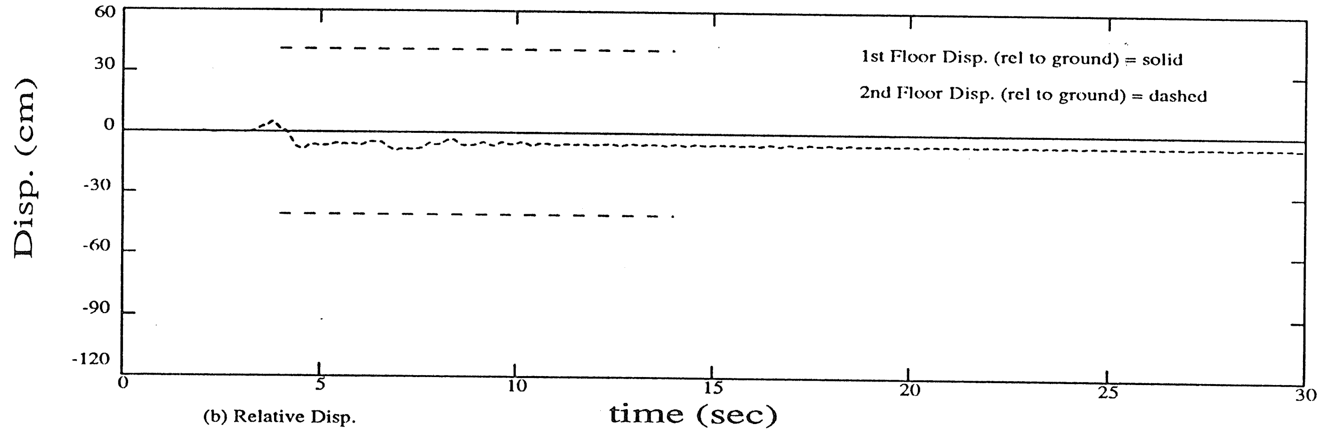

(b) Relative Disp.

Figure 7.8 **TBIB-Fixed-base** second floor acceleration and the first and second floor displacement histories (relative to the foundation) using the **Sylmar** County Hosp. free field record as the excitation. Also given are the maximum striking velocity and the maximum ductility demand of the first story.

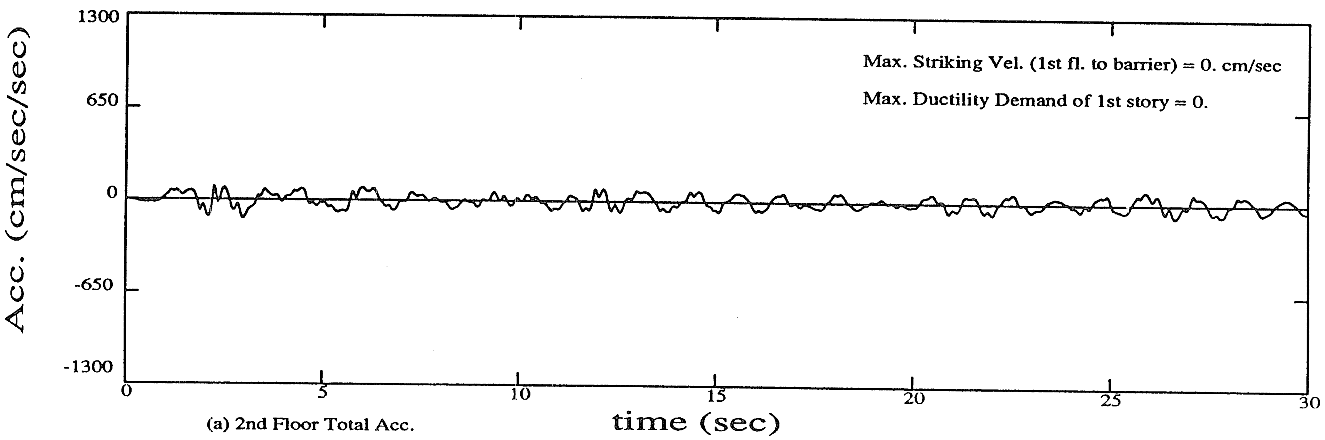

(a) 2nd Floor Total Acc.

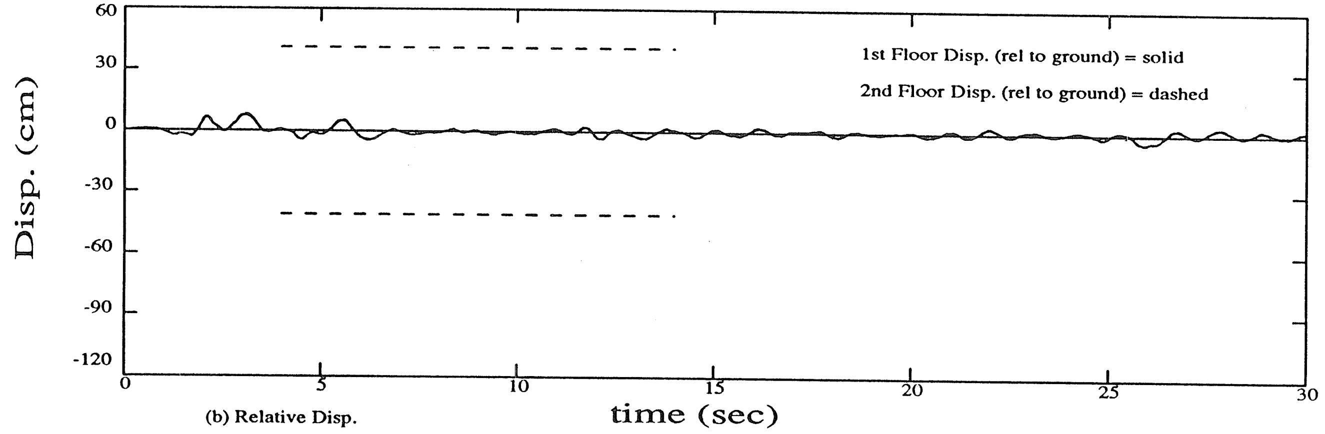

(b) Relative Disp.

Figure 7.9 TBIB-**model 2** second floor acceleration and the first and second floor displacement histories (relative to the foundation) using the **El Centro** record as the excitation. Also given are the maximum striking velocity and the maximum ductility demand of the first story.

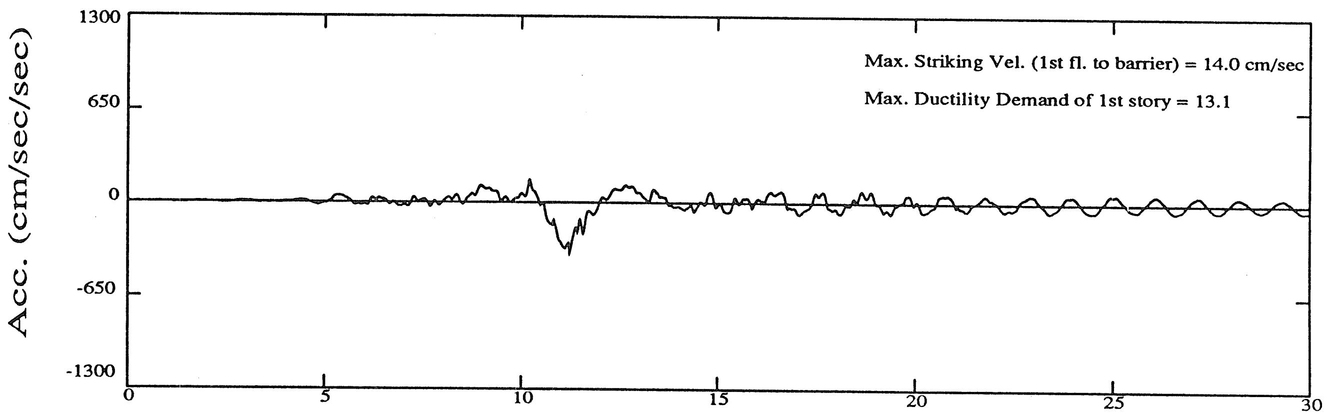

(a) 2nd Floor Total Acc.

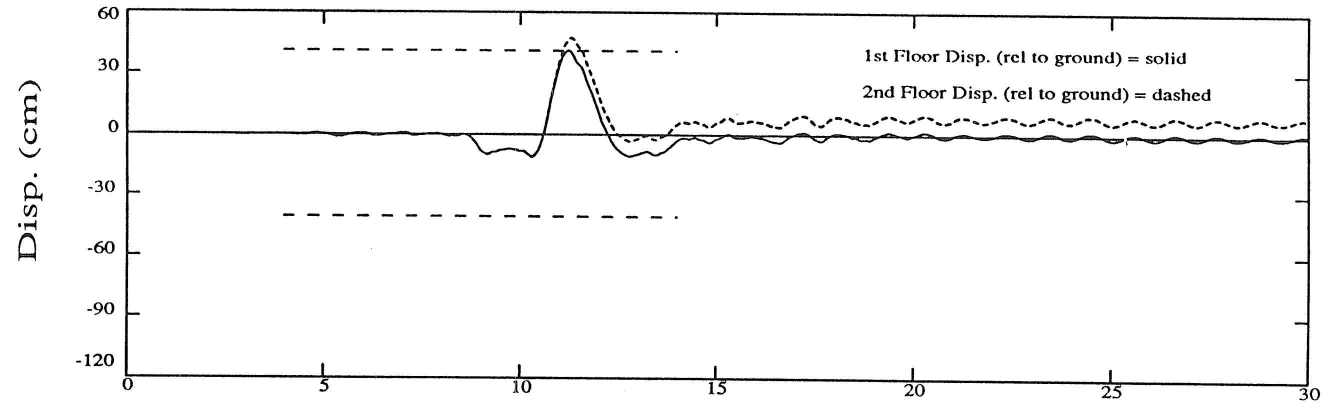

(b) Relative Disp.

Figure 7.10 **TBIB-model 2** second floor acceleration and the first and second floor displacement histories (relative to the foundation) using the **Lucerne** record as the excitation. Also given are the maximum striking velocity and the maximum ductility demand of the first story.

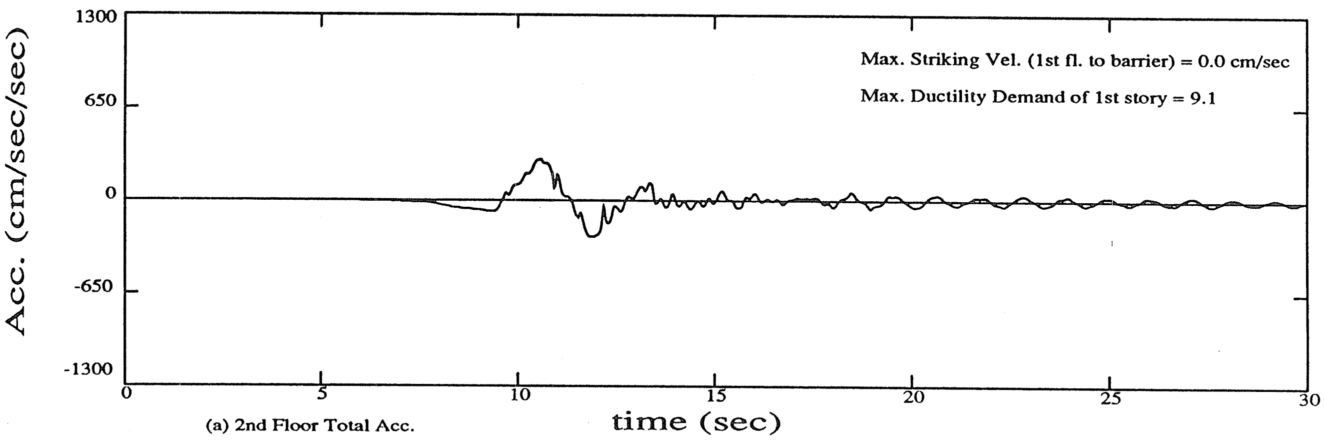

(a) 2nd Floor Total Acc.

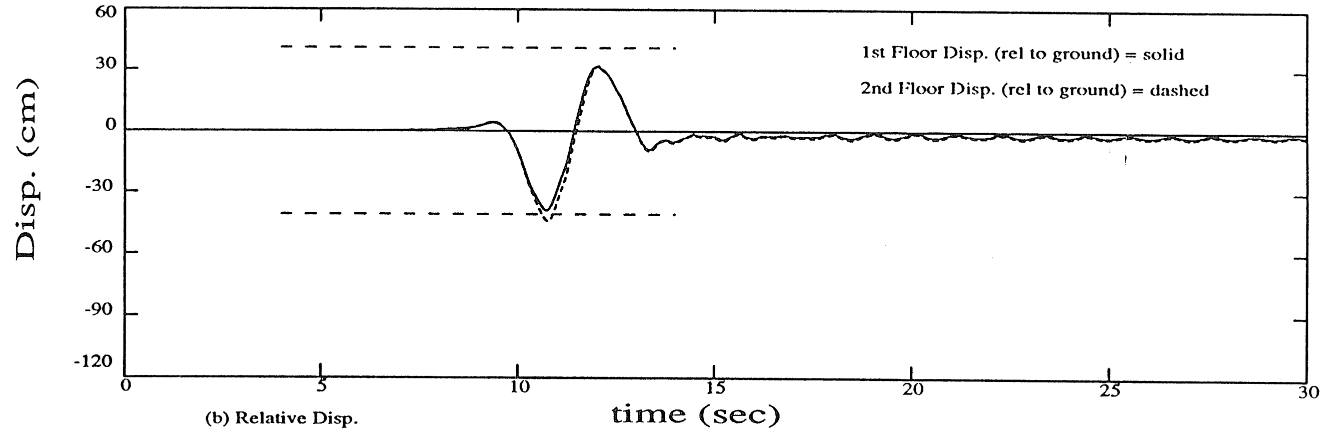

(b) Relative Disp.

Figure 7.11 **TBIB-model 2** second floor acceleration and the first and second floor displacement histories (relative to the foundation) using the **B06** record as the excitation. Also given are the maximum striking velocity and the maximum ductility demand of the first story.

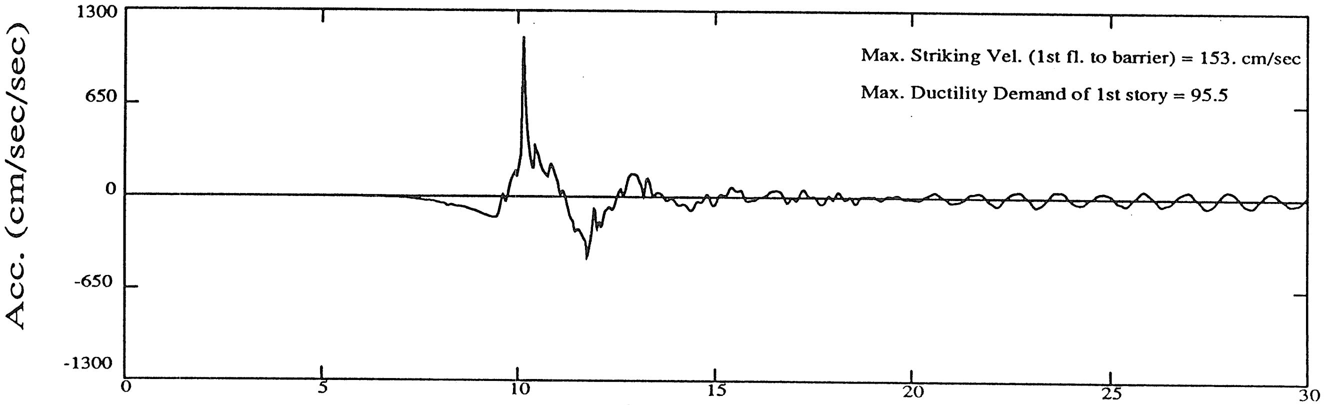

(a) 2nd Floor Total Acc. time (sec)

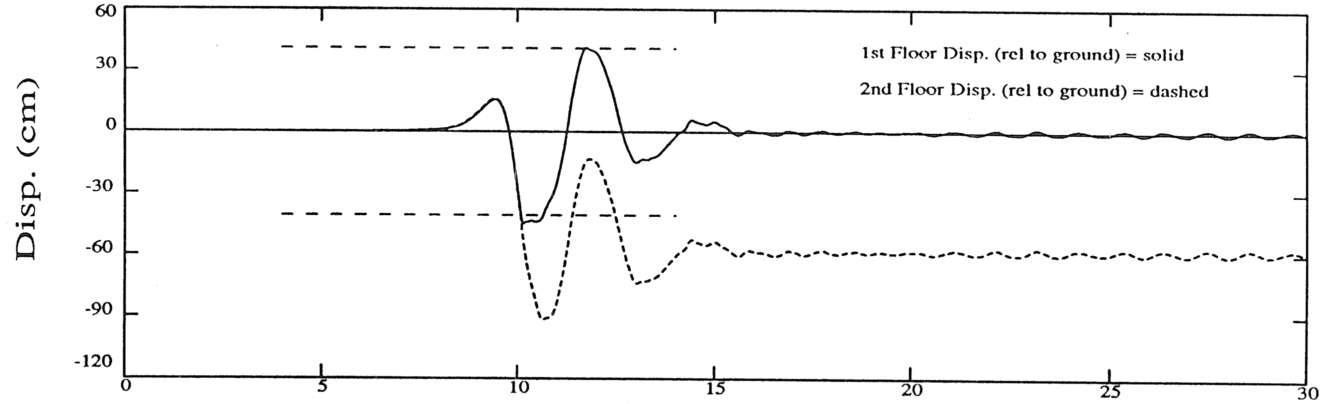

(b) Relative Disp. time (sec)

Figure 7.12 **TBIB-model 2** second floor acceleration and the first and second floor displacement histories (relative to the foundation) using the **D05** record as the excitation. Also given are the maximum striking velocity and the maximum ductility demand of the first story.

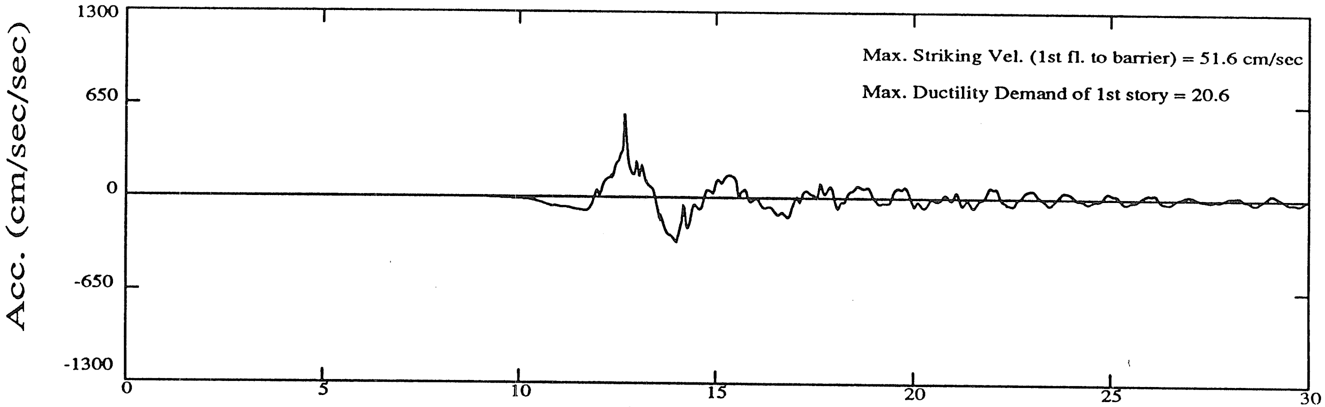

(a) 2nd Floor Total Acc.

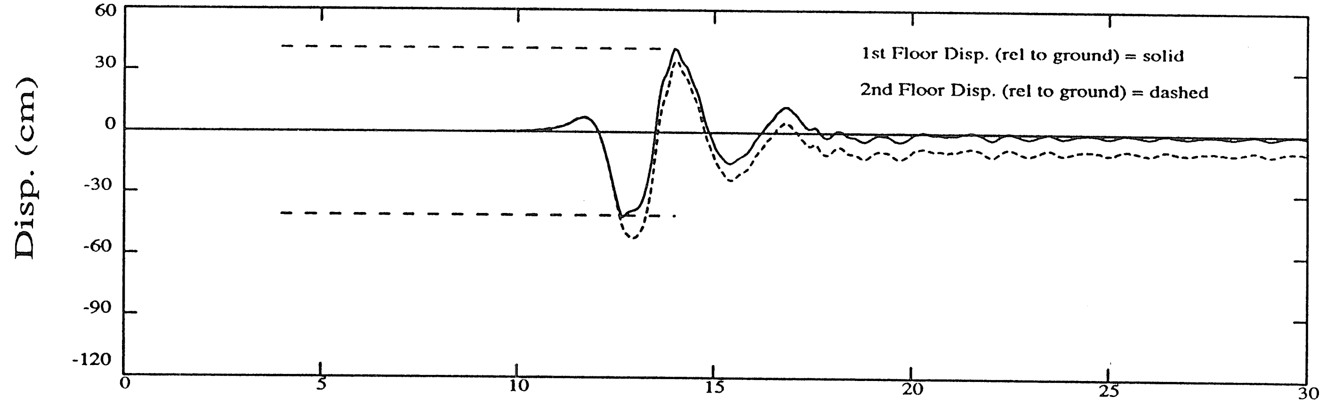

(b) Relative Disp.

Figure 7.13 **TBIB-model 2** second floor acceleration and the first and second floor displacement histories (relative to the foundation) using the **H04** record as the excitation. Also given are the maximum striking velocity and the maximum ductility demand of the first story.

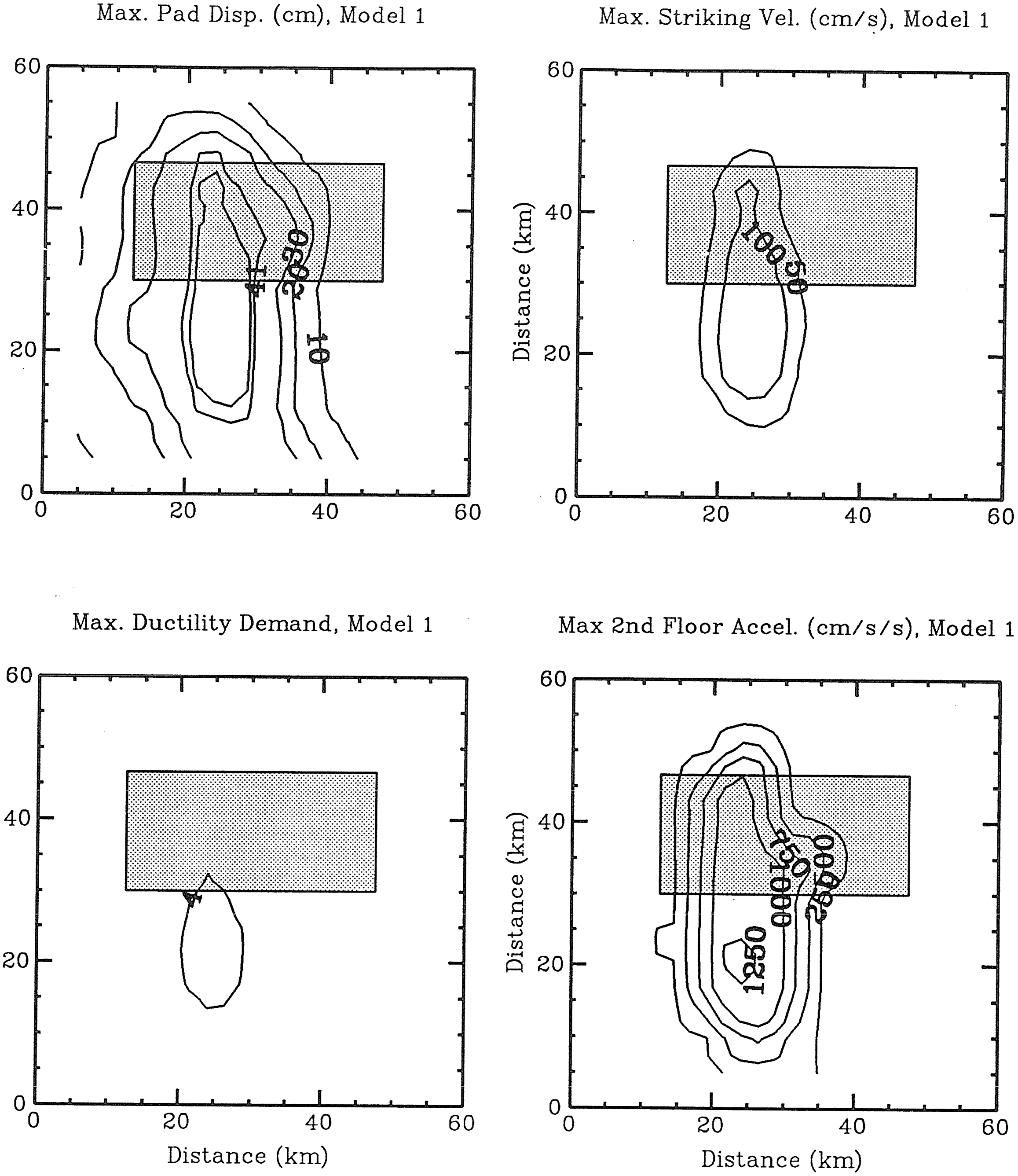

Figure 7.14 **TBIB-model 1** contours of maximum bearing (pad) displacement (first floor displacement), maximum striking velocity, maximum ductility demand, and maximum second floor acceleration using the **complete set** of synthetic motion stations.

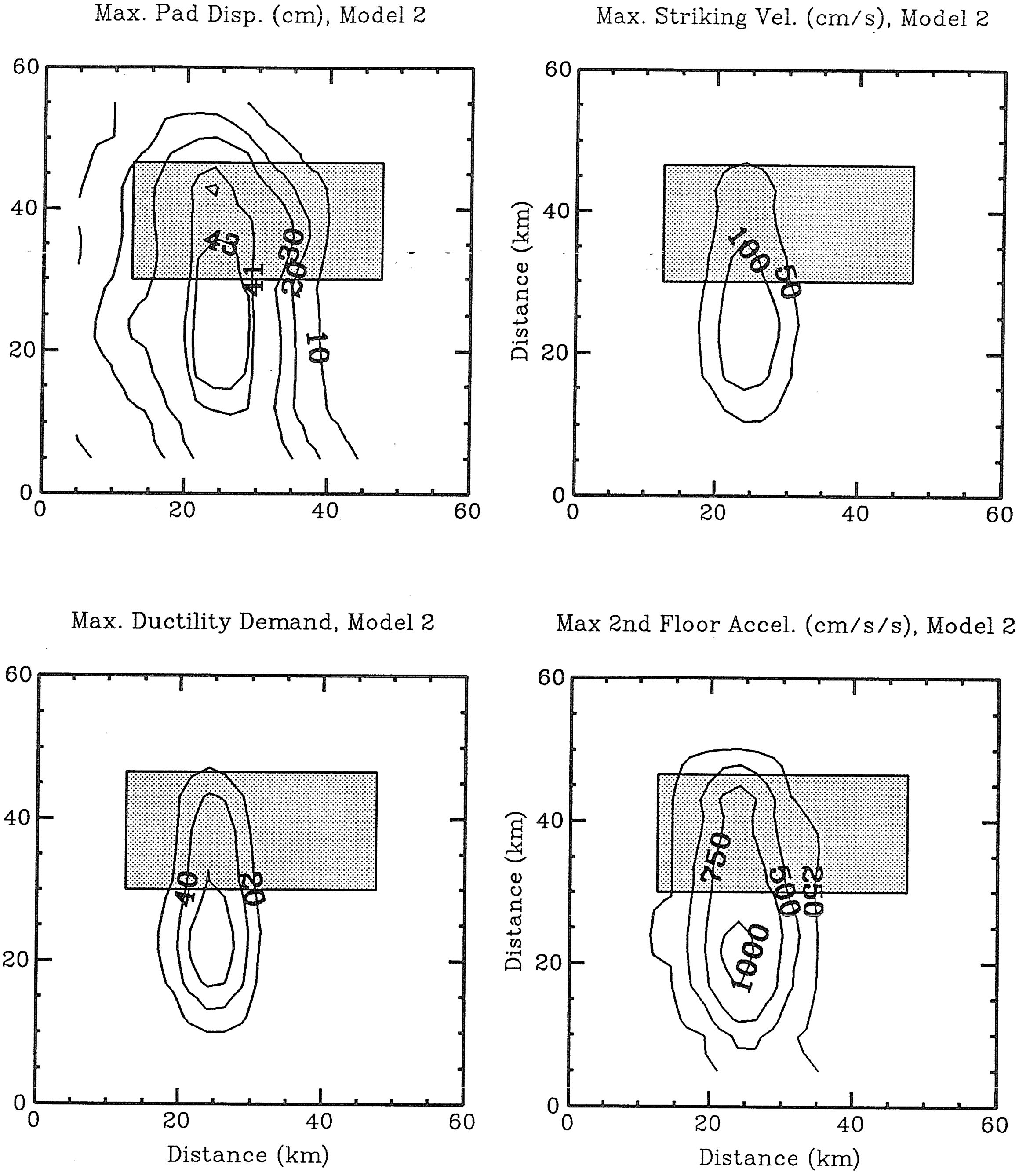

Figure 7.15 TBIB-**model 2** contours of maximum bearing (pad) displacement (first floor displacement), maximum striking velocity, maximum ductility demand, and maximum second floor acceleration using the **complete set** of synthetic motion stations.

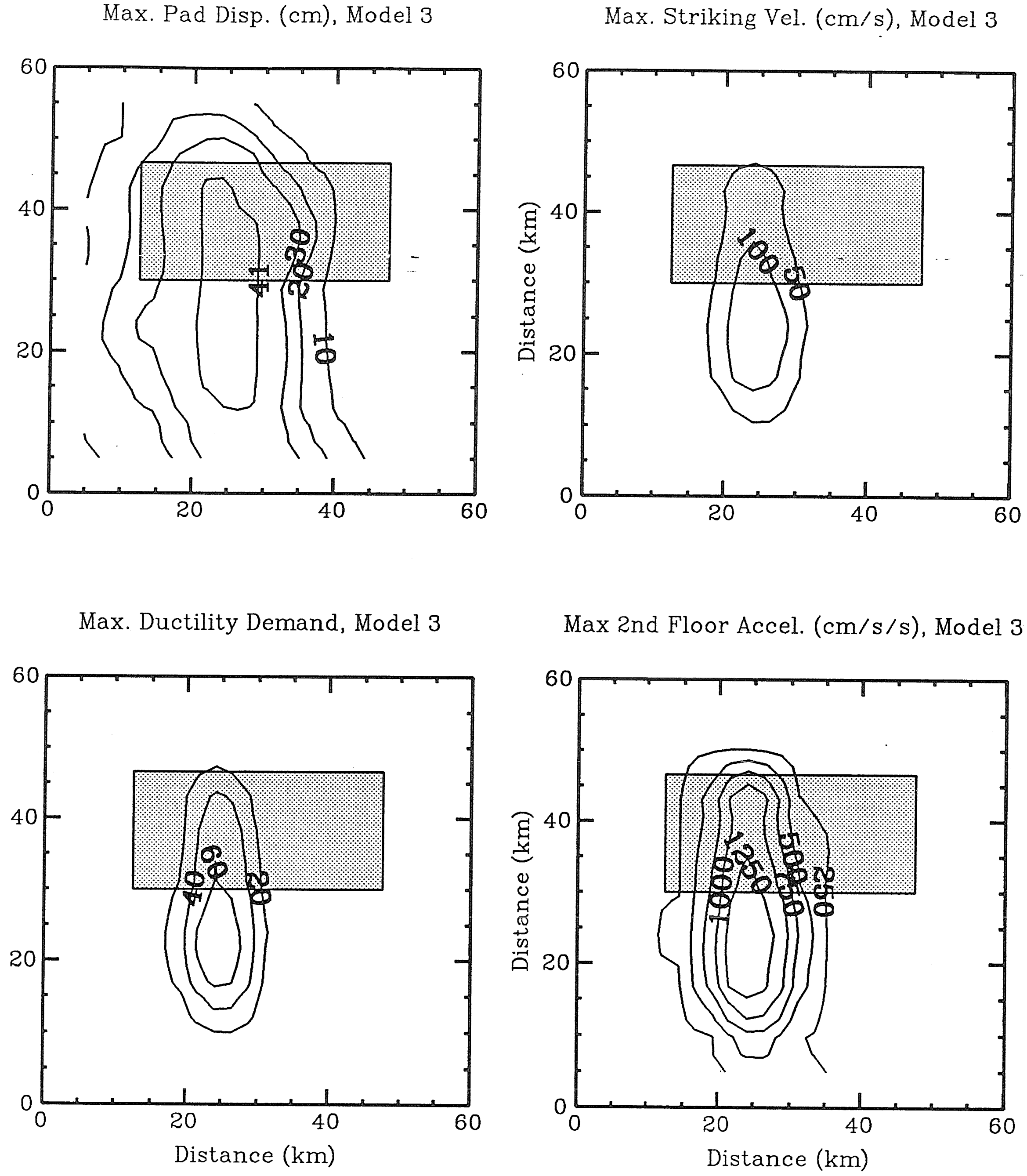

Figure 7.16 TBIB-**model 3** contours of maximum bearing (pad) displacement (first floor displacement), maximum striking velocity, maximum ductility demand, and maximum second floor acceleration using the **complete set** of synthetic motion stations.

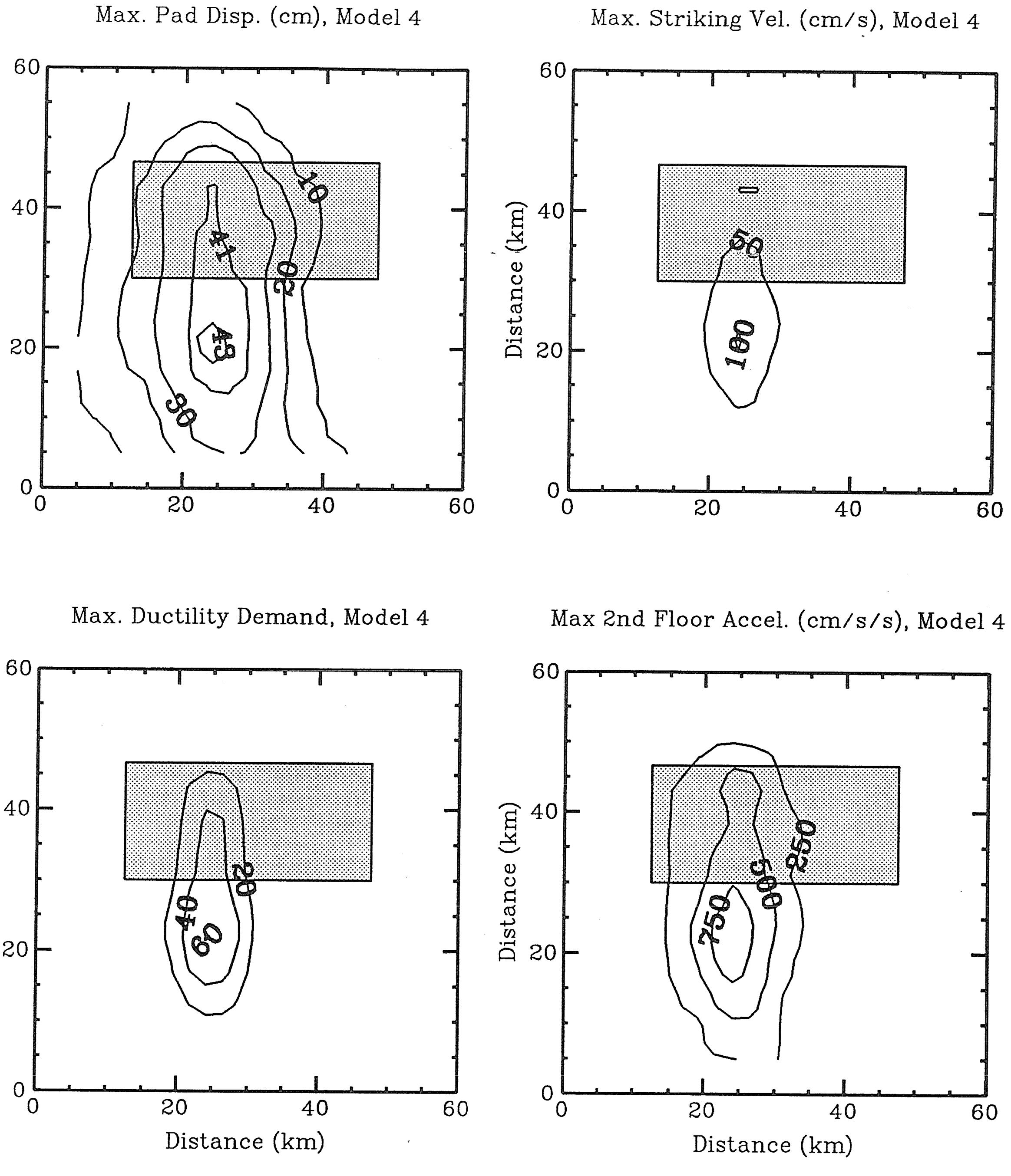

Figure 7.17 TBIB-**model 4** contours of maximum bearing (pad) displacement (first floor displacement), maximum striking velocity, maximum ductility demand, and maximum second floor acceleration using the **complete set** of synthetic motion stations.

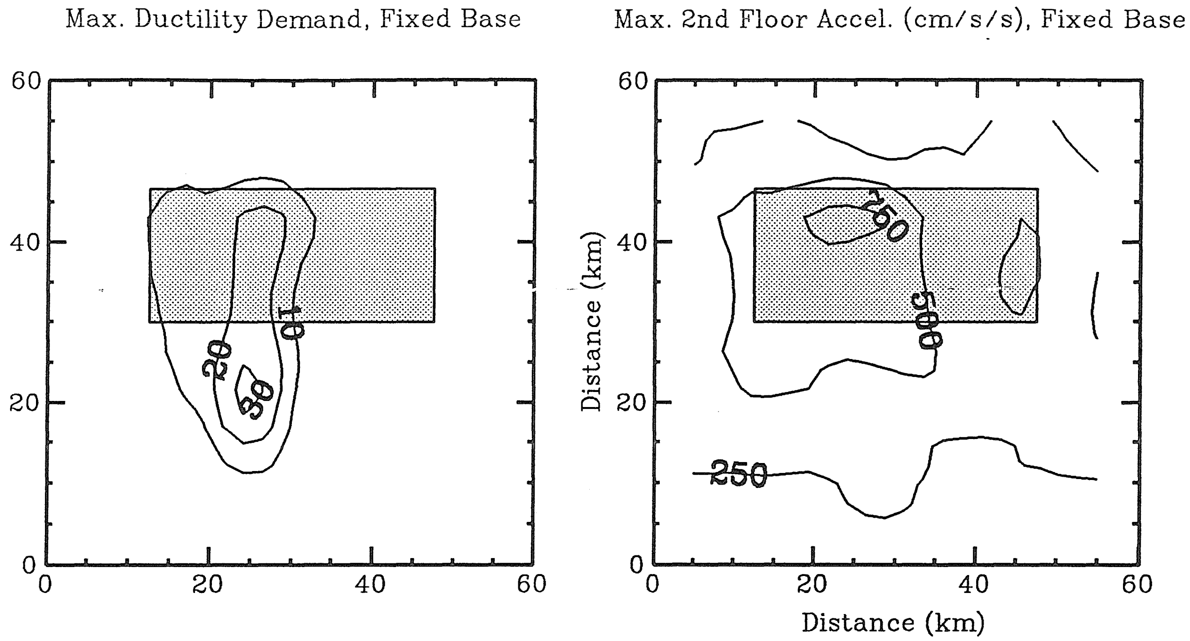

Max. Ductility Demand, Fixed Base

Max. 2nd Floor Accel. (cm/s/s), Fixed Base

Figure 7.18 **TBIB-Fixed-base** contours of maximum ductility demand, and maximum second floor acceleration using the **complete set** of synthetic motion stations.

Appendix A

GROUND MOTION QUANTITIES

PEAK GROUND DISPLACEMENT IN DIRECTION OF ANGLE (CM)

	1	2	3	4	5	6	7	8	9	10	11
K	28.	30.	36.	48.	57.	53.	45.	35.	23.	11.	13.
J	32.	34.	46.	71.	94.	93.	51.	49.	32.	16.	16.
I	36.	36.	57.	95.	144.	137.	49.	59.	39.	21.	20.
H	37.	37.	63.	109.	168.	152.	68.	67.	43.	33.	28.
G	36.	35.	62.	117.	178.	154.	82.	61.	40.	44.	39.
F	35.	33.	67.	122.	184.	157.	74.	54.	41.	51.	48.
E	34.	33.	70.	129.	196.	180.	72.	49.	52.	57.	60.
D	34.	35.	68.	128.	200.	173.	80.	57.	66.	73.	73.
C	34.	34.	61.	117.	184.	163.	95.	64.	76.	84.	73.
B	33.	35.	54.	96.	151.	146.	82.	59.	89.	84.	57.
A	34.	33.	46.	74.	110.	117.	72.	52.	75.	78.	71.

PEAK GROUND VELOCITY IN DIRECTION OF ANGLE (CM/SEC)

	1	2	3	4	5	6	7	8	9	10	11
K	40.	41.	52.	49.	46.	38.	31.	27.	24.	19.	18.
J	48.	52.	58.	73.	92.	63.	39.	37.	32.	31.	19.
I	51.	82.	99.	118.	162.	108.	55.	43.	35.	33.	20.
H	53.	82.	103.	96.	179.	117.	72.	46.	40.	34.	24.
G	49.	83.	87.	103.	171.	112.	74.	39.	45.	33.	24.
F	49.	88.	72.	112.	153.	105.	66.	43.	44.	35.	25.
E	50.	95.	80.	119.	155.	123.	66.	49.	48.	36.	25.
D	51.	87.	73.	118.	158.	117.	66.	56.	58.	38.	28.
C	49.	71.	65.	107.	140.	113.	80.	77.	59.	42.	29.
B	47.	61.	58.	85.	116.	100.	81.	71.	57.	47.	27.
A	46.	52.	50.	67.	82.	80.	87.	76.	61.	45.	33.

PEAK GROUND ACCELERATION IN DIRECTION OF ANGLE (CM/SEC/SEC)

	1	2	3	4	5	6	7	8	9	10	11
K	294.	294.	267.	225.	200.	176.	177.	235.	332.	386.	303.
J	272.	452.	384.	338.	351.	255.	307.	367.	467.	595.	339.
I	536.	744.	791.	948.	1039.	865.	479.	380.	598.	593.	323.
H	503.	732.	779.	835.	910.	847.	440.	433.	632.	561.	317.
G	501.	700.	772.	793.	842.	888.	462.	450.	672.	541.	300.
F	481.	671.	743.	738.	803.	864.	525.	462.	616.	487.	270.
E	463.	624.	710.	640.	658.	659.	637.	529.	492.	468.	335.
D	425.	579.	595.	485.	448.	349.	582.	519.	353.	472.	314.
C	395.	384.	402.	333.	397.	330.	299.	220.	230.	333.	400.
B	332.	313.	297.	243.	295.	287.	240.	199.	212.	304.	335.
A	183.	225.	244.	208.	225.	251.	192.	195.	179.	196.	216.

ANGLE FOR EACH STATION (degrees, clockwise from north)

	1	2	3	4	5	6	7	8	9	10	11
K	-8.	-26.	-31.	-36.	-47.	-52.	-67.	-86.	59.	16.	0.
J	-27.	-22.	-27.	-34.	-39.	-58.	-37.	-89.	64.	18.	-8.
I	-22.	-17.	-23.	-26.	-38.	-61.	-19.	-86.	48.	17.	-12.
H	-15.	-13.	-19.	-24.	-37.	-54.	-24.	85.	38.	5.	-14.
G	-13.	-9.	-16.	-17.	-27.	-31.	-22.	80.	24.	-3.	-19.
F	-9.	-6.	-9.	-9.	-14.	-17.	-10.	-21.	3.	-11.	-25.
E	-4.	-7.	-2.	1.	1.	4.	14.	-8.	-18.	-14.	-6.
D	0.	4.	6.	10.	17.	28.	26.	2.	-31.	-13.	-12.
C	4.	8.	12.	18.	33.	57.	78.	-56.	-31.	-8.	19.
B	5.	10.	18.	26.	42.	69.	-69.	-52.	-23.	3.	30.
A	23.	12.	20.	26.	41.	72.	-60.	-38.	-18.	-15.	-8.

SDOF OSCILLATOR PEAK VALUES IN DIR OF ANGLE

PEAK OSCILLATOR DISP. (cm), PER=2.2 SEC, DAMP=10%

	1	2	3	4	5	6	7	8	9	10	11
K	18.	21.	27.	30.	27.	17.	15.	14.	11.	6.	5.
J	17.	23.	33.	46.	50.	28.	18.	15.	12.	8.	5.
I	17.	23.	35.	53.	69.	39.	28.	18.	12.	9.	6.
H	16.	22.	37.	57.	73.	41.	37.	17.	14.	11.	7.
G	14.	23.	34.	57.	69.	49.	39.	13.	12.	10.	5.
F	17.	27.	37.	61.	67.	50.	26.	13.	11.	10.	6.
E	19.	30.	44.	71.	77.	59.	30.	18.	11.	8.	4.
D	20.	29.	42.	70.	81.	54.	32.	14.	12.	8.	4.
C	19.	26.	36.	59.	74.	52.	29.	18.	11.	8.	3.
B	18.	23.	30.	44.	59.	44.	26.	20.	13.	8.	4.
A	15.	19.	26.	36.	42.	42.	40.	22.	15.	7.	5.

PEAK OSCILLATOR DISP. (cm), PER=2.2 SEC, DAMP=20%

K	13.	15.	20.	22.	21.	14.	12.	11.	8.	5.	4.
J	14.	17.	23.	34.	36.	24.	15.	11.	10.	6.	4.
I	14.	18.	29.	44.	57.	33.	21.	16.	10.	7.	5.
H	13.	17.	31.	43.	60.	35.	29.	15.	12.	9.	5.
G	11.	18.	29.	46.	59.	42.	30.	11.	11.	9.	4.
F	12.	21.	31.	48.	56.	43.	20.	11.	10.	8.	4.
E	14.	24.	35.	54.	63.	51.	22.	15.	10.	7.	4.
D	14.	23.	35.	54.	67.	46.	25.	13.	10.	7.	3.
C	13.	21.	30.	48.	63.	44.	25.	16.	10.	7.	3.
B	13.	18.	25.	36.	49.	37.	22.	17.	11.	7.	4.
A	12.	15.	21.	30.	36.	35.	32.	20.	14.	6.	5.

PEAK OSCILLATOR DISP. (cm), PER=1.4 SEC, DAMP=20%

K	6.	7.	8.	10.	8.	6.	5.	4.	3.	2.	2.
J	5.	8.	11.	15.	17.	9.	7.	6.	5.	3.	2.
I	6.	10.	16.	22.	27.	14.	7.	6.	5.	3.	2.
H	7.	10.	16.	19.	25.	17.	9.	6.	5.	4.	2.
G	6.	10.	13.	21.	27.	19.	11.	5.	4.	4.	2.
F	7.	11.	12.	22.	28.	17.	8.	4.	4.	3.	2.
E	6.	14.	15.	25.	28.	22.	8.	6.	4.	3.	2.
D	8.	11.	15.	25.	31.	19.	8.	4.	4.	3.	2.
C	7.	8.	12.	22.	27.	16.	10.	5.	4.	3.	2.
B	6.	7.	10.	16.	20.	14.	8.	6.	5.	3.	2.
A	5.	7.	9.	13.	15.	12.	10.	7.	5.	3.	2.

PEAK OSCILLATOR DISP. (cm), PER=3.0 SEC, DAMP=20%

K	22.	26.	29.	32.	31.	22.	19.	15.	12.	9.	7.
J	26.	28.	35.	48.	57.	37.	22.	20.	15.	11.	7.
I	27.	29.	41.	59.	80.	54.	35.	24.	17.	12.	8.
H	25.	27.	43.	66.	90.	58.	44.	26.	20.	15.	8.
G	23.	25.	41.	67.	92.	57.	59.	20.	18.	14.	8.
F	23.	29.	46.	71.	91.	67.	40.	20.	18.	13.	7.
E	25.	32.	51.	78.	97.	76.	43.	23.	16.	12.	7.
D	25.	31.	50.	78.	103.	75.	43.	24.	17.	12.	5.
C	23.	28.	43.	69.	93.	70.	44.	30.	17.	11.	5.
B	23.	25.	37.	54.	73.	63.	47.	30.	20.	13.	7.
A	22.	24.	30.	44.	57.	55.	50.	43.	32.	14.	9.

MODEL 1

MAX BEARING DISPLACEMENT (cm)

	1	2	3	4	5	6	7	8	9	10	11
K	7.	11.	17.	17.	14.	7.	4.	3.	5.	3.	2.
J	6.	12.	22.	39.	42.	18.	9.	7.	5.	3.	3.
I	8.	20.	31.	43.	45.	35.	15.	9.	5.	4.	3.
H	11.	19.	33.	42.	43.	41.	33.	9.	5.	4.	4.
G	9.	21.	29.	43.	44.	42.	42.	6.	5.	3.	4.
F	11.	26.	29.	43.	45.	42.	18.	5.	4.	5.	3.
E	10.	30.	34.	44.	45.	43.	21.	6.	4.	4.	2.
D	14.	28.	34.	44.	46.	43.	24.	5.	5.	5.	3.
C	12.	20.	28.	43.	45.	42.	22.	9.	4.	3.	3.
B	12.	16.	21.	40.	43.	41.	21.	10.	5.	4.	4.
A	8.	12.	15.	29.	38.	37.	36.	17.	10.	3.	2.

MAX STRIKING VELOCITY (cm/sec)

	1	2	3	4	5	6	7	8	9	10	11
K	0.	0.	0.	0.	0.	0.	0.	0.	0.	0.	0.
J	0.	0.	0.	0.	63.	0.	0.	0.	0.	0.	0.
I	0.	0.	0.	86.	136.	0.	0.	0.	0.	0.	0.
H	0.	0.	0.	69.	117.	0.	0.	0.	0.	0.	0.
G	0.	0.	0.	92.	137.	59.	43.	0.	0.	0.	0.
F	0.	0.	0.	103.	148.	69.	0.	0.	0.	0.	0.
E	0.	0.	0.	127.	151.	103.	0.	0.	0.	0.	0.
D	0.	0.	0.	127.	165.	82.	0.	0.	0.	0.	0.
C	0.	0.	0.	101.	140.	69.	0.	0.	0.	0.	0.
B	0.	0.	0.	0.	98.	26.	0.	0.	0.	0.	0.
A	0.	0.	0.	0.	0.	0.	0.	0.	0.	0.	0.

MAX DUCTILITY DEMAND

	1	2	3	4	5	6	7	8	9	10	11
K	0.	0.	0.	0.	0.	0.	0.	0.	0.	0.	0.
J	0.	0.	0.	0.	1.	0.	0.	0.	0.	0.	0.
I	0.	0.	0.	2.	5.	0.	0.	0.	0.	0.	0.
H	0.	0.	0.	2.	5.	0.	0.	0.	0.	0.	0.
G	0.	0.	0.	3.	4.	1.	0.	0.	0.	0.	0.
F	0.	0.	0.	3.	5.	2.	0.	0.	0.	0.	0.
E	0.	0.	0.	4.	6.	3.	0.	0.	0.	0.	0.
D	0.	0.	0.	4.	9.	2.	0.	0.	0.	0.	0.
C	0.	0.	0.	3.	7.	2.	0.	0.	0.	0.	0.
B	0.	0.	0.	0.	3.	0.	0.	0.	0.	0.	0.
A	0.	0.	0.	0.	0.	0.	0.	0.	0.	0.	0.

MAX 2ND FLOOR ACCELERATION (cm/sec/sec)

	1	2	3	4	5	6	7	8	9	10	11
K	97.	133.	166.	155.	137.	96.	90.	81.	103.	97.	84.
J	94.	130.	179.	289.	1068.	158.	117.	91.	101.	110.	90.
I	152.	226.	251.	1149.	1189.	253.	150.	118.	114.	105.	86.
H	143.	211.	266.	1076.	1219.	310.	251.	114.	118.	107.	88.
G	152.	199.	252.	1191.	1214.	992.	840.	111.	109.	98.	89.
F	150.	228.	220.	1216.	1202.	1114.	161.	129.	109.	101.	90.
E	149.	252.	264.	1224.	1217.	1156.	185.	113.	113.	105.	87.
D	142.	240.	263.	1224.	1335.	1131.	196.	109.	121.	119.	87.
C	136.	191.	217.	1208.	1218.	1134.	186.	104.	90.	83.	99.
B	122.	160.	181.	301.	1193.	662.	181.	113.	88.	90.	98.
A	118.	137.	146.	234.	286.	269.	272.	153.	116.	76.	73.

MODEL 2

	1	2	3	4	5	6	7	8	9	10	11
MAX BEARING DISPLACEMENT (cm)											
K	7.	11.	17.	17.	14.	7.	4.	3.	5.	3.	2.
J	6.	12.	22.	34.	39.	18.	9.	7.	5.	3.	3.
I	8.	20.	30.	42.	44.	34.	15.	9.	5.	4.	3.
H	11.	19.	32.	42.	43.	40.	31.	9.	5.	4.	4.
G	9.	21.	28.	42.	44.	41.	36.	6.	5.	3.	4.
F	11.	25.	29.	43.	44.	42.	18.	5.	4.	5.	3.
E	10.	29.	33.	43.	44.	43.	21.	6.	4.	4.	2.
D	14.	27.	33.	43.	45.	42.	24.	5.	5.	5.	3.
C	12.	20.	27.	43.	44.	42.	22.	9.	4.	3.	3.
B	12.	16.	21.	37.	43.	39.	21.	10.	5.	4.	4.
A	8.	12.	15.	28.	36.	33.	34.	17.	10.	3.	2.
MAX STRIKING VELOCITY (cm/sec)											
K	0.	0.	0.	0.	0.	0.	0.	0.	0.	0.	0.
J	0.	0.	0.	0.	0.	0.	0.	0.	0.	0.	0.
I	0.	0.	0.	70.	126.	0.	0.	0.	0.	0.	0.
H	0.	0.	0.	52.	100.	0.	0.	0.	0.	0.	0.
G	0.	0.	0.	78.	121.	31.	0.	0.	0.	0.	0.
F	0.	0.	0.	88.	134.	49.	0.	0.	0.	0.	0.
E	0.	0.	0.	114.	138.	90.	0.	0.	0.	0.	0.
D	0.	0.	0.	112.	153.	65.	0.	0.	0.	0.	0.
C	0.	0.	0.	88.	128.	57.	0.	0.	0.	0.	0.
B	0.	0.	0.	0.	87.	0.	0.	0.	0.	0.	0.
A	0.	0.	0.	0.	0.	0.	0.	0.	0.	0.	0.
MAX DUCTILITY DEMAND											
K	0.	0.	0.	0.	0.	0.	0.	0.	0.	0.	0.
J	0.	0.	1.	5.	9.	0.	0.	0.	0.	0.	0.
I	0.	0.	3.	22.	44.	4.	0.	0.	0.	0.	0.
H	0.	0.	4.	21.	74.	6.	4.	0.	0.	0.	0.
G	0.	0.	3.	27.	75.	13.	8.	0.	0.	0.	0.
F	0.	2.	2.	32.	75.	19.	0.	0.	0.	0.	0.
E	0.	3.	4.	47.	85.	33.	0.	0.	0.	0.	0.
D	0.	2.	4.	47.	96.	28.	1.	0.	0.	0.	0.
C	0.	0.	2.	30.	69.	24.	0.	0.	0.	0.	0.
B	0.	0.	0.	7.	33.	9.	0.	0.	0.	0.	0.
A	0.	0.	0.	3.	6.	4.	5.	0.	0.	0.	0.
MAX 2ND FLOOR ACCELERATION (cm/sec/sec)											
K	97.	133.	166.	155.	137.	96.	90.	81.	103.	97.	84.
J	94.	130.	193.	289.	294.	158.	117.	91.	101.	110.	90.
I	152.	226.	256.	738.	1017.	282.	150.	118.	114.	105.	86.
H	143.	211.	265.	593.	875.	308.	261.	114.	118.	107.	88.
G	152.	199.	262.	802.	987.	453.	282.	111.	109.	98.	89.
F	150.	235.	246.	832.	1031.	569.	161.	129.	109.	101.	90.
E	149.	249.	284.	953.	1030.	889.	188.	113.	113.	105.	87.
D	142.	242.	276.	968.	1117.	732.	205.	109.	121.	119.	87.
C	136.	187.	228.	832.	1045.	680.	189.	104.	90.	83.	99.
B	122.	160.	181.	303.	866.	288.	180.	113.	88.	90.	98.
A	118.	137.	146.	243.	291.	276.	282.	153.	116.	76.	73.

MODEL 3

	1	2	3	4	5	6	7	8	9	10	11
MAX BEARING DISPLACEMENT (cm)											
K	7.	11.	17.	17.	14.	7.	4.	3.	5.	3.	2.
J	6.	12.	22.	34.	39.	18.	9.	7.	5.	3.	3.
I	8.	20.	30.	42.	42.	34.	15.	9.	5.	4.	3.
H	11.	19.	32.	41.	42.	40.	31.	9.	5.	4.	4.
G	9.	21.	28.	42.	42.	41.	36.	6.	5.	3.	4.
F	11.	25.	29.	42.	42.	41.	18.	5.	4.	5.	3.
E	10.	29.	33.	42.	42.	42.	21.	6.	4.	4.	2.
D	14.	27.	33.	42.	42.	42.	24.	5.	5.	5.	3.
C	12.	20.	27.	42.	42.	42.	22.	9.	4.	3.	3.
B	12.	16.	21.	37.	42.	39.	21.	10.	5.	4.	4.
A	8.	12.	15.	28.	36.	33.	34.	17.	10.	3.	2.
MAX STRIKING VELOCITY (cm/sec)											
K	0.	0.	0.	0.	0.	0.	0.	0.	0.	0.	0.
J	0.	0.	0.	0.	0.	0.	0.	0.	0.	0.	0.
I	0.	0.	0.	70.	126.	0.	0.	0.	0.	0.	0.
H	0.	0.	0.	52.	100.	0.	0.	0.	0.	0.	0.
G	0.	0.	0.	78.	121.	31.	0.	0.	0.	0.	0.
F	0.	0.	0.	88.	134.	49.	0.	0.	0.	0.	0.
E	0.	0.	0.	114.	138.	90.	0.	0.	0.	0.	0.
D	0.	0.	0.	112.	153.	65.	0.	0.	0.	0.	0.
C	0.	0.	0.	88.	128.	57.	0.	0.	0.	0.	0.
B	0.	0.	0.	0.	87.	0.	0.	0.	0.	0.	0.
A	0.	0.	0.	0.	0.	0.	0.	0.	0.	0.	0.
MAX DUCTILITY DEMAND											
K	0.	0.	0.	0.	0.	0.	0.	0.	0.	0.	0.
J	0.	0.	1.	5.	9.	0.	0.	0.	0.	0.	0.
I	0.	0.	3.	22.	46.	4.	0.	0.	0.	0.	0.
H	0.	0.	4.	21.	72.	6.	4.	0.	0.	0.	0.
G	0.	0.	3.	27.	76.	14.	8.	0.	0.	0.	0.
F	0.	2.	2.	33.	75.	19.	0.	0.	0.	0.	0.
E	0.	3.	4.	48.	84.	34.	0.	0.	0.	0.	0.
D	0.	2.	4.	48.	95.	28.	1.	0.	0.	0.	0.
C	0.	0.	2.	30.	71.	24.	0.	0.	0.	0.	0.
B	0.	0.	0.	7.	32.	9.	0.	0.	0.	0.	0.
A	0.	0.	0.	3.	6.	4.	5.	0.	0.	0.	0.
MAX 2ND FLOOR ACCELERATION (cm/sec/sec)											
K	97.	133.	166.	155.	137.	96.	90.	81.	103.	97.	84.
J	94.	130.	193.	289.	294.	158.	117.	91.	101.	110.	90.
I	152.	226.	256.	856.	1560.	282.	150.	118.	114.	105.	86.
H	143.	211.	265.	761.	1238.	308.	261.	114.	118.	107.	88.
G	152.	199.	262.	991.	1413.	554.	282.	111.	109.	98.	89.
F	150.	235.	246.	1083.	1464.	728.	161.	129.	109.	101.	90.
E	149.	249.	283.	1215.	1487.	1082.	188.	113.	113.	105.	87.
D	142.	242.	276.	1282.	1567.	877.	205.	109.	121.	119.	87.
C	135.	187.	228.	1082.	1525.	818.	189.	104.	90.	83.	99.
B	122.	160.	181.	302.	1041.	288.	180.	113.	88.	90.	98.
A	118.	137.	146.	243.	291.	276.	282.	153.	116.	76.	73.

MODEL 4

MAX BEARING DISPLACEMENT (cm)

	1	2	3	4	5	6	7	8	9	10	11
K	6.	8.	15.	15.	12.	6.	4.	3.	4.	3.	2.
J	5.	10.	16.	29.	31.	16.	8.	6.	4.	3.	2.
I	7.	15.	26.	40.	43.	29.	11.	8.	5.	3.	3.
H	9.	14.	27.	39.	42.	34.	24.	8.	5.	3.	3.
G	7.	15.	24.	41.	42.	36.	27.	6.	4.	3.	3.
F	9.	19.	25.	42.	43.	38.	14.	5.	3.	5.	3.
E	8.	23.	29.	42.	43.	42.	15.	5.	4.	4.	2.
D	11.	21.	28.	42.	44.	41.	17.	5.	5.	5.	3.
C	10.	16.	23.	42.	43.	40.	19.	8.	4.	3.	3.
B	10.	12.	17.	32.	42.	34.	16.	9.	5.	4.	3.
A	6.	10.	13.	24.	31.	29.	26.	14.	9.	3.	2.

MAX STRIKING VELOCITY (cm/sec)

	1	2	3	4	5	6	7	8	9	10	11
K	0.	0.	0.	0.	0.	0.	0.	0.	0.	0.	0.
J	0.	0.	0.	0.	0.	0.	0.	0.	0.	0.	0.
I	0.	0.	0.	0.	95.	0.	0.	0.	0.	0.	0.
H	0.	0.	0.	0.	41.	0.	0.	0.	0.	0.	0.
G	0.	0.	0.	28.	78.	0.	0.	0.	0.	0.	0.
F	0.	0.	0.	44.	98.	0.	0.	0.	0.	0.	0.
E	0.	0.	0.	75.	102.	54.	0.	0.	0.	0.	0.
D	0.	0.	0.	75.	123.	23.	0.	0.	0.	0.	0.
C	0.	0.	0.	45.	97.	0.	0.	0.	0.	0.	0.
B	0.	0.	0.	0.	58.	0.	0.	0.	0.	0.	0.
A	0.	0.	0.	0.	0.	0.	0.	0.	0.	0.	0.

MAX DUCTILITY DEMAND

	1	2	3	4	5	6	7	8	9	10	11
K	0.	0.	0.	0.	0.	0.	0.	0.	0.	0.	0.
J	0.	0.	0.	4.	4.	0.	0.	0.	0.	0.	0.
I	0.	0.	3.	11.	35.	4.	0.	0.	0.	0.	0.
H	0.	0.	3.	13.	58.	5.	2.	0.	0.	0.	0.
G	0.	0.	2.	19.	60.	8.	3.	0.	0.	0.	0.
F	0.	0.	2.	24.	60.	11.	0.	0.	0.	0.	0.
E	0.	1.	3.	35.	67.	26.	0.	0.	0.	0.	0.
D	0.	1.	3.	35.	76.	21.	0.	0.	0.	0.	0.
C	0.	0.	1.	22.	55.	14.	0.	0.	0.	0.	0.
B	0.	0.	0.	5.	25.	5.	0.	0.	0.	0.	0.
A	0.	0.	0.	2.	4.	3.	3.	0.	0.	0.	0.

MAX 2ND FLOOR ACCELERATION (cm/sec/sec)

	1	2	3	4	5	6	7	8	9	10	11
K	92.	117.	143.	149.	129.	94.	97.	91.	112.	102.	82.
J	88.	120.	158.	255.	267.	153.	112.	101.	113.	125.	91.
I	121.	216.	247.	336.	853.	285.	131.	121.	135.	116.	92.
H	136.	220.	250.	311.	543.	331.	209.	121.	139.	107.	94.
G	126.	216.	253.	390.	763.	312.	237.	115.	122.	97.	89.
F	129.	213.	228.	513.	851.	319.	140.	120.	111.	111.	90.
E	147.	236.	257.	722.	854.	610.	149.	123.	112.	114.	88.
D	131.	217.	252.	735.	960.	385.	161.	113.	119.	122.	93.
C	126.	165.	219.	514.	871.	310.	177.	101.	92.	86.	99.
B	115.	141.	170.	268.	636.	270.	149.	110.	84.	91.	101.
A	106.	130.	136.	209.	263.	257.	229.	141.	108.	85.	64.

FIXED-BASE MODEL

MAX BEARING DISPLACEMENT (cm)

	1	2	3	4	5	6	7	8	9	10	11
K	0.	0.	0.	0.	0.	0.	0.	0.	0.	0.	0.
J	0.	0.	0.	0.	0.	0.	0.	0.	0.	0.	0.
I	0.	0.	0.	0.	0.	0.	0.	0.	0.	0.	0.
H	0.	0.	0.	0.	0.	0.	0.	0.	0.	0.	0.
G	0.	0.	0.	0.	0.	0.	0.	0.	0.	0.	0.
F	0.	0.	0.	0.	0.	0.	0.	0.	0.	0.	0.
E	0.	0.	0.	0.	0.	0.	0.	0.	0.	0.	0.
D	0.	0.	0.	0.	0.	0.	0.	0.	0.	0.	0.
C	0.	0.	0.	0.	0.	0.	0.	0.	0.	0.	0.
B	0.	0.	0.	0.	0.	0.	0.	0.	0.	0.	0.
A	0.	0.	0.	0.	0.	0.	0.	0.	0.	0.	0.

MAX STRIKING VELOCITY (cm/sec)

K	0.	0.	0.	0.	0.	0.	0.	0.	0.	0.	0.
J	0.	0.	0.	0.	0.	0.	0.	0.	0.	0.	0.
I	0.	0.	0.	0.	0.	0.	0.	0.	0.	0.	0.
H	0.	0.	0.	0.	0.	0.	0.	0.	0.	0.	0.
G	0.	0.	0.	0.	0.	0.	0.	0.	0.	0.	0.
F	0.	0.	0.	0.	0.	0.	0.	0.	0.	0.	0.
E	0.	0.	0.	0.	0.	0.	0.	0.	0.	0.	0.
D	0.	0.	0.	0.	0.	0.	0.	0.	0.	0.	0.
C	0.	0.	0.	0.	0.	0.	0.	0.	0.	0.	0.
B	0.	0.	0.	0.	0.	0.	0.	0.	0.	0.	0.
A	0.	0.	0.	0.	0.	0.	0.	0.	0.	0.	0.

MAX DUCTILITY DEMAND

K	1.	2.	2.	2.	2.	1.	1.	1.	1.	1.	1.
J	2.	3.	5.	4.	4.	3.	3.	3.	1.	2.	1.
I	3.	5.	19.	12.	26.	19.	4.	3.	2.	1.	1.
H	3.	4.	20.	8.	31.	16.	4.	2.	2.	2.	1.
G	3.	4.	18.	8.	32.	8.	7.	2.	2.	2.	1.
F	2.	4.	14.	10.	32.	7.	4.	3.	2.	2.	1.
E	2.	6.	12.	18.	34.	14.	3.	3.	3.	2.	1.
D	2.	3.	6.	17.	43.	8.	1.	3.	2.	2.	1.
C	1.	2.	3.	10.	31.	4.	2.	2.	2.	1.	1.
B	1.	2.	1.	2.	10.	3.	1.	1.	2.	1.	1.
A	0.	1.	0.	1.	2.	2.	1.	1.	1.	1.	1.

MAX 2ND FLOOR ACCELERATION (cm/sec/sec)

K	235.	239.	260.	237.	199.	203.	216.	205.	294.	329.	229.
J	237.	363.	297.	317.	302.	258.	304.	267.	397.	505.	288.
I	388.	608.	642.	847.	906.	730.	391.	287.	489.	502.	268.
H	370.	571.	627.	747.	681.	708.	348.	395.	525.	484.	262.
G	371.	560.	568.	670.	666.	780.	367.	397.	573.	467.	242.
F	351.	559.	597.	630.	604.	733.	433.	345.	534.	399.	226.
E	344.	629.	590.	537.	473.	619.	535.	432.	391.	375.	278.
D	316.	487.	509.	449.	367.	311.	483.	415.	322.	384.	255.
C	299.	316.	342.	313.	359.	359.	239.	215.	250.	274.	342.
B	253.	243.	240.	227.	301.	314.	222.	208.	241.	247.	261.
A	161.	190.	220.	194.	232.	244.	212.	202.	210.	199.	180.